

Di-electron spectroscopy in HADES and CBM:

**from $p + p$ and $n + p$ collisions at GSI
to $Au + Au$ collisions at FAIR**

Dissertation
zur Erlangung des Doktorgrades
der Naturwissenschaften

vorgelegt am Fachbereich Physik
der Goethe-Universität
in Frankfurt am Main

von
Tetyana Galatyuk
aus Kuznetsovsk, Ukraine

Frankfurt 2009
(D 30)

vom Fachbereich Physik der
Goethe-Universität als Dissertation angenommen.

Dekan: Prof. Dr. D. Rischke
Gutachter: Prof. Dr. J. Stroth, Prof. Dr. P. Senger
Datum der Disputation: 17 Juli 2009

Kurzfassung

Untersuchungen der elektromagnetischen Struktur von Hadronen spielen eine wichtige Rolle um die Eigenschaften von stark wechselwirkender Materie zu verstehen. Insbesondere die Emission von Leptonenpaare aus der heißen und dichten Phase in Schwerionenkollisionen stellt eine vielversprechende Probe in der Untersuchung von veränderten Eigenschaften der Hadronen im Medium und der Eigenschaften von Materie unter extremen Bedingungen dar. Das DLS Experiment [1] beobachtete einen Überschuss der Elektronenpaarausbeute über die Erwartungen im invarianten Massenbereich von $0.3 - 0.7 \text{ GeV}/c^2$ in $p+Be$ -Kollisionen bei $4.9 \text{ GeV}/u$ Strahlenergie [2]. Neuere Ergebnisse des HADES Experimentes bestätigen diese DLS Resultate und zeigen einen Überschuss von Elektronenpaare über den erwarteten Beiträgen von η Dalitz-Zerfällen für $^{12}C+^{12}C$ -Reaktionen bei 1 und 2 GeV/u Strahlenergie [3, 4]. Diese Beobachtung wird in verschiedenen theoretischen Ansätzen unterschiedlich erklärt, die meisten Deutungen konzentrieren sich auf Veränderungen der Eigenschaften der Vektormesonen im Medium. Allerdings bleibt diese Interpretation insbesondere bei diesen niedrigen Strahlenergien wegen der großen Unsicherheiten in den elementaren Elektronenpaarquellen unsicher.

In dieser Arbeit wurde die mit dem HADES Experiment gemessene Produktion von Elektronenpaare in $p+p$ und in aus $d+p$ extrahierten $n+p$ -Reaktionen bei Strahlenergien von $1.25 \text{ GeV}/u$ untersucht. Bei Energien von $E_{kin} = 1.25 \text{ GeV}/u$ befindet man sich in Proton-Proton Stößen noch unterhalb der Schwelle für η -Mesonproduktion, daher ist der Δ Dalitz-Zerfall die dominante Quelle für Elektronenpaare oberhalb der π^0 Dalitz-Zerfallsregion. Man beobachtet einen großen Unterschied in den Spektren aus $p+p$ und $n+p$ Reaktionen bei derselben Strahlenergie. Dieser Vergleich ermöglicht es, die Beiträge der Δ Dalitz-Zerfälle von denen aus np -Bremsstrahlung zu trennen. Das wesentliche Interesse liegt hier auf der Untersuchung von Isospin-Effekten in der Anregung baryonischer Resonanzen Produktion von Vektormesonen jenseits der Massenschale [5]. Ergebnisse der hier vorgestellten Analyse werden mit neueren Rechnungen verglichen. Ein experimentell bestimmter Cocktail zum Vergleich mit der Elektronenpaar-Produktion in $C+C$ wird vorgestellt.

Auch Ergebnisse der CERES [6] und NA60 [7] Kollaborationen bei höherer Strahlenergie einen Überschuss der Elektronenpaar-Produktion über den Erwartungen im invarianten Massenbereich von $0.3-0.7 \text{ GeV}/c^2$ zeigen. Erklärungen dieses Überschusses weisen auf einen starken Einfluss von Baryonen auf die Leptonenpaar-Emission hin. Es existieren allerdings noch keine Messungen im Bereich höchster Kompression von baryonischer Materie bzw. höchster Netto-Baryonendichte, die mit Schwerionenkollisionen bei $8-45 \text{ GeV}/u$ Strahlenergie erreicht werden können. Solche Bedingungen erlauben die Untersuchung der erwarteten Wiederherstellung der spontan gebrochenen Chiralen Symmetrie durch die Messung von Modifikationen der hadronischen Eigenschaften im Medium. Ein solches experimentelles Programm ist einer der Kernpunkte des geplanten CBM-Experimentes an FAIR. Die experimentelle Herausforderung besteht darin, den großen physikalischen Untergrund zu unterdrücken sowie eine saubere Elektronen Identifizierung zu erhalten. In dieser Arbeit wurden detaillierte Machbarkeitsstudien hierzu durchgeführt und es wurde gezeigt, dass mit der entwickelten Strategie der kombinatorische Untergrund mit der vorgeschlagenen Detektoranordnung hinreichend unterdrückt werden kann.

Abstract

The study of the electromagnetic structure of hadrons plays an important role in understanding the nature of matter. In particular the emission of lepton pairs out of the hot and dense collision zone in heavy-ion reactions is a promising probe to investigate in-medium properties of hadrons and in general the properties of matter under such extreme conditions. The first experimental observation of an enhanced di-electron yield in the invariant-mass region $0.3 - 0.7 \text{ GeV}/c^2$ in $p+Be$ collisions at $4.9 \text{ GeV}/u$ beam energy [2] was announced by the DLS collaboration [1]. Recent results of the HADES collaboration show a moderate enhancement above η Dalitz decay contributions for $^{12}C+^{12}C$ at 1 and 2 GeV/u [3, 4] confirming the DLS results. There are several theoretical explanations of this observation, most of them focusing on possible in-medium modifications of the properties of vector mesons. At low beam energies the question whether the observed excess is related to any in-medium effects remains open because of uncertainties in the description of elementary di-electron sources.

In this work the di-electron production in $p+p$ and $d+p$ reactions at a kinetic beam energy of $1.25 \text{ GeV}/u$ measured by the HADES spectrometer is discussed. At $E_{kin} = 1.25 \text{ GeV}/u$, i.e. below the η meson production threshold in proton-proton reactions, the Δ Dalitz decay is expected to be the most abundant source above the π^0 Dalitz decay region. The observed large difference in di-electron production in $p+p$ and $d+p$ collisions suggests that di-electron production in the $d+p$ system is dominated by the $n+p$ interaction. In order to separate Δ Dalitz decays and np bremsstrahlung the di-electron yield observed in $p+p$ and $n+p$ reactions, both measured at the same beam energy, has been compared. The main interest here is the investigation of iso-spin effects in baryonic resonance excitations and the off-shell production of vector mesons [5]. We indeed observe a large difference in di-electron production in $p+p$ and $n+p$ reactions. Results of these studies will be compared to recent calculations. We will also present our experimentally defined cocktail for heavy-ion data.

At much higher beam energies experimental results of the CERES [6] and NA60 [7] collaborations also show an enhancement in the invariant mass region $0.3 - 0.7 \text{ GeV}/c^2$, in principle similar to the situation in DLS. A strong excess of lepton pairs observed by recent high energy heavy-ion dilepton experiments hint to a strong influence of baryons, however no data exist at highly compressed baryonic matter, achievable in heavy-ion collisions from $8 - 45 \text{ GeV}/u$ beam energy. These conditions would allow to study the expected restoration of chiral symmetry by measuring in-medium modifications of hadronic properties, an experimental program which is foreseen by the future CBM experiment at FAIR. The experimental challenge is to suppress the large physical background on the one hand and to provide a clean identification of electrons on the other hand. In this work, strategies to reduce the combinatorial background in electron pair measurements with the CBM detector are discussed. The main goal is to study the feasibility of effectively reducing combinatorial background with the currently foreseen experimental setup, which does not provide electron identification in front of the magnetic field.

To my family.

Contents

Contents	i
List of Figures	iv
List of Tables	xiv
1 Introduction	1
1.1 Strongly interacting matter	2
1.1.1 The QCD phase diagram	2
1.1.2 The origin of hadron masses	4
1.1.3 The electromagnetic structure of hadrons	5
1.1.4 In-medium modifications	7
In-medium "dropping" mass scenario	7
In-medium "broadening" mass scenario	7
1.2 Probing extreme matter with virtual photons	9
1.3 Strongly interacting matter in models	11
1.3.1 Transport models	11
1.3.2 Fireball model	12
1.4 Strongly interacting matter in experiments	13
1.4.1 Dilepton production in elementary collisions	14
1.4.2 Dilepton production in heavy-ion collisions	15
1.4.3 Dilepton production in NN collisions	19
1.4.4 DLS and HADES: "Just a little bit of history repeated?"	20
2 The HADES experiment	25
2.1 Target and Start detector	26
2.1.1 The Target	26
2.1.2 The Start detector	27
2.2 The hadron-blind gaseous Ring Imaging Cherenkov detector (RICH)	27
2.3 HADES tracking system	28
2.4 The Multiplicity Electron Trigger Array detectors	29
2.4.1 The TOF scintillator walls	29
2.4.2 The Pre-Shower detector	30
2.5 The Forward hodoscope Wall	31
2.6 The Trigger System	32
2.7 Detector setups and running conditions	34
2.7.1 The $p+p$ run	34
2.7.2 The $d+p$ run	34

3	Methods for data analysis	35
3.1	Event selection	36
3.1.1	Study of pp elastic scattering reactions	36
3.1.2	Selection of the $n + p$ subreactions with the Forward hodoscope Wall	39
3.2	Event reconstruction	40
3.2.1	Track reconstruction and momentum determination	40
3.2.2	RICH ring reconstruction	42
3.2.3	Time-of-flight measurements without start detector	44
3.3	Electron identification	46
3.3.1	The spatial Ring - Inner Track Segment correlations	46
3.3.2	Electron identification using time-of-flight information	47
3.3.3	Electron identification using electromagnetic shower information	48
3.3.4	Single lepton spectra	49
3.4	Di-electron analysis	51
3.4.1	Estimation of the combinatorial background	51
	Same-event combinatorial background	52
3.4.2	Background rejection strategy	54
	Single lepton cuts	54
	Pair cut	54
	Vertex cut	55
3.5	Efficiency evaluations	57
3.5.1	Determination of the reconstruction efficiency	58
3.5.2	Determination of the trigger efficiency	60
	First level trigger efficiency	60
	Second level trigger efficiency	60
3.6	Normalization procedure	61
3.6.1	π^0 cross section	61
3.6.2	Number of elastic pairs: from accepted to extrapolated to 4π	61
3.6.3	Neutral pion multiplicity	62
3.7	Determination of systematical uncertainties	63
3.8	The HADES acceptance	64
4	Results and discussion	66
4.1	Invariant mass spectra	66
4.2	Transverse momentum and rapidity spectra	67
4.3	Comparison to the DLS results	69
4.4	$p + p$ and $n + p$ data in transport model calculations	70
4.5	$p+p$ and $n+p$ data in Pluto	72
4.6	Possible avenues for understanding the experimental dilepton spectra from $p+p$ to $^{12}C+^{12}C$ collisions	76
4.6.1	Experimental ansatz for understanding the di-electron production in NN interactions	76
4.6.2	Experimental ansatz for understanding the di-electron production in AA interactions	78

5	Di-electron measurements with the CBM detector system at FAIR	81
5.1	The CBM research program	82
5.2	The CBM detector	83
5.2.1	The Silicon Tracking System (MVD and STS)	84
	The main tracker	85
	The Micro-Vertex Detector	85
5.2.2	Superconducting dipole magnet	86
5.2.3	Ring Imaging Cherenkov detector	87
5.2.4	Transition Radiation detector	88
5.2.5	The timing Resistive Plate Chambers (RPC)	89
5.2.6	The Electromagnetic Calorimeter	90
5.2.7	The Projectile Spectator detector	90
5.2.8	The Data Acquisition and online event selection (DAQ)	90
6	Data analysis	91
6.1	Input to the simulations	92
6.1.1	Event generator	92
6.1.2	Characteristics of the background	94
6.1.3	Modifications of the detector set-up	95
6.2	Event reconstruction	97
6.3	Track reconstruction	98
6.4	Electron identification	100
6.5	Background rejection strategy	103
6.5.1	Conversion pair cut	104
6.5.2	Single track cuts	105
	Hit topology cut	105
	Track topology cut	106
	Transverse momentum of identified leptons	107
6.5.3	Pair cuts	108
	Opening angle cut	108
	π^0 Dalitz decay reconstruction	108
7	Results	109
7.1	Mass spectra	109
7.2	The phase space coverage	113
7.3	Comparison of the expected performance to existing dilepton experiments	117
8	Summary and Outlook	123
A	The Clebsh-Gordan coefficients	132
	Bibliography	133

List of Figures

- 1.1 The phase diagram of QCD including data points in T and μ_B describing the final hadron ratios in a statistical model [8, 9]. The hadrochemical freeze-out points are determined from a thermal model analysis of heavy-ion collision data at SIS, AGS, SPS and RHIC energies. The condensate ratio $\langle q\bar{q} \rangle_{T, \mu_B} / \langle q\bar{q} \rangle_{T=0, \mu_B=0}$ in dependence on T and μ_B is shown as 3rd dimension in color code [10]. The condensate ratio is reduced for high T and μ_B as predicted by the Nambu Jona Lasinio model. 3
- 1.2 Left: Diagram for $e^+e^- \rightarrow \pi^+\pi^-$ annihilation; this process is caused by one-photon exchange in the time-like momentum-transverse region. The total cross section for the annihilation reaction is modified by the internal structure of the pions. Right: The same diagram for the one-photon exchange process in the VMD model. 7
- 1.3 ρ -meson self-energy diagrams in matter. Left: $\Delta(1232)$ -nucleon-hole polarization. Right: The modification of ρ -meson self-energy through its coupling to resonance-hole states. 8
- 1.4 Left: Transversal spectral function of the ρ in nuclear matter as a function of its invariant mass \mathbf{m} and \mathbf{q} for $\rho_N = \rho_0, T = 0$ MeV [11]. Right: ρ meson spectral functions under SPS (red line) and FAIR (blue line) conditions, as well as in vacuum (green line), in the hadronic many-body approach of Ref. [12]. 8
- 1.5 Schematic spectral distribution of lepton pairs emitted in ultra-relativistic heavy-ion collisions (picture taken from [13]). 10
- 1.6 Shift parameter α . Circle: CLAS result for the $Fe-Ti$ data, square: E325 result for Cu data, triangle: the prediction of the Hatsuda and Lee model. For the E325 result, the error is smaller than the symbol. 15
- 1.7 **Left:** CERES results on the e^+e^- pair yield after subtraction of the "hadronic cocktail", $Pb+Au$ collisions at a kinetic beam energy of 158 GeV/u, 7% most central reactions. In addition to the statistical error bars, systematic errors of the data (horizontal ticks) and the systematic uncertainty of the subtracted cocktail (shaded boxes) are indicated. The broadening scenario (long-dashed line) is compared to a broadening scenario excluding baryon effects (dotted line). **Right:** NA60 results [14] on the comparison of the excess mass spectrum for semi-central $In+In$ collisions at 158 GeV/u to model predictions: cocktail $\rho \rightarrow \mu^+\mu^-$ (thin solid line), unmodified ρ (dashed line), in-medium broadened ρ [15] (thick solid line), dropping ρ mass scenario [16] (dashed-dotted line). Lower dashed line: QGP radiation. The errors shown are purely statistical. The systematic errors of the continuum are about 25%. The open data points show the excess mass spectrum assuming the η yield to be lowered by 10% (which also gives an estimate on the systematic error). 16

1.8	PHENIX results on the e^+e^- pair yield measured in $p+p$ compared to the yield measured in $Au+Au$ collisions. Statistical (bars) and systematic (boxes) uncertainties are shown separately; the mass range covered by each data point is given by the horizontal bars.	17
1.9	Inclusive multiplicity of the pair excess (N_{exc}) in the mass range $M_{ee} = 0.15 - 0.50 \text{ GeV}/c^2$ as function of beam energy E_b (black triangles: HADES, green triangle: DLS). Also shown are the π^0 (red circles) and η (blue circles, blue line) inclusive multiplicities in $C+C$ collisions [17], as well as the corresponding η Dalitz decay (black circles, blue dashed line) contribution integrated over $M_{ee} = 0.15 - 0.50 \text{ GeV}/c^2$. For comparison with N_{exc} , down-scaled π^0 curve is shown as dashed red line [3].	18
1.10	Left: Evolution of average baryon density as a function of time in inclusive $1 \text{ GeV}/u$ $Ca+Ca$ collisions as extracted from the transport model of Zhang and Gale [18] (solid curve); the dashed curve is a simple parameterization thereof with a maximum temperature of $T_{max} = 100 \text{ MeV}$ in the high density phase and a time-independent baryon chemical potential of $\mu_B = 0.76 \text{ GeV}$. Right: Composition of a hot $\pi\Delta N$ gas as a function of temperature at a fixed baryon density of $\rho_B = \rho_N + \rho_\Delta = 0.16 \text{ fm}^{-3}$ [15].	19
1.11	Acceptance corrected mass spectra for the $p+d$ (filled circles) and $p+p$ (open circles) systems measured by the DLS collaboration. The error bars are statistical and do not include the normalization uncertainties. The brackets above and below the low mass data points indicate systematic uncertainties in the shape of the spectra. The dashed lines indicate the kinematical upper limit on the pair mass in the pp system [19].	21
1.12	Radiation from external proton lines in $n+p$ scattering.	22
1.13	A representative set of Feynman diagrams for emission of dileptons in nucleon-nucleon collisions. (a) denotes emission after the NN collision, (b) before the NN collision and (c) during the NN collision. The box represents an off-shell nucleon ($p^2 \neq m^2, c = 1$) or a Δ isobar [20] emitting virtual photons.	22
1.14	Feynman diagrams for the emission of dileptons in nucleon-nucleon collisions, contact (seagull) term.	22
1.15	The contribution of the NN bremsstrahlung to the invariant mass distribution for dilepton spectra in $p+p$ (left) and $n+p$ (right) collisions at a beam energy of 1.04 GeV . Solid lines: OBE-SM [20], dashed lines: OBE-KK.	23
2.1	Schematic view of the HADES detector.	25
2.2	View of the liquid hydrogen target vessel. The entrance window is glued on a stainless steel cylinder with a diameter of 1.5 cm , whereas the target vessel diameter is 2.5 cm	26
2.3	The HADES Ring Imaging Cherenkov detector.	27
2.4	Left: The MDC plane I (GSI chamber). Right: The HADES magnet (ILSE), during the installation.	28
2.5	The META detectors (view from the target region). All 6 sectors of TOF are visible. Two opposite sectors are also equipped with the Pre-Shower detector. Currently all 6 sectors of the Pre-Shower detector are installed.	29
2.6	Side view of the Pre-Shower detector. Three gas chambers and two lead converters are shown. Lepton/hadron discrimination is performed by comparing the number of particles measured in the chambers before and behind lead converters.	31

2.7	Left: Arrangement of the FW cells. Only operational cells are shown. Compilation by K. Lapidus. Right: The detection efficiency for protons versus the PMT high voltage.	31
2.8	A schematic view of the HADES multi-level trigger system. Data readout is initiated by a centrality trigger, indicated as 1 st Level Trigger. The triggered data are analyzed for electron patterns in the RICH and META detectors: indicated as 2 ^d Level Trigger.	32
3.1	Sketch of an elastic scattering collision in the laboratory frame (left panel) and in the center-of-mass frame of two protons (right panel).	36
3.2	Left: Coplanarity of elastic pp pairs. Right: The angular correlation between two tracks using the relation $\tan \theta_1 \cdot \tan \theta_2 = \gamma_{CM}^{-2}$	37
3.3	The momentum resolution for pp elastic pairs (integral over all sectors).	38
3.4	Left: Coplanarity of elastic pp pairs as a function of azimuthal angle. Right: the angular correlation between two tracks using the relation $\tan \theta_1 \cdot \tan \theta_2$ as a function of azimuthal angle. Numbers given in the plot are the sector numbers. The 6 bands and 6 gaps present the six sectors of HADES and show the nice azimuthal coverage of the detector.	38
3.5	Left: Kinematics of the process $dp \rightarrow ppne^+e^-$ within the spectator mechanism. Right: Momentum distribution of the spectator proton p_{sp} detected in the Forward hodoscope Wall at $2^\circ < \theta < 4^\circ$	39
3.6	Event display of a real event. Two opposite sectors are shown (sector 0, sector 3). Detector systems are shown in different colors (from left to right): dark red - RICH, green - MDCs, blue - TOF, red - Pre-Shower. Black ring: reconstructed RICH ring, crossed orange lines: fired wires in MDCs, black points: reconstructed hits in the TOF or Pre-Shower detector.	40
3.7	Left: Schematic view of the track candidate search in the track reconstruction procedure [21]. Right: Momentum resolution $\frac{1/p_{PRK} - 1/p_{GEOANT}}{1/p_{GEOANT}}$ as a function of momentum reconstructed with the Runge-Kutta algorithm. Red circle: positrons, black circle: electrons.	41
3.8	Dependence of the momentum kick on the charge. The contour plot shows the main component of the magnetic field at an azimuthal angle $\phi = 90^\circ$ (compilation A. Rustamov [22]). The 4 planes of MDC chambers are shown by black lines. Blue line: electron track, red line: positron track.	42
3.9	Left: 11×11 pattern matrix mask. Right: The pattern matrix parameter A_{pm} , red line: positively charged tracks, dashed black line: negatively charged tracks. The dotted dashed line indicates the applied cut.	43
3.10	Left: Ring centroid distribution. Right: Number of fired pads. Red line: positively charged tracks, dashed black line: negatively charged tracks. The dotted dashed line indicates the applied cut.	44
3.11	The momentum times polarity ($p \cdot q$) versus velocity (β) distribution for LVL1 triggered events. The statistics shown corresponds to one day of data taking.	45
3.12	Spatial correlations between RICH ring and inner MDC track segment in polar angle. Left: for tracks with momenta below 100 MeV/c, right: for $300 < p/(\text{MeV}/c) < 400$	46
3.13	Angular correlations between RICH ring center and inner track segment after a $\pm 3\sigma$ cut in $\Delta\theta$ and $\Delta\phi \cdot \sin(\theta)$ around the electron peak has been applied.	47

3.14	The momentum times polarity ($p \cdot q$) versus velocity (β) distribution for LVL2 triggered events. Left: TOF/TOFino systems, zoom into the electron/pion region, right panel: after time-of-flight cut has been applied.	48
3.15	Left: Sum of charge measured in the post1- and post2-chambers with subtracted charge measured in the pre-chamber. Electrons with momenta ~ 500 MeV/c (triangles) produce electromagnetic cascades in the lead converters which result in a larger deposited charge compared to the charge produced by hadrons, here - pions (dots). Right: Pion suppression as a function of momentum, i.e. the fraction of pions rejected after the algorithm for lepton recognition (electromagnetic cascade) has been applied.	49
3.16	Momentum times polarity ($p \cdot q$) distributions of lepton candidates.	50
3.17	Example of uncorrelated (left panel) and correlated (right panel) combinatorial pairs. The correlated combinatorial pair is created by a single π^0 Dalitz decay.	52
3.18	Left: Multiplicity distribution of identified electrons versus positrons. Right: Electron (blue) and positron (red) multiplicity per one event.	52
3.19	Left: Invariant mass spectra of signal electron-positron pairs after the background subtraction measured in $p+p$ interactions after the double-hit rejection, close-pair candidate rejection and pair cuts applied. Right: same-event like-sign pairs. The vertex cut is not applied here.	55
3.20	GEANT simulation of the HADES detector. Zoom into the target region. A conversion process on the RICH flange is seen. Green: LH_2 target, yellow: RICH flange.	55
3.21	Polar angle versus reconstructed event vertex z (experimental $p+p$ data). Left: tracks with momenta below 150 MeV/c, red lines indicate the cut region. Right: tracks with momenta $150 < p/(\text{MeV}/c) < 200$	56
3.22	Polar angle versus reconstructed event vertex z (experimental $n+p$ data). Left: tracks with momenta below 150 MeV/c, black lines indicate the cut region. Right: tracks with momenta $150 < p/(\text{MeV}/c) < 200$	56
3.23	Left: Invariant mass spectra of the combinatorial background without background rejection cuts (black circles) and after all cuts applied (blue triangles). Right: final signal-to-background ratios for $p+p$ data (black circles) and for $n+p$ data (green squares); note that the signal and background spectra, used for signal-to-background ratios estimation, are efficiency corrected.	57
3.24	Efficiency correction as a function of polar and azimuthal angles.	59
3.25	Left: Invariant mass spectra of signal electron-positron pairs measured in $p+p$ interactions. Black triangle: uncorrected data points, black circle: efficiency corrected data. Right: ratio of efficiency corrected to raw data.	59
3.26	Left: Invariant mass spectra of signal electron-positron pairs measured in $n+p$ interactions. Black triangle: uncorrected data points, black circle: efficiency corrected data. Right: ratio of efficiency corrected to raw data.	60
3.27	The efficiency of the LVL2 trigger as a function of invariant mass, transverse momentum, rapidity (from left to right). The horizontal line is the fit to the data, fitting results are shown as well.	61
3.28	Left: Comparison of θ (polar angle) distribution of measured efficiency corrected (black solid line) and simulated (dashed red line) elastic pp pairs. Right: θ distribution of elastic pairs in 4π (red dashed line) and in the HADES acceptance (black solid line).	63

3.29	The fitted $1\pi^0$ -production cross sections (solid line) in comparison to the data [23]. Left: Resonance model [24], right: parametrization based on generalized Laguerre polynomials [25] in comparison to the data [26, 27].	64
3.30	The polar angle as a function of the reconstructed vertex z of the e^+e^- pairs after all background rejection cuts. Left: $C+C$ data, middle panel: $p+p$ data, right: $n+p$ data.	65
3.31	Comparison of the geometrical acceptance for electrons in $C+C$ collisions at 1 GeV/u and $p+p$ interactions at 1.25 GeV as a function of momentum (left), azimuthal angle (middle, only one sector is shown), polar angle (right panel). Dashed red line: $C+C$ system, black line: $p+p$ system.	65
3.32	Comparison of the geometrical acceptance for positrons in $C+C$ collisions at 1 GeV/u and $p+p$ interactions at 1.25 GeV as a function of momentum (left), azimuthal angle (middle, only one sector is shown), polar angle (right panel). Dashed red line: $C+C$ system, black line: $p+p$ system.	65
4.1	Invariant mass distribution of e^+e^- pairs measured within the detector acceptance for $p+p$ (left panel) and $n+p$ (right panel) interactions at a beam energy of 1.25 GeV/u. Statistical errors are shown with bars, systematic by horizontal lines.	66
4.2	Transverse momentum distributions of the signal e^+e^- pairs measured in $p+p$ and $n+p$ interactions at a beam energy of 1.25 GeV/u. Open circle: $p+p$ system, filled circle: $n+p$ system.	67
4.3	Transverse momentum distributions of the signal e^+e^- pairs measured in $p+p$ and $n+p$ interactions at a beam energy of 1.25 GeV/u for the invariant mass region $M_{ee} > 0.15$ GeV/c ² . Red triangle: $p+p$ system scaled by factor of 4, filled circle: $n+p$ system.	68
4.4	Rapidity distributions of the signal e^+e^- pairs measured in $p+p$ and $n+p$ interactions at a beam energy of 1.25 GeV/u. Open circle: $p+p$ system, filled circle: $n+p$ system. Vertical dashed-dotted line shows midrapidity. Solid lines are Gaussian fits to the data.	68
4.5	Left: The di-electron invariant mass distribution from DLS [1] for $p+p$ collision at a beam energy of 1.04 GeV in comparison to model calculations [20]. Right: Invariant mass distribution of measured e^+e^- pairs. Black circles: HADES data for $p+p$ at 1.25 GeV, open red circles: DLS data for $p+p$ at 1.27 GeV, blue triangles: DLS data for $p+p$ at 1.04 GeV.	70
4.6	Invariant mass distribution of e^+e^- pairs measured in $p+p$ interactions at a beam energy of 1.25 GeV compared with HSD (left panel) and IQMD (right panel) transport model calculations. Dashed-dotted line: π^0 Dalitz, red solid line: Δ^+ Dalitz, green dashed line: NN bremsstrahlung, black solid line: total cocktail.	71
4.7	Invariant mass distribution of e^+e^- pairs measured in $d+p$ interactions at a beam energy of 1.25 GeV/u compared with HSD (left panel) and IQMD (right panel) transport model calculations. Dashed-dotted line: π^0 Dalitz, red solid line: $\Delta^{+,0}$ Dalitz, green dashed line: NN bremsstrahlung, blue dashed line: η . Dashed magenta line: HSD - πN bremsstrahlung, IQMD - ρ meson production via $\pi\pi$ annihilation. Black solid line: total cocktail.	71

4.8	Total cross sections for the quasi-free $pn \rightarrow pn\eta$ reaction together with other free and quasi-free $p+N$ reactions as a function of the center-of-mass energy. The errors shown are statistical only. Black circles: $pn \rightarrow pn\eta$ channel Ref. [28], yellow and blue circles: $pn \rightarrow d\eta$ channel Refs. [29, 30], violet triangle, inverse green triangle, blue square and red square: $pp \rightarrow pp\eta$ channel Ref. [31, 32, 33, 29].	73
4.9	Invariant mass distribution of e^+e^- pairs in proton-proton collisions: the dashed (dotted) curves depict the contribution of diagrams with bremsstrahlung from $\gamma\Delta N$ (γNN) vertices. The solid lines are the results of calculations of the total cross section as coherent sum of nucleon and Δ contributions. Left: Pluto parametrization, right: picture from Ref. [34].	74
4.10	Invariant e^+e^- mass distribution measured in $p+p$ (left panel) and $n+p$ (right panel) interactions at a beam energy of 1.25 GeV/u. Blue dashed-dotted line: π^0 Dalitz decay, red solid line: Δ Dalitz decay (dipole fit, $G_M = 3$), green dashed line: NN bremsstrahlung component á-la Kaptari <i>et al.</i> , blue dashed line: η -meson, black solid line: total incoherent cocktail.	74
4.11	The di-electron yield ratio as a function of invariant mass measured in $n+p$ and $p+p$ interactions at 1.25 GeV/u kinetic beam energy with the prediction for HADES. Black solid circle: data, blue open circles: $(\sigma^{np} + \sigma^\eta)/\sigma^{pp}$ from Kaptari <i>et al.</i> [34].	75
4.12	Invariant mass distribution of e^+e^- pairs measured in $p+p$ (left panel) and $n+p$ (right panel) interactions at a beam energy of 1.25 GeV/u. Blue dotted-dashed line: π^0 Dalitz, black solid line: coherent sum (NN bremsstrahlung, Δ) from Kaptari <i>et al.</i> , blue dashed line: Δ from Kaptari <i>et al.</i> , blue solid line: Δ from Krivoruchenko <i>et al.</i> (Dipole fit), blue (dotted) dashed line demonstrates the effect of including the Δ form factor from the VMD model.	75
4.13	Left: Difference of the di-electron yield measured in $n+p$ and $p+p$ interactions at 1.25 GeV after subtraction of the η contribution from the $n+p$ data. Black circles: data, red dashed line: NN bremsstrahlung á-la Kaptari <i>et al.</i> Right: after subtraction of the NN bremsstrahlung contribution separately from each system, $p+p$ and $n+p$. The grey box shows the region where the $\Delta(1232)$ is still contributing to the di-electron spectrum.	77
4.14	The dilepton production cross section $pp \rightarrow e^+e^-pp$ through the nucleon resonances Δ , N^* , and Δ^* at a kinetic beam energy of $E_{kin} = 1.61$ GeV [35].	77
4.15	Comparison of the η production in $C+C$ collisions at 1 GeV/u and in $n+p$ collisions at 1.25 GeV/u. Dashed red line: the η multiplicity is taken from the TAPS measurement in the two-gamma decay channel Refs.[36, 37]. Black line: the η production in $n+p$ interactions measured by CELSIUS collaboration Refs. [28]. No extra scaling then the one to the π^0 production is done.	78
4.16	HADES invariant mass spectra for $1/2 \cdot (M_{ee}^{pp} + M_{ee}^{np})$ at 1.25 GeV/u and $C+C$ at 1 GeV/u systems. Open black circle: $C+C$ system, close black circle: $1/2 \cdot (M_{ee}^{pp} + M_{ee}^{np})$ experimental cocktail.	80
5.1	Layout of the FAIR accelerator complex.	82
5.2	Layout of the CBM experiment with detectors for electron identification [38].	83
5.3	Schematic cross section of the Silicon Tracking and Vertex Detection System. The dashed lines indicate the maximum and minimum angular coverage of the STS.	84

5.4	First design studies of the MVD detector. 1: MAPS stations can be moved to allow beam tuning, 2: target holder, 3: engine to move detector stations.	85
5.5	Possible realization of the superconducting dipole magnet [38].	86
5.6	RICH detector as implemented into the CBM simulation framework. Light green: gas vessel made of aluminum walls filled with the Cherenkov radiator gas. Two rectangular sectors of the spherical mirrors are positioned in the downstream part of the gas vessel. The photodetector consists of two rectangular planes positioned inside the gas vessel on its upstream wall [39].	87
5.7	Momentum threshold for Cherenkov light production for pions and kaons in dependence on γ_{th} . Also shown is the momentum at which the opening angle of pions corresponds to 90% of the opening angle of electrons. The green/grey band thus indicates the approximate region of pion identification in dependence on γ_{th} [39].	88
5.8	Layout of the MWPC prototypes built at GSI and in Bucharest	88
5.9	TOF wall as implemented into the CBM simulation framework. Rear view of the TOF wall, divided into 9 towers [38].	89
6.1	Invariant mass distribution for central $Au+Au$ collisions at 25 GeV/u (full phase space). Description: from left to right. Red: π^0 Dalitz decay; dark blue: η Dalitz decay; blue: ω Dalitz decay; green: ρ^0 , magenta: ω , violet: ϕ direct dilepton decay.	92
6.2	Transverse momentum versus rapidity distribution. Left: for π^0 Dalitz decay, right: for ρ^0 meson.	93
6.3	Left: Opening angle distribution for central $Au+Au$ collisions at 25 GeV/u (full phase space). Right: Momentum distribution of di-electron sources (central $Au+Au$ collisions at 25 GeV/u, full phase space).	94
6.4	Number of STS stations traversed by e^+ vs. e^- from γ conversion (left panel) and π^0 Dalitz decay (right panel).	94
6.5	Trajectories of γ (green), e^+ (magenta), e^- (blue) from π^0 Dalitz decay. Left: $B_{max} = 1.1$ T, right: $B_{max} = 0.7$ T.	96
6.6	Distribution of x versus y hit positions for e^+ and e^- from γ conversion (left panel) and π^0 Dalitz decay (right panel) extrapolated from $z = 20$ cm to $z = 30$ cm.	96
6.7	Left: Radial vs. longitudinal distribution of emission sites for positrons created through γ conversion. Contributions come from the target, the tracking stations, the beam pipe and the magnet yoke. The y component of the magnetic field is also shown (black circles). Right: Number of γ /event from conversion in the target material as a function of the target thickness.	97
6.8	Track reconstruction efficiency ($p < 1$ GeV/c) for tracks coming from the target region (left panel); momentum resolution in the STS (right panel).	99
6.9	The momentum resolution integrated for a $p < 1$ GeV/c as a function of the maximum y component of the magnetic field value (B_y).	99
6.10	Distance between track extrapolation and ring center as a function of reconstructed momentum. Left: all matches, right: truly identified electrons. The black line indicates the cut region.	100
6.11	Rich ring quality selection with artificial neural network, $-1 =$ wrong electrons, $+1 =$ true electrons (left panel). Radius versus momentum for reconstructed rings (right panel).	101

6.12	Energy loss of pions and electrons at 1.5 GeV/c momentum measured for a single TRD layer.	101
6.13	Left: Squared mass versus momentum measured in the TOF wall after electron identification in RICH. Right: a zoom into the electron and pion region is shown. The black line indicates the cut region.	102
6.14	Left: Electron identification efficiency: magenta line - ring reconstruction efficiency. Right: Pion suppression factor. Black line: identification efficiency and pion suppression using RICH information only, green line: combination of RICH, TRD and TOF.	102
6.15	Topology of the combinatorial background. Blue: tracks from π^0 Dalitz decay, red: tracks from γ conversion. Schematic view of the MVD and STS (black line), and the RICH detector (green line).	104
6.16	Left: Invariant mass spectra of reconstructed e^+e^- from π^0 Dalitz (red) and γ (black). Right: Distance to the nearest neighbor hit in the 1 st MVD station. The magnetic field is even reduced to 30% of its nominal value. Black: e_γ + closest MVD hit; blue: true γ conversion; red: e_{ρ^0} + closest MVD hit, scaled by factor 200. The figure shows the distribution after the previous (γ) cut. The black line indicates the chosen cut value.	104
6.17	Distance to nearest neighbor hit in the 1 st MVD station versus momentum of the fully identified e^\pm from ρ^0 (left panel) and from γ (right panel). Black line indicates the cut region.	105
6.18	Correlation between $\theta_{e^\pm, \text{rec}}$ vs. $\sqrt{p_{e^\pm} \cdot p_{\text{rec}}}$. The distribution is separately shown for cases where the Full Track stems from ρ^0 (left panel) and photon conversion (right panel), respectively. The figure shows the distribution after the previous cuts. Tracks belonging to a pair inside the triangle are rejected.	106
6.19	Left: Transverse momentum distribution. Red: leptons from background sources, blue: leptons from signal (enhanced by factor of 1000). The cut value is 0.2 GeV/c. The figure shows the distributions after all previous cuts. Right: Opening angle distribution for electron pairs from π^0 Dalitz decay (red), γ conversion (green), η Dalitz decay (blue) and ρ^0 decay (magenta). The figure shows the distribution after all previous cuts.	107
7.1	Invariant mass spectra before (left panel) and after (right panel) all cuts. The simulation was performed for $2 \cdot 10^5$ central Au+Au collisions at 25 GeV/u. From left to right the different contributions are shown: red: π^0 Dalitz, dark green: γ , dark blue: η Dalitz, blue: ω Dalitz, magenta: ω , green: ρ^0 , violet: ϕ , black fill: all e^+e^- pairs, grey fill: combinatorial background.	109
7.2	Cut efficiency for signal and background pairs in different mass regions. Red circle: signal, black triangle: background. Note that pairs from γ conversion ($M_{ee} < 0.2 \text{ GeV}/c^2$) are counted as signal.	110
7.3	Cut efficiency of different signal sources after each cut applied.	111
7.4	Left: Signal-to-background ratio as a function of cut type. Right: Signal-to-background ratio for central Au+Au collisions at different beam energies after all cuts have been applied.	112
7.5	Invariant mass spectra before (left panel) and after (right panel) all cuts for $6.5 \cdot 10^4$ central Au+Au collisions at 15 GeV/u. From left to right the different contributions are shown: red: π^0 Dalitz, dark green: γ , dark blue: η Dalitz, blue: ω Dalitz, magenta: ω , green: ρ^0 , violet: ϕ , black fill: all e^+e^- pairs, grey fill: combinatorial background.	112

- 7.6 Invariant mass spectra before (left panel) and after (right panel) all cuts for $6.5 \cdot 10^4$ central $Au+Au$ collisions at 35 GeV/u. From left to right the different contributions are shown: red: π^0 Dalitz, dark green: γ , dark blue: η Dalitz, blue: ω Dalitz, magenta: ω , green: ρ^0 , violet: ϕ , black fill: all e^+e^- pairs, grey fill: combinatorial background. 113
- 7.7 Left: Combinatorial background cocktail. Right: Detail composition of the combinatorial background contributing to the physical sources. All identification and background rejection cuts are applied. 114
- 7.8 Transverse momentum versus rapidity distribution for ρ^0 in the full phase space (left panel) and after all cuts (right panel) for 2×10^5 central $Au+Au$ collisions at 25 GeV/u. Midrapidity for 25 GeV/u beam energy is equal 2. 114
- 7.9 Transverse momentum versus invariant mass distribution of the identified dilepton pairs obtained from experimental data of the NA60 dimuon experiment (left panel) and the di-electron CERES experiment (right panel). Note that the mass axis is zero suppressed. Compilation by S. Damjanovic (NA60 collaboration). . 115
- 7.10 Distribution of accepted signal e^+e^- pairs in the transverse momentum and invariant mass plane after all cuts. Left: including p_t cut of 0.2 GeV/c, right: excluding any p_t cut. The data shown correspond to $2 \cdot 10^5$ simulated central $Au+Au$ collisions at 25 GeV/u. 115
- 7.11 Invariant mass distribution after all cuts excluding any p_t cut. The data shown correspond to $2 \cdot 10^5$ simulated central $Au+Au$ collisions at 25 GeV/u. 116
- 7.12 Acceptance and signal pair detection probability as a function of the invariant mass after all analysis steps. (a): CERES experimental data, (b): NA60 experimental data (compilation by S. Damjanovic), (c) CBM simulated data. . . 117
- 7.13 Left: Inclusive e^+e^- spectra in $S+Au$ collisions at 200 GeV/u beam energy showing the data (full circles) and various contributions from known hadron decays only; the shaded region indicates the systematic error on the summed contributions [40]. Right: Inclusive e^+e^- mass spectrum in $Pb+Au$ collisions at 40 GeV/u beam energy, compared to the hadron decay cocktail with (lower lines) and without medium modifications (upper lines) [41]. 118
- 7.14 Left: Inclusive e^+e^- mass spectrum from CERES in $Pb+Au$ collisions at 158 GeV/u beam energy normalized to the observed charged-particle density. Statistical errors are shown as bars, the systematic errors are given independently as brackets. The full line represents the e^+e^- yield from hadron decays scaled from p-induced collisions. The contributions of individual decay channels are also shown [42]. Right: same distribution after the CERES upgrade [6]. 118
- 7.15 Left: Mass spectra of the opposite-sign dimuons (upper histogram), combinatorial background (dashed line), signal fake matches (dashed-dotted line), and resulting signal (histogram with error bars) from the NA60 collaboration for minimum bias $In+In$ collisions at 158 GeV/u beam energy [7]. Right: Invariant e^+e^- pair yield compared to the yield from expected hadronic decays from the PHENIX collaboration in minimum bias $Au+Au$ collisions at $\sqrt{s_{NN}} = 200$ GeV. Statistical (bars) and systematic (grey boxes) uncertainties are shown separately; the mass range covered by each data point is given by the horizontal bars [43]. 119

- 7.16 Left: Enhancement factors observed by different experiments as a function of the center of mass energy. Circles: NA60 data ($In+In$) for four centrality bins; inverse filled triangle: CERES data ($Pb+Au$ at 40 GeV/u); open circle: CERES data ($Pb+Au$ at 158 GeV/u, 28% most central collisions); open triangle: CERES data ($Pb+Au$ at 158 GeV/u, 7% most central collisions); filled triangle: ($S+Au$ at 200 GeV/u, no centrality selection); square: PHENIX data. Right: The energy dependence of experimental hadron yields at midrapidity produced in central nucleus-nucleus collisions [44]. 121
- 7.17 Integrated S/B ratios for M_{inv} larger than 0.2 GeV/c² measured by existing dilepton experiments as a function of the number of charged particles at midrapidity in one rapidity unit. Circles: NA60 data for four centrality bins; triangles, open circle: CERES data, square: PHENIX data, star: CBM assuming an enhancement factor of 6. 121
- 8.1 Invariante Massenverteilung von e^+e^- Paare in $p+p$ (links) und $n+p$ (rechts) Reaktionen bei einer Strahlenergie von 1.25 GeV/u. Statistische Fehler sind als vertikale Striche, systematische Fehler mit horizontalen Balken dargestellt. . 127
- 8.2 Invariante Massenverteilung von e^+e^- Paare in $C+C$ -Kollisionen bei einer Strahlenergie von 1 GeV/u (offene Kreise) sowie der kombinierten Daten aus $p+p$ und $n+p$ -Kollisionen als $1/2 \cdot (M_{ee}^{pp} + M_{ee}^{np})$ bei 1.25 GeV/u (schwarze Kreise). Die Spektren sind je auf die Anzahl der π^0 normiert. 128
- 8.3 Signal-zu-Untergrund Verhältnis in Leptonenpaare Massenspektren für $M_{inv} > 0.2$ GeV/c², gemessen von Experimenten an SPS (CERES (Dreiecke und offene Kreise), NA60 (Kreise)) und RHIC (PHENIX (Quadrat)), in Abhängigkeit von der Anzahl der geladenen Teilchen bei mittlerer Rapidität. Im Vergleich dazu (Sterne) sind nach den jetzigen Simulationen erwartete S/B Verhältnisse für CBM eingezeichnet unter Annahme eines Leptonenpaar-Überschusses um einen Faktor 6 für $M_{inv} > 0.2$ GeV/c². 130

List of Tables

1.1	Characteristic quantities of light vector mesons [45].	6
3.1	Cuts established for electron identification and cut efficiency for lepton candidates identified in the TOF detector.	50
3.2	Cuts established for electron identification and cut efficiency for lepton candidates identified in the TOFinio and Pre-Shower detectors.	50
3.3	cross sections for exclusive channels of π^0 production in $p+p$ [25] (experimental values) and in $n+p$ reactions [24, 25] (values calculated within the resonance model).	62
3.4	Systematic uncertainties of the dilepton yield due to different sources.	63
6.1	Mean meson multiplicities, their dominant leptonic decay channels and branching ratios for central $Au+Au$ collisions at 25 GeV/u beam energy	92
6.2	Cuts established for background rejection and their optimized cut values.	108
7.1	Mean pion and vector meson multiplicities from UrQMD for central $Au+Au$ collisions at 15, 25 and 35 GeV/u beam energy.	113
7.2	Signal-to-Background ratio and signal efficiency for central $Au+Au$ collisions at 25 GeV/u with and without single electron p_t cut.	116
7.3	Overview of existing dilepton experiments. S/B ratios for integrating invariant masses larger than 0.2 GeV/c^2 . For CBM S/B ratios can of course only be given without any medium contribution, i.e. "free hadronic cocktail" only.	120
7.4	Estimated particle yields for minimum bias $Au+Au$ collisions at 25 GeV/u based on HSD calculations. N = multiplicity in minimum bias collisions (= 1/5 of central collisions), BR = branching ratio, ε = efficiency ($p_t > 0.2 GeV/c$), R/s = reaction rate, Y/s = particle yield per second, and $Y/10 w$ = particle yield per 10 weeks [46].	122
A.1	Decay channels with isospin-3 components of $\Delta(1232)$	132
A.2	Branching ratios for $\Delta^+(1232)$ and $\Delta^0(1232)$	132

Chapter 1

Introduction

Over the last decades a lot of effort has been devoted to the study of nuclear matter far from its ground state. The goal of this initiative is to explore the phase structures of strongly interacting matter governed by the laws of Quantum Chromo Dynamics (QCD) by creating new states of matter in the laboratory. Experiments studying heavy-ion collisions are the only possibility on earth to explore nuclear matter under conditions similar to those which appeared a few microseconds after the "Big Bang", or as they still exist in the interior of compact stellar objects. At the upcoming international FAIR¹ at GSI² nuclear matter under extreme conditions will be studied with the CBM³ Experiment. With the high quality beams then provided by FAIR the investigation of nuclear matter at densities several times higher than nuclear ground state density using so-called rare and penetrating probes will be possible for the first time. One of this penetrating probes are electromagnetic decays of hadrons inside the dense medium into pairs of leptons. Such purely leptonic final states carry important information of the decaying objects to the detectors without being affected by strong final state interaction while traversing the medium.

Systematic investigations of dilepton production are performed already now at the SIS⁴ accelerator of GSI with the HADES⁵ spectrometer. The goal of this program is a detailed understanding of di-electron emission from hadronic systems at moderate temperatures and densities. In this work, new results obtained in HADES experiments focussing on electron pair production in elementary collisions are presented. They pave the way to a better understanding of the origin of so-called excess pairs earlier on observed in heavy-ion collisions by the DLS⁶ collaboration and lately confirmed in two measurements of the HADES collaboration using carbon-carbon collisions. In a second section, a strategy is developed to reconstruct the di-electron signal in the future CBM experiment. The challenge here is to obtain good signal to background ratios with a detection system which does not provide electron identification before the produced pairs are opened in the strong magnetic field of the spectrometer. Such a configuration is dictated by the request of a high rate capability of the spectrometer at simultaneously high momentum resolution.

This work is structured as follows. In this section, the field of nuclear- and quark-matter physics is introduced briefly addressing both, relevant theoretical concepts as well as the most

¹Facility for Antiproton and Ion Research

²Gesellschaft für Schwerionenforschung

³Compressed Baryonic Matter

⁴SchwerIonen Synchrotron

⁵High Acceptance Di-Electron Spectrometer

⁶Di-Lepton Spectrometer

important experimental results related to dilepton production in heavy-ion collisions. In the following chapter the HADES spectrometer is discussed. Chapter 3 describes the data analysis leading to the di-electron signal obtained from $p+p$ and $d+p$ collisions at 1.25 GeV/ u . The results are discussed in chapter 4. Chapter 5 and 6 introduce the CBM experiment and the analysis strategy for di-electron reconstruction, respectively. The expected performance of di-electron spectroscopy in gold-gold collisions at 25 GeV/ u with CBM is presented in chapter 7. The work is concluded in chapter 8.

1.1 Strongly interacting matter

*We learnt a lot in the last 25 – 35 years.
Its quite amusing when you look back
how much we did not know.
But its even more amusing to consider
how much we do not know yet!
(David Gross)*

1.1.1 The QCD phase diagram

A qualitative picture of the phase diagram of nuclear matter as a function of temperature (T) and baryochemical potential (μ_B) is shown in Figure 1.1. The matter formed in the early universe about ten microseconds after the big bang traversed the phase diagram essentially downwards along the temperature axis, i.e. at vanishing chemical potential (indicated by the white arrow). Compact stellar objects like neutron stars, on the other hand, have very small temperatures and exist in the region of high net baryon density, that is at large baryochemical potential. Nuclei exist at nuclear matter ground state density ($\rho_0 = 0.16 \text{ fm}^{-3}$) and at zero temperature. Nuclei are well-defined systems containing up to a few hundred nucleons held together by the nuclear forces. Nucleons, i.e. protons and neutrons comprise three valence quarks uud and ddu , respectively. In general, at low T and μ_B , quarks and gluons are bound to colorless objects, called hadrons. As T and/or μ_B increase hadrons occupy more and more of the available space and thus start to overlap. The initially confined quarks and gluons separate thus creating new degrees of freedom other than hadronic ones. This deconfined phase is named Quark-Gluon Plasma (QGP). The present expectation is that the transition from the QGP to the hadronic phase is of first order in the region of large baryochemical potential. For a first order phase transition a coexistent phase should exist where the phase is characterized by droplets of deconfined matter embedded in a gas of hadrons. Towards smaller baryochemical potentials the coexistence phase terminates in a critical point [47, 48] having special and universal thermodynamic properties. At even smaller baryochemical potentials lattice QCD predicts a smooth cross-over between the two phases [47]. The possible new physics in the QCD phase diagram are Color Superconducting phases which might be important at asymptotically high baryon number density and low temperatures [49]. At finite temperature and density the existence of a new phase of QCD, Quarkyonic matter, has been suggested in [50, 51, 52]. Quarkyonic matter is distinct from the confined and deconfined phases and represent the matter which is confined, yet chirally symmetric.

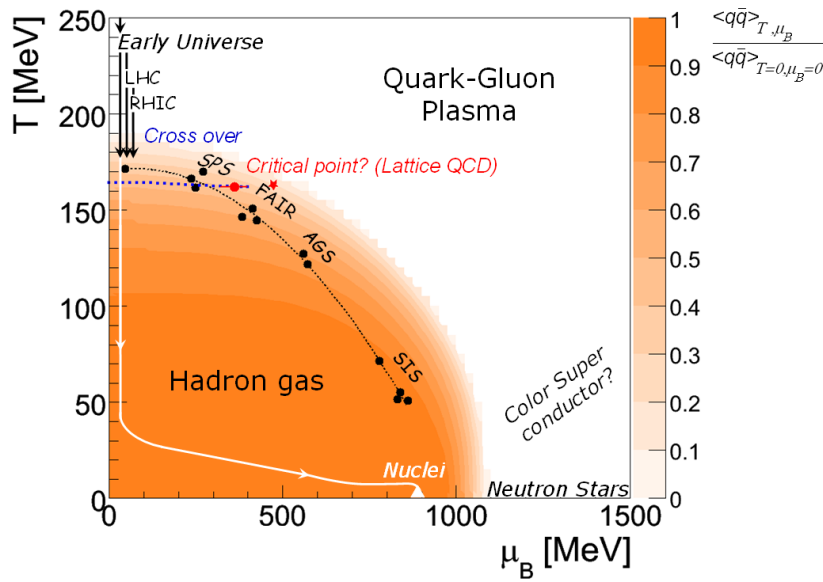


Figure 1.1: The phase diagram of QCD including data points in T and μ_B describing the final hadron ratios in a statistical model [8, 9]. The hadrochemical freeze-out points are determined from a thermal model analysis of heavy-ion collision data at SIS, AGS, SPS and RHIC energies. The condensate ratio $\langle q\bar{q} \rangle_{T, \mu_B} / \langle q\bar{q} \rangle_{T=0, \mu_B=0}$ in dependence on T and μ_B is shown as 3rd dimension in color code [10]. The condensate ratio is reduced for high T and μ_B as predicted by the Nambu Jona Lasinio model.

The temperature of the universe around ten microseconds after the "Big Bang" was approximately 150 – 200 MeV. Current and future experiments at the RHIC⁷ at the Brookhaven National Laboratory [53] and at the LHC⁸ at CERN⁹ [54] energies concentrate on the study of matter at such high temperatures and at very low net-baryon densities (baryochemical potential), i.e. in this region where a smooth crossover from a deconfined to hadronic phase is predicted by Lattice QCD calculations. The accelerator facilities AGS¹⁰ at Brookhaven National Laboratory and the SPS¹¹ at CERN accessed extreme states of matter at still high temperature but at higher net-baryon densities. Probably, in this energy regime deconfined matter was created for the first time in heavy-ion collisions. At even lower bombarding energies (of $E_{lab} \simeq 1 - 2 \text{ GeV}/u$) at the Bevalac¹² and current GSI SIS18 facilities a large region in the nuclear matter phase diagram ranging from ground state matter density ρ_0 up to about $3\rho_0$ can be accessed with a proper choice of the collision system. The reaction volume is heated up to rather moderate temperatures $T \leq 80 \text{ MeV}$ very likely without reaching the QGP phase boundary.

The challenge still today is to detect these phases in the laboratory by isolating unambiguous signals. The NA49¹³ collaboration has systematically studied the production of strange hadrons scanning in beam energy from top SPS energies of 158 GeV/ u down to 20 GeV/ u [55]. The global trend of the excitation functions of the multiplicity of strange particles normalized

⁷Relativistic Heavy Ion Collider

⁸Large Hadron Collider

⁹Conseil Européen pour la Recherche Nucléaire

¹⁰Alternating Gradient Synchrotron

¹¹Super Proton Synchrotron

¹²Billions of eV Synchrotron joined to the SuperHILAC linear accelerator as an injector for heavy ions

¹³Large acceptance hadron detector situated in the SPS North Area at CERN

to the pion multiplicity can be understood as a consequence of chemical freeze-out at decreasing baryochemical potential and rising temperature as the beam energy increases. In the energy range between AGS and SPS there is a transition from baryon dominated to meson dominated matter in the collision zone. The pronounced kink structure in the K^+/π^+ ratio of NA49 has provoked speculations on a possible deconfinement phase transition reached at a beam energy around 30 GeV/u [56]. In the vicinity of the deconfinement phase transition, critical density fluctuations have been predicted to cause non-statistical event-by-event fluctuations of several experimental observables [57, 58]. Ideally, a sudden non-monotonous change in dynamical fluctuations measured as function of beam energy would also be a signal for a system freezing out near the critical endpoint. The investigation of dynamical fluctuations of particle ratios or mean transverse momenta is ongoing, and interesting observations in K/π fluctuations have been made [59]. However, their interpretation is strongly debated and more comprehensive studies with reduced statistical and systematic errors are needed. To find a phase transition between hadronic and partonic matter, and eventually the critical endpoint, one presumably has to stay at even lower bombarding energies as indicated by NA49. The CBM experimental program has the potential to discover this most prominent landmarks of the QCD phase diagram expected to exist at high net baryon densities. Moreover, predictions based on effective field theories expect that the spontaneously broken chiral symmetry should be almost recovered in this region of the phase diagram.

Among the promising observables for investigating these phases are short-lived vector mesons decaying into lepton pairs inside the hot and dense matter. An enhanced yield of low-mass lepton pairs above contribution from decays of long-lived mesons has been found in central heavy-ion collisions [6, 7]. This observation has triggered an enormous theoretical activity aimed at understanding in-medium hadron properties and its relation to a partial restoration of the chiral symmetry. In this context, the symmetry breaking mechanism and the origin of particle masses are key questions.

1.1.2 The origin of hadron masses

Most of the mass of the visible Universe (99.9%) is represented by nuclei. The mass of the nucleus is the sum of the masses of its constituents, the protons and neutrons. However, the binding energy is strong enough to reduce the mass by a fraction of a percent ($\sim 10^{-8}$ in atoms). But what about the nucleon? The mass of the proton amounts to about 1 GeV/c² which is ~ 50 times larger than the sum of the masses of its valence quarks, $2 \cdot m_u + m_d \simeq 20 \text{ MeV}/c^2$. The formation of massive protons out of almost massless quarks and gluons is a unique feature of non-perturbative QCD and a key question addressed by large community of theoreticians and experimentalists.

In the second half of the 20th century symmetry has been the most prominent concept in the exploration and formulation of the fundamental laws of physics. Guided by symmetry QCD required three distinct charges (and their anti-charges) to which the Strong Force couples. These charges were named color by Y. Nambu [60]). The biggest advance of the early 1960's was the discovery of an approximate symmetry of hadrons, SU(3) symmetry, by Gell-Mann and Y. Neeman [61]. Another symmetry of the QCD Lagrangian, the chiral symmetry, exactly realized if quarks have zero mass¹⁴, was found to be spontaneously broken in nature. The bare

¹⁴In the interaction between massless quarks by gluon exchange right-handed quarks q_R (spin and momentum parallel) stay right-handed and left-handed quarks q_L stay left-handed which means that the chirality is conserved and the QCD Lagrangian is invariant under the $SU(3)_R \otimes SU(3)_L$ transformation.

(or current) quark masses are derived from experiment and amount to approximately $5 \text{ MeV}/c^2$ for the up-quark and to approximately $7 \text{ MeV}/c^2$ for the down-quark. Compared with the hadronic mass spectrum the masses of up and down quarks are indeed very small, so that chiral symmetry may be considered an approximate symmetry of the strong interaction. The ground state of QCD is populated by scalar quark-antiquark pairs ($\langle q\bar{q} \rangle$ condensate) and does not share the symmetry of the Lagrangian. A left-handed quark q_L can be converted into a right-handed quark q_R by interaction with a scalar $q\bar{q}$ pair. Due to the condensate chiral symmetry is spontaneously broken and hadron masses are determined by the existence of this chiral condensate $\langle q\bar{q} \rangle$. Since the nucleon consists of three quarks, the quark mass should approximately be one third the mass of the nucleon, i.e. about $300 \text{ MeV}/c^2$. Such quark states, which are dressed by a virtual cloud of quark-antiquark pairs and gluons, are called constituent quarks. The mass of the quarks depends then on the distance over which it is probed by another quark. The shorter the distance between quarks, the weaker the interaction and the smaller the mass. It is expected that thermal excitation of the QCD vacuum induces a melting of the condensate thus forcing the restoration of the spontaneously broken chiral symmetry ($\langle q\bar{q} \rangle \rightarrow 0$) and the deconfinement of the color-neutral quark states. A similar situation is achieved in a state of high baryon density where the chiral condensate is literally squeeze out. The "melting" of the chiral condensate, i.e. the reduction of the $\langle q\bar{q} \rangle$ expectation value calculated within the Nambu-Jona-Lasinio model, is shown in Fig. 1.1 as a color gradient.

However, the chiral condensate is not a direct observable and a still open question is how it can be probed experimentally. QCD Sum Rules establish a connection between hadronic observables and the condensate via integrals over hadronic spectral functions and operator product expansion Ref. [62, 63]. But QCD Sum Rules do not provide definite predictions for masses and widths of hadrons, they nevertheless constitute powerful constraints on model spectral functions, especially when applied at finite baryon density and temperature, where the condensate is expected to change appreciably.

1.1.3 The electromagnetic structure of hadrons

*Photons with a billion times more energy than
Photons of visible light
exhibit properties once thought to belong solely
to hadrons.
(Frederick V. Murphy and David E. Yount.)*

The classical method of studying subatomic structures by means of electromagnetic probes dates back to the Rutherford experiment in which the structure of atoms was analyzed by scattering α -particles in the Coulomb field of heavy atoms and the atomic nucleus was discovered. The differential cross section for the scattering of an electron by a particle with a specific spatial structure can be written in the form:

$$\frac{d\sigma}{d\mathbf{q}^2} = \left[\frac{d\sigma}{d\mathbf{q}^2} \right]_{\text{point like}} [F(\mathbf{q}^2)]^2, \quad (1.1)$$

where \mathbf{q} is the momentum transferred to the electron. The function $F(\mathbf{q}^2)$ is the form factor of a particle and describes the deviation of the differential cross section for the case of a point-like charge distribution. Since electrons are carrying a charge and spin the form factor has

a electric and the magnetic contribution, respectively. The form factors gives an exhaustive characterization of the spatial distribution of the charge and the currents of an extended object. Particle interactions are commonly represented by Feynman diagrams (see Fig. 1.2). The arrows express the flow of conserved charges like the electric charge or color. Undetectable virtual particles are introduced to explain how energy and momentum are transferred during a reaction. Two interaction processes with an intermediate virtual photon are important in our context: electron-hadron scattering and electron-positron annihilation. Since the virtual photon exists for an exceedingly short time, there is, according to Heisenberg's uncertainty principle, a correspondingly large uncertainty in its energy. Within this uncertainty, momentum and energy need not balance each other. Therefore the virtual photon can have nonzero mass during this short interaction period. In the relativistic description of particle scattering it is convenient to use the 4-momentum transfer defined as $q^2 = (\Delta E_e)^2 - (\Delta p_e)^2$. In case the virtual photon transfers essentially momentum but not energy ($q^2 < 0$) the messenger of the interaction is called space-like photons. The corresponding electromagnetic form factors can be obtained from e^-p , e^-n and $\pi^\pm e^-$ scattering experiments. Another method for producing virtual photons is particle-antiparticle annihilation (see Fig. 1.2). Annihilation experiments offer the possibility to study the form factor in the time-like region where the virtual photon has energy but no momentum. Annihilation and scattering experiments are complementary and allow to measure as well temporal as spacial properties of hadronic states, respectively.

The elementary particles are classified by the quantum numbers assigned to them. The neutral vector mesons have the same quantum numbers as the photon: spin 1 and negative parity ($J^P = 1^-$). Three light, neutral vector mesons are known, the ρ^0 , the ω and ϕ meson, whose characteristic quantities are presented in Table 1.1. The first prediction that vector mesons

Particle	Mass, MeV/c ²	Decay width, MeV/c ²	Lifetime, fm/c	Branching Ratio e^+e^-
ρ	769	152	1.3	4.44×10^{-5}
ω	783	8.43	23.4	7.07×10^{-5}
ϕ	1020	4.43	44.4	3.09×10^{-4}

Table 1.1: Characteristic quantities of light vector mesons [45].

might exist were made by Y. Nambu in 1957. A particularly useful model of photon-hadron interactions, called the VMD¹⁵ model, was introduced by J.J. Sakurai in 1960 [64]. It essentially states, that energetic photons acquire a hadronic character by fluctuating into $q\bar{q}$ pairs with the quantum numbers of the photon, i.e. into neutral vector mesons. In this picture, the interaction of a virtual photon with a hadron is mediated by a vector meson. This type of photon-hadron interaction is shown in Fig. 1.2 (right panel). The Gell-Mann and Zweig quark model predicts that the photon should behave as if it was composed of 75% ρ -meson, 8% ω -meson and 17% ϕ -meson. Thus the ρ is the most important of the vector mesons in mediating photon-hadron interactions [65].

The cleanest method for studying the vector meson composition of the photon is e^+e^- annihilation which isolates the production of vector mesons from other interactions. The annihilation of a positron and an electron into a virtual photon is purely electromagnetic and can be calculated with much confidence and precision. The pion form factor in the time-like region predicted from Wilsonian matching [66] is in a good agreement with experimental data obtained from $e^+e^- \rightarrow \pi\pi$ measurements [67]. Experimental points are satisfactorily described by the ρ -meson excitation curve with ρ - ω interference taken into account. Detailed experimen-

¹⁵Vector Meson Dominance



Figure 1.2: Left: Diagram for $e^+e^- \rightarrow \pi^+\pi^-$ annihilation; this process is caused by one-photon exchange in the time-like momentum-transverse region. The total cross section for the annihilation reaction is modified by the internal structure of the pions. Right: The same diagram for the one-photon exchange process in the VMD model.

tal data on the pion form factor in the time-like region permit a very accurate determination of the properties of the ρ -meson. Hadrons, embedded inside nuclei, obviously change their properties. In heavy-ion collisions nucleons are excited into baryonic resonance states (Δ , N^*) which itself decay by emission of mesons. Hence, the presence of baryons influences the vector meson spectral function in the medium.

1.1.4 In-medium modifications

Phenomenologically, in-medium effects associated with the intermediate ρ meson can be classified according to the following extreme scenarios: in a "dropping" scenario, the ρ mass essentially changes its mass without affecting the width of the state (e.g. Hatsuda Lee and Brown Rho). A simple "broadening" of the ρ spectral function without substantial variations of the pole mass is observed in hadronic models (e.g. Rapp, Wambach *et al.* [15]). It is currently debated to which extend these effects are independent of each other and whether they are more driven by baryonic density or by temperature (i.e. pion density). Experimentally one can address this question by comparing in-medium ρ -decay in cold and hot/dense matter as obtained in $p+A$ and $A+A$ collisions, respectively, at different energies (see section 1.4). What are the theoretical expectations?

In-medium "dropping" mass scenario

The concept of in-medium "dropping" ρ masses was introduced by Brown and Rho [16, 68], and is commonly called "BR-scaling". Their argumentation is based on chiral symmetry arguments and scale invariance. In the chiral limit (defined as the limit in which bare quark masses are equal to zero), the whole hadron mass of e.g. a nucleon or a vector meson can be expressed in terms of the chiral ($\langle q\bar{q} \rangle$) condensate. The role of the $\langle q\bar{q} \rangle$ quark condensate is to produce most of the ρ -meson mass, according to the relation $\langle q\bar{q} \rangle^* / \langle q\bar{q} \rangle = m_\rho^* / m_\rho$. With a reduced condensate, the ρ -meson mass is therefore expected to drop. Within the "BR-scaling" the mass of the ρ meson should drop by about 15% at normal nuclear density.

In-medium "broadening" mass scenario

In-medium scenarios leading essentially to a broadening of the ρ -meson mass, interactions of it with the hadrons of the medium play a dominant role. The modification of the pion cloud due



Figure 1.3: ρ -meson self-energy diagrams in matter. Left: $\Delta(1232)$ -nucleon-hole polarization. Right: The modification of ρ -meson self-energy through its coupling to resonance-hole states.

to $\Delta(1232)$ -hole (ΔN^{-1}) excitations (see Fig. 1.3 left panel) has been included in the ρ spectral function and investigated in Ref. [69, 70]. Later, the investigation of the ρ properties in medium has focussed on effects due to a direct coupling of the ρ to resonance-hole states (N^*N^{-1}) [71, 72, 73] excitations (see Fig. 1.3 right panel). The basic result obtained by this approach for cold nuclear matter is a substantial broadening of the ρ spectral function accompanied by a slight upward mass-shift of the peak position. A collective ΔN^{-1} mode induces additional strength (or even a peak structure) around a mass of $400 - 500 \text{ MeV}/c^2$, while N^*N^{-1} modes are found to be instrumental in shifting additional strength to low masses including masses below the 2π threshold. As seen in the left panel of Fig. 1.4, a strong momentum dependence of the spectral function [71, 11] is expected. From kinematical considerations it follows that the position of the strength associated to the resonance-hole states moves down to lower invariant masses with increasing momentum \mathbf{q} of the vector meson, relative to nuclear matter. Therefore, a substantial amount of strength in the ρ spectral function is shifted to lower invariant masses.

Theoretical investigations of ρ properties in a hot pion gas found rather moderate effects [74]. Comparing the ρ spectral function in mesonic matter at $T = 150 \text{ MeV}$, $\rho = 0$ to the one in cold nuclear matter at $\rho_N = \rho_0$ reveals substantially stronger medium effects for the latter, especially in terms of the enhancement below the free ρ meson pole mass. When investigating the ρ spectral function in hot hadronic matter the calculations have simultaneously to account for both, baryon density and temperature. Figure 1.4 (right panel) shows the characteristic features of medium modifications expected for vector mesons. To illustrate the sensitivity to the modi-

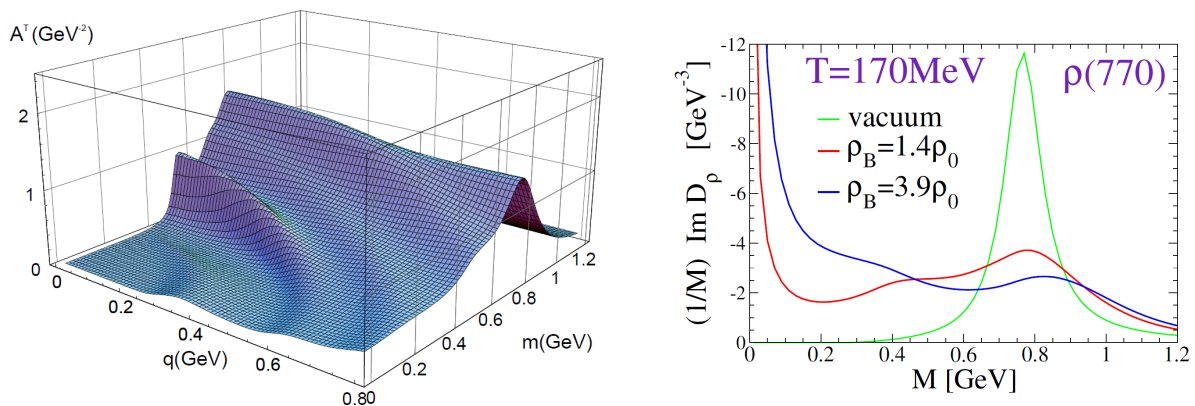


Figure 1.4: Left: Transversal spectral function of the ρ in nuclear matter as a function of its invariant mass \mathbf{m} and \mathbf{q} for $\rho_N = \rho_0$, $T = 0 \text{ MeV}$ [11]. Right: ρ meson spectral functions under SPS (red line) and FAIR (blue line) conditions, as well as in vacuum (green line), in the hadronic many-body approach of Ref. [12].

fications caused by the baryonic component of the medium, the hadronic many-body ρ meson spectral function [12] is shown for $T = 170$ MeV and net baryon densities $\rho_B = 1.4\rho_0$ and $\rho_B = 3.9\rho_0$, somewhat resembling SPS and FAIR conditions, respectively. For comparison, the vacuum spectral function is shown as well. The plots suggests that the largest sensitivity is in the mass region below 0.4 GeV/ c^2 and for not too high transverse momenta of the ρ meson.

1.2 Probing extreme matter with virtual photons

The best approach to study the predicted phenomena of vector mesons in medium is dilepton spectroscopy. The composition of the nuclear fireball produced in heavy-ion collisions strongly depends on the temperatures and densities achieved: at low temperature (or beam energy) it is dominated by the primordial nucleons, at high temperature the meson density exceeds the baryon density by factors and the baryon to anti-baryon ratio approaches unity in the central region of the reaction. However, the lifetime of the hot and dense phase is about $\tau \leq 15$ fm/ c only, i.e. rather short compared to the lifetime of the lowest hadronic excitations. To experimentally access the microscopic properties of these extreme forms of matter is a formidable task. Short-lived vector mesons (ρ , ω and ϕ) have a lifetime comparable to the lifetime of the fireball. Moreover, they couple directly to the electromagnetic current as discussed in the previous section. Once decayed into a purely leptonic final state, the daughter particles will traverse the dense medium without substantial (i.e. only electromagnetic) final state interaction. By means of their 4-momentum reconstructed from the lepton pair, such states provide a direct link to the properties of the medium.

The lepton pair gives access to its mesonic parent state directly via the kinematic description of the intermediate virtual photon, i.e. by its invariant mass (M_{l+l-} , $l = e, \mu$), transverse momentum (p_t), and laboratory rapidity (y). The dilepton pair mass is equivalent to the energy transferred which is given by the Lorentz invariant mass of the virtual photon:

$$M_{l+l-} \cdot c^2 = \sqrt{(E_{l+} + E_{l-})^2 - (\vec{p}_{l+} \cdot c + \vec{p}_{l-} \cdot c)^2} \quad (1.2)$$

where $E_{l\pm}$ is the total energy, $p_{l\pm}$ is the momentum in the laboratory system and c is the velocity of light. Equation 1.3 can be simplified since the rest mass of the lepton is small compared to the energies involved and the relativistic limit $E_{l\pm} \approx |p|$ holds. This allows to determine the invariant mass from the three momenta of the leptons and their opening angle (θ):

$$M_{l+l-} = 2 \cdot \sin \frac{\theta_{l+l-}}{2} \cdot \sqrt{p_{l+} \cdot p_{l-}}. \quad (1.3)$$

The transverse momentum is invariant under a boost in beam (z) direction and can be calculated from the pair member momentum projections as:

$$p_t = \sqrt{(p_{l+x} + p_{l-x})^2 + (p_{l+y} + p_{l-y})^2}. \quad (1.4)$$

The parallel component of the momentum is obtained as the laboratory rapidity which transforms by an additive constant under a boost in the beam direction and it can be calculated as:

$$y = \frac{1}{2} \cdot \ln \frac{(p_{l+} + p_{l-}) + (p_{l+z} + p_{l-z})}{(p_{l+} + p_{l-}) - (p_{l+z} + p_{l-z})}. \quad (1.5)$$

Figure 1.5 schematically illustrates the spectral distribution of dileptons produced in ultra-relativistic heavy-ion collisions. Dileptons are emitted in each phase and in all regions of the space-time history of the colliding and expanding nuclear system. As the produced dileptons can escape the medium essentially undistorted from their production vertex into the detector, they carry important information about their parent particles. In first-chance nucleon-nucleon interactions ($\tau \sim 1 \text{ fm}/c$) dileptons can be produced in hard interactions such as e.g. the Drell-Yan process. This process is characterized by the annihilation of a quark in one nucleus with a sea anti-quark from the other nucleus into a virtual photon which subsequently converts into a lepton pair. In very energetic collisions the formed matter is likely of partonic nature (deconfinement phase) and it rapidly expands and thermalizes. In the partonic phase dileptons are abundantly produced via $q\bar{q}$ annihilation. While the system expands it cools down crossing the phase boundary to a hot and dense hadronic phase ($\tau < 10 \text{ fm}/c$). Here, dileptons are created mainly in pion annihilation processes and resonance Dalitz decays. At lower beam energies, coherent or non-coherent virtual bremsstrahlung is a dominant source of lepton pairs. Finally, the system freezes out at approximately $10 - 12 \text{ fm}/c$ after the $A+A$ collision. After freeze-out dileptons are produced by decays of long-lived hadrons and neutral mesons (π^0 , η but also ω , ϕ) according to their vacuum lifetimes. Those long-lived sources do not contain any information on in-medium properties of the parent particles and are commonly called "hadronic decay" contribution or "hadronic cocktail" of the dilepton spectra. While vector meson decays give rise to narrow structures in the spectral distribution, Dalitz decays, correlated semi-leptonic decays (like from charmed mesons pairs) and the Drell-Yann process result in continuous contributions.

Invariant mass covered in experiments is typically grouped into three regions: the low-mass region ($M_{l+l-} \leq 1 \text{ GeV}/c^2$), the intermediate and finally the high-mass region ($M_{l+l-} \geq 3 \text{ GeV}/c^2$). Drell-Yan annihilation leaves its trace mainly at large invariant masses. The high mass region includes also the J/ψ and ψ' resonances. For intermediate masses the semi-leptonic decays of the charmed mesons $D\bar{D}$ dominate. The low mass region includes the Dalitz decays of the neutral mesons (π^0 , η , η' , ω) and the resonance decays of the ρ , ω and ϕ . At such high energies, contributions from baryonic resonances are small.

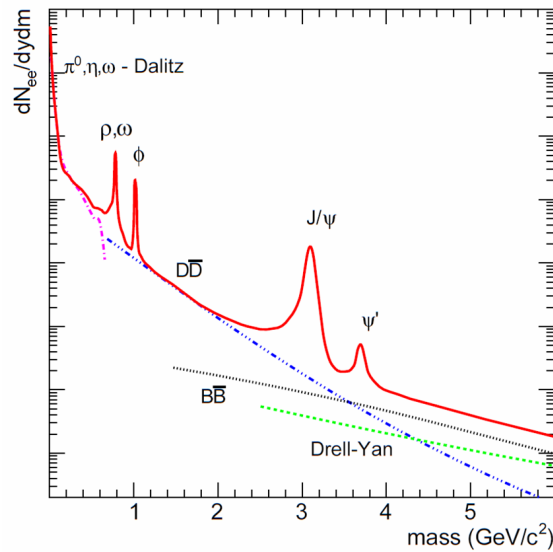


Figure 1.5: Schematic spectral distribution of lepton pairs emitted in ultra-relativistic heavy-ion collisions (picture taken from [13]).

Dileptons, however, are a very rare probe. While the production of real photons is suppressed relative to hadrons by about one power of the electromagnetic coupling constant, $\alpha = 1/137$, dilepton emission (i.e. virtual photons with subsequent decay $\gamma^* \rightarrow e^+e^-$ or $\gamma^* \rightarrow \mu^+\mu^-$) is further suppressed by an additional power of α . The branching ratios for hadronic decays of vector mesons are thus typically 4 orders of magnitude larger than for dilepton decays, unless they are suppressed by phase space factors. This is a huge penalty factor compared to hadronic decay channels like e.g. the for the decay $\rho \rightarrow \pi\pi$). However the strong final state interactions of pions in a dense medium makes an interpretation of the signal a least model-dependent, if not impossible. Observed effects could be interpreted both as due to medium modifications of the vector meson spectral function or due to the final state interaction of the decay products.

1.3 Strongly interacting matter in models

One of the main task of theoretical heavy-ion physics is to link experimental observables to the different phases and manifestations of hadronic matter. For this, a detailed understanding of the dynamics of heavy-ion reactions is essential. Consequently also calculations of the dilepton production rate in hot and dense matter require the knowledge of the space-time history of the colliding and expanding nuclear system. The created matter changes its properties very rapidly with strong variations in density and temperature which complicates the interpretation of the data in terms of medium modifications. In the following we will discuss two different approaches to simulate the reaction dynamics in their application to evaluate dilepton spectra. The emission of lepton pairs can be calculated from thermal fireball expansion models or from microscopic transport calculations.

1.3.1 Transport models

Transport theory has always played an important role in the interpretation of experimental results and in predicting new interesting effects in relativistic heavy-ion reactions. It is particularly well suited for non-equilibrium situations, rapid time-dependencies of the system parameters, finite size effects and non-homogeneity, particle and resonance production as well as collective dynamics. Microscopic transport models attempt to describe the full time-evolution from the initial state of the heavy-ion reaction over a broad range of collision energies. Examples of such transport theories are the Boltzmann-Uehling-Uhlenbeck (BUU) approach [75] and its relativistic extensions (RBUU) [76], the Hadron-String Dynamics (HSD) [77], and Quantum Molecular Dynamics (QMD) [78] and its relativistic versions RQMD [79] and UrQMD [80].

The BUU [81] model provides an unified transport framework in the MeV and GeV energy regimes for elementary reactions on nuclei and for heavy-ion collisions. In this approach the flow of particles is modeled in a Boltzmann-Uehling-Uhlenbeck formulation. The relevant degrees of freedom are mesons and baryons. The BUU model includes 61 baryonic and 31 mesonic states. The necessary parameters (e.g. pole masses, life times in vacuum, branching ratios) are based on the PDG compilation [45]. The BUU equation is solved applying a test-particle ansatz in parallel ensembles which guarantees locality in the scattering processes of the test-particles. In the BUU approach particle propagation is being represented by propagation through space and time of $2 \cdot 10^5$ test-particles. Resonances are explicitly propagated. The HSD has been developed based on the BUU model and includes also particle production

through string fragmentation above a certain NN center of mass energy and off-shell propagation of shortlived states. The dilepton spectra in HSD are calculated perturbatively with the time integration method.

The QMD approach or "equation of motion" approach is an N -body theory to describe heavy-ion reactions. The QMD combines the advantages of the classical molecular dynamics approach (explicit two-body interactions) with the important quantum features (known from the Vlasov-Uehling-Uhlenbeck theory), which are essential to describe the reaction dynamics properly. The QMD model at very high bombarding energies ($E_{kin} = 3 - 200 \text{ GeV}/u$) is called "relativistic quantum molecular dynamics", it explicitly follows the trajectories of all hadrons (including produced particles), thus providing the full information about the dynamical evolution of the system. There are two main differences to the non-relativistic QMD model: the explicit Lorentz invariance and the opened inelastic reaction channels via string excitation. The extension of the QMD model up to the center-of-mass energy of $200 \text{ GeV}/u$ is realized in the UrQMD transport model developed at the University of Frankfurt.

The isospin quantum molecular dynamics (IQMD) model [82] is a semiclassical transport model. Nucleons, deltas and pions interact via Skyrme forces and via binary collisions. The individual nucleons are described by Gaussian wave packets with fixed width. The collisions allow for elastic and inelastic channels. The Tübingen relativistic quantum molecular dynamics (RQMD) transport code is in principle similar to the IQMD model. The RQMD transport model combines a resonance dominance model for nucleon-nucleon scattering with an extended vector meson dominance (eVMD) model. The nucleon resonance dominance is an effective principle which assumes that the vector meson production runs over the excitation of nucleon resonances only. The extended vector dominance model introduces radially excited ρ and ω mesons in the $RN\gamma$ transition form factors [83]. This allows a kinematically complete, fully relativistic, and unified description of the nucleon resonance transition amplitudes $R \rightarrow NV$ ($V = \rho, \omega$), $R \rightarrow N\gamma$, $\gamma^*N \rightarrow R$ (electro-production), and $R \rightarrow Ne^+e^-$ with arbitrary spin and parity in terms of the magnetic (G_M), electric (G_E), and Coulomb (G_C) transition form factors. The parameters of eVMD are fixed by fitting to experimental data of photo- and electro-production [35]. In the RQMD and IQMD models only pions are included as explicit mesonic degrees of freedom. Heavier mesons such as K , η , ρ , ω , are treated perturbatively. These models are in particular suited to study subthreshold meson production at SIS energies.

Transport models account for complicated reaction dynamics. A drawback of such a procedure is the dependence on the phenomenology and an extended set of input parameters entering the models. Some of those parameters (electromagnetic form factors, decay branching ratios, production cross sections) can't be constrained by data or theoretical approaches.

1.3.2 Fireball model

Because of the complexity of the relativistic quantum mechanical many-body problem, severe approximations or simple models have been invoked to reduce the theoretical problem to a tractable form. The "fireball" model for heavy-ion collisions was originally proposed by Westfall *et al.* [84]. In the fireball model, the collision of the projectile and target nuclei are approximated in terms of two uniform spheres whose participants sweep out cylindrical cuts from each other. The participants then form a single "fireball", which is at rest in the fireball center-of-mass system. The inelastic energy from the collision of the participants is assumed to be completely thermalized in the fireball center-of-mass frame, and then the fireball

expands isotropically with momentum distributions of the participants described by Maxwell-Boltzmann distributions. The effective temperature of the fireball, and the relative numbers of participants and spectators are determined entirely from geometry. The time scale of the volume expansion is taken from experiment [85].

Schematically, the emitted spectrum of dileptons from an evolving thermalized system can be found from the convolution:

$$\frac{d^3 N}{dM dP_t dy} = \text{fireball evolution} \otimes \frac{dN}{d^4 x d^4 q} \otimes \text{acceptance}, \quad (1.6)$$

where e.g. the emission rate for virtual photons from ρ decay is found from the spectral function $R(q, T, \mu_B)$ as:

$$\frac{dN}{d^4 x d^4 q} = \frac{\alpha^2}{12\pi^4} \frac{R(q, T, \rho_B)}{e^{\beta q_0} - 1}. \quad (1.7)$$

Here, q is the 4-momentum of the emitted lepton pair, T is the temperature of the emitting volume element, $\beta = 1/T$, and ρ_B its baryon density. The fireball evolution encodes information on the radiating volume, the temperature T , the baryon chemical potential μ_B , the transverse flow velocity v_T , the longitudinal rapidity y and chemical non-equilibrium properties such as pion chemical potential μ_π [86].

In case the fireball evolution is known the in-medium spectral function $R(q, T, \rho_B)$ can be deduced from the spectral distribution measured. If $R(q, T, \rho_B)$ is known the fireball evolution can be studied. Therefore, it is important to measure (experimentally) the ρ meson spectral function at different beam energies and different system sizes to have a better understanding of the local emissivity as well as knowledge of the space-time evolution of the radiating matter. This will also help to clarify the connection of the measured spectral function to chiral symmetry restoration and to provide additional constraints for the model calculations.

1.4 Strongly interacting matter in experiments

The interest in continuum lepton-pair production in high-energy collisions arose already in the Seventies with the theoretical work on massive lepton pair production in hadron-hadron collisions at high energies [87]. The detection of the Drell-Yan process and J/ψ triggered a lot of attention for lepton pairs at intermediate masses ($1 < M_{l+l-}/(\text{GeV}/c^2) < 2.5$) as well as for lepton pairs at low masses ($M_{l+l-} < 1 \text{ GeV}/c^2$). Several experimental groups have taken up the challenge to search for medium modifications of mesons in this spectral region. By varying experimental conditions such as the collision energy or the collision system one can cover a broad range in temperature and baryon density of the formed matter. Medium modifications can be studied in elementary reactions (photon, proton, or pion induced reactions) or in heavy-ion collisions. With respect to studying in-medium properties of hadrons one separates experiments addressing:

- cold nuclear matter, i.e. matter that exists at nuclear ground state density $\rho_0 = 0.16 \text{ fm}^{-3}$ and below this in the periphery of the nucleus and energy density $\varepsilon_0 = 150 \text{ MeV}/\text{fm}^3$ and without thermal excitation $T = 0 \text{ MeV}$;
- hot and dense matter, i.e. $\rho > \rho_0$ and $T > 0 \text{ MeV}$.

The properties of cold nuclear matter can be studied in elementary collisions, i.e. $p+A$, $\gamma+A$, $\pi+A$. To create hot and dense medium in the laboratory heavy-ion collisions are used. In heavy-ion collisions nuclear matter can be compressed to several times normal nuclear ground state density and heated to above the critical temperature for the transition to deconfined matter at $T_c \simeq 160 - 190 \text{ MeV}$ (for $\mu_B = 0 \text{ MeV}$).

1.4.1 Dilepton production in elementary collisions

Information on the ρ meson in cold nuclear matter has been obtained in two experiments at KEK [88] and JLAB¹⁶ [89]. The experiments were motivated by the path breaking studies on the role of spontaneous symmetry breaking in hadronic mass generation by Brown and Rho (see section 1.1.4) Hatsuda and Lee. From the derived scaling laws for the density dependence of light vector meson masses it was obvious, that substantial mass shifts in the order of 10 to 20% should already be observable in cold nuclear matter [62]. In this approach the mass of the vector meson is characterized by the shift parameter α , i.e. $m = m_0 \cdot (1 - \alpha \frac{\rho}{\rho_0})$ (see Fig. 1.6).

The experiment E325 [88] is installed at the KEK¹⁷ 12 GeV Proton Synchrotron to measure the invariant mass spectra of ρ , ω , $\phi \rightarrow e^+e^-$ in $p+A$ reactions. The measurements have been performed for two targets, carbon (C) and copper (Cu). The KEK collaboration finds a significant enhancement over the known hadronic sources on the low-mass side of the ω -meson peak for C and Cu data. The spectrometer has two electron arms and two kaon arms (for $\phi \rightarrow K^+K^-$ measurements), which share a dipole magnet and tracking devices. By requiring each a track of an e^+e^- pair in both arms, the low-mass region of the spectrum is largely suppressed with increasing forward laboratory momentum. Moreover, the E325 experiment eliminates all electron pair candidates having an apparent e^+e^+ or e^-e^- configuration. The combinatorial background was evaluated by the event-mixing method, however, since like-sign pairs have not been recorded it is not possible to constrain the mixed event background by the same-event like-sign background. Hence, the normalization of the event-mixed background is obtained by fitting the measured distribution with a combined signal and background cocktail where the shape of the background is taken from event mixing. Moreover, possible correlated background (for details see section 3.4.1) can not be described by the event-mixing technique. Nevertheless, the E325 collaboration concludes that the observed modification can be understood if the masses of the ρ and ω mesons decrease by 9% at normal nuclear density while they exhibit no in-medium broadening (see Fig. 1.6, filled square).

The ρ meson mass spectra have also been extracted for H , C and $Fe-Ti$ targets by the CLAS¹⁸ at JLAB using photon induced reactions at energies $E_\gamma = 0.6 - 3.8 \text{ GeV}$. By analyzing the ratio of the $Fe-Ti$ to the H mass distributions, a value of 0.02 ± 0.02 for the mass shift parameter α was obtained (see Fig. 1.6, circle). Beyond mass shifts, there can also be a broadening of the ρ meson spectral shape. From simultaneous fits to the mass spectra and their ratios, the extracted widths are consistent with collisional broadening and show no signs of further modifications [89]. The results of the E325 and CLAS collaborations differ significantly: the E325 collaboration claims to see a mass shift and no broadening of the ρ meson, the CLAS collaboration sees no mass shift, but collisional broadening. A strong momentum dependence of the spectral function is expected as has been discussed in section 1.1.4. One should mention here that the CLAS detector acceptance is such that only ρ -mesons with

¹⁶Thomas Jefferson National Accelerator Facility

¹⁷High Energy Accelerator Research Organization, Japan

¹⁸CEBAF Large Acceptance Spectrometer

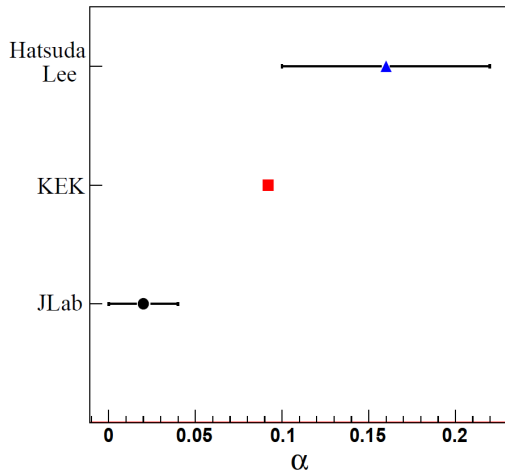


Figure 1.6: Shift parameter α . Circle: CLAS result for the $Fe-Ti$ data, square: E325 result for Cu data, triangle: the prediction of the Hatsuda and Lee model. For the E325 result, the error is smaller than the symbol.

momenta $p_\rho > 0.8 \text{ GeV}/c$ are measurable. This might be too high in order to be sensitive to expected medium modifications.

Lesson 1: Get your background right! We learned from the E325 collaboration that it is very important to measure lepton pairs of any charge combination. For the background determination both like-sign (same charge) and unlike-sign (opposite charged) pairs should be taken into account in order to precisely determine the background.

Lesson 2: Cover the relevant phase space! We learned from the CLAS collaboration that experiments have to provide acceptance for low momentum mesons in order to be sensitive to medium modifications of the ρ -meson.

It should be mentioned here, that in-medium modification of low-mass vector mesons are also studied by experiments focusing on hadron decay channels. The TAPS/CB-ELSA¹⁹ collaboration used photo production of ω meson off nuclei and reconstructed the vector meson in the Dalitz decay channel. The signal is then obtained in a 4-photon final state measured with a highly segmented electromagnetic calorimeter. The TAPS calorimeter is now installed at MAMI²⁰ to continue this investigations with much improved statistics.

1.4.2 Dilepton production in heavy-ion collisions

Dilepton spectra measured by the CERES/HELIOS²¹ and NA60 experiments at CERN-SPS energies ($40 - 158 \text{ GeV}/u$) demonstrate a significant in-medium modification of the ρ meson spectral function signaled by an additional yield (excess) of lepton pairs in the invariant mass region below the ρ meson pole mass. As mentioned already in the previous section, the main theoretical scenarios for in-medium changes of the ρ meson spectral function find baryon density being more important than temperature. Consequently, stronger in-medium effects would be expected for lower beam energies, i.e. at $40 \text{ GeV}/u$ compared to the situation at the highest SPS energy of $160 \text{ GeV}/u$.

In-medium spectral functions from heavy-ion reactions were measured by CERES [6] (in $^{108}Pb+^{197}Au$ collisions at $158 \text{ GeV}/u$ and $40 \text{ GeV}/u$), and by NA60 [7] (in $^{115}In+^{115}In$ col-

¹⁹Two Arm Photon Spectrometer/Crystal Barrel Elektronen-Stretcher-Anlage

²⁰MAinz MIcrotron accelerator

²¹ChErenkov Ring Electron Spectrometer

lisions at 158 GeV/u). In order to exhibit the shape of the contribution of radiation from the medium, the "hadronic cocktail" was subtracted (excluding the ρ meson) from the data. The resulting spectrum is assumed to essentially emerge from the ρ meson form by $\pi\pi$ annihilation: the resulting invariant mass spectra of pairs emitted from the early stage of the reaction are shown in Fig. 1.7. It should be noted that the resulting spectral distribution is not necessarily showing the integrated (over space-time evolution) spectral function of the ρ meson but is modified by kinematical factors and the detector acceptance. The respective corrections are either part of the calculations (kinematical factors) and applied to the results of the calculation (experimental filter).

The yield and spectral shapes of the CERES results are well described by a broadening scenario for the ρ but are not consistent with a dropping mass scenario (discussed in Ref. [6]). Below 0.2 GeV/c² (see Fig. 1.7, left panel), the large errors arise from the fractionally small contribution of medium radiation in the π^0 Dalitz decays region and do not allow for a definite conclusion. However, the trend indicates a further increase of the in-medium contribution towards the photon point at $M_{l+l^-} = 0$ GeV/c² [6]. The broadening mass scenario implies a strong coupling of the ρ meson to baryons which adds strength to the dilepton yield at low invariant masses. Also the associated space-time averaged ρ spectral function from NA60 measurements shows a strong broadening and essentially no shift in mass [7]. The NA60 collaboration also claimed to see first direct evidence for thermal radiation of partonic origin. This conclusion came from the scaling of inverse slope parameters T_{eff} extracted from exponential

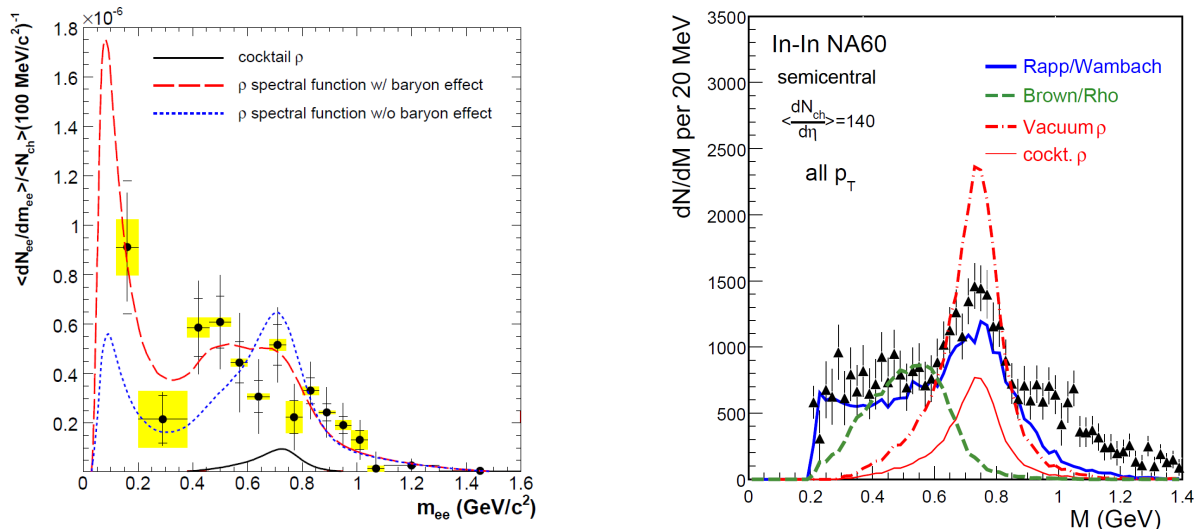


Figure 1.7: **Left:** CERES results on the e^+e^- pair yield after subtraction of the "hadronic cocktail", $Pb+Au$ collisions at a kinetic beam energy of 158 GeV/u, 7% most central reactions. In addition to the statistical error bars, systematic errors of the data (horizontal ticks) and the systematic uncertainty of the subtracted cocktail (shaded boxes) are indicated. The broadening scenario (long-dashed line) is compared to a broadening scenario excluding baryon effects (dotted line). **Right:** NA60 results [14] on the comparison of the excess mass spectrum for semi-central $In+In$ collisions at 158 GeV/u to model predictions: cocktail $\rho \rightarrow \mu^+\mu^-$ (thin solid line), unmodified ρ (dashed line), in-medium broadened ρ [15] (thick solid line), dropping ρ mass scenario [16] (dashed-dotted line). Lower dashed line: QGP radiation. The errors shown are purely statistical. The systematic errors of the continuum are about 25%. The open data points show the excess mass spectrum assuming the η yield to be lowered by 10% (which also gives an estimate on the systematic error).

fits to the m_T spectra from ρ decay taken for different invariant mass bins [14]. The theoretical interpretation of the data is not yet conclusive [90].

Lesson 3: high statistics is essential! We learned from the NA60 that high statistics and multi-differential analyses are needed in order to be capable of differentiating between different models.

An extension of dilepton spectroscopy to even higher collision energies was achieved at RHIC. The PHENIX²² experiment has measured the di-electron production in $^{197}\text{Au}+^{197}\text{Au}$ collisions at $\sqrt{s} = 200 \text{ GeV}/u$ [91]. The electron-positron pair yield per inelastic collision as function of the pair mass in $p+p$ and $\text{Au}+\text{Au}$ collisions is shown in Fig. 1.8. For the most central collisions the pair excess over the "hadronic cocktail" is found to be almost 3-times larger as the one measured by the CERES collaboration at $\sqrt{s} = 17.2 \text{ GeV}/u$ and indicates an even larger strength at low masses. The enhancement has a strong centrality dependence and is fully absent in peripheral collisions, where the observed yield agrees well with the calculated "hadronic cocktail". In Fig. 1.8 the yield measured in $p+p$ interactions is compared with the yield measured in $\text{Au}+\text{Au}$. The continuum yield in the low mass region is significantly enhanced for $\text{Au}+\text{Au}$ collisions with respect to $p+p$, confirming the enhancement measured with respect to the "hadronic cocktail" at SPS. However, PHENIX results await theoretical interpretations. First tries to apply the same model as for the SPS data had no success in describing the data.

At much lower beam energies ($1 - 2 \text{ GeV}/u$) di-electron production was studied by the DiLepton Spectrometer (DLS) collaboration at Bevalac [1]. A large electron pair excess over the "hadronic cocktail" has been observed in $^{12}\text{C}+^{12}\text{C}$ and $^{40}\text{Ca}+^{40}\text{Ca}$ collisions. However, in contrast to the high-energy experiments, for a long time the excess could not be satisfactorily explained by any the theoretical model and the situation hence became famous as the "DLS puzzle". The excess of electron pairs in $\text{C}+\text{C}$ collisions was recently re-investigated by the HADES experiment at GSI for beam energies of 1 and 2 GeV/u [3, 4]. The excitation function of the excess-pair multiplicity with masses just larger than those from π^0 Dalitz decays, i.e. masses in the range from $0.15 \text{ GeV}/c^2$ to $0.5 \text{ GeV}/c^2$, are shown in Fig. 1.9 together with

²²Pioneering High Energy Nuclear Interaction eXperiment

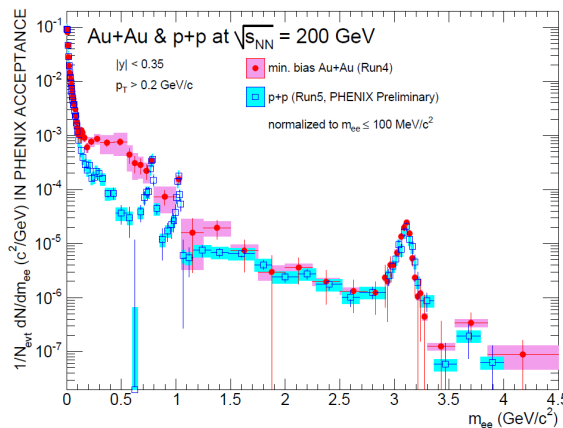


Figure 1.8: PHENIX results on the e^+e^- pair yield measured in $p+p$ compared to the yield measured in $\text{Au}+\text{Au}$ collisions. Statistical (bars) and systematic (boxes) uncertainties are shown separately; the mass range covered by each data point is given by the horizontal bars.

the pair multiplicity from η Dalitz decays ($\text{BR}_{\gamma e^+ e^-} = 0.6\%$) within the same mass range. Within experimental errors, the excess scales like π^0 multiplicity, not like the η multiplicity, as is demonstrated by the direct comparison of the excess with the scaled pion and η curves in Fig. 1.9. This fact provides a hint to the possible origin of the excess yield; pion production at these low energies is known to be dominantly coming from the excitation and decay of baryonic resonances (mainly the $\Delta(1232)$ resonance).

Support for this conjecture comes also from theory. Figure 1.10 (left panel) shows the average baryon density evolution as a function of time in 1 GeV/u $Ca+Ca$ collisions calculated in a transport approach by Zhang and Gale [18]. Quantitative descriptions of heavy-ion collisions indicate that due to the stopping a high baryon density of up to two times nuclear ground state density is achieved in the center of the collision zone at bombarding energies of 1–2 GeV/u. The accompanying temperatures, a quantity not rigorously defined since the thermalization criterium is not necessarily fulfilled when reaching the highest densities, are around $T = 80 - 100$ MeV. One therefore should expect the system not to cross the phase boundary to deconfined matter but rather stay in the hadronic phase throughout. Figure 1.10 (right panel) shows that the pion densities are small at this temperature. Therefore, the dominant medium radiation should be driven by nucleons and baryonic resonances in the system (note that at $T = 100$ MeV already 25% of the baryons are thermally excited into Δ 's). Therefore, radiation of baryonic matter involving Dalitz decays of Δ , N^* and nucleon-nucleon bremsstrahlung dominates the dilepton yield in the excess region at 1 – 2 GeV/u beam energy. Vector meson production proceeds via multi-step processes involving intermediate resonances and off-shell effects [5]. The detailed description of these processes in models, however, is difficult. The relevant cross sections are to a large extent unknown and new precise data on elementary pro-

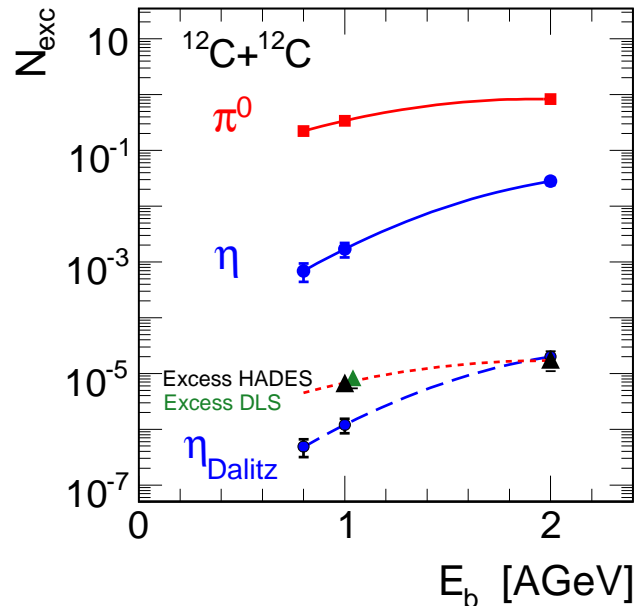


Figure 1.9: Inclusive multiplicity of the pair excess (N_{exc}) in the mass range $M_{ee} = 0.15 - 0.50$ GeV/ c^2 as function of beam energy E_b (black triangles: HADES, green triangle: DLS). Also shown are the π^0 (red circles) and η (blue circles, blue line) inclusive multiplicities in $C+C$ collisions [17], as well as the corresponding η Dalitz decay (black circles, blue dashed line) contribution integrated over $M_{ee} = 0.15 - 0.50$ GeV/ c^2 . For comparison with N_{exc} , down-scaled π^0 curve is shown as dashed red line [3].

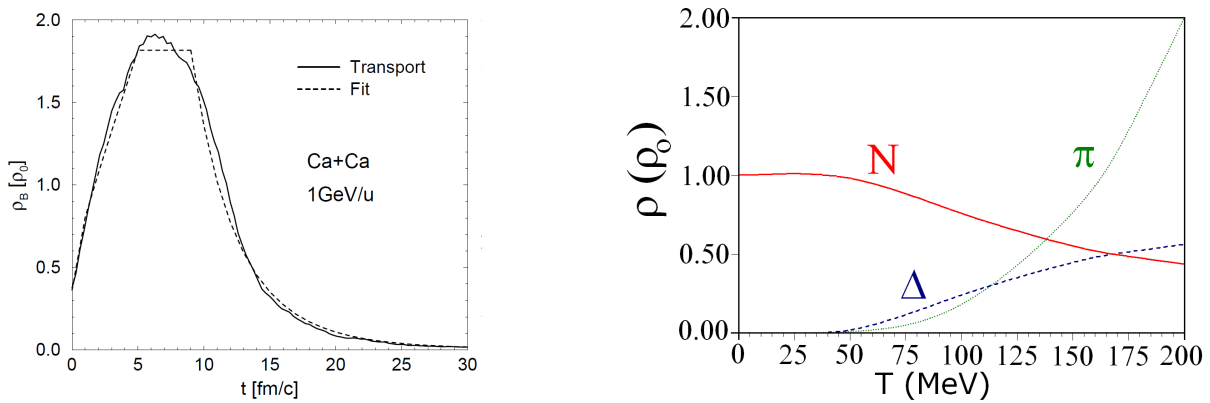


Figure 1.10: Left: Evolution of average baryon density as a function of time in inclusive 1 GeV/u $Ca+Ca$ collisions as extracted from the transport model of Zhang and Gale [18] (solid curve); the dashed curve is a simple parameterization thereof with a maximum temperature of $T_{max} = 100$ MeV in the high density phase and a time-independent baryon chemical potential of $\mu_B = 0.76$ GeV. Right: Composition of a hot $\pi\Delta N$ gas as a function of temperature at a fixed baryon density of $\rho_B = \rho_N + \rho_\Delta = 0.16$ fm $^{-3}$ [15].

duction amplitudes are highly needed. Furthermore, the question whether the observed excess of dileptons is related to any in-medium effect remains open because of uncertainties in the description of elementary di-electron sources.

1.4.3 Dilepton production in NN collisions

In this section I would like to concentrate on the HADES energy range of 1 – 2 GeV/u, briefly summarize the relevant sources of di-electrons, and discuss some unresolved issues in the theoretical description of their yield and spectral distribution. For a beam energy of 1.25 GeV the sources of di-electron production fall into two categories: hadron decays and bremsstrahlung. The hadron decays by their own can further be divided into two sub-categories: two-body and three-body (or Dalitz) decays. Unlike two-body decays, which can produce recognizable peaks in the invariant mass spectra, Dalitz decays produce continuous mass distributions making the isolation of their individual contributions a more difficult task. Estimating the role of specific Dalitz-decay sources is somewhat easier in the $p+p$ system since one can compare the shape of the mass spectra above and below the absolute energy threshold for the formation of a certain source. In $p+p$ reactions, the contribution from the Δ Dalitz decays can be related to the pion yield by the simple isospin relation $\sigma_{\Delta^+} = 3/2 \cdot \sigma_{\pi^0}$, assuming that all π^0 are produced via the Δ^+ resonance. Due to the isospin effect, the π^0 production in $n+p$ reactions is expected to be a factor of two higher compared to $p+p$ reactions, since π^0 are produced via the Δ^+ and Δ^0 (for details see Appendix A). However, different theoretical models differ by factors in the production of the Δ resonance itself (Refs. [34, 92]) and furthermore there is considerable uncertainty about the shape of the mass spectrum produced by Δ Dalitz decays. E.g. it has been found that Δ cross sections are larger in Ref. [34] compared to the Δ cross section from Ref. [93]. The branching ratio for the Δ Dalitz decay $NN \rightarrow N\Delta \rightarrow NN\gamma^*$ is predicted but unmeasured. It is important to mention that higher lying baryonic resonances (N^*1520 , N^*1535 , ...) can also contribute to the mass region below the vector meson pole mass due to off-shell propagation of intermediate vector mesons (ρ , ω correspondingly) [5].

Resonance like or narrow contributions to the di-electron mass spectrum are only expected from vector meson decay, which can branch into an exclusive electron-positron final state. In general, also mesons with a two photon-decay decay into such final states. However, the respective Feynman diagrams are governed by an internal electron line in which the electron/positron from one internal conversion vertex is absorbed as positron/electron in the other internal pair conversion vertex. Hence, such a process can only occur if the helicity of the internal lepton is not conserved. Consequently the respective branching ratios are small or even only upper bounds are known. Helicity non-conservation is more likely if muons are involved. Indeed, a clear peak originating from η decay was found in the dimuon invariant mass spectrum taken by the NA60 collaboration.

Di-electron production from bremsstrahlung processes forms the second category of sources. This is perhaps the most uncertain di-electron source, and surely one which attracted most of the attention over the last years for the case of low beam energies.

1.4.4 DLS and HADES: "Just a little bit of history repeated?"

Di-electron production in collisions at $E_{kin} < 5 \text{ GeV}/u$ was also studied by the DLS collaboration. For $p+p$ and $p+d$ collision systems, complete excitation functions were established [19] (see Fig. 1.11). Invariant mass spectra for the $p+d$ and $p+p$ systems are denoted by filled and unfilled circles, respectively. The kinematical upper limits on the pair mass produced in the $p+p$ system are indicated by dotted lines. The error bars of each data point indicate only the statistical uncertainties. At low energies, the $p+d$ cross section differs significantly from what one would expect from a naive $\sigma \approx m_{p+d}/m_{p+p} \approx 2$ scaling. However, its detailed dependence on pair mass is unknown because of insufficient pair statistics in the DLS data.

Data on dilepton production in elementary collisions obtained with the DLS spectrometer have been available for about 10 years. First theoretical descriptions of di-electron production [94] stated that pp bremsstrahlung is negligible and that np bremsstrahlung should grow and dominate the di-electron yield as the beam energy increases. This scenario, however, had to be reconsidered after the $\sigma^{p+d}/\sigma^{p+p}$ di-electron yield ratios measured by the DLS experiment became available. The di-electron yield ratio at 4.88 GeV/u kinetic beam energy was found to be just a factor of 2 [95, 96] while it is much higher at lower energies. The theoretical approaches were based on the soft-photon approximation (SPA), where only radiation from the external baryon lines is considered (see Fig. 1.12) and the strong-interaction vertex is treated as on shell ($p^2 = m^2$, $c = 1$). This approximation is valid if the energy carried by the photon is less than the inverse of the strong interaction collision time, e.g. $E_\gamma < \tau_{NN}^{-1} \approx 100 - 200 \text{ MeV}$. A semiclassical SPA model requires accurate parameterizations of the elastic scattering cross sections.

Another approach followed up in Ref. [97, 92] is based on an effective One Boson Exchange model (OBE). Unlike the SPA, the OBE formalism allows radiation from internal lines of the interaction diagrams. Drawbacks of the OBE approach include the large number of diagrams which have to be evaluated and ambiguities in adjusting the parameters of the theory. A representative set of Feynman diagrams contributing to the dilepton production within an effective OBE model is shown in Fig. 1.13. The intermediate nucleons or resonances (grey box in Figs. 1.13(a) and 1.13(b)) can radiate a virtual photon which decays into a dilepton. Diagrams of the same type where a virtual photon is emitted from the nucleon line on the right side are also included in the calculations. Virtual photon emission resulting in dilepton pairs from the internal meson line can also occur in case the exchanged meson is charged (see Fig. 1.13(c)).

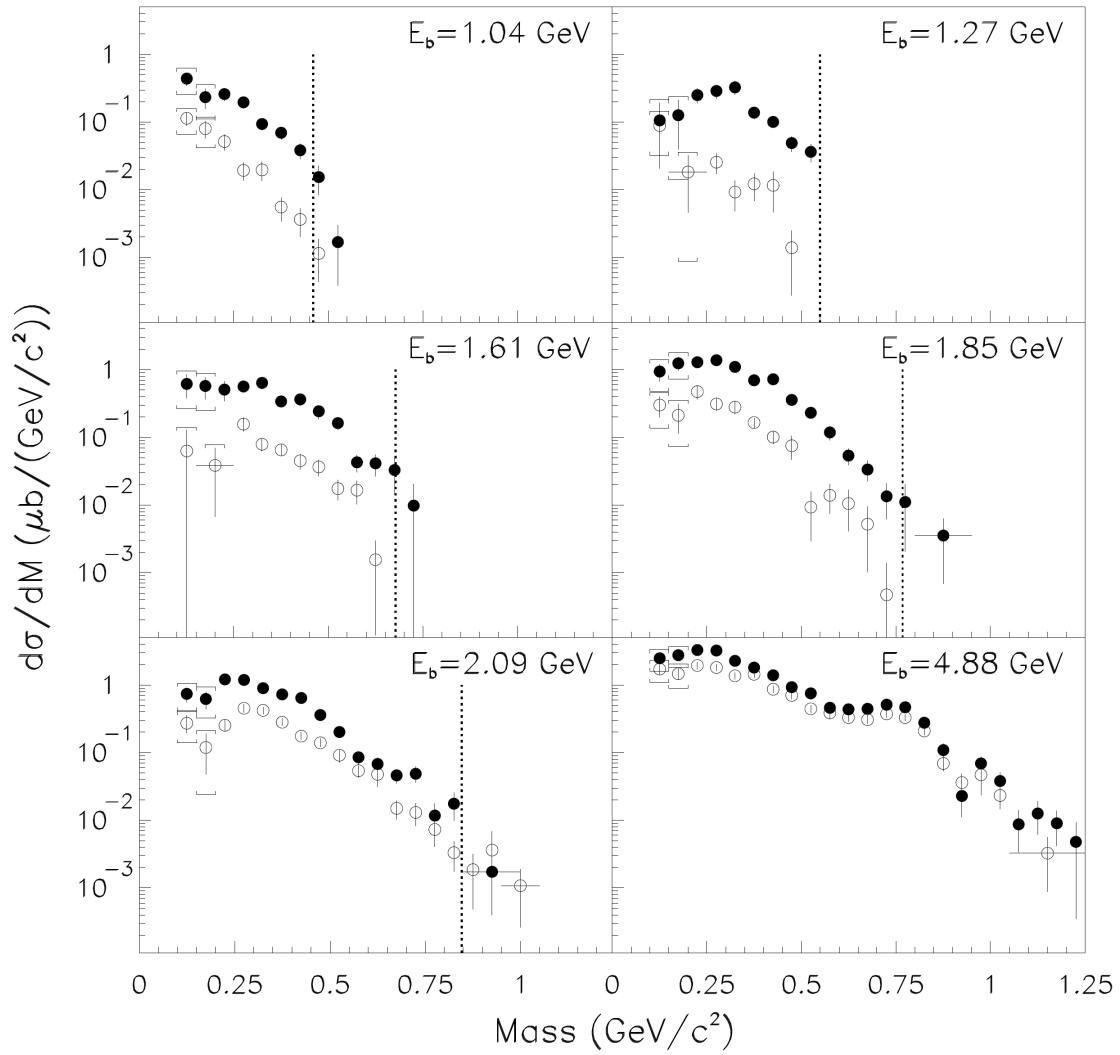


Figure 1.11: Acceptance corrected mass spectra for the $p+d$ (filled circles) and $p+p$ (open circles) systems measured by the DLS collaboration. The error bars are statistical and do not include the normalization uncertainties. The brackets above and below the low mass data points indicate systematic uncertainties in the shape of the spectra. The dashed lines indicate the kinematical upper limit on the pair mass in the pp system [19].

The theoretical picture of virtual bremsstrahlung was thought to be consistent until a new covariant OBE calculation was performed by L.P. Kaptari and B. Kämpfer [34] (to be referred as OBE-KK). The authors choose the free parameters of their theory similar to the ones used in [92] (to be referred as OBE-SM), but the restoration of the gauge invariance (for $n+p$) has been realized in a different way. The gauge invariance is automatically fulfilled for $n+p$ interactions if the exchanged meson is uncharged (meson exchange is indicated with dashed lines in Fig. 1.13 (a) and (b)). This is not any longer true if a charged meson is exchanged (see Fig. 1.13 (c)). In order to restore the gauge invariance, contact terms (see Fig. 1.14) were introduced in Ref. [34]. This leads to different types of the form factors and quite different results. Indeed, it is found to differ by a factor of 4 for $n+p$ interactions (see Fig. 1.15, right panel), but also by a factor of about 3 for $p+p$ reactions (see Fig. 1.15, left panel) at 1 GeV kinetic beam energy compared to the ones of Ref. [98, 20]. It should be noted however, that although for the $p+p$ bremsstrahlung calculations in both models, i.e. in the OBE-SM and in the OBE-KK model,

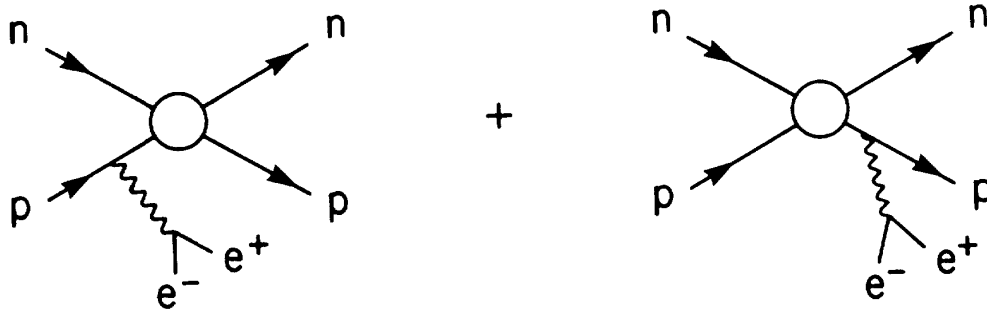


Figure 1.12: Radiation from external proton lines in $n+p$ scattering.

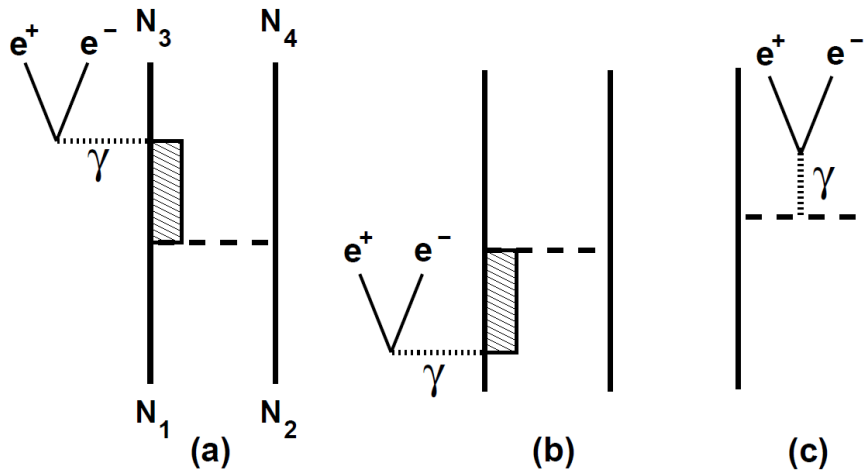


Figure 1.13: A representative set of Feynman diagrams for emission of dileptons in nucleon-nucleon collisions. (a) denotes emission after the NN collision, (b) before the NN collision and (c) during the NN collision. The box represents an off-shell nucleon ($p^2 \neq m^2$, $c = 1$) or a Δ isobar [20] emitting virtual photons.

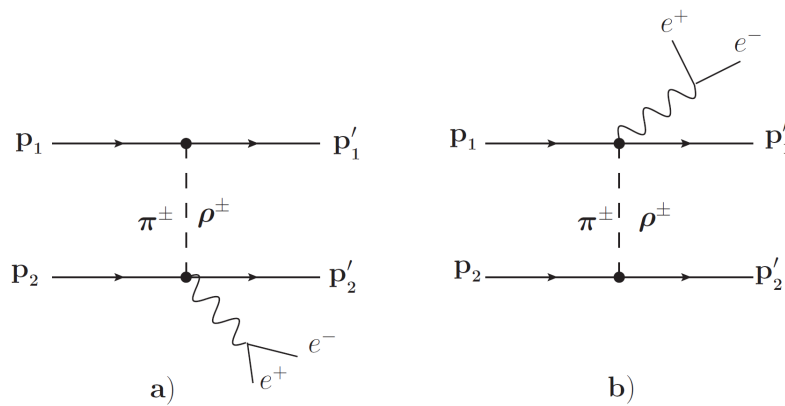


Figure 1.14: Feynman diagrams for the emission of dileptons in nucleon-nucleon collisions, contact (seagull) term.

the Lagrangians, coupling constants, form factors, and cut-off parameters are believed to be the same, yet the $p+p$ bremsstrahlung cross section from OBE-SM appears lower than the one from OBE-KK. In the OBE calculations all amplitudes (graphs), in particular with or without intermediate resonance excitation, are treated coherently. However, in the available transport model calculations of dilepton production in NN collisions this is not possible. In the transport approach dileptons from virtual nucleon bremsstrahlung are calculated within the SPA model restricting the emission process to elastic NN collisions and the Δ contribution by explicitly producing and decaying the resonance within a Dalitz-decay model in inelastic collisions. In this way, the interference of elastic and inelastic channels is neglected. The HSD transport model uses a parametrization of virtual bremsstrahlung motivated by a recent OBE-KK calculation, treating only the elastic channel, since the Δ decay is treated in the code explicitly. By adjusting the calculations such as to reproduce the cross section for virtual bremsstrahlung as calculated in the OBE-KK approach for elastic channels, the HSD code is now able to interpret the $p+p$ and $d+p$ data measured by the DLS collaboration, and even more can describe the heavy-ion data of both, the DLS and HADES experiments, and declares the solution of the "DLS puzzle" [98].

In the following, the results obtained by HADES for di-electron production in elementary collisions will be used to check this conclusion. Since electron pairs from virtual bremsstrahlung show a similar spectral and transverse momentum distributions as pairs produced in Δ decay a separation of the two contributions is difficult. To further contribute to a better understanding of the contributions to di-electron production in the early stage of heavy-ion collisions, HADES has studied $p+p$ and $d+p$ interactions at $E_{kin} = 1.25 \text{ GeV}/u$. The main goal of the latter experiment is to understand the $n+p$ bremsstrahlung component for e^+e^- production in the tagged reaction channel $np \rightarrow npe^+e^-$ and to establish an experimental cocktail of di-electrons from "free", i.e. non-medium hadron decays for SIS energies.

The investigation of di-electron production in elementary reactions attracts a lot of attention not only because of its important for the interpretation of heavy-ion results. It also provides insight into the electromagnetic structure of hadrons. E.g. the electromagnetic transition form factor of the Δ decay has not been studied in detail so far. In order to learn about this process

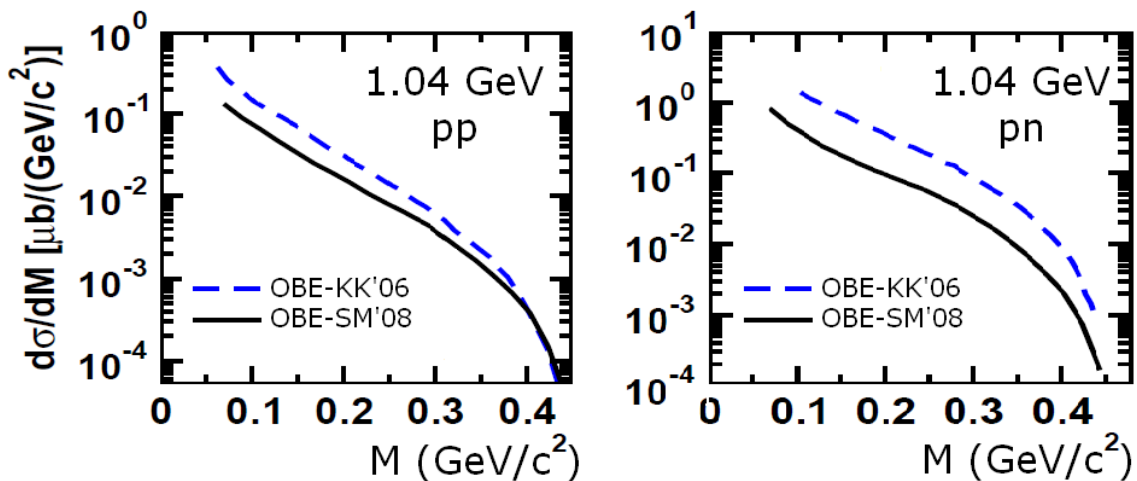


Figure 1.15: The contribution of the NN bremsstrahlung to the invariant mass distribution for dilepton spectra in $p+p$ (left) and $n+p$ (right) collisions at a beam energy of 1.04 GeV . Solid lines: OBE-SM [20], dashed lines: OBE-KK.

a dedicated exclusive measurement of the $pp \rightarrow p\Delta^+ \rightarrow ppe^+e^-$ is required. Such a measurement will also provide valuable constraints on the Δ production in $n+p$ reactions. A precise understanding of the $np \rightarrow npe^+e^-$ and $pp \rightarrow ppe^+e^-$ reactions by studying the invariant mass, phase space (p_t, y) and angular distributions of the dilepton sources, is very important to clarify the dynamics of processes that transport model calculations use for the interpretation of di-electron emission in heavy-ion reactions. The latter is the subject of the first part of this work.

Chapter 2

The HADES experiment

HADES is an unique apparatus installed at the heavy-ion synchrotron SIS18 at GSI Darmstadt. The major part of the HADES physics program focuses on in-medium properties of the light vector mesons ρ , ω and ϕ . It also addresses several important problems in hadron physics like the studies of vector meson-nucleon coupling strengths, the electromagnetic form factor of the nucleon in the time-like region and the validity of the Vector Meson Dominance model hypothesis in the description of meson and baryon Dalitz decays. A comparison of di-electron invariant mass spectra from $\pi+p$ and $p+p$ reactions with $p+A$ and $A+A$ collisions allows to study these effects as a function of the hadronic matter density and size of the collision system. For these investigations di-electron spectroscopy will systematically be performed in various reactions like $p+p$, $p+A$, $A+A$ and $\pi+p$, $\pi+A$ at $1 - 2 \text{ GeV}/u$ beam energies using the variety of beams provided by the SIS accelerator facility.

The major experimental challenge is to discriminate the penetrating but very rare leptons from the huge hadronic background which exceeds the electron signal by many orders of magnitude. The HADES detector has been specifically designed to overcome these difficulties. The HADES spectrometer (see Fig. 2.1) consists of 6 identical sectors covering the full azimuthal

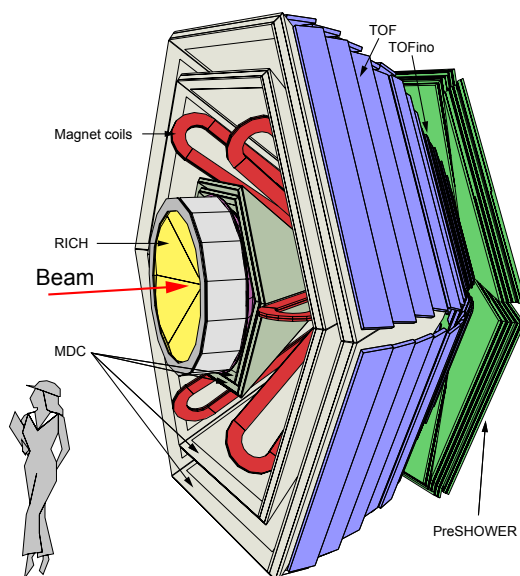


Figure 2.1: Schematic view of the HADES detector.

angle and polar angles from 18° to 85° measured relative to the beam direction. Each sector of the spectrometer contains a RICH operating in a magnetic field-free region, inner MDCs in front of the magnetic field, outer MDCs behind the magnetic field, TOF and TOFino time-of-flight detectors and a electromagnetic cascade detector (Pre-Shower). Momentum measurement for charged particles is achieved by tracking the particles in front off and behind a toroidal field generated by six superconducting coils arranged around the beam axis. A powerful and flexible trigger systems selects events containing di-electron candidates in real time. With these design features, HADES can obtain data with high quality and statistical significance.

2.1 Target and Start detector

2.1.1 The Target

The investigation of elementary processes leading to di-electron production is carried out with proton, deuteron and pion beams on a liquid hydrogen target (LH_2). The LH_2 target has been developed at IPN, Orsay and consists of a 5 cm long cylinder with a diameter of 2.5 cm in which liquid hydrogen at atmospheric pressure and a temperature of 20 K is filled. The shell of the vessel as well as the entrance and exit windows are build from 100 μm thick Mylar foils (see Fig. 2.2).

An external carbon fiber housing, 4 cm in diameter with 0.5 mm wall thickness, is placed around the liquid vessel which is thermally insulated by 10 layers of superinsulation material (6 μm thick aluminized Mylar). The forward end cap of this cylindrical carbon fiber cap is also made out of 100 μm thick Mylar foil. The 5 cm long liquid part of the target provides 1% interaction probability. The cooling from room temperature down to 20 K takes 12 hours. Empty target measurements are made in order to estimate the background from beam reactions within the target material.



Figure 2.2: View of the liquid hydrogen target vessel. The entrance window is glued on a stainless steel cylinder with a diameter of 1.5 cm, whereas the target vessel diameter is 2.5 cm.

2.1.2 The Start detector

For heavy-ion beams a segmented diamond detector has been used to provide the start signal for the time-of-flight measurement. These detectors are fast and radiation hard and can be operated at particle intensities of up to 10^9 ions/second. However, for proton beams, the diamond start detector cannot be used since the deposited energy is too small and, moreover, at beam intensities higher than 10^7 protons/sec the RICH (see section 2.3) encountered high voltage stability problems due to the large charged particle background resulting from interactions of beam particles with the start detector and other material in front of the RICH, and from the halo of the beam. Optimization of the target area by an installation of a vacuum beam pipe, removal of the start detector and better beam tuning reduced the background and allowed for stable production runs. The remaining background of this origin is rejected later by applying specific vertex cuts (for details see section 3.4.2).

2.2 The hadron-blind gaseous Ring Imaging Cherenkov detector (RICH)

The RICH detector constitutes the innermost part of the HADES spectrometer and is designed to identify electrons with momenta larger than $0.1 \text{ GeV}/c$. Very selective electron identification is done using the Cherenkov effect (the basic concept of a RICH detector is discussed in section 5.2.3). The RICH detector is shown in Fig. 2.3. The photon detector is placed upstream of the target to spatially decouple the registration of the Cherenkov light from charged particle tracks emitted from the target. The radiator gas Peruorobutan (C_4F_{10}) offers high transparency for UV photons down to $\lambda \geq 145 \text{ nm}$ and a Cherenkov threshold of $\gamma_{th} = 18$ to suppress radiation from muons and hadrons. The radiator volume is separated from the active volume of the UV detector by a CaF_2 window of 5 mm thickness. The UV detector is operated with pure methane (CF_4). The Cherenkov light emitted along the particle trajectory in the radiator is reflected by a low mass spherical mirror ($R = 872 \text{ mm}$) onto the photosensitive CsI cathodes of six multi-wire proportional chambers operated with CH_4 and equipped with individual pad readout. To minimize multiple scattering and photon conversion the panels of the RICH mirror

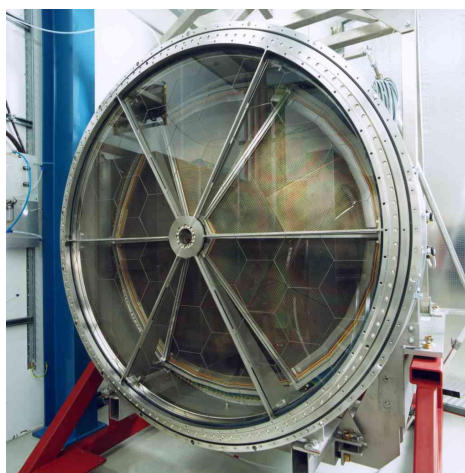


Figure 2.3: The HADES Ring Imaging Cherenkov detector.

are made from pure carbon (low Z material, $Z = 6$). They are machined to a thickness of 2 mm, polished, and coated with a thin $Al + MgF_2$ layer. The average reflectivity is $\sim 80\%$.

The performance of the RICH is governed by the average number of photons detected for each electron-positron ring. The number of detected photons per ring depends on the available radiator length and a figure of merit $N_0 = \frac{370}{[eV \cdot cm]} \cdot \int_{E_{\min}}^{E_{\max}} \epsilon(E_\gamma) dE_\gamma$ which includes the optical and electrical properties ϵE_γ of the system [99]. The figure of merit N_0 has been calculated for each of the six RICH sectors separately and values between 70 and 85 have been found [100], slightly lower than in the original design (design $N_0 \approx 109 \text{ cm}^{-1}$). The overall performance of the RICH detector system, although slightly lower than in the original design, is sufficient for electron/positron identification in $A + A$ collisions.

2.3 HADES tracking system

To reconstruct the particle trajectories and to determine the particle momenta four planes of low-mass multi-wire drift chambers (MCD) are installed. Two in front of and two behind the high magnetic field region with a maximum field strength of 0.7 Tesla. The design criteria for the HADES spectrometer are to provide particle tracking in a large solid angle ($\theta = 18^\circ - 85^\circ$) and with a momentum resolution of $\Delta p/p = 1.5\% - 2\%$. Moreover, a field free region around the target and inside the active volume of the RICH detector is required.

This is achieved by a superconducting toroid [101] that consists of 6 coils surrounding the beam axis (see Fig. 2.4, right panel). The bending power provided by the magnetic field has a polar angle dependence approximately matching the variation of the average lepton momentum as a function of the laboratory polar emission angle. Particle momentum p approximately determined by the polar deflection p_K provided by the field:

$$p = \frac{p_K}{2 \cdot \sin(\xi/2)}, \quad (2.1)$$

where ξ is a deflection angle of a charged particle in a field [102].

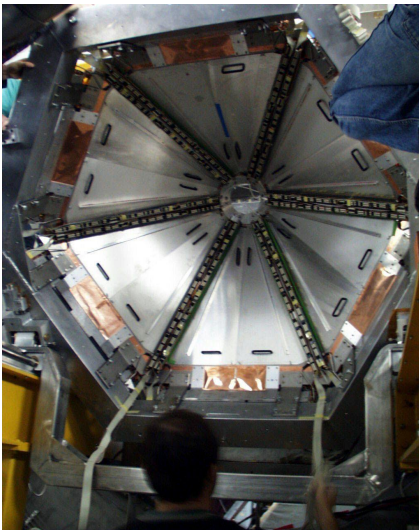


Figure 2.4: Left: The MDC plane I (GSI chamber). Right: The HADES magnet (ILSE), during the installation.

The HADES tracking system consists of 24 low-mass, trapezoidal multi-layer drift chambers symmetrically arranged in six identical sectors providing about 30 m^2 of active area (see Fig. 2.4, left panel). It provides a polar angle coverage between 18 and 85 degrees around the beam axis, forming four tracking planes (I-IV) of increasing size [103]. All chambers are composed of six sense/field wire layers oriented in five different stereo angles ($0, \pm 20^\circ, \pm 40^\circ$). This allows for maximum spatial resolution in polar direction, which points in the direction of the momentum kick, minimization of double hits, and resolving power with respect to track ambiguities. All four chamber types contain about 1100 drift cells each. The cell sizes vary from $5 \times 5 \text{ mm}^2$ to $14 \times 10 \text{ mm}^2$ from plane I to IV to achieve a constant detector occupancy (for central $Au+Au$ collisions at $1 \text{ GeV}/u$ beam energy a maximum cell occupancy of 30% is estimated). The total detector thickness per chamber in units of radiation length is below $5 \cdot 10^{-4}$ and hence low multiple scattering guarantees the required momentum resolution [104, 105, 103]. Low multiple scattering is further ensured by using helium-based gas mixtures and aluminum cathode and field wires.

2.4 The Multiplicity Electron Trigger Array detectors

The META detectors are positioned downstream behind the outer MDCs and are used for particle identification and triggering. The first level trigger is obtained via a multiplicity measurement provided by the META system. The META detector system is shown in Fig. 2.5 and consists of time-of-flight detectors (TOF/TOFino scintillator walls) and an electromagnetic shower detector.

2.4.1 The TOF scintillator walls

The TOF detector [106] covers the large polar angles from 44° to 88° . It consists of 384 scintillator rods (6 sectors, each consisting of 64 rods) coupled on both sides to photomultipliers. The selected scintillating material is BC408 from Bicron, mainly due to its good attenuation length combined with high scintillation efficiency. The rod cross section is a square, $20 \times 20 \text{ mm}^2$ for the inner and $30 \times 30 \text{ mm}^2$ for the outer rods. The rod length varies from 1 m to 2 m



Figure 2.5: The META detectors (view from the target region). All 6 sectors of TOF are visible. Two opposite sectors are also equipped with the Pre-Shower detector. Currently all 6 sectors of the Pre-Shower detector are installed.

from smaller to larger polar angles, respectively. With this geometry the double hit probability (probability that two particles hit the same rod) is reduced to less than 10%.

From the measured signals the time-of-flight (t_{tof}) of a particle, its hit position (x) along the rod and the deposited energy (ΔE) can be extracted:

$$t_{\text{tof}} = \frac{1}{2}(t_{\text{left}} + t_{\text{right}} - \frac{L}{v_{\text{group}}}) \quad (2.2)$$

$$x = \frac{1}{2}(t_{\text{left}} - t_{\text{right}}) \cdot v_{\text{group}} \quad (2.3)$$

$$\Delta E = k \sqrt{A_{\text{left}} \cdot A_{\text{right}}} e^{L/\lambda_{\text{at}}} \quad (2.4)$$

where t_{left} and t_{right} are the time interval between the signal in the start detector and the signal generated in one of the two multiplier, A_{left} and A_{right} are the corresponding light signal amplitudes, v_{group} is the average group velocity of the light in the rod, λ_{at} is its attenuation length, L is the length of the rod and k a proportionality constant. The time resolution of the TOF detector is about 150 ps.

The region between 18° to 44° is covered by a low granularity system called TOFino. It is divided into six sectors each consisting of four scintillator pads, arranged radially with respect to the beam axis. Each scintillator pad has a trapezoidal form of about 130 cm height and 10 mm thickness. The light is collected from only one side (wide side, width 32 cm) of each paddle with a Hamamatsu PMT. The TOFino subdetector is mounted directly behind the Pre-Shower detector (described in the next section), which provides the coordinate information of the particle hit on the paddle (x). In order to calculate the time-of-flight (t_{tof}) of the charged particle the following equation is used:

$$t_{\text{tof}} = t - \frac{x}{v_{\text{group}}} \quad (2.5)$$

where t represents the time interval between the signal of the start detector and the arrival of the light pulse at the PMT, v_{group} the group velocity in the pad and x the distance from the particle hit position to the PMT. The time resolution of the TOFino detector is about 420 ps, which is determined mainly by the properties of the light collection. The replacement of the TOFino detector by a Resistive Plate Chamber (RPC) wall [107, 108] is foreseen in the near future.

2.4.2 The Pre-Shower detector

The inner TOFino detector is accompanied by the Pre-Shower detector probing electromagnetic showering of traversing particles. The time-of-flight resolution obtained by the low-granularity TOFino detector is not enough to achieve a clean discrimination of electron from pion. To provide additional hadron suppression the Pre-Shower detector has been introduced to the HADES setup. It is composed of a stack of three wire chambers separated by two plates of lead converters of $d_1 = 2 \cdot X_0$ and $d_2 = 1.5 \cdot X_0$ thickness, respectively, where $X_0 = 0.56$ cm is the radiation length in lead (see Fig.2.6). Electron/hadron discrimination is obtained by comparing the charge multiplication induced when the particle traverse the lead converter. At such energies secondary particles are emitted into the forward hemisphere around the particle trajectory. The charge in the electromagnetic shower is proportional to $1/X_0$. In order to obtain the complete charge of the electromagnetic shower an integration over several pads around the pad with the highest local charge value is performed. The integration area has been limited to

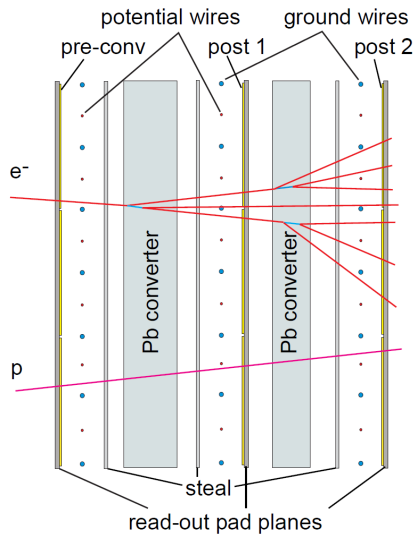


Figure 2.6: Side view of the Pre-Shower detector. Three gas chambers and two lead converters are shown. Lepton/hadron discrimination is performed by comparing the number of particles measured in the chambers before and behind lead converters.

3×3 pads independently of the hit position. This choice allows for a simple implementation of the electron identification in programmable logic as the Image Processing Unit performing fast electromagnetic shower search in the second level trigger.

2.5 The Forward hodoscope Wall

The Forward hodoscope Wall (FW) was installed lately 2007 and it was successfully used for tagging the spectator proton in the deuteron beam experiment in May 2007. The FW was placed at 7 m behind the target and it covers polar angles $0.33^\circ < \theta < 7.17^\circ$. The mechanical set-up of the detector consists of 287 scintillator modules read out by photomultipliers. 263 modules were operational during data taking in May 2007. In order to achieve a reasonable angular and position resolution the size of the cells was selected in the following way: the innermost part was covered with cell sizes $4 \times 4 \text{ cm}^2$ (see Fig. 2.7, left panel, red squares), which increased to cell sizes of $8 \times 8 \text{ cm}^2$ (see Fig. 2.7, left panel, green squares) and the outer region was covered with $16 \times 16 \text{ cm}^2$ cells (see Fig. 2.7, left panel, blue squares). The scintillating material is BC408 (used also for the TOF detector). The thickness of the cells is

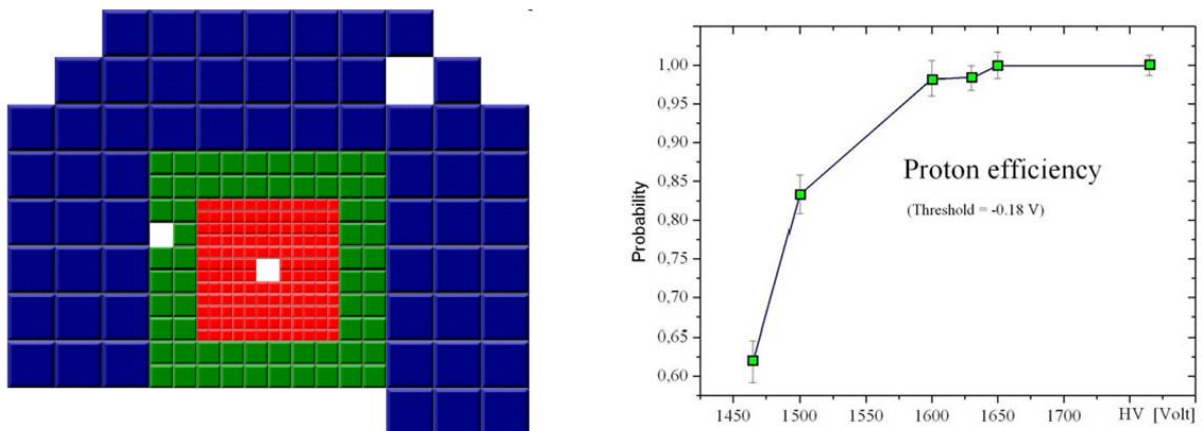


Figure 2.7: Left: Arrangement of the FW cells. Only operational cells are shown. Compilation by K. Lapidus. Right: The detection efficiency for protons versus the PMT high voltage.

2.54 cm. Each cell is equipped with an individual PMT readout. The detection efficiency for protons as a function of the PMT high voltage is shown in Fig. 2.7 (right panel) for a selected PMT. The high voltage of each PMT was individually tuned in order to achieve overall high detection efficiency for protons. The estimated time resolution of the FW is about 500 ps; thus the estimated momentum resolution of the detected particles (protons) is about 11%.

2.6 The Trigger System

In order to measure the rare di-electron decays of low mass vector mesons, interaction rates of up to 10 MHz must be handled by the HADES spectrometer. This requires a trigger system which is able to reduce the event rate to a factor of 10^4 by pre-selecting interesting events with relevant signatures. A two-level trigger is used by HADES. A schematic view of the HADES multi-level trigger system is shown in Fig. 2.8. The Trigger and Data Acquisition System of HADES is a distributed system. Triggers are generated and distributed to the individual subsystems by a CTU¹. The CTU reacts on external trigger input sources such as multiplicity triggers provided by the META detector. A digital level1 (LVL1) trigger signal is generated by the CTU. The CTU generates digital trigger information, containing the trigger number and the physics source of the trigger. This information is forwarded via DTUs² to the readout modules where it is converted into sub detector specific signals. After the data have been read out

¹Central Trigger Unit

²Detector Trigger Units

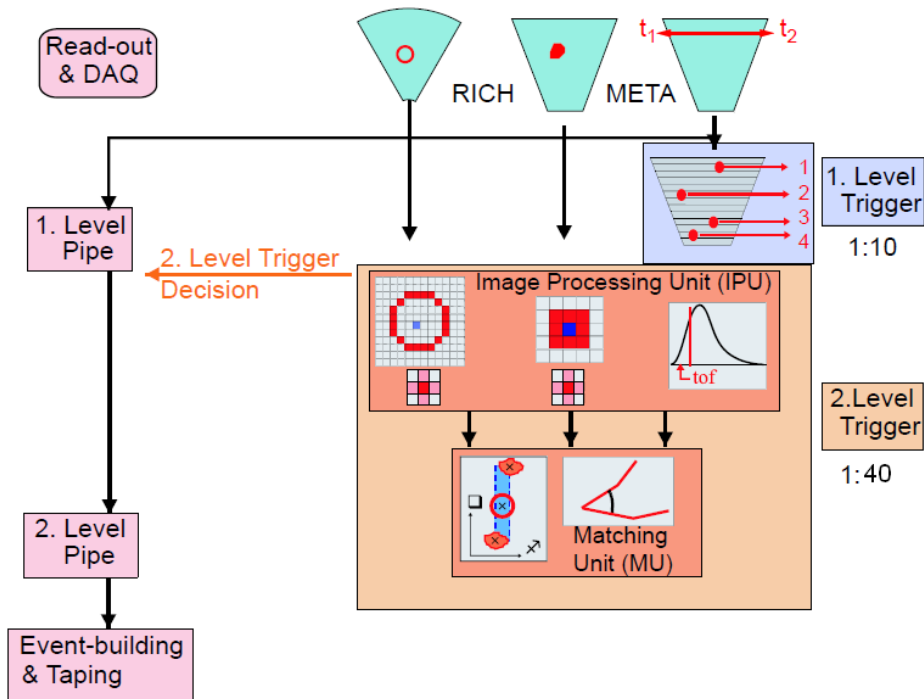


Figure 2.8: A schematic view of the HADES multi-level trigger system. Data readout is initiated by a centrality trigger, indicated as 1st Level Trigger. The triggered data are analyzed for electron patterns in the RICH and META detectors: indicated as 2^d Level Trigger.

from the front-end electronics, a level-2 (LVL2) trigger algorithm selects events by searching for lepton pairs. This is done by RICH and META IPU³ using dedicated lepton recognition algorithms. The LVL1 Trigger is created after one of the signal inputs of the CTU has been activated. Here the fast signal information from the META detector is used. Precisely $(M_{\text{TOF}} + 2 \cdot M_{\text{TOFino}})/2 > M_{\text{th}}$ is required. M_{TOF} and M_{TOFino} are the multiplicities of photomultipliers with signals from TOF or TOFino, respectively. At the same time a common start signal is provided for time measurements. In case of a missing start detector (like in the proton runs) the first particle observed in the TOF/TOFino detectors is used as a reference. During the signal distribution to all sub-detectors (500 – 600 ns), the CTU inputs are locked until all DTUs have realized the trigger bus. The readout capabilities of the individual sub-systems makes the HADES trigger system not dead time free. The aim of the HADES LVL2 trigger is to perform fast ($t < 10 \mu\text{s}$) di-electron identification and to limit data written on tape to events with at least one electron candidate. First, the image processing units detect electron/positron signatures in the RICH, Pre-Shower and TOF detectors: Cherenkov rings in the RICH, fast particles in the TOF, development of electromagnetic showers in the Pre-Shower. For each of these signatures position and angle information is provided. Second, the Matching Unit, connected to all IPUs, combines the angle information from the ring in the RICH detector, hits in the TOF and Pre-Shower detectors, taking into account bending in the magnetic field. During the processing time of a single event in the LVL2, the raw data of the sub-detectors is stored after zero suppression in the first level pipe until a LVL2 trigger decision becomes available. Readout programs finally transport the data to the Event Builder, a PC which combines the data from different asynchronous data sources into complete events and finally writes them to mass storage. Approximately 100 events per second can finally be written to tape.

For small collision systems like $C+C$, $p+p$, $d+p$ typical trigger rates are 17 kHz for LVL1 and 2 – 3 kHz for positive LVL2 triggers with a transported data rate of 4 MB/s. In addition to the LVL2 events, which contain at least one lepton candidate, some LVL1 events are selected with a preset downscaling factor. This increases the amount of transported and stored data, but at the same time provides an unbiased event sample for a study of the LVL2 trigger bias (see section 3.5.2). The down-scaling factor ranges from 1 : 3 to 1 : 9 depending on the event size. It was tuned to keep the reduction of the accepted LVL1 trigger rate below 10% [109]. The LVL1 triggerbox designed in the way that it is possible to combine signals coming from different detectors and different sectors in order to impose more restrictive selections, such as that two opposite sectors have fired (M2opp trigger). Thus, pp elastically scattered events can be taken simultaneously with the main LVL1 trigger at the suppression factor of 64 (each 64's event regarding the LVL1 trigger is recorded). The information about the type of event trigger is stored inside the data stream and can be retrieved on the analysis level.

The currently used data acquisition system was designed ten years ago. The upgrade of the HADES trigger and readout system was driven by the addition of the new RPC detector that provides a time resolution of less than 100 ps. The new HADES data acquisition based on new technologies and new developments. The new Trigger and Readout Board (TRB) was developed by HADES and successfully used for the HADES Forward hodoscope Wall [109]. The TRB would also be very helpful for the experiments to be installed at the FAIR facility at GSI (PANDA and CBM).

³Image Processing Units

2.7 Detector setups and running conditions

2.7.1 The $p+p$ run

The systematic investigation of electron pair production in elementary reactions started with a $p+p$ experiment at 1.25 GeV kinetic beam energy. A beam of up to 10^7 protons per second was incident on a 5 cm long liquid hydrogen target. The outer tracking system was only partially operational, e.g. MDC plane III, sector 0, sector 1 and MDC plane IV sector 5 were not turned on. Data were taken with a magnet current of $I = 2497$ A, corresponding to 72% of the maximum strength of the magnetic field. The start detector was not used during the data taking.

The LVL1 trigger conditions required an overall multiplicity in TOF and TOFino of at least 3 charged particles (M3 trigger). This LVL1 trigger condition was found to be optimal for an exclusive reconstruction of a four-prong final state (e.g. of the type ppe^+e^-). The M3 trigger condition appeared with rates of ~ 10 kHz and the LVL2 condition reduced this rate by a factor of 5. A coincidence multiplicity module allowed to trigger on charge particles detected in opposite sectors. By using a special trigger settings, e.g. 2 charged particles detected in opposite sectors (M2opp trigger), we recorded at the same time elastic pp collisions. The elastic pp interactions are needed in order to normalize the final results (see section 3.1.1). In total about 778 M events have been stored on tape, corresponding to $2.8 \cdot 10^9$ LVL1 trigger events.

2.7.2 The $d+p$ run

In order to record $n+p$ reactions, events with a deuteron beam of 1.25 GeV/u kinetic beam energy on a LH_2 target were recorded in May 2007. The running conditions were similar to the ones used in April 2006 for the $p+p$ run. During the $d+p$ production run the complete outer tracking system was in operation. A new LH_2 target geometry was used which improved the background situation in the RICH detector (see section 3.4.2).

In contrast to the DLS collaboration who recorded events with proton beam on a deuterium target we used $d+p$ reactions because the spectator protons could be detected in the HADES detector setup this way selecting $n+p$ interactions. The $p+p$ reactions were suppressed by measuring the spectator proton in the Forward hodoscope Wall covering the polar angles between 1 and 7 degree. The LVL1 trigger conditions required a multiplicity in TOF and TOFino of at least 2 charged particles and a signal from the Forward hodoscope Wall (M3 trigger). M2opp trigger events were collected as well. In total 1287 M events were taken during a period of 13 days in May 2007, 2 times more events than in April 2006. A detailed description of the analysis of $d+p$ interactions measured by HADES will be given in the PhD work of K. Lapidus [110].

Chapter 3

Methods for data analysis

*The only source of knowledge
is experience.
(Albert Einstein)*

All experiments measuring low-mass di-electrons face the following major experimental challenge: first, the distinction of signal electrons from hadrons being more abundant by typically two orders of magnitude requires a detector system with superior particle identification capabilities; second, only a small fraction of all electrons come from non-trivial sources other than γ conversion and Dalitz decay of π^0 . The latter give rise to a large combinatorial background not only by random combination of electron/positrons from true signal pairs but also from combination with electron/positrons from incompletely reconstructed pairs. A sophisticated data analysis is a necessity in order to extract a significant di-electron and to suppress as much as possible the combinatorial background. The various analysis steps needed to achieve high quality data are:

- calibration of the raw data delivered by the detectors including position calibration (alignment) of the detector systems with respect to each other and to the magnetic field ;
- reconstruction of the particle hits in each detector;
- track reconstruction, momentum determination and particle identification;
- rejection of the combinatorial background;
- single track efficiency corrections by means of Monte Carlo detector simulations;
- absolute normalization of the final spectra.

The HADES on-line and off-line analysis package is realized within the HYDRA¹ framework [102, 111], based entirely on the C++ class package ROOT [112]. The initialization of geometry, setup and calibration parameters is obtained by the HADES data base (implemented in ORACLE) [113] and from ROOT files. A detailed description of the analysis strategy can be found in [114, 115, 116, 117]. This chapter will mostly be focused on the changes introduced

¹HADES sYstem for Data Reduction Analysis

to the analysis chain for this work. Full event reconstruction (section 3.2) including particle identification (section 3.3) will be discussed briefly. The pair analysis procedure including the discussion of the combinatorial background rejection strategy will be covered in section 3.4.

3.1 Event selection

3.1.1 Study of pp elastic scattering reactions

*If you are out to describe the truth,
leave elegance to the tailor.
(Albert Einstein)*

During the $p+p$ data taking period in 2006 we also acquired an event sample with two charged particles in opposite sectors (so called M2opp trigger, see section 2.8). From this event sample pp elastic scattering reaction are reconstructed using respective kinematical constraints. These event class allows evaluating the quality of the detector alignment and tracking performance. Moreover this proton pair data is used to normalize our e^+e^- as described below. In Fig. 3.1 a diagrammatic sketch of kinematical observables for elastic scattering collision is shown for the target rest frame as well as for the center of mass system.

After the track reconstruction procedure (see section 3.2.1) proton candidates are identified and their 3-momenta are reconstructed. For further analysis only fitted tracks were taken into account, i.e. a condition on the quality of the track segment reconstruction in the inner and outer MDC stack of $\chi^2 > 0$, and a $\chi^2 < 500$ for the Runge Kutta track following and momentum reconstruction were required. In a first step, the coplanarity $|\phi_1 - \phi_2| = 180^\circ$ of the two outgoing protons is checked as it is imposed by momentum conservation (see Figure 3.2 (left panel)). The distribution shows a nearly perfect Gaussian distribution centered around 180° and with minimal background. Only pairs which fall in a region of $\pm 3\sigma$ around the maximum are accepted for further analysis.

Beside the coplanarity, also the collinearity of the collision partners in the center of mass system can be used as constrain. It results in a correlation in the laboratory polar angle (θ)

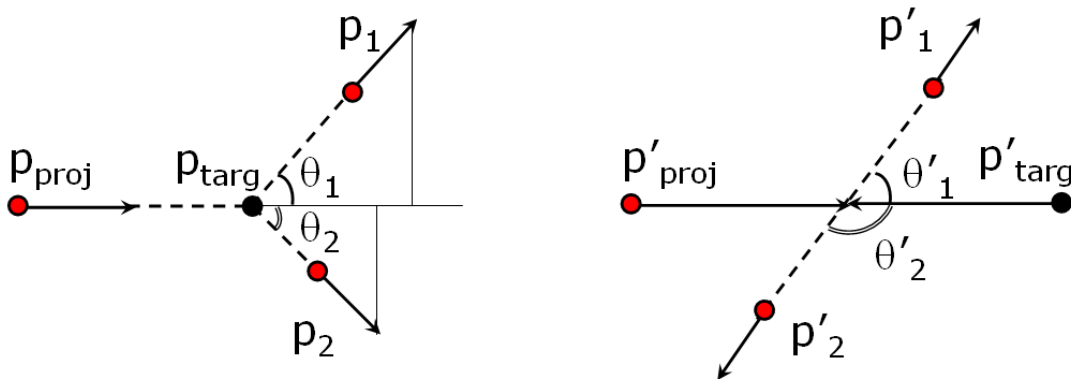


Figure 3.1: Sketch of an elastic scattering collision in the laboratory frame (left panel) and in the center-of-mass frame of two protons (right panel).

between the protons as is defined by the relation

$$\tan \theta_1 \cdot \tan \theta_2 = \frac{1}{\gamma_{CM}^2}, \quad (3.1)$$

where γ_{CM} is the Lorentz factor of the center-of-mass system in the laboratory system. This Lorentz factor is obtained from the relation

$$\gamma_{CM} = \sqrt{\frac{E_{tot} + m_p}{m_p}}, \quad (3.2)$$

where E_{tot} is the total energy of the incoming proton and m_p is the proton rest mass. For a kinetic beam energy of 1.25 GeV γ_{CM} amounts to 1.29, and hence $\gamma_{CM}^{-2} = 0.6$. Figure 3.2 (right panel) shows the laboratory polar angle correlation between the two protons. The peak indicates elastic pp events and is centered around the expected value. In elastic scattering events the emission angle is strictly correlated with the emission angle of protons according to

$$p(\theta) = \frac{p_{proj}}{\cos \theta + \gamma_{CM}^2 \cdot \sin \theta \cdot \tan \theta} \quad (3.3)$$

where p_{proj} is the momentum of the incoming proton. By comparing $p(\theta)$ theoretically calculated with the one reconstructed the momentum resolution of the tracking system can be checked. The distribution of the respective residuals is shown in Fig. 3.3 normalized to the calculated momentum according to

$$\Delta p = \frac{1/p_{reconstructed} - 1/p_{calculated}}{1/p_{calculated}}. \quad (3.4)$$

From a fit to the distribution the momentum resolution for protons is estimated to be 5.2% with a slight systematic deviation of 1.4% indicating limitations in the current alignment procedure.

Presently HADES is developing an improved alignment procedure based on straight track reconstruction from runs without magnetic field. In this, also pp elastic scattering events will be included to provide additional valuable information. By testing the apparent coplanarity

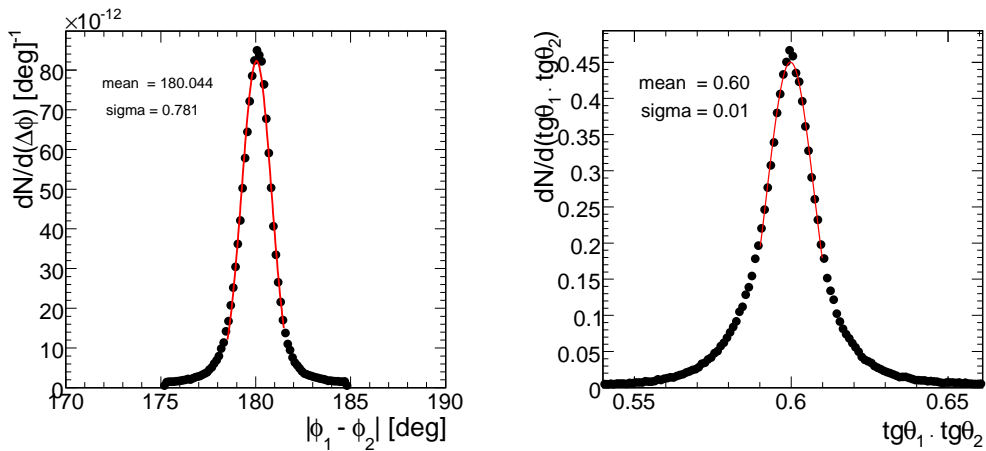


Figure 3.2: Left: Coplanarity of elastic pp pairs. Right: The angular correlation between two tracks using the relation $\tan \theta_1 \cdot \tan \theta_2 = \gamma_{CM}^{-2}$.

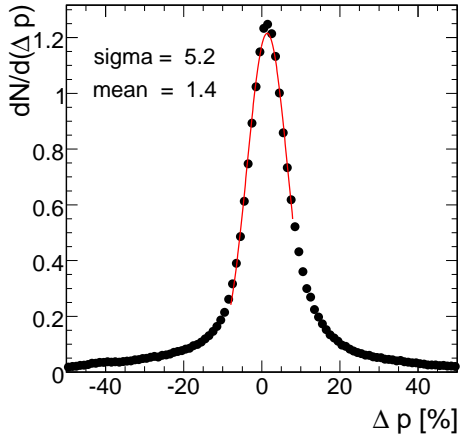


Figure 3.3: The momentum resolution for pp elastic pairs (integral over all sectors).

of elastic pp pairs and the collinearity as a function of the azimuth further constraints are imposed in the procedure. Figure 3.4 shows the current performance of our tracking precision for elastic pairs. In the left panel the coplanarity signal of elastic pp pairs as a function of azimuthal angle is presented. The right plot demonstrates obtained polar angle correlations for proton pairs fulfilling the coplanarity condition as a function of the azimuthal angle.

Another reason for the small but systematic deviations is the fact that the beam direction is not exactly collinear to the symmetry axis of the spectrometer (i.e. to the z -axis of the cave coordinate system). Furthermore, it is important to note that during the April 2006 run there was no pair of opposite sectors with full MDC setup, which also effects the tracking performance. It is expected that both, the width and the shift visible in the distributions of the residuals could be improved by better geometry parameters and by taking into account the beam direction with respect to the z -axis.

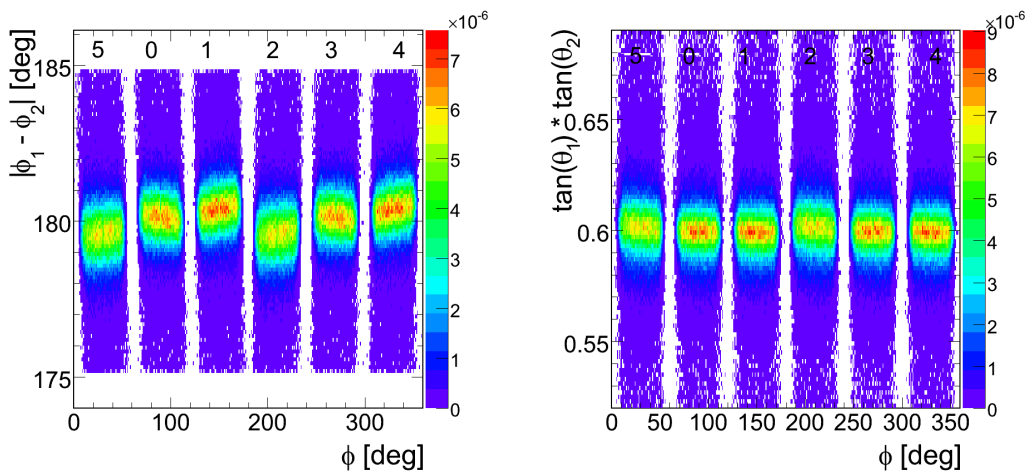


Figure 3.4: Left: Coplanarity of elastic pp pairs as a function of azimuthal angle. Right: the angular correlation between two tracks using the relation $\tan \theta_1 \cdot \tan \theta_2$ as a function of azimuthal angle. Numbers given in the plot are the sector numbers. The 6 bands and 6 gaps present the six sectors of HADES and show the nice azimuthal coverage of the detector.

3.1.2 Selection of the $n + p$ subreactions with the Forward hodoscope Wall

As mentioned before, the aim of the $d+p$ experiment is to constrain the bremsstrahlung component for e^+e^- production in the tagged sub-reaction $np \rightarrow npe^+e^-$. The internal neutron of the deuteron interacts with the target proton, while the forward detected proton acts as a spectator. A schematic picture of the $d+p$ reaction is shown in Fig. 3.5 (left panel). The spectator is detected essentially in the same direction ($\theta < 7^\circ$) as the incident deuteron with approximately the same velocity ($|p_{sp}| \simeq p_d$). This angular region corresponds just to the geometrical acceptance of the Forward hodoscope Wall. The momentum of the spectator proton (p_{sp}) detected in the Forward hodoscope Wall and integrated over all emission angles is shown in Fig. 3.5 (right panel). Only events with multiplicity in the Forward hodoscope Wall $M_{FW} \geq 1$ and with a spectator proton in the momentum range $1.6 < p_{sp}/(\text{GeV}/c) < 2.4$ were selected for the further $n+p$ data analysis.

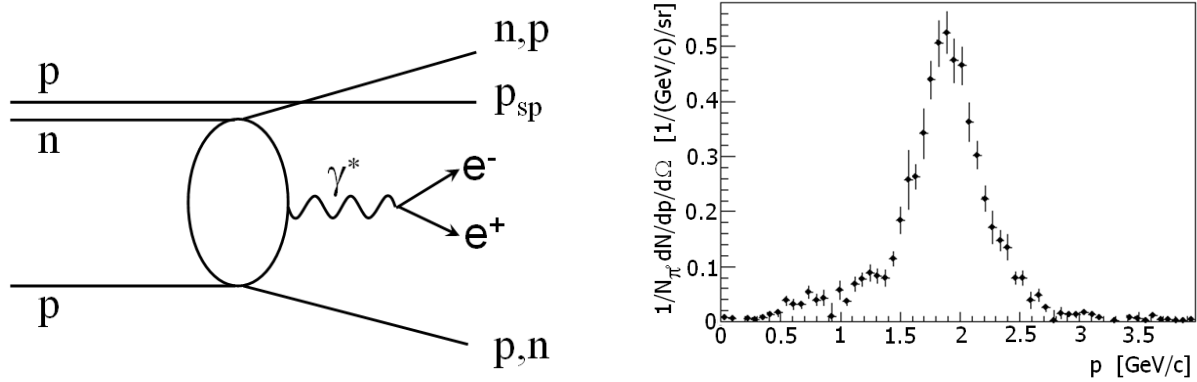


Figure 3.5: Left: Kinematics of the process $dp \rightarrow ppne^+e^-$ within the spectator mechanism. Right: Momentum distribution of the spectator proton p_{sp} detected in the Forward hodoscope Wall at $2^\circ < \theta < 4^\circ$.

3.2 Event reconstruction

The event reconstruction performed in several steps by combining information from various sub-detectors. The data obtained from the data acquisition, are unpacked and the first data level of each detector are produced. The unpacking takes the information from the readout electronics which is organized in channels and reorders it to data classified in terms of detectors, modules etc. In a second step, each detector have to be calibrated. As a result of the calibration one gets the physical information of the detected particles like position, energy loss, time-of-flight, etc. An example of a reconstructed real event is presented in Fig. 3.6.

3.2.1 Track reconstruction and momentum determination

The momentum of particles traversing the HADES detector can be obtained from their deflection in the magnetic field. This requires a measurement of the particle direction in front of and behind the magnetic field. To achieve this, independent inner and outer straight track segments are reconstructed from the hit information in the pairs of drift chambers in front of and behind the field region, respectively. Then, exploring a simple track model, track candidates are formed by combining pairs of inner and outer track segments. In a final step, the deflection (transverse kick) of a track is reconstructed by following the track through the field by means of a Runge Kutta algorithm. The quality of the reconstruction is used to reject fake track candidates formed from random combinations of inner and outer track segments.

First, the raw MDC data are calibrated to derive the drift time and information on energy loss. From the width of the drift time signal a measure proportional to the energy loss of the particle can be extracted. The measured drift time depends on the gas mixture, the electric field strength, the track geometry and the drift cell size. The spatial correlation of fired drift cells in the drift chambers is performed by the track candidate search based on the identification of wire clusters (see Fig. 3.6, crossed orange lines). The fired wires from both modules (MDC-I and MDC-II) are projected from the target on a common projection plane (see Fig. 3.7, left panel) which is in the middle between the inner modules. Here, only the extension of the target

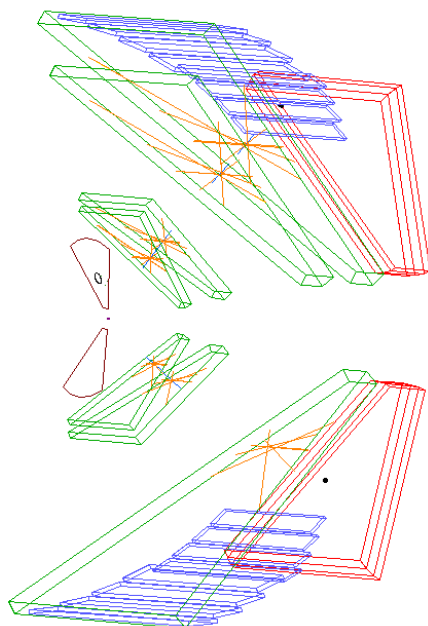


Figure 3.6: Event display of a real event. Two opposite sectors are shown (sector 0, sector 3). Detector systems are shown in different colors (from left to right): dark red - RICH, green - MDCs, blue - TOF, red - Pre-Shower. Black ring: reconstructed RICH ring, crossed orange lines: fired wires in MDCs, black points: reconstructed hits in the TOF or Pre-Shower detector.

along the beam axis is taken into account. When searching for wire clusters in the outer drift chambers, the same strategy is followed as for the inner ones, except that the target position is replaced by the intersection point of an inner segment with the virtual momentum-kick plane. The deflection of a charged particle on its way through the toroidal field of the HADES magnet is substituted by a single kick occurring on a two-dimensional virtual surface, called "kick plane" (see Fig. 3.7, left panel). Fitting two chambers simultaneously is performed employing a straight-line track model (the residual fringe fields in the chamber region is neglected). The quality of the fitting (χ^2 distribution) of inner and outer MDCs are used to select only good track candidates. Track candidates are finally obtained through the matching of track segments in the inner and outer drift chambers of one sector.

The particle momentum is determined by a track interpolation using the Runge Kutta algorithm [118]: this is one of the methods to determine the momentum of a particle traversing a known magnetic field by solving its equations of motion in the field region. If the Runge Kutta fit does not converges, its quality parameter (χ^2) is set to 10^6 . The experimental momentum resolution is determined by the accuracy of the measurement of the deflection between detectors before and after the magnetic field. It is composed of the single detector resolution and the momentum dependent multiple scattering. The main difficulty comes from the fact that the magnetic field of HADES is inhomogeneous. This point can be nicely demonstrated by a comparison of the obtained momentum resolution for positive and negative tracks. The momentum resolution for electrons and positrons obtained with the Runge Kutta method is presented in Fig. 3.7 (right panel). The difference in momentum resolution for electrons and positrons, especially for momenta below 0.5 GeV/c, is clearly visible and can be explained by the field configuration. Consider, e.g. an electron and positron track with the same momentum and both emitted with the same angle at the field entry. Positrons are always bent towards the beam pipe and electrons are bent away from it. This means that an electron will see a weakening field along its path while a positron will enter the high field region with highest inhomogeneity, as shown in Fig. 3.8. To reconstruct positively charged tracks thus meets more difficulties. For a small deflection, i.e. for high momentum tracks, the resolution is dominated by the intrinsic detector resolution and reaches about 3% for particle momenta $p > 1$ GeV/c.

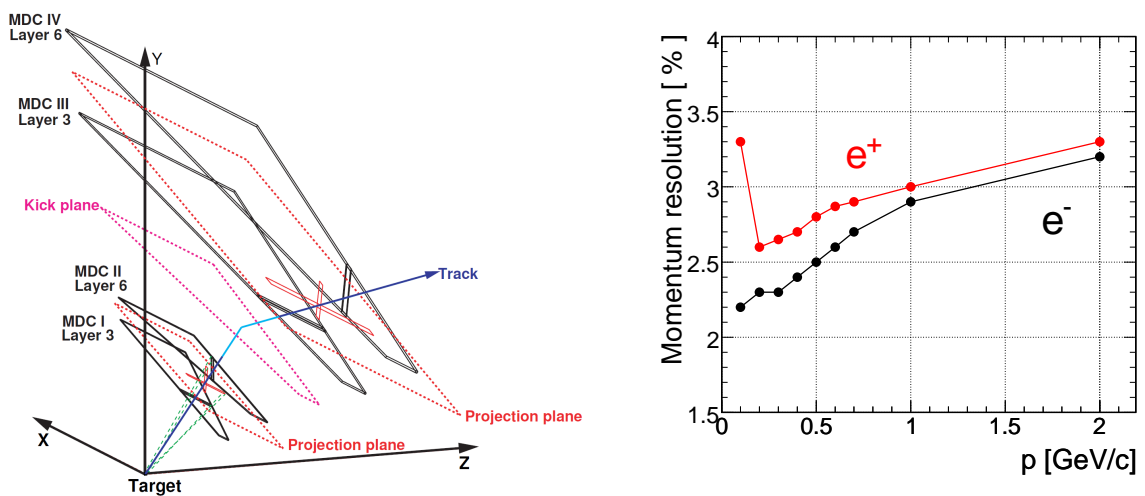


Figure 3.7: Left: Schematic view of the track candidate search in the track reconstruction procedure [21]. Right: Momentum resolution $\frac{1/p_{PRK} - 1/p_{GEANT}}{1/p_{GEANT}}$ as a function of momentum reconstructed with the Runge-Kutta algorithm. Red circle: positrons, black circle: electrons.

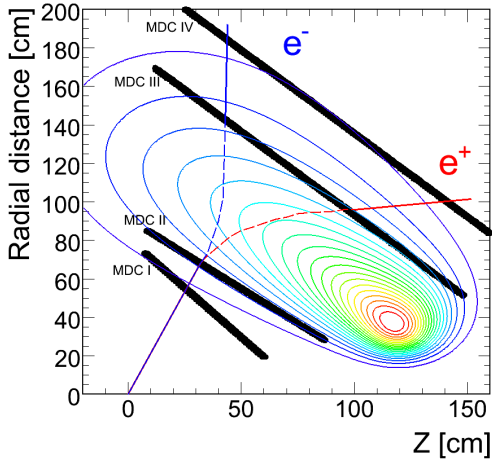


Figure 3.8: Dependence of the momentum kick on the charge. The contour plot shows the main component of the magnetic field at an azimuthal angle $\phi = 90^\circ$ (compilation A. Rustamov [22]). The 4 planes of MDC chambers are shown by black lines. Blue line: electron track, red line: positron track.

If the Runge Kutta track candidate fit converges ($\chi^2 < 10^6$) and a META hit exists, the track is propagated from the last MDC to the META. Outer segments are matched with META hits using straight lines (neglecting the curvature of the track after the magnetic field). From the difference between the original META hit position and the intersection point of the Runge Kutta track on the META a quality factor (normalized by the errors) is calculated and the matching window is defined [22] by a $\pm 3\sigma$ region around the mean value of a quality factor. If no META hit, the track is propagated to an (infinitely large) plane positioned. The position and direction at the META is used to calculate an outer segment, newly fitted with Runge Kutta. The fitted Runge Kutta track candidate is propagated to a plane parallel to MDC-I at a distance of 300 mm. With the position and direction at the intersection point the inner track segment is newly calculated with Runge Kutta fit. Inner segments are then matched to reconstructed RICH ring centers (see section 3.2.2).

3.2.2 RICH ring reconstruction

In a first step of the offline ring reconstruction all fired pads are calibrated and isolated pads as well as large track clusters due to charged particles removed. After such contributions to the detector information are removed, a ring search is performed in the full acceptance. The goal of the ring recognition algorithms is to identify the position of rings formed by photoelectrons extracted from the pad plane. The ring finder selects a ring if a significance parameter desired from the so-called Pattern Matrix algorithm supersede a given threshold. In this algorithm, that overlays a mask of the ring image on the pad plane, each pad in the region of interest is weighted with a factor proportional to the the likelihood that this pad is active.

The pattern matrix mask is shown in Fig. 3.9 (left panel), it contains as well positive as negative weights. Each cell of the matrix corresponds to a pads on the pad plane. The positive values of the weights on the mask form a ring. By shifting the pattern matrix through the full image each pad is assigned a value A_{pm}^i indicating the likelihood that the i -th pad is the location of a ring center. The significance parameter A_{pm} (see Fig. 3.9, right panel) is derived as a weighted sum of all fired pads in the region of interest with their respective weight taken from the patten matrix. Another ring finder algorithm is the Hough Transform [119]. The Hough algorithm transforms the pad distribution to a distribution of hypothetical ring centers deduced from random combinations of three fired pads. Each combination of three pads defines uniquely a ring center and radius under the constrained that all three pads lie on the ring

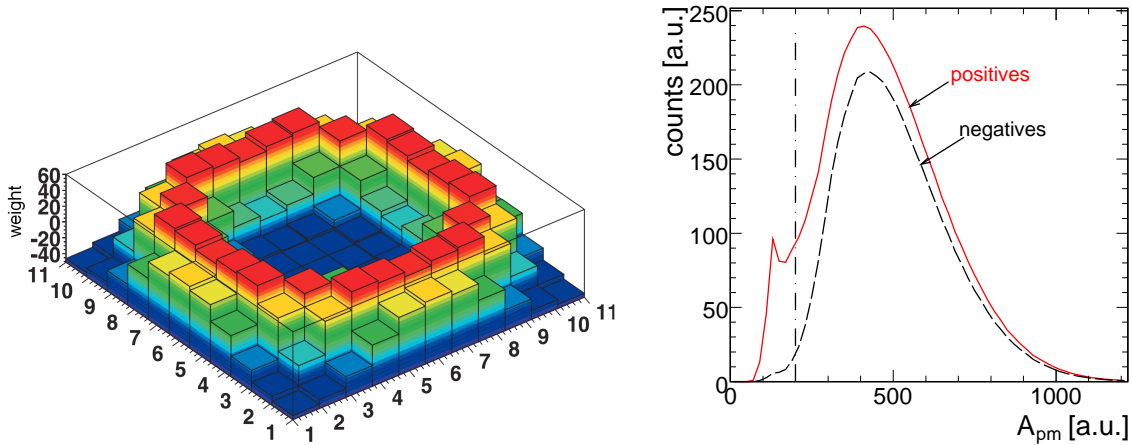


Figure 3.9: Left: 11×11 pattern matrix mask. Right: The pattern matrix parameter A_{pm} , red line: positively charged tracks, dashed black line: negatively charged tracks. The dotted dashed line indicates the applied cut.

circumference. An additional threshold setting on the local ring maximum is applied. However, if a ring image is incomplete, it might not be recognized. A coincidence between the two algorithms defines a found ring. The ring finder algorithms provide different information on the ring quality:

- the number of fired pads per ring;
- the pattern matrix parameter;
- the ring centroid, i.e. the difference between the center of gravity of charge as deduced from the pulse heights and the fitted geometrical center of the ring;
- the integrated charge per ring.

Figure 3.10 shows the distribution of the number of fired pads (right panel) and the ring centroid (left panel) separately for positive and negative tracks. The dashed lines correspond to the applied cuts. These cuts allow to suppress misidentified rings which have a significantly low ring quality. Due to the charge conservation in $p+p$ interactions the number of positively charged particles is higher compared to the negatively charged one. Moreover, the acceptance for the positively charged tracks is higher, and that is why the probability for positively charged tracks to be misidentified as a positron is also higher. Therefore, contributions at low ring quality parameters are more prominent for positron candidates. The rather large threshold for the ring centroid is chosen, because it may happen that a ring image is distorted by a coincidental direct hit to the pad plane. In order to not cut distorted true rings, the cut on the ring centroid is applied at quite large values.

Finally, a ring is accepted if the integrated charge on the pad in the ring is larger than 4 ADC channels/pad, the quality parameter from the pattern matrix algorithm is larger than 200, the number of the pads that build the ring is larger than 5, and the ring centroid is smaller than 5.

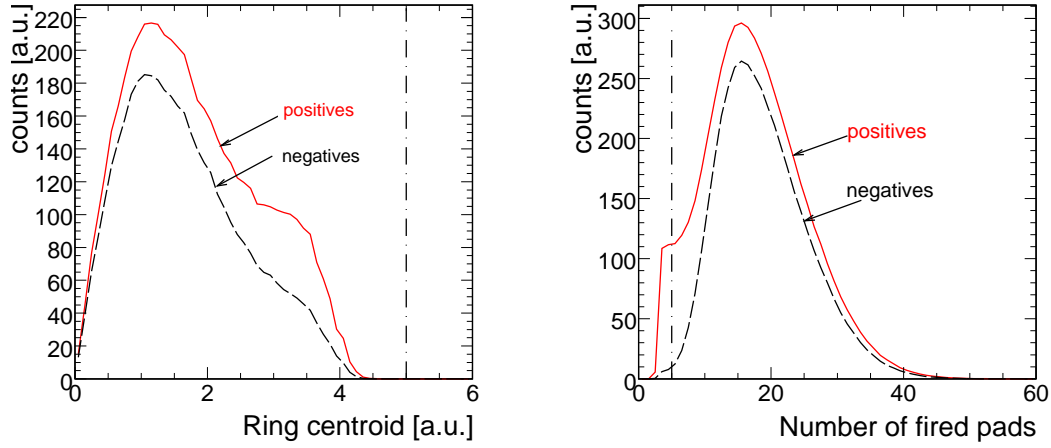


Figure 3.10: Left: Ring centroid distribution. Right: Number of fired pads. Red line: positively charged tracks, dashed black line: negatively charged tracks. The dotted dashed line indicates the applied cut.

3.2.3 Time-of-flight measurements without start detector

Protons and pions can be identified using the information on the momentum of the particle, and its time of flight in the TOF/TOFino detectors. However, as it has been mentioned in section 2.1 for high intensity proton beams ($\sim 10^7$ protons/s) it is not possible to use a start detector because too much background is created by beam interactions with detector material which does not allow for a stable RICH operation. As a consequence, there is no common start time for tracks in the same event. In order to overcome this disadvantage it has been shown that a time-of-flight measurement with respect to the fastest particle can be used. This capability is an important issue. An algorithm for the time calibration of the TOF and TOFino systems as well as a procedure reconstructing the start time of the reaction has been developed [120].

First, the time calibration of the TOF and TOFino systems has to be performed. Lepton pairs from the same event were used to calculate their TOF difference (Δt). Assuming that both leptons traveled the same path length, their Δt must be equal to zero. Thus by setting the Δt distributions to zero on a pad by pad basis, all time offsets were defined [120].

The start time reconstruction relies on the assumption that particle can be identified by other means than by time-of-flight measurement. This condition can be fulfilled for electron/positron identified in the RICH. In events without identified ring the algorithm searches for a negatively charged track and assumes that this track is a pion (π^-). From the known mass and the measured momentum the theoretical time-of-flight is calculated, and thus the offset to the measured start time of the reaction is defined. The theoretical time-of-flight of the known particle can be calculated by the formula:

$$t_{\text{theor.}} = \frac{L}{c} \cdot \frac{1}{\beta} = \frac{L}{c} \cdot \frac{\sqrt{p^2 + m^2}}{p}, \quad (3.5)$$

where the path length L and momentum p are obtained from the track reconstruction algorithm, c is the speed of light and m is the mass of the particle. The time offset is then defined as:

$$t_{\text{offset}} = t_{\text{exp}} - t_{\text{theor.}}, \quad (3.6)$$

where t_{exp} is the time-of-flight of the particle which started the data acquisition. Finally, t_{offset} has to be added to the measured time of all other particles in the same event.

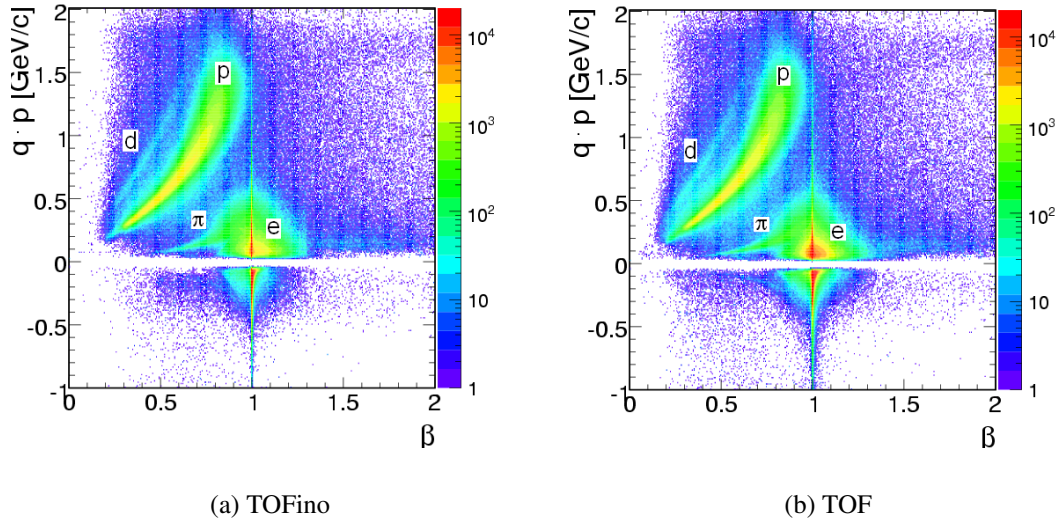


Figure 3.11: The momentum times polarity ($p \cdot q$) versus velocity (β) distribution for LVL1 triggered events. The statistics shown corresponds to one day of data taking.

The average time resolution obtained by this method is $\sigma_{\Delta\text{tof}} = 340 \text{ ps}$ and the efficiency of the method is about 92% for events with a lepton. The resolution is $\sigma_{\Delta\text{tof}} = 440 \text{ ps}$ with an efficiency of the method of about 93% for events with a negative pion. The current algorithm has the capability to provide particle identification even without a start detector being present and, thus allowing to run the experiment at a much higher rate in a cleaner environment. Figure 3.11 shows the momentum times polarity versus velocity distribution after start time reconstruction for tracks reconstructed in the TOF (right panel) and TOFino (left panel) systems. As one can see protons and pions are well resolved, for lepton identification additional RICH information is definitely needed (see section 3.3).

3.3 Electron identification

An important pre-request for the identification of vector mesons via their di-electronic decay is to obtain a very pure electron and positron sample. While the probability to falsely reconstruct a true hadron final state in a pair decay as electron-positron pair is significantly low, uncorrelated hadron contamination contribute to the combinatorial background. Electrons and positrons are identified with the RICH (see section 3.2.2) and TOF/TOFino detectors (see section 3.3.2) supplemented by an electromagnetic Pre-Shower detector in the forward hemisphere to further discriminate against fast hadrons (see section 3.3.3).

3.3.1 The spatial Ring - Inner Track Segment correlations

An essential element in the electron identification is a matching of a track to reconstructed ring center. Matching is done in polar and azimuthal angles, i.e. the difference of the polar angle $\Delta\theta = \theta_{\text{MDC}} - \theta_{\text{RICH}}$ and the azimuthal angle $\Delta\phi = \phi_{\text{MDC}} - \phi_{\text{RICH}}$ of the ring centers and inner track segments. In order to keep the solid angle spanned by the correlation constant, the correlation of azimuthal angle ($\Delta\phi$) is corrected by a factor $\sin(\theta)$. In the first analysis stage, the reconstructed RICH ring center is correlated with the inner track segment within a wide matching window $\Delta\theta = \pm 7^\circ$ and $\Delta\phi \cdot \sin(\theta) = \pm 7^\circ$. In order to define a more narrow matching window, the residuals ($\Delta\theta$, $\Delta\phi \cdot \sin(\theta)$) are plotted sector-wise for different momentum bins. Figure 3.12 shows the $\Delta\theta$ distributions for two momentum bins: $p < 100 \text{ MeV}/c$ (left panel) and $300 < p/(\text{MeV}/c) < 400$ (right panel). These distributions can be described by three components, i.e. signal contribution, correlated and uncorrelated background.

The signal contribution is fitted with a Gaussian function. The width of the signal contribution is mainly due to the momentum dependent multiple scattering in the RICH material (mostly in the RICH mirror made of carbon). The multiple scattering can be calculated as:

$$\theta_0 = \frac{13.6 \text{ MeV}}{\beta c p} z \sqrt{\frac{x}{X_0}} [1 + 0.038 \cdot \ln(\frac{x}{X_0})] \quad [121], \quad (3.7)$$

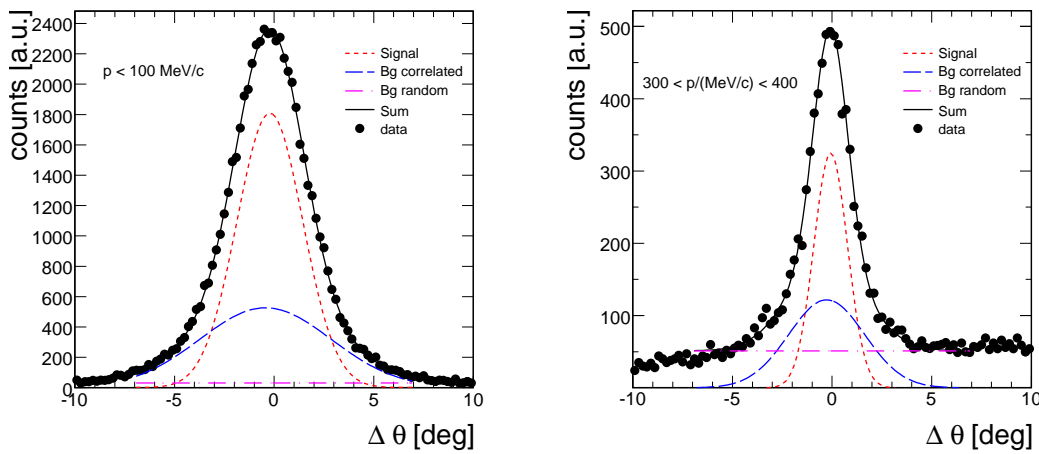


Figure 3.12: Spatial correlations between RICH ring and inner MDC track segment in polar angle. Left: for tracks with momenta below 100 MeV/c, right: for $300 < p/(\text{MeV}/c) < 400$.

where p , β , and z are the momentum, velocity, and charge number of the incident particle, and x/X_0 is the thickness of the scattering medium in radiation lengths, c is the velocity of light. The multiple scattering angle for a particle with momentum of 100 MeV/c in the RICH mirror can be estimated using simplified Eq. 3.7:

$$\theta_0 = \frac{10 \text{ MeV}}{p} \cdot \sqrt{\frac{x}{X_0}} = \frac{10 \text{ MeV}}{100 \text{ MeV}} \cdot \sqrt{\frac{0.2 \text{ cm}}{18.8 \text{ cm}}} = 0.1 \cdot 0.1 = 10 \text{ mrad} \simeq 0.6^\circ, \quad (3.8)$$

where $x = 0.2 \text{ cm}$ is the thickness of the RICH mirror, $X_0 = 18.8 \text{ cm}$ is the radiation length of ^{12}C . The effect of the multiple scattering is also reflected in the signal width visible in Fig. 3.12. The contribution of the RICH angle resolution to the total width of the signal was determined to be around 0.6° . The correlated background due to correlations between the track segment and unresolved double rings (see Fig. 3.12, long-dashed line) is described by a broad Gaussian function. To get the proper modeling of the uncorrelated background (see Fig. 3.12, dotted-dashed line), random correlations between RICH ring centers and MDC track segments are produced by a rotation of the RICH detector relative to the MDC detector by 60° in azimuthal angle.

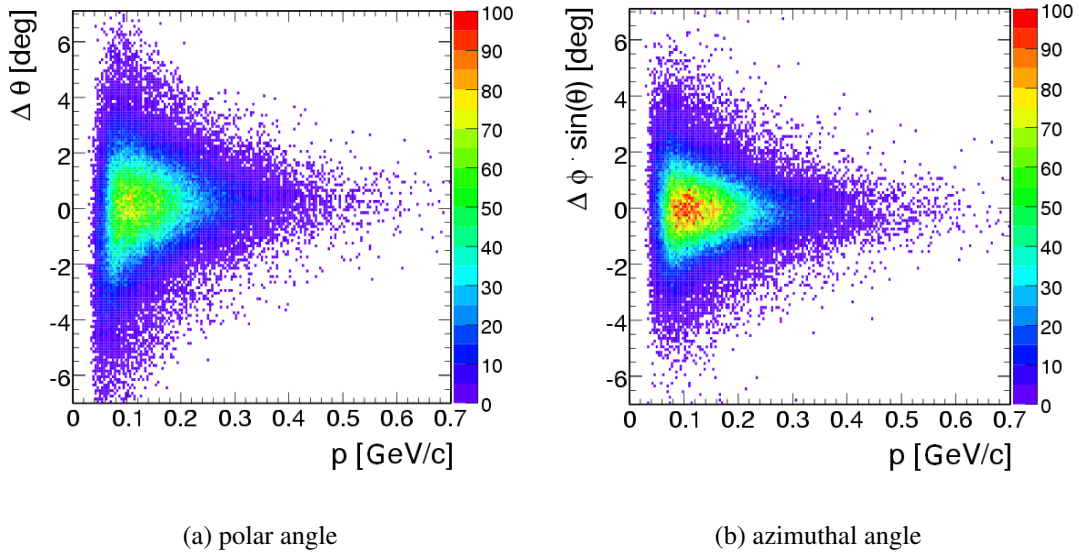


Figure 3.13: Angular correlations between RICH ring center and inner track segment after a $\pm 3\sigma$ cut in $\Delta\theta$ and $\Delta\phi \cdot \sin(\theta)$ around the electron peak has been applied.

The matching condition of rings and inner track segments has been chosen to be 3σ around the peak for polar and azimuthal angles. Figure 3.13 shows the $\Delta\theta$ and $\Delta\phi$ residuals as a function of momentum for all found rings and all reconstructed inner MDC track segments inside this 3σ matching window.

3.3.2 Electron identification using time-of-flight information

Figure 3.14 (left panel) presents the momentum versus velocity distribution after start time reconstruction for all particles reconstructed in events with positive LVL2 trigger decision and after applying a cut on the quality of the track reconstruction (e.g. χ^2 of inner and outer track segments larger than zero, and $\chi^2_{\text{Runge Kutta}} < 10^5$). As one can see from Fig. 3.14 (left panel) at

momenta larger than $\sim 300 \text{ MeV}/c$ and velocities larger than ~ 0.8 electrons and pions start to overlap. A lower limit cut on β is important in order to reject the contamination from pion and also proton tracks. A momentum dependent threshold velocity has been defined as:

$$\beta = 0.43 \cdot \sqrt{p} + 0.7. \quad (3.9)$$

Such a condition on the upper limit of β is not applied since there is no contamination of true particles at $\beta > 1$. If an individual cell of the detector has been hit by more than one particle, the correct reconstruction of the time-of-flight is very difficult. Typically, one of these particles has a very low value of the time-of-flight and as consequence has a β larger than 1. Applying a too strict cut on an upper β value would remove those particles. Moreover, the probability of double hits in the same detector cell (especially in the TOFino detector) has to be taken into account. An upper limit on β of 1.3 independent of momentum has been used. Figure 3.14 (right panel) shows the momentum versus β distribution after time-of-flight cut has been applied.

3.3.3 Electron identification using electromagnetic shower information

Redundant identification of electron tracks at forward angles, where the separation of electron and hadron by time-of-flight measurements is difficult, is provided by the Pre-Shower detector. The significantly larger charge deposition in the Shower Post-Converter chamber for electrons compared to hadrons is used for electron identification. In addition, the information on the energy loss in the Shower Pre-Converter is used to eliminate slow hadrons with large energy losses. Basing on these observations detailed Monte Carlo simulations have been performed in order to develop an electron identification procedure [122, 123].

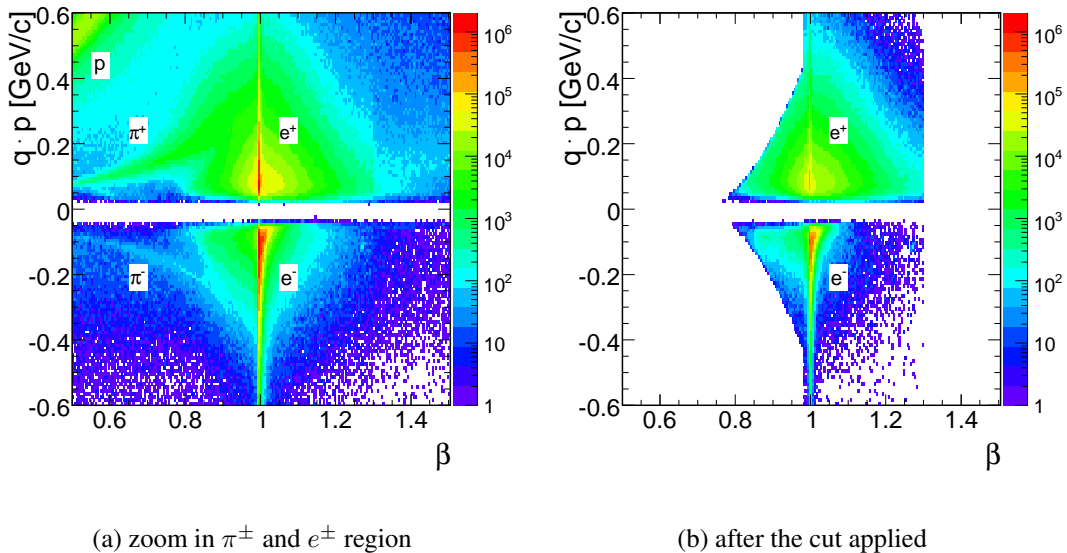


Figure 3.14: The momentum times polarity ($p \cdot q$) versus velocity (β) distribution for LVL2 triggered events. Left: TOF/TOFino systems, zoom into the electron/pion region, right panel: after time-of-flight cut has been applied.

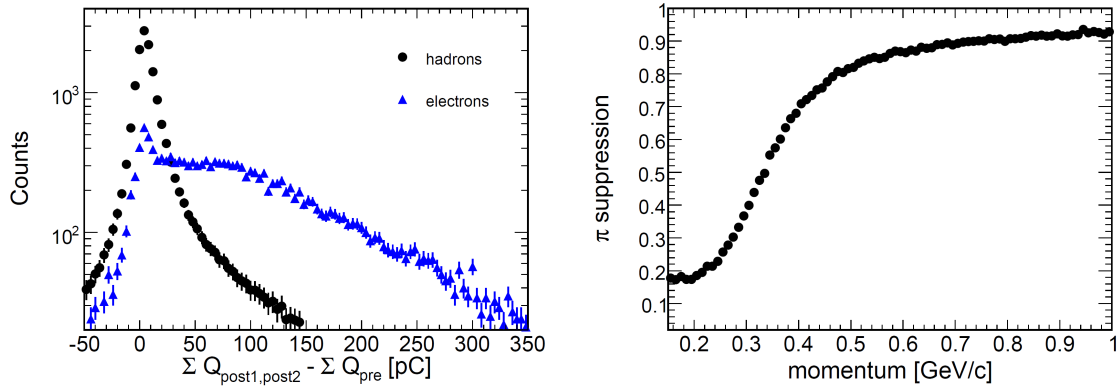


Figure 3.15: Left: Sum of charge measured in the post1- and post2-chambers with subtracted charge measured in the pre-chamber. Electrons with momenta ~ 500 MeV/c (triangles) produce electromagnetic cascades in the lead converters which result in a larger deposited charge compared to the charge produced by hadrons, here - pions (dots). Right: Pion suppression as a function of momentum, i.e. the fraction of pions rejected after the algorithm for lepton recognition (electromagnetic cascade) has been applied.

The separation of electrons from hadrons is based on the comparison of the integrated charge on the pads contributing to the cluster on a pad plane behind and in front of the lead converter:

$$\sum Q_{\text{post1,post2}}(p) - \sum Q_{\text{pre}}(p) \geq Q_{\text{Thr}}(p). \quad (3.10)$$

The momentum-dependent thresholds $Q_{\text{Thr}}(p)$ were optimized to obtain a constant electron identification efficiency of 80% over a wide momentum range ($0.1 < p/(\text{GeV}/c) < 1.5$). The left panel of Fig. 3.15 shows the difference (see Eq. 3.10) measured for electrons with a momentum of about 0.5 GeV/c and minimum-ionizing pions. Using these distributions the electron to hadron rejection can be evaluated for a given charge threshold ($Q_{\text{Thr}}(p)$) as a function of momentum. Finally, the pion suppression factor (see Fig. 3.15, right panel) can be obtained for a threshold yielding constant electron efficiency of 80%.

3.3.4 Single lepton spectra

The momentum times polarity spectrum of lepton candidates including full event reconstruction and electron identification cuts is shown in Fig. 3.16 (right panel). For comparison, the respective contribution before electron identification cuts have been applied is shown in the left panel Fig. 3.16. In Fig. 3.16 (left panel) one can see that at momenta $p > 0.5$ GeV/c positron sample is significantly contaminated by misidentified pions and protons in the TOFino/Pre-Shower region mainly. The resulting misidentification of electrons is due to ring-track mismatches typically of rings from secondary electrons with hadron tracks from the primary vertex. These misidentified electrons are suppressed by using information from the TOF and Pre-Shower detectors.

All cuts established for electron identification are summarized in Tables 3.1, 3.2 in the order they are applied. The relative reduction of the initial number of lepton candidates is defined as the ratio of lepton candidates after the identification cut to lepton candidates before any cut has been applied (also shown in Table 3.1, 3.2). The most effective electron identification cuts are the cut applied on the time-of-flight and electromagneticshower information of the lepton candidate. Those cuts remove successfully a large fraction of misidentified hadrons in the

momentum region $p > 0.5 \text{ GeV}/c$. After all electron identification cuts have been applied momentum times polarity distributions become symmetrical. Still for $p > 0.5 \text{ GeV}/c$ momentum distributions deviates from the steep exponential decrease. Further suppression of the hadron contamination is possible on the pair analysis level (will be discussed in the section 3.4).

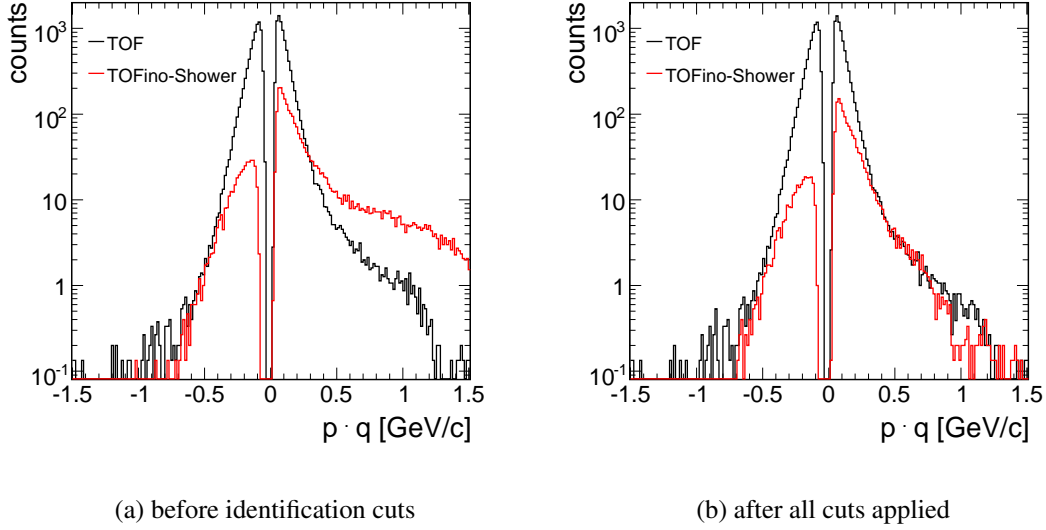


Figure 3.16: Momentum times polarity ($p \cdot q$) distributions of lepton candidates.

Cut type	positrons		electrons	
	$p < 0.5 \text{ GeV}/c$	$p > 0.5 \text{ GeV}/c$	$p < 0.5 \text{ GeV}/c$	$p > 0.5 \text{ GeV}/c$
ring-track matching	100%	100%	100%	100%
RICH ring quality	99.5%	79%	99.8%	99%
time-of-flight	98.4%	75%	99.4%	97%

Table 3.1: Cuts established for electron identification and cut efficiency for lepton candidates identified in the TOF detector.

Cut type	positrons		electrons	
	$p < 0.5 \text{ GeV}/c$	$p > 0.5 \text{ GeV}/c$	$p < 0.5 \text{ GeV}/c$	$p > 0.5 \text{ GeV}/c$
ring-track matching	100%	100%	100%	100%
RICH ring quality	98%	76%	98%	92%
time-of-flight	89%	65%	86%	79%
electromagneticshower	67%	19%	67%	52%

Table 3.2: Cuts established for electron identification and cut efficiency for lepton candidates identified in the TOFino and Pre-Shower detectors.

3.4 Di-electron analysis

In the final step of data processing, identified electron and positron tracks are combined into pairs. Pairing is done by creating all possible combinations of electron and positron tracks from the same event. Many of the unlike-sign pairs, however, represent combinatorial background and have to be suppressed. The contributions of the main background sources e.g. π^0 Dalitz decay, γ conversions in the detector material and single tracks of partially reconstructed pairs would overwhelm the number of signal pairs by orders of magnitude if no further background rejection would be applied. It is important to find the best way to reject tracks stemming from the sources mentioned before and keeping the efficiency for track pairs high. On the other hand, reconstructed π^0 Dalitz decays should not be cut substantially, as they allow for a better comparison to theory and a validation of the normalization.

3.4.1 Estimation of the combinatorial background

SIMILARITY

*No cow's like a horse,
and no horse like a cow.
That's one similarity anyhow.
(Piet Hein)*

The distinguishing feature of signal pairs is the correlation between the pair members. The actual signal of correlated di-electrons (N_{+-}^{signal}) in a given phase space bin is the difference between the total observed unlike-sign pairs (N_{+-}^{tot}) and the combinatorial pairs ($B_{+-}^{comb.}$):

$$N_{+-}^{signal}(p_t, y, M_{ee}) = N_{+-}^{tot} - B_{+-}^{comb.} \quad (3.11)$$

Background pairs essentially result from a random combination of two electrons/positrons of the following processes: γ conversion, π^0 and Δ Dalitz decays and misidentified hadron. The combinatorial background can be divided into two categories: uncorrelated and correlated background. The schematic view of the uncorrelated $B_{+-}^{comb.}$ is shown in Fig. 3.17 (left panel). The uncorrelated combinatorial background is created by random combinations between leptons originating from two independent sources. Because of that, the invariant mass distribution of uncorrelated pairs is rather smooth. Correlated background is coming mostly from the $\pi^0 \rightarrow \gamma\gamma$ decay or the π^0 Dalitz decay as shown in Fig. 3.17 (right panel). Combinations between positrons and electrons originating from γ conversion or from decay of the virtual photon in the same π^0 decay will create correlated pairs. In contrast to the invariant mass distribution of uncorrelated pairs a correlated pairs create a peak structure at around half of the π^0 mass.

The unlike-sign combinatorial background can be estimated by the same-event like-sign technique. The combinatorial background can as well be estimated via mixing of electrons and positrons across different events. An advantage of the latter approach is that a very high degree of statistical precision can be reached in the construction of $B_{+-}^{comb.}$. However, the true background cannot violate the conservation of energy on an event by event basis, while the event mixed background is not similarly constrained. Moreover, systematic errors may be introduced by this method since the $B_{+-}^{comb.}$ derived from the event mixing technique cannot

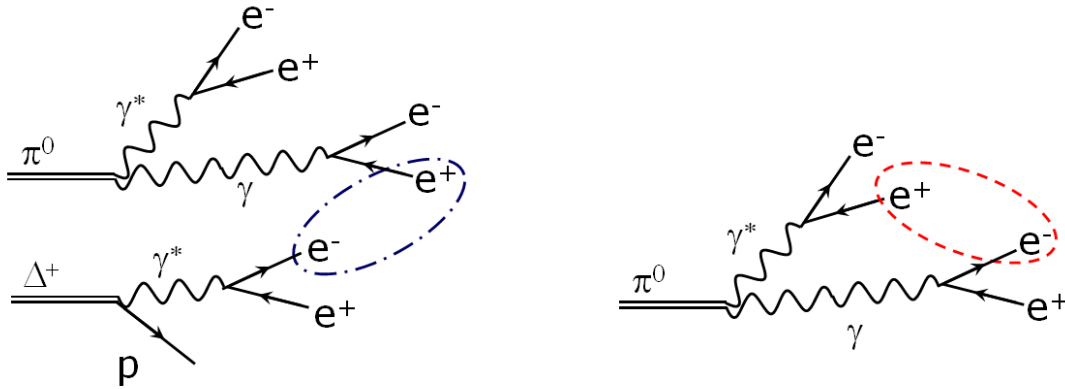


Figure 3.17: Example of uncorrelated (left panel) and correlated (right panel) combinatorial pairs. The correlated combinatorial pair is created by a single π^0 Dalitz decay.

reproduce subtle correlations in the actual opposite-sign background (leptons coming from different events are uncorrelated by construction). For the current analysis the same-event like-sign method was used for the unlike-sign background estimation.

Same-event combinatorial background

In order to obtain the combinatorial background like-sign e^+e^+ and e^-e^- pairs were formed and subjected to the same selection criteria as the opposite-sign pairs. The method is based on the fact that the same-event like-sign combinatorial background is identical to the unlike-sign combinatorial background. In the experiment a certain number of positron tracks N_{e^+} and electron tracks N_{e^-} is measured per event. The multiplicity distribution is shown in the Fig. 3.18. The measured multiplicity of electrons N_{e^-} or positrons N_{e^+} are almost identical (see Fig. 3.18, right panel). Starting from the fact that both charges have about the same acceptance and the same reconstruction efficiency, one can demonstrate that the mean unlike-

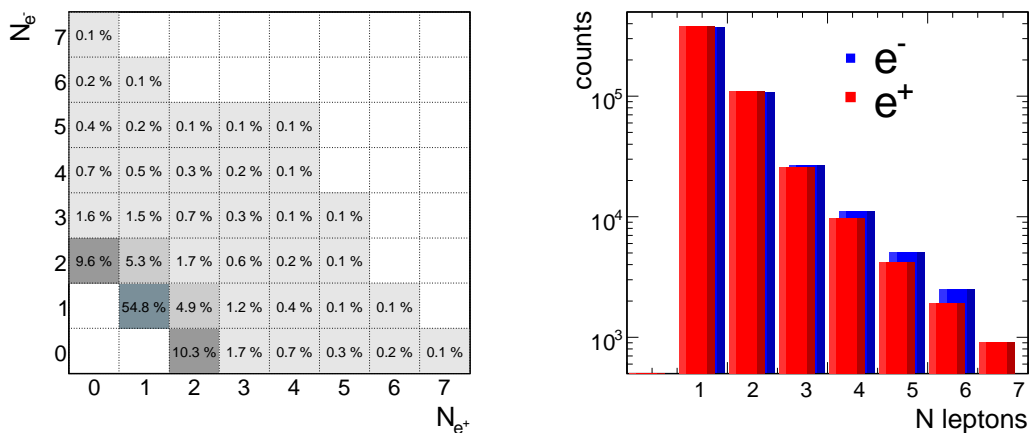


Figure 3.18: Left: Multiplicity distribution of identified electrons versus positrons. Right: Electron (blue) and positron (red) multiplicity per one event.

sign combinatorial background is given by twice the geometrical mean of the like-sign pairs. A detailed derivation can be found in [124].

From the reconstructed like-sign invariant-mass distributions the respective combinatorial background distribution can be obtained as the geometrical or the arithmetical mean of like-sign e^+e^+ (N_{++}) and e^-e^- (N_{--}) pairs:

$$B_{+-}^{comb.} = 2 \cdot \sqrt{N_{++} \cdot N_{--}}, \quad (3.12)$$

$$B_{+-}^{comb.} = N_{++} + N_{--}. \quad (3.13)$$

The geometrical mean of N_{++} and N_{--} is very robust and becomes a standard procedure to calculate the combinatorial background in many heavy-ion experiments. It is also needed for normalization of the combinatorial background estimated by the event-mixing technic. The combinatorial background can be estimated as well by the arithmetical mean of N_{++} and N_{--} . Even with a slight charge asymmetry in heavy-ion collisions the combinatorial background estimated via arithmetic or geometric mean is nearly identical. In elementary collisions, however, this slight charge asymmetry is a crucial point and can leads to an underestimation of the $B_{+-}^{comb.}$ and because of that the signal contribution can be overestimated.

In mathematics, the inequality of arithmetic and geometric means states that the arithmetic mean of a list of non-negative real numbers is greater than or equal to the geometric mean of the same list; and further, that the two means are equal if and only if every number in the list is the same. The arithmetic mean of a list of n numbers N_1, N_2, \dots, N_n is the sum of the numbers divided by n :

$$\frac{N_1 + N_2 + \dots + N_n}{n}. \quad (3.14)$$

The geometric mean is similar, except that it is only defined for a list of nonnegative real numbers:

$$\sqrt[n]{N_1 \cdot N_2 \cdot \dots \cdot N_n}. \quad (3.15)$$

For a list of n nonnegative real numbers (N_1, N_2, \dots, N_n) both means are not equal:

$$\frac{N_1 + N_2 + \dots + N_n}{n} \geq \sqrt[n]{N_1 \cdot N_2 \cdot \dots \cdot N_n}. \quad (3.16)$$

This can be proven in several ways. As an example the proof by Cauchy [125] for the subcase $ns = 2$ is shown. If $n = 2$, one has two terms, N_1 and N_2 , and since not all terms are equal, one has:

$$N_1 \neq N_2 \quad (3.17)$$

$$N_1 - N_2 > 0 \quad (3.18)$$

$$(N_1 - N_2)^2 > 0 \quad (3.19)$$

$$N_1^2 - 2 \cdot N_1 \cdot N_2 + N_2^2 > 0 \quad (3.20)$$

$$N_1^2 + 2 \cdot N_1 \cdot N_2 + N_2^2 > 4 \cdot N_1 \cdot N_2 \quad (3.21)$$

$$(N_1 + N_2)^2 > 4 \cdot N_1 \cdot N_2 \quad (3.22)$$

$$N_1 + N_2 > 2 \cdot \sqrt{N_1 \cdot N_2}. \quad (3.23)$$

Here, the arithmetic mean of the same-event like-sign pairs for the unlike-sign combinatorial background estimation was used.

3.4.2 Background rejection strategy

As it has been shown in section 3.4.1, the correlated dilepton signal has to be extracted from the observed number of unlike-sign pairs by the subtraction of the independent combinatorial background pairs (see Eq. 3.11). The combinatorial background arises mostly from multiple $\pi^0 \rightarrow \gamma\gamma$ decays followed by photon conversion, either in the target region or in the RICH radiator, and from π^0 Dalitz decays. In this section we will explain how to suppress the background and obtain a significant signal. The background rejection strategy includes two steps: the first step is to remove single tracks where the true partner was not fully reconstructed (single lepton cuts), the second step is to reject reconstructed pairs from the background sources mentioned above (pair cuts).

Single lepton cuts

Conversion pairs are emitted with small opening angles ($\theta_{e^+e^-} < 4^\circ$) and can easily be distinguished from other sources if both leptons from the pair are fully reconstructed. This is, however, only true for 10% of the conversion events. Due to the small opening angle of the conversion pairs and the limited detector resolution electrons and positrons are often not resolved as separate tracks neither in the RICH detector nor in the inner MDC detectors. Unresolved close tracks that are identified as one lepton track should be rejected from the analysis before further combinatorics. It has been shown in previous analysis, that very often (60% of all cases) the e^+ and e^- coming from close pairs share the same hit in RICH or in MDC detectors. Tracks with double hits are thus excluded in the analysis (so called **Double-hit rejection cut**).

Another problem comes from partially reconstructed tracks. Conversion leptons produced between the target and the RICH mirror will be reconstructed if they have large enough momentum to pass through the magnetic field. The magnetic field of the HADES spectrometer puts a cut on the particle momenta such that only particles with $p > 50 \text{ MeV}/c$ can pass the magnetic field. In case one of the leptons from a γ conversion does not have large enough momentum to pass the magnetic field, the double track piece before the field is matched with a single META hit of the accepted lepton. To reject such partially recognized leptons we search for its closest partner before the magnetic field. If the closest track segment was not fitted, i.a. has a $\chi^2 < 0$, the fully reconstructed electron track is rejected. The fully reconstructed track will also be removed from the final electron sample if its closest tracks segment is found within an angle with respect to the reconstructed track of 9° . Those two cuts belong to the so called **Close-pair candidate rejection cuts**.

Pair cut

The double-hit rejection cut and close-pair candidate rejection cut remove single lepton tracks. In case both partners were reconstructed in the detector, pair cuts can be applied. A very powerful pair cut is the **Opening angle cut**. To select the best cut value dedicated Monte Carlo studies were performed. A 9° opening angle cut will reject more than 90% of close pairs and only 5% of open pairs. From the remaining, well separated tracks only those are involved in the combinatorics which have an opening angle larger than 9 degree ($\theta_{e^+e^-} > 9^\circ$). The resulting e^+e^- distributions comprises a signal part (see Fig. 3.19, left panel), originating from meson and baryon decays, and a combinatorial background contribution (see Fig. 3.19, right panel).

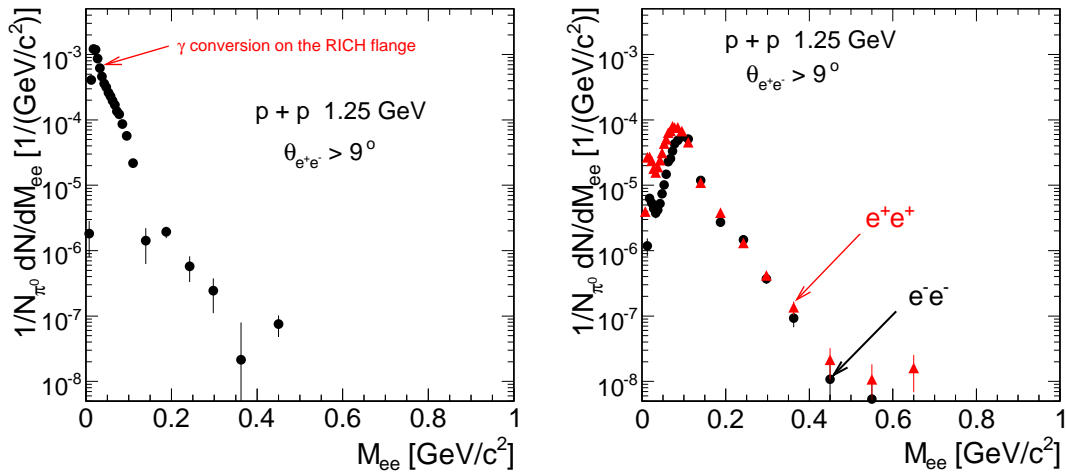


Figure 3.19: Left: Invariant mass spectra of signal electron-positron pairs after the background subtraction measured in $p+p$ interactions after the double-hit rejection, close-pair candidate rejection and pair cuts applied. Right: same-event like-sign pairs. The vertex cut is not applied here.

The rejection capability of the cuts described above, however, turned out to be not enough to detect a significant signal. From the invariant mass spectra of the signal and combinatorial background one can see that an extra contribution arises in the signal spectrum at very small invariant mass $M_{ee} < 50 \text{ MeV}/c^2$, most likely from the γ conversion process.

Vertex cut

The probability of the production of conversion pairs depends on the material and length of the trajectory of the photon in the material. In order to identify the source of the γ conversions, we had a closer look to the detector material which is crossed by particles. Figure 3.20 shows a GEANT simulation of the HADES detector, zoomed into the target region. As one can clearly see from the plot, photons emitted at the beginning of the target ($z < -50 \text{ mm}$) and at large polar angle ($\theta > 50^\circ$) have a large probability to convert in the RICH flange made from steel. Since positrons are bent inwards by the magnetic field, their probability is larger to be reconstructed. Electrons with such kinematics will not be accepted. Therefore this effect is stronger for positrons. This explains the asymmetry in the number of like-sign background N_{++} and N_{--} which is larger for N_{++} combinations (see Fig. 3.19, right panel).

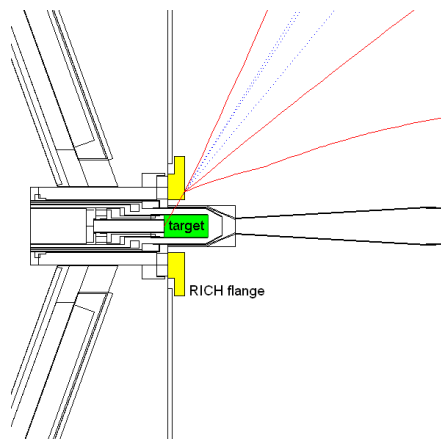


Figure 3.20: GEANT simulation of the HADES detector. Zoom into the target region. A conversion process on the RICH flange is seen. Green: LH_2 target, yellow: RICH flange.

Figure 3.21 presents an example of the z coordinate of the reconstructed event vertex as a function of polar angle for two momentum bins. Such distributions were plotted for different momentum bins. It has been seen that the contribution of tracks from conversion is very prominent at small momenta, starting already from $p > 150 \text{ MeV}/c$ this contribution is very much suppressed. A square cut is used to reject the background. If particles with momenta below $150 \text{ MeV}/c$ are emitted at $\theta > 50^\circ$ and the reconstructed z position of the track is smaller than -50 mm , the particle is rejected from the electron/positron sample. During the $d+p$ run, a new target geometry was used. Due to the shorter length of the target it was possible to pull the target inwards. This target position helps to avoid a strong background contribution from conversion in the RICH flange. However, a small contribution from the background mentioned above still remains (see Fig. 3.22) and has been rejected by applying the following cut: if particles with momenta below $150 \text{ MeV}/c$ are emitted at $\theta > 65^\circ$ and the reconstructed z position of the track is below -50 mm , the track is rejected from the electron/positron sample. The invariant mass spectrum of the combinatorial background after all rejection cuts applied

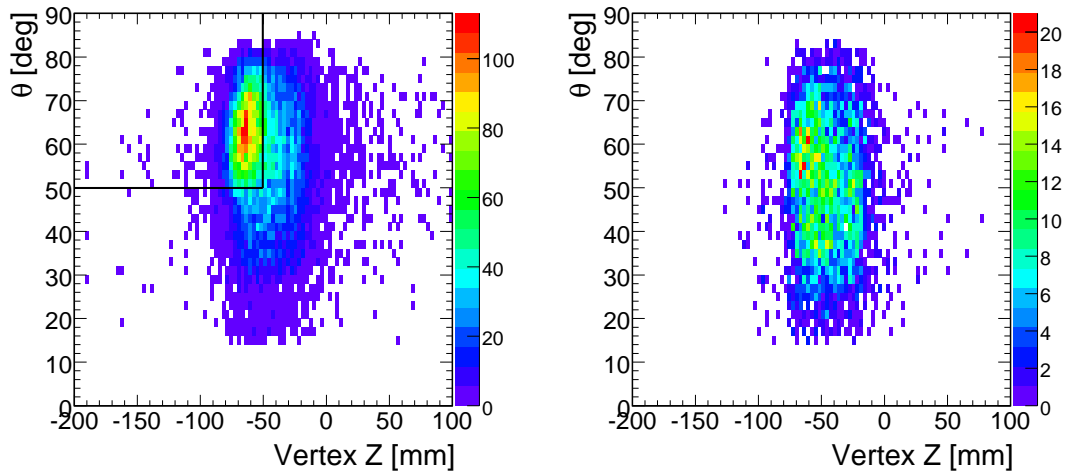


Figure 3.21: Polar angle versus reconstructed event vertex z (experimental $p+p$ data). Left: tracks with momenta below $150 \text{ MeV}/c$, red lines indicate the cut region. Right: tracks with momenta $150 < p/(\text{MeV}/c) < 200$.

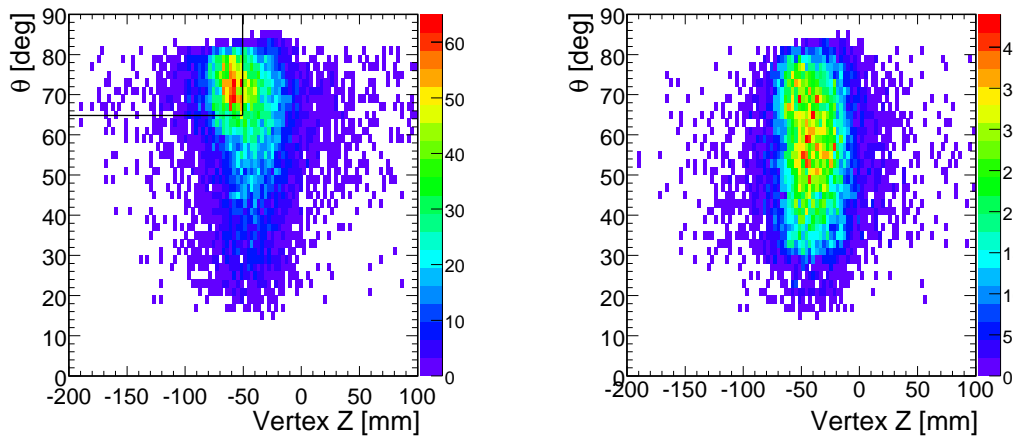


Figure 3.22: Polar angle versus reconstructed event vertex z (experimental $n+p$ data). Left: tracks with momenta below $150 \text{ MeV}/c$, black lines indicate the cut region. Right: tracks with momenta $150 < p/(\text{MeV}/c) < 200$.

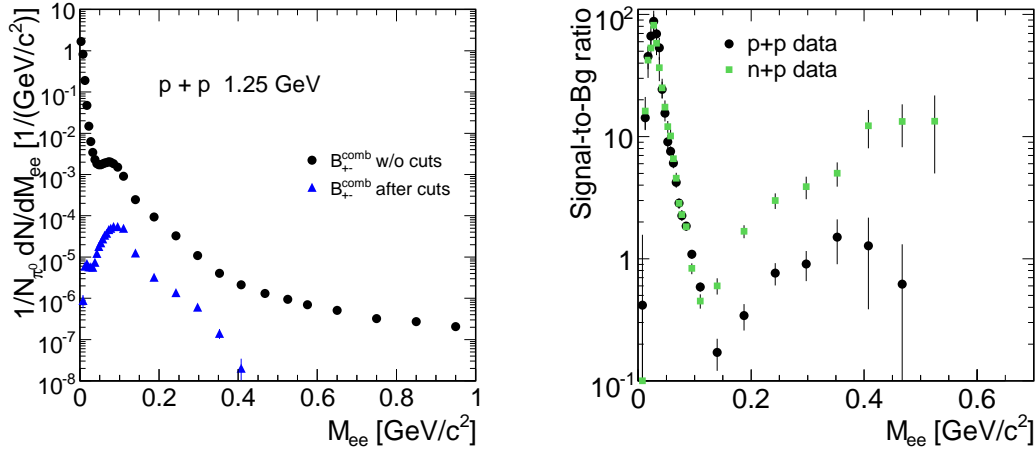


Figure 3.23: Left: Invariant mass spectra of the combinatorial background without background rejection cuts (black circles) and after all cuts applied (blue triangles). Right: final signal-to-background ratios for $p+p$ data (black circles) and for $n+p$ data (green squares); note that the signal and background spectra, used for signal-to-background ratios estimation, are efficiency corrected.

is shown in Fig. 3.23 (left panel) with the blue triangles. For comparison, the respective contribution before background rejection is shown in the same picture with the black circles. The reduction of the combinatorial background is very effective and suppress the background by more than 2 orders of magnitude. Final signal-to-background ratios are shown in Fig. 3.23 (right panel) for $p+p$ and $n+p$ data respectively, and they are significantly better than 10 for the low-mass region dominated by π^0 Dalitz decays, and slightly above 1 in the high-mass region ($M_{ee} > 0.3 \text{ GeV}/c^2$) for $p+p$ data and above 5 for $n+p$ data.

3.5 Efficiency evaluations

The final goal of the experimental data analysis is to provide pair spectra (M_{ee}, p_t, y) for comparison to the various theoretical models. HADES does not provide data corrected for the geometrical acceptance. The acceptance discussed here is the probability for a particle emitted from the reaction to path the active detector volumes. This includes the effect of the particle's deflection in the magnetic field which depends on momentum. The acceptance is determined as the ratio of accepted test particles to test particles within the full phase space:

$$\text{Acceptance}(p, \theta, \phi) = \frac{N_{\text{accepted}}(p, \theta, \phi)}{N_{4\pi}(p, \theta, \phi)}. \quad (3.24)$$

In the acceptance determination efficiency effects due to the analysis cuts as well as the intrinsic detection efficiency are not accounted for. Those are corrected for directly during the data analysis before any comparison between final data and theory is done. Probability that an electron is fully reconstructed and contribute to the spectrum is determined using the ratio of reconstructed test particles to test particles within the geometrical acceptance of the HADES spectrometer:

$$\text{Efficiency}(p, \theta, \phi) = \frac{N_{\text{reconstructed}}(p, \theta, \phi)}{N_{\text{accepted}}(p, \theta, \phi)}. \quad (3.25)$$

The possible trigger bias has to be evaluated as well. In this section, the losses due to the known sources will be addressed and the corrections applied to the final di-electron yield will be quantified.

3.5.1 Determination of the reconstruction efficiency

The observed experimentally number of lepton pairs must be corrected with the actual reconstruction efficiency ε_{ee} of each pair:

$$N_{ee}^{\text{corr}} = N_{ee} \cdot \frac{1}{\varepsilon_{ee}} \quad (3.26)$$

The pair reconstruction efficiency can be defined by the detection probability ε_{ei} of a single track:

$$\varepsilon_{ee} = \varepsilon_{e1} \cdot \varepsilon_{e2}. \quad (3.27)$$

Such an assumption is valid only if ε_{e1} and ε_{e2} are uncorrelated. One of such correlated effects is related to the small opening angle between two tracks. Relatively large opening angle cut (opening angle $> 9^\circ$) is applied to the experimental (as well simulated data) thus ensured that the correlation effect due to the opening angle is negligible. The single track efficiency can be expressed as a function of the phase space parameters: momentum (p), polar (θ) and azimuthal (ϕ) angles:

$$\varepsilon_{ei} = \varepsilon_{ei}(p, \theta, \phi). \quad (3.28)$$

The reconstruction efficiency of a single track was determined using a track embedding technique and involves several steps:

- **EVENT GENERATION:** Electrons and positrons are generated uniformly distributed in p , θ and ϕ , with the Pluto [126, 127] simulation package.

- **EVENT SIMULATION:** Simulated events are produced by the HADES simulation package HGEANT built upon GEANT3. HGEANT is used to describe the passage of generated leptons through the detector material and simulates the interaction of the particle with the active detector materials. The geometry used in the simulation is implemented down to the level of active detector plane. The simulated events show the same structure as the real ones and can be used as input for the reconstruction program instead of real ones.

- **DIGITIZATION:** In the next step, the GEANT information is digitized to account for the detector response. The hit positions of all particles as well as their energy deposition is determined by response functions of the individual detectors taking internal physics and electronics effects into account. All parameters needed by the digitizers are taken from the ORCALE data base ensuring the consistent use in the analysis of simulated and experimental data.

- **TRACK EMBEDDING:** A number of $1.8 \cdot 10^9$ simulated tracks were embedded into real events on a one-to-one basis for the study of the single-track reconstruction efficiency. As it has been discussed in section 3.4.2 a vertex cut has to be applied to reject strong contributions of $e^{+/-}$ from γ conversion in the RICH flange. In order to properly estimate the losses because of such a cut, special care has been taken about the emission point of generated leptons. That is why, x , y , and z vertex coordinates reconstructed from the real event used for embedding. In addition, an event sequence number is stored for synchronization of the embedded events with the real events. Only events where the vertex coordinates could be calculated are taken into account.

• **EVENT RECONSTRUCTION:** Finally, the full event reconstruction and electron identification, and single track background rejection cuts are applied in the way identical to the real data.

The efficiency correction matrices were computed with $50 \text{ MeV}/c^2$ momentum bin width, 2 degree polar angle bins and 4 degree azimuthal angle bins. Only electron tracks within the fiducial region of each sector were selected, i.e. a 1 degree cut in ϕ on the left and right side of each sector was applied. Such a selection is used in order to avoid large fluctuations in the reconstruction efficiency. Figure 3.24 shows the efficiency correction for electrons (left panel) and positrons (right panel) averaged over all momenta. The reconstruction efficiency for large polar angles $\theta > 50^\circ$ is about 60% while for small polar angle it is only about 30%.

The effect of the efficiency correction is shown in Fig. 3.25 and 3.26 for the di-electron invariant mass spectra measured in $p+p$ and $n+p$ reactions correspondingly. The efficiency correction is largest for the lowest masses, i.e. $F_{\text{corr}}^{\text{low}} \simeq 10$ for $p+p$ and approximately 8 for the $n+p$ analysis. This is because the reconstruction, identification and background rejection procedure is more restrictive for low mass pairs mostly due to their smaller di-electron open-

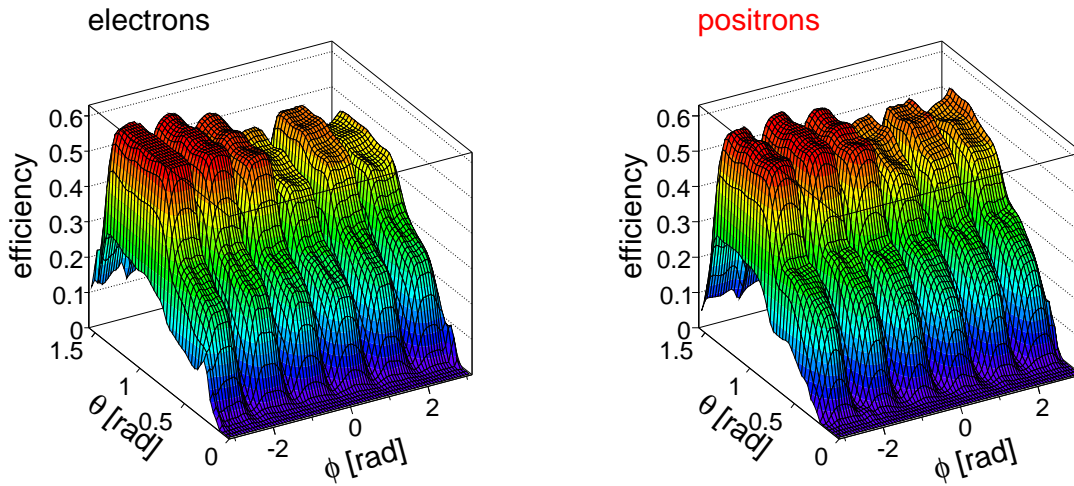


Figure 3.24: Efficiency correction as a function of polar and azimuthal angles.

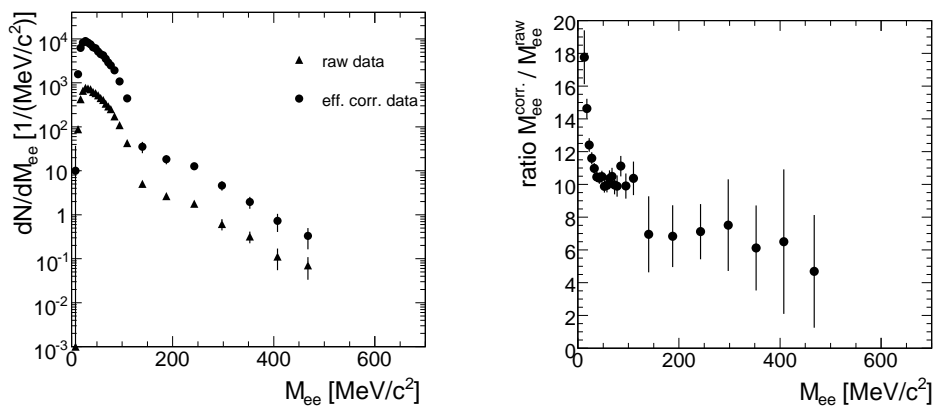


Figure 3.25: Left: Invariant mass spectra of signal electron-positron pairs measured in $p+p$ interactions. Black triangle: uncorrected data points, black circle: efficiency corrected data. Right: ratio of efficiency corrected to raw data.

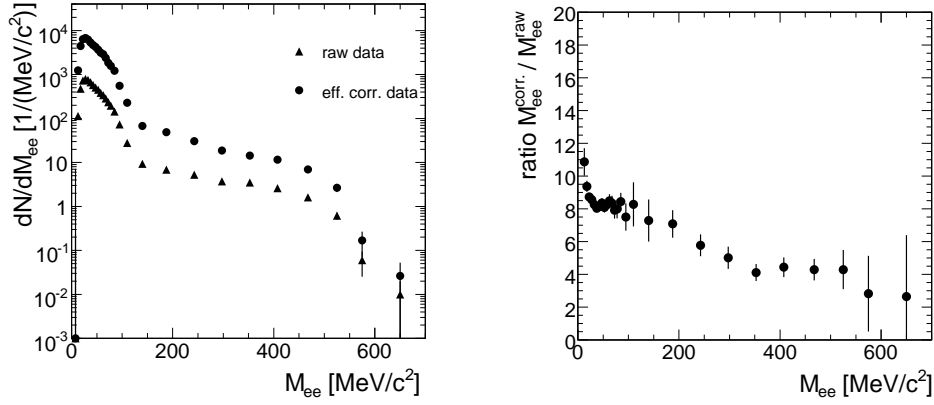


Figure 3.26: Left: Invariant mass spectra of signal electron-positron pairs measured in $n+p$ interactions. Black triangle: uncorrected data points, black circle: efficiency corrected data. Right: ratio of efficiency corrected to raw data.

ing angles. In the high invariant mass region the correction factor saturates at approximately $F_{\text{corr}}^{\text{high}} \simeq 4$ for $p+p$ and $n+p$ data, within statistical errors. Efficiency correction factors for $n+p$ data are smaller compared to the one for $p+p$ data because of the different vertex cut applied for background rejection (see section 3.4.2).

3.5.2 Determination of the trigger efficiency

First level trigger efficiency

As it has been mentioned already (see section 2.7.1), in $p+p$ interactions the LVL1 trigger required an overall multiplicity in TOF and TOFino of at least 3 charged particles (M3 trigger). The possible trigger bias from this M3 trigger was calculated for different di-electron sources (e.g. π^0 Dalitz decay, Δ Dalitz decay). The invariant mass spectra of π^0 Dalitz decay and Δ Dalitz decay were plotted with and without the M3 trigger condition. It was found that the pair reduction induced by the M3 trigger is $F_{\text{M3 trigger bias}} = 0.84$ and it is mass independent [128].

For $d+p$ collisions the selection of the $n+p$ subreaction is done by tagging forward emitted spectator protons in the Forward hodoscope Wall. The reduction of electron-positron pairs because of this trigger is $F_{\text{FW trigger bias}} = 0.84$ [110].

Second level trigger efficiency

The main goal here is to understand the efficiency and the potential bias introduced by the LVL2 trigger on the different physics observables. One has to correct the measured di-electron yield for this selection. The relative efficiency of the LVL2 trigger with respect to LVL1 can be estimated as the ratio between the number of leptons/dileptons found in LVL2 events and the number of leptons/dileptons found in LVL1 events.

Figure 3.27 shows the efficiency of the LVL2 trigger for unlike-sign pairs as a function of the invariant mass, rapidity and transverse momentum after all identification and background rejection cuts applied. The efficiency for dileptons was estimated to be on average 0.85 independent on mass, p_t and rapidity, and has been taken into account during the normalization (see section 3.6).

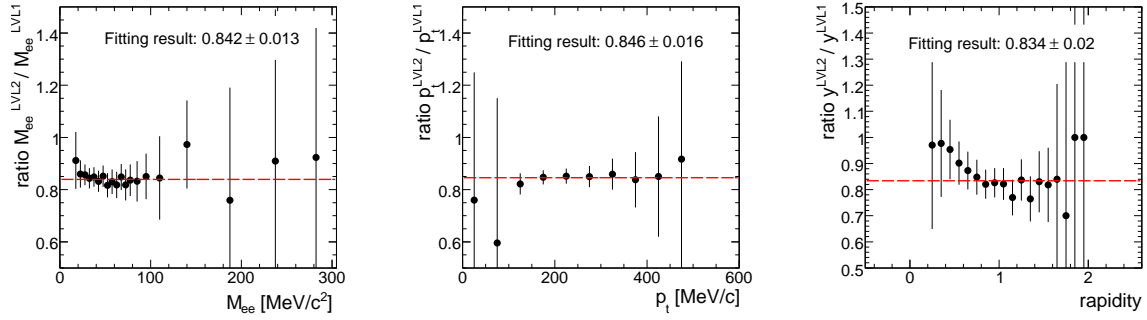


Figure 3.27: The efficiency of the LVL2 trigger as a function of invariant mass, transverse momentum, rapidity (from left to right). The horizontal line is the fit to the data, fitting results are shown as well.

3.6 Normalization procedure

The electron pairs yield measured in heavy-ion collisions is normalized to the number of neutral pions produced in the same event sample. In isospin symmetric collision systems the average number of charged pions is a perfect measure of the neutral pion yield [129], i.e. $N_{\pi^0} = 1/2 \cdot (N_{\pi^+} + N_{\pi^-})$. In order to keep the same method of normalization as used for heavy-ion collisions the total number of π^0 emitted in the full solid angle is needed. In elementary $p+p$ and $n+p$ interactions this number can be estimated using the known cross sections for inclusive neutral pion production [25] and pp elastic scattering. The number of neutral pions can be estimated using the following equation:

$$N_{\pi^0} = \frac{\sigma_{\pi^0}^0}{\sigma_{\text{elastic}}} \cdot N_{\text{elastic}} \cdot F_{\text{trigger bias}} \quad (3.29)$$

where $\sigma_{\pi^0}^0$ is the sum of all measured exclusive π^0 cross sections which are presented in Table 3.3. σ_{elastic} is the measured elastic cross section [45], and N_{elastic} is the number of elastic pairs (see section 3.6.2), while $F_{\text{trigger bias}}$ is the estimated LVL1 trigger bias (see section 3.5.2).

3.6.1 π^0 cross section

The inclusive π^0 cross sections can be constructed by adding all cross sections for exclusive channels of π^0 production. Either experimental ones when available or theoretical parameterizations in the other cases can be used. Exclusive cross sections of pion production in $p+p$ are all known at least up to 3.5 GeV incident laboratory kinetic energy. The situation for $n+p$ reactions is less favorable, since there is no experimental data of the π^0 cross section available for 1.25 GeV kinetic beam energy. In this case, cross sections for reactions with final pionic states are derived with the resonance model [24], which assumes a dominant role of intermediate Δ production. Table 3.3 shows the cross sections for exclusive channels of π^0 production in $p+p$ reaction for a kinetic beam energy of 1.25 GeV. Calculated cross sections for π^0 measured in $n+p$ reactions are also shown in Table 3.3.

3.6.2 Number of elastic pairs: from accepted to extrapolated to 4π

The absolute normalization of di-electron spectra is done by using the recorded elastic pp events. The number of elastic pp events measured in the HADES acceptance is extrapolated to

$p+p$ reaction	σ , mb	$n+p$ reaction	σ , mb
$pp \rightarrow pp \pi^0$	4	$pn \rightarrow pn\pi^0$	8
$pp \rightarrow pp \pi^0\pi^0$	0.1	$pn \rightarrow pn\pi^0\pi^0$	0.1
$pp \rightarrow pn \pi^+\pi^0$	0.25	$pn \rightarrow pp\pi^+\pi^0$	0.18
		$pn \rightarrow nn\pi^-\pi^0$	0.18
sum π^0 ($p+p$)	4.45	sum π^0 ($n+p$)	8.56

Table 3.3: cross sections for exclusive channels of π^0 production in $p+p$ [25] (experimental values) and in $n+p$ reactions [24, 25] (values calculated within the resonance model).

the full solid angle based on simulations and the reference cross section measured by the EDDA experiment in the same angular range [130, 130]. The Pluto event generator was used to simulate elastically scattered protons. The simulated elastic pp pairs were propagated through the detector system with the HADES simulation tool HYDRA using the GEANT3 package. Figure 3.28 (right panel) shows the simulated elastic pp collisions for the full solid angle and in the HADES acceptance.

At 1.25 GeV kinetic beam energy 16.7% of the elastically scattered proton events are accepted by the HADES detector. The efficiency of the spectrometer for elastic pp pairs was calculated as a function of momentum, polar and azimuthal angles and used to perform an efficiency correction of the data in a procedure similar to that used in the di-electron data (see section 3.5). The acceptance correction procedure has been applied to the experimental data and obtained results have been compared to simulated ones. The polar angle distribution of experimental together with simulated events is shown in Fig. 3.28 (left panel). The experimental and simulated data are in nice agreement. Now one can estimate the number of pp elastic scattering pairs emitted in the full solid angle (4π):

$$N_{\text{elastic}} = N_{\text{acc.}}^{pp} \cdot F_{\text{eff.corr.}} \cdot F_{\text{acc.}} \cdot F_{\text{LVL1}}^{\text{DS}} \cdot F_{\text{M2opp}}^{\text{DS}} \quad (3.30)$$

$N_{\text{acc.}}^{pp} = 5.6 \cdot 10^6$ is the amount of elastic pp events in the HADES acceptance, $F_{\text{eff.corr.}} = 1.26$ is the efficiency correction factor for the event reconstruction, $F_{\text{LVL1}}^{\text{DS}} = 5$ is the down scaling factor of LVL1 triggered events, $F_{\text{M2opp}}^{\text{DS}} = 64$ is the down scaling factor of elastic scattering events and $F_{\text{acc.}} = 1/0.167$ is the acceptance factor discussed above. The total number of elastic pp interactions measured in $p+p$ reactions is $N_{\text{elastic}}|_{pp} = 1.57 \cdot 10^{10}$. The number of elastic scattering pairs measured in $n+p$ interactions were estimated in the same way. The total number of elastic pp interactions is $N_{\text{elastic}}|_{np} = 6.23 \cdot 10^9$.

3.6.3 Neutral pion multiplicity

Finally, the numbers of neutral pions measured in $p+p$ and $n+p$ reactions are:

$$N_{\pi^0}|_{pp} = \frac{\sigma_{\pi^0}}{\sigma_{\text{elastic}}} \cdot N_{\text{elastic}}|_{pp} \cdot F_{\text{M3}} = \frac{4.45}{22.1} \cdot 15.7 \cdot 10^9 = 3.2 \cdot 10^9, \quad (3.31)$$

$$N_{\pi^0}|_{np} = \frac{\sigma_{\pi^0}}{\sigma_{\text{elastic}}} \cdot N_{\text{elastic}}|_{np} \cdot F_{\text{FW}} = \frac{8.56}{22.1} \cdot 6.23 \cdot 10^9 = 2.4 \cdot 10^9, \quad (3.32)$$

where 4.45 mb and 8.56 mb are the cross sections for π^0 measured in $p+p$ and $n+p$ reactions (see section 3.6.1), 22.1 mb is the elastic cross section from [45].

The final di-electron spectra can be presented in two ways: normalized to the number of neutral pions ($1/N_{\pi^0} dN/dM_{ee}$) or in absolute cross sections ($d\sigma/dM_{ee}$). In the second case σ_{π^0} in Eq. 3.31 and 3.32 is not included for the normalization factor.

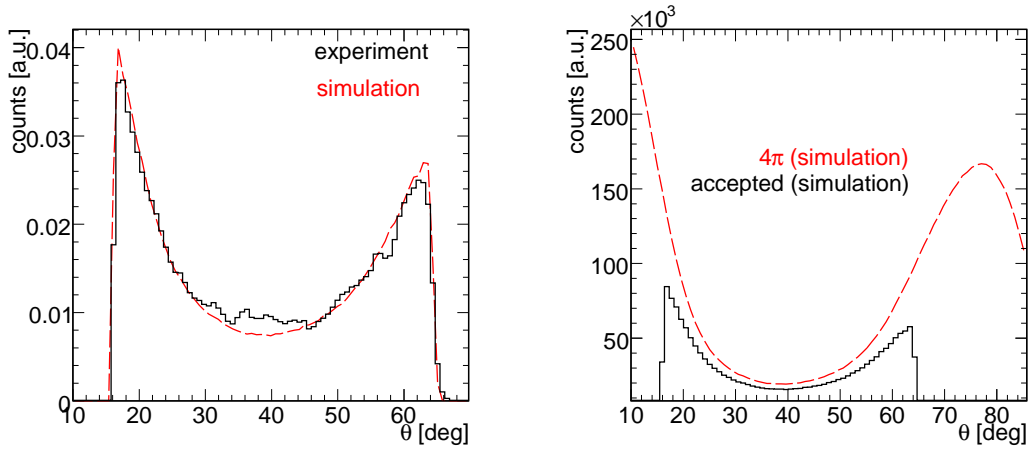


Figure 3.28: Left: Comparison of θ (polar angle) distribution of measured efficiency corrected (black solid line) and simulated (dashed red line) elastic pp pairs. Right: θ distribution of elastic pairs in 4π (red dashed line) and in the HADES acceptance (black solid line).

3.7 Determination of systematical uncertainties

There are several sources for systematic errors for the determination of yields and kinematic distributions for di-electrons. The various contributions to the total systematic uncertainty, which are summarized in Table 3.4, are described in the following. One main source of the total systematic errors is the uncertainties caused by the electron/positron efficiency correction. The introduced systematic error due to the efficiency correction procedure is $\sigma_{\text{eff.corr.}} = \pm 20\%$ [116, 117]. Another prominent source of the systematic errors come from the uncertainty in the pp elastic scattering efficiency and acceptance corrections ($\sigma_{pp \text{ elastic acc. corr.}} = \pm 10\%$).

Additional 20% error comes from the uncertainty due to the knowledge of the π^0 cross section in the dominant process $pp \rightarrow pp\pi^0$. The π^0 production cross section in $p+p$ reactions at a kinetic beam energy of 1.25 GeV is found to be $\sigma_{\pi^0} = 4$ mb within the resonance model [24] (see Fig. 3.29, left panel), and $\sigma_{\pi^0} = 5$ mb when using a fit of the experimental data by a series of generalized Laguerre polynomials insuring a correct threshold behaviour of individual reactions [25] (see Fig. 3.29, right panel). This contribution to the total systematic uncertainty, however, has to be taken into account only if the normalization to the π^0 yield is performed.

As it was discussed in section 3.4.1 the same-event like-sign method to estimate the combinatorial background has been used. Thus, no additional source of systematic errors due to the background estimation is introduced.

The systematic errors described above are independent from each other and have been added quadratically to estimate the total systematical error, which is (without π^0 cross section) $\sigma_{\text{sys.}}^{\text{tot}} = \sqrt{(\sigma_{\text{eff.corr.}})^2 + (\sigma_{pp \text{ elastic acc. corr.}})^2} = 22\%$, and including the error due to the π^0

Systematic uncertainty component	$p+p$	$n+p$
efficiency correction	$\pm 20\%$	$\pm 20\%$
π^0 cross section	+20%	+20%
acceptance correction (pp elastic reactions)	$\pm 10\%$	$\pm 10\%$

Table 3.4: Systematic uncertainties of the dilepton yield due to different sources.

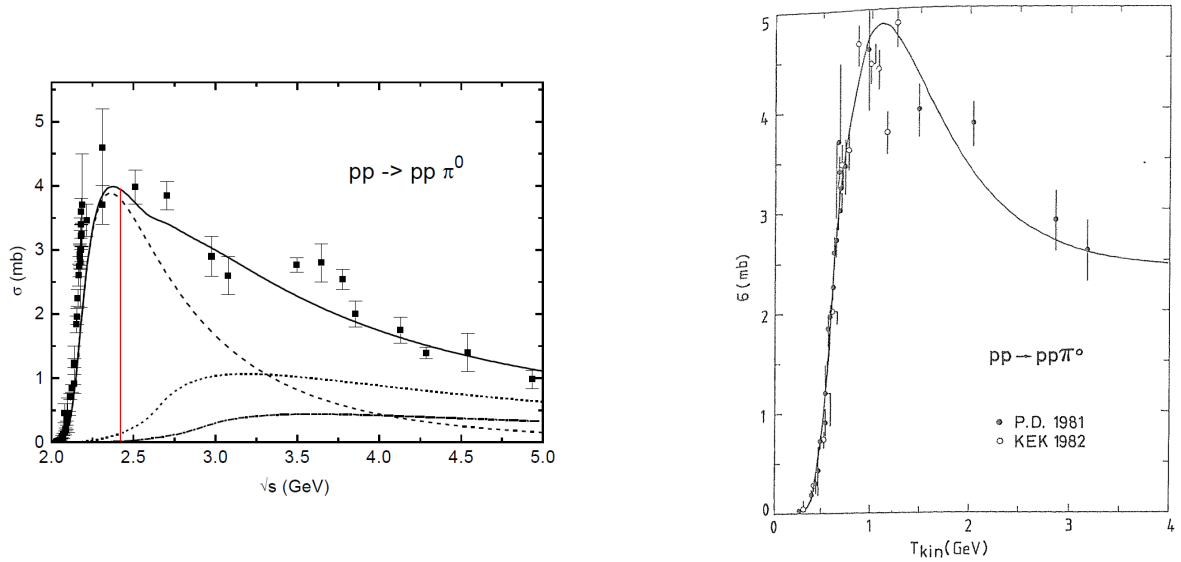


Figure 3.29: The fitted $1\pi^0$ -production cross sections (solid line) in comparison to the data [23]. Left: Resonance model [24], right: parametrization based on generalized Laguerre polynomials [25] in comparison to the data [26, 27].

cross section $\sigma_{\text{sys.}}^{\text{tot}} = \sqrt{(\sigma_{\text{eff. corr.}})^2 + (\sigma_{\text{pp elastic acc. corr.}})^2 + (\sigma_{\pi^0 \text{ cross section}})^2} = 30\%$. These errors are applied to the whole di-electron mass range.

3.8 The HADES acceptance

Experimental efficiency corrected distributions can be compared to a theoretical di-electron cocktail processed with the HADES acceptance and smeared with a realistic momentum and angular detector resolution. The acceptance matrices are created in the same way as the efficiency correction matrices (see section 3.5.1).

For the later discussion (see section 4.6.2) we compare the acceptance for leptons from heavy-ion collisions ($C+C$) to dileptons from elementary reactions ($p+p$, $n+p$). HADES measured $C+C$ and $p+p$, $n+p$ reactions at 1 and 1.25 GeV/ u . All sets of measurements were done with a reduced magnetic field (72% of its nominal value). A cylindrical target made of ^{nat}C was used for $C+C$ data (4.5 mm long and 6.5 mm diameter). The position of the target is an important issue when the acceptance is discussed. Figure 3.30 shows the target position in polar angle and reconstructed vertex z coordinate for the final lepton sample (e.g. all reconstruction, identification and background rejection cuts applied). The positions of the interaction points versus polar angle (θ) are very similar and no bias from here is expected.

Figures 3.31 and 3.32 show the geometrical acceptance for electrons and positrons, respectively, versus momentum, azimuthal, and polar angles. The difference in the single lepton acceptance is 15% (higher for $C+C$ data compared to the $p+p$ data due to the different beam energies), which makes 28% difference in the pair acceptance. This difference has to be taken into account when a comparison between $C+C$ and $p+p$, $n+p$ data is performed.

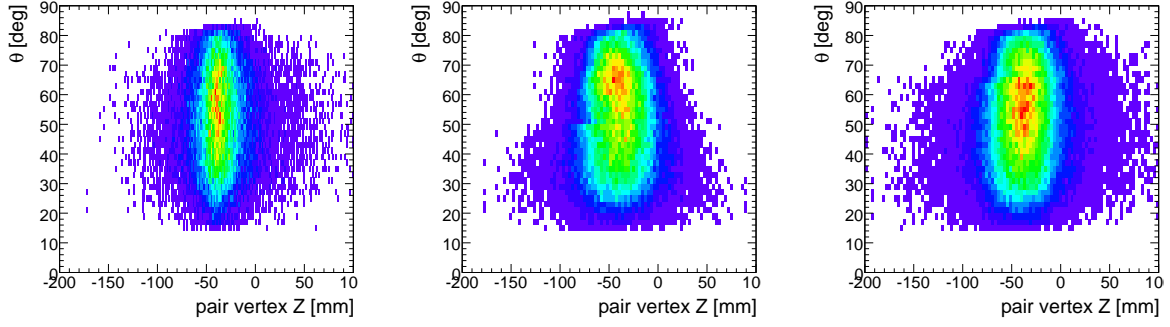


Figure 3.30: The polar angle as a function of the reconstructed vertex z of the e^+e^- pairs after all background rejection cuts. Left: $C+C$ data, middle panel: $p+p$ data, right: $n+p$ data.

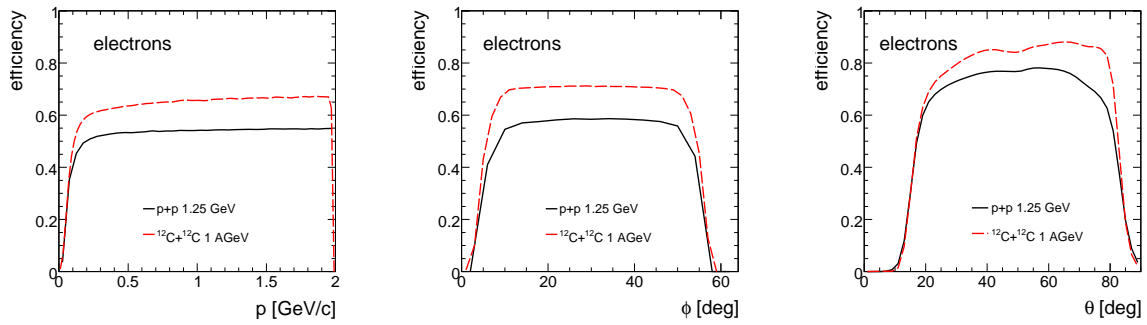


Figure 3.31: Comparison of the geometrical acceptance for electrons in $C+C$ collisions at $1 \text{ GeV}/u$ and $p+p$ interactions at 1.25 GeV as a function of momentum (left), azimuthal angle (middle, only one sector is shown), polar angle (right panel). Dashed red line: $C+C$ system, black line: $p+p$ system.

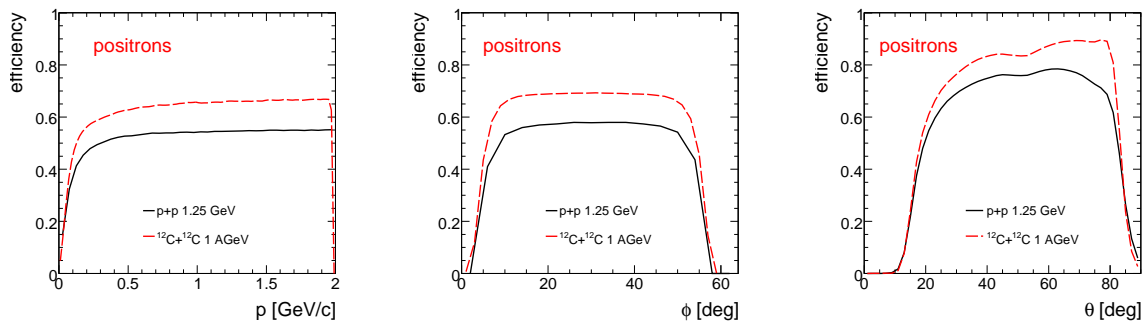


Figure 3.32: Comparison of the geometrical acceptance for positrons in $C+C$ collisions at $1 \text{ GeV}/u$ and $p+p$ interactions at 1.25 GeV as a function of momentum (left), azimuthal angle (middle, only one sector is shown), polar angle (right panel). Dashed red line: $C+C$ system, black line: $p+p$ system.

Chapter 4

Results and discussion

4.1 Invariant mass spectra

The di-electron yield measured in HADES was corrected for detection and reconstruction efficiencies (see section 3.5.1). Figure 8.1 shows the resulting e^+e^- invariant-mass distributions after background subtraction of true pairs normalized to the number of pp elastic scattering events measured in HADES and extrapolated to the full solid angle (see section 3.6). The error bars on each data point indicate the statistical and systematic uncertainties. The total statistics of signal pairs entering the mass spectrum of Fig. 8.1 ($p+p$ reactions, left panel) amounts to 3.8×10^4 and corresponds to 2.8×10^9 accepted LVL1 triggers. Approximately 350 signal pairs contribute to the mass region above the π^0 Dalitz mass ($M_{ee} > 0.15 \text{ GeV}/c^2$). The numbers for $n+p$ reactions Fig. 8.1 (right panel) are 3.6×10^4 and 1454, respectively, and correspond to 4.04×10^9 accepted LVL1 triggers.

As can be seen from the spectra, the di-electron yield in the π^0 Dalitz region is a factor of two larger in the $n+p$ case compared to the $p+p$ case. This is readily explained by assuming

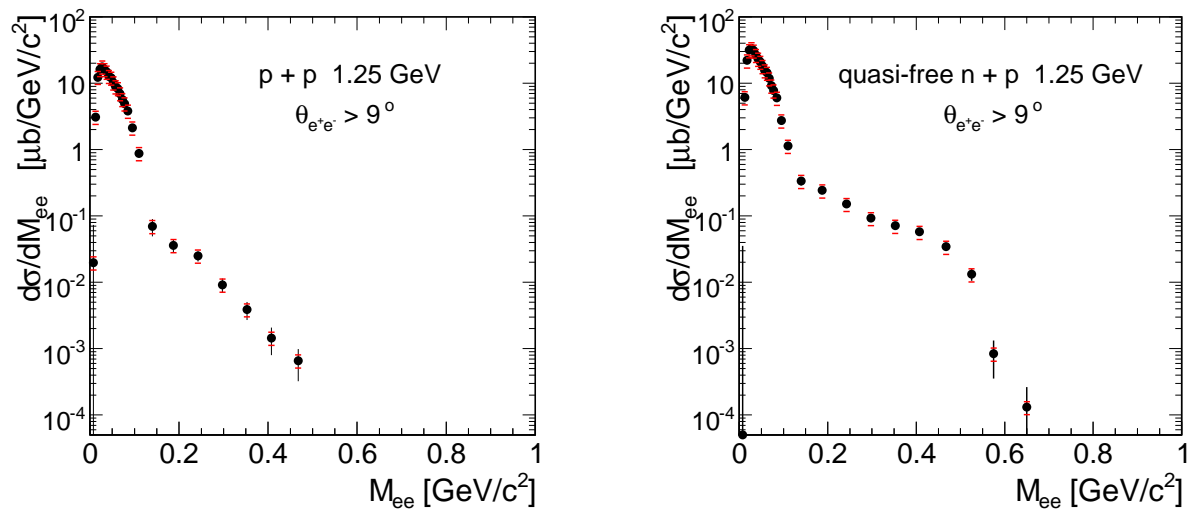


Figure 4.1: Invariant mass distribution of e^+e^- pairs measured within the detector acceptance for $p+p$ (left panel) and $n+p$ (right panel) interactions at a beam energy of 1.25 GeV/u. Statistical errors are shown with bars, systematic by horizontal lines.

a dominance of the Δ resonance in the pion production as it is demonstrated by the success of the resonance model [24], describing respective data very well. In $n+p$ reactions there are two intermediate Δ isospin states (Δ^+ and Δ^0) contributing to neutral pion production while for $p+p$ only the Δ^+ excitations can contribute (see Appendix A). Assuming Δ resonances as source of the pions and using the isospin selection rules of above one can show that $\sigma_{\pi^0}^{pp} = 0.5 \cdot \sigma_{\pi^0}^{np}$. This results agrees with our analysis and justifies the normalization procedure.

The shape of the mass spectra changes dramatically when going from $p+p$ to $n+p$ reactions. First of all, the $p+p$ mass spectrum is much steeper than the one for $n+p$, which can be partially explained by the smaller available energy in the proton-proton system. In $d+p$ reactions the neutron momentum distribution in the deuteron can increase the n energy somewhat. It has been checked, however, that the shape of the mass spectrum for $n+p$ does not change when a condition is put on the emission angle of the forward spectator proton, i.e. when the emission is restricted to $\theta < 2^\circ$ instead of the full acceptance of the Forward hodoscope Wall of $\theta < 7^\circ$. A more precise investigation of such effects would be possible, if HADES would provide a magnetic spectrometer under forward angles. Since this is not the case, momentum measurement is possible through time-of-flight and position only, given rise to a moderate resolution. Nevertheless, the dilepton cross section in the mass region above $0.15 \text{ GeV}/c^2$ in $n+p$ reactions has a different mass dependence and is nearly an order of magnitude larger than in $p+p$ reactions.

4.2 Transverse momentum and rapidity spectra

The transverse momentum (p_t) and laboratory rapidity (y) of the parent virtual photon can also be reconstructed from the measured four momenta of the electron pairs. Transverse momentum spectra normalized to N_{π^0} for pairs in the acceptance are shown in Fig. 4.2. The p_t spectra for

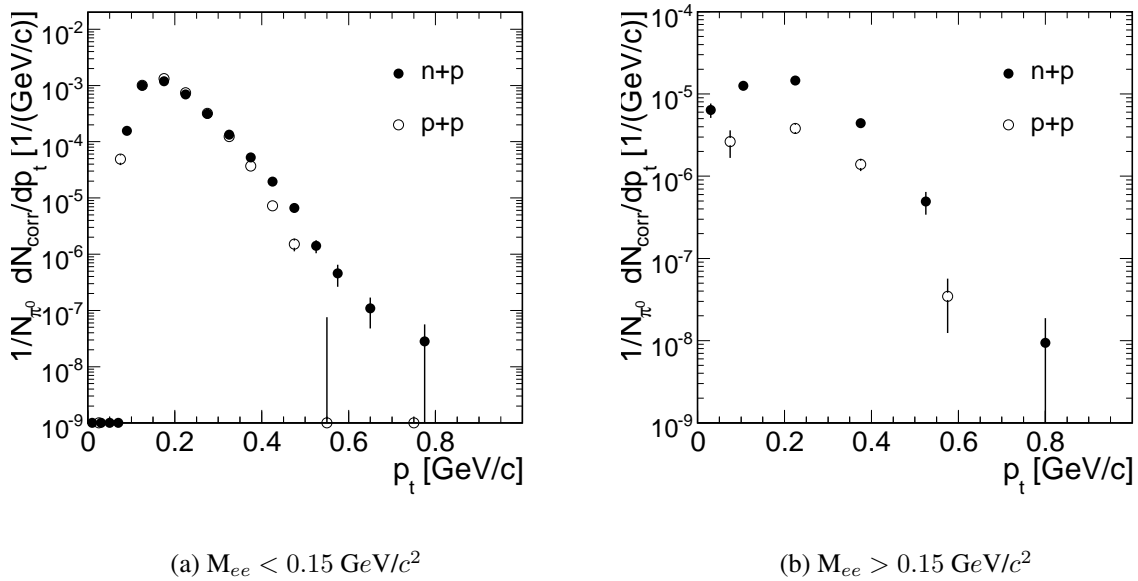


Figure 4.2: Transverse momentum distributions of the signal e^+e^- pairs measured in $p+p$ and $n+p$ interactions at a beam energy of $1.25 \text{ GeV}/u$. Open circle: $p+p$ system, filled circle: $n+p$ system.

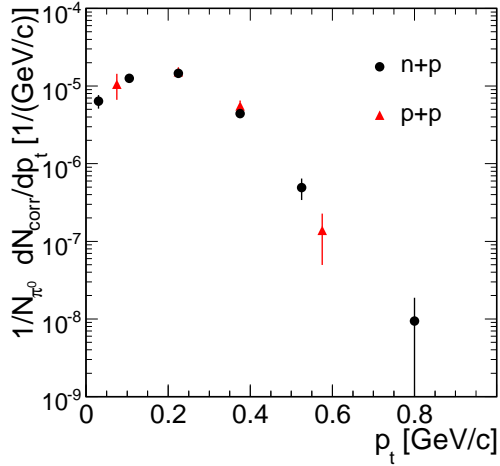
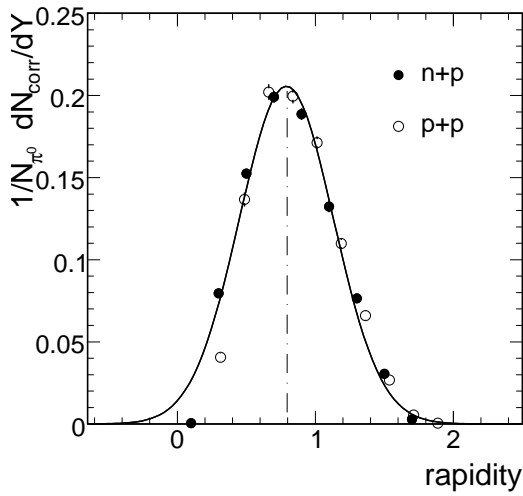
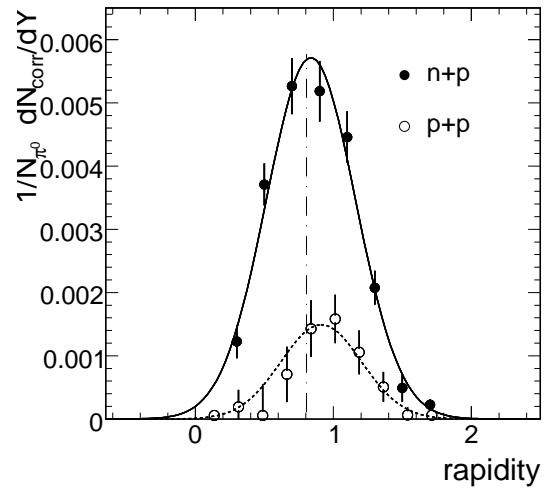


Figure 4.3: Transverse momentum distributions of the signal e^+e^- pairs measured in $p+p$ and $n+p$ interactions at a beam energy of 1.25 GeV/u for the invariant mass region $M_{ee} > 0.15$ GeV/c². Red triangle: $p+p$ system scaled by factor of 4, filled circle: $n+p$ system.



(a) $M_{ee} < 0.15$ GeV/c²



(b) $M_{ee} > 0.15$ GeV/c²

Figure 4.4: Rapidity distributions of the signal e^+e^- pairs measured in $p+p$ and $n+p$ interactions at a beam energy of 1.25 GeV/u. Open circle: $p+p$ system, filled circle: $n+p$ system. Vertical dashed-dotted line shows midrapidity. Solid lines are Gaussian fits to the data.

masses less than 0.15 GeV/c² are dominated by the contribution from π^0 Dalitz decay. The shape of the $p+p$ transverse momentum distributions deviates slightly from the $n+p$ spectrum for higher transverse momenta. This is attributed to slight acceptance differences for very large emission angles, which affects in particular the acceptance in the phase space region populated by pairs with small invariant masses (i.e. small opening angles) and large transverse momentum. In the low p_t region, where more than 99% of the statistics is located, the shape is identical as to be expected if dominated by π^0 Dalitz decay. The transverse momentum distributions for the high-mass bin are nearly identical. To allow for a better comparison, the p_t distribution for the $p+p$ system was scaled by a factor of four in Fig. 4.3 and overlaid to the spectrum for $n+p$ reactions. As can be seen, the data points fall on top of each other within statistical errors. At transverse momenta above 0.4 GeV/c the statistics for the $p+p$ data is limited and conclusions concerning the slopes cannot be drawn.

The laboratory rapidity distribution of the di-electron yield for the two mass regions defined above is shown in Fig. 4.4. Both spectra are normalized to the respective number of π^0 . The position of the dashed dotted line indicates midrapidity. As it was the case for the transverse momentum spectra, the shapes of the rapidity spectra for $n+p$ and $p+p$ collisions are very similar. The rapidity distributions for the invariant mass region $M_{ee} < 0.15 \text{ GeV}/c^2$ (dominated by π^0 Dalitz decay) are well described by a Gaussian distribution with the width which is 0.34 for both, $p+p$ and $n+p$ collisions, but note the slight difference in the region of highest backward rapidity also pointing to differences in acceptance. The distributions peak at midrapidity. For the invariant mass region $M_{ee} > 0.15 \text{ GeV}/c^2$ the width amounts to 0.32 units of rapidity for both systems with a slight shift towards higher rapidity. The fitted Gaussian distributions peak at 0.93 and 0.84 units of rapidity for the $p+p$ and $n+p$ systems, respectively.

4.3 Comparison to the DLS results

*If the facts don't fit the theory,
change the facts.
(Albert Einstein)*

The Di-Lepton Spectrometer (DLS) at the Lawrence Berkeley National Laboratory Bevatron was a two-arm magnetic dipole spectrometer, and is described in Ref. [131]. Electrons were discriminated from hadrons using two arrays of threshold Cherenkov gas radiators coupled to photo tubes. In each arm, one stack of counters was placed upstream of the dipole field and a second stack downstream of the field. The momenta of the electrons were derived by reconstructing their paths through the magnetic field using space points from three drift chambers in each arm, one before and two behind the dipole fields. Proton beams were provided by the Bevatron with kinetic beam energies of 1.04, 1.27, 1.61, 1.85, 2.09, and 4.88 GeV. Figure 4.5 (left panel), shows a comparison of the total cross sections of dilepton production measured by DLS in $p+p$ collisions at a beam energy of 1.04 GeV with theoretical model calculations. It can be seen that the cross section derived by Kaptari *et al.* [34] overestimates the DLS data for masses below $0.3 \text{ GeV}/c^2$ while the cross section calculated by the Shyam *et al.* [20] underestimates the DLS data for masses above $0.3 \text{ GeV}/c^2$. It is evident that data of higher statistics would be needed in order to distinguish between the models. A direct comparison of the HADES with the DLS results is not straight forward. The geometrical acceptances of the two spectrometer are quite different in particular as much as small momenta are of concern. Moreover, the geometry of the two-arm setup of DLS and together with the trigger condition (coincident leptons in both arms) used in experiments allowed to measure electron pairs only in a very specific phase space region. A comprehensive method to compare the $C+C$ data sets of DLS and HADES was developed by the HADES Collaboration [3, 117]. It is realized by a direct mapping of the di-electron yield observed with HADES and extrapolated into phase space regions not covered into the DLS acceptance. However, the very poor statistics of the electron pairs measured in elementary reactions does not favor using the method applied for heavy-ion data. In order to compare the $p+p$ data set of HADES to DLS the following filter was applied to the HADES data: the geometry of the DLS spectrometer is such that only pairs with an opening angle larger than 40 degrees can be accepted. From the published DLS data [132] one can see that only the rapidity region $y > 0.6$ is covered. For comparison, these two cuts were applied to the HADES

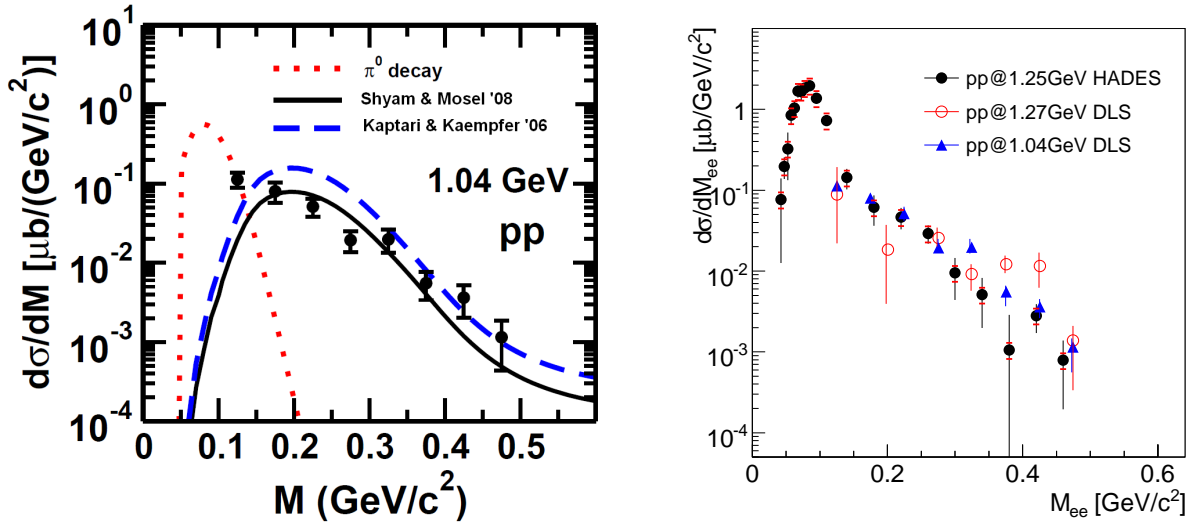


Figure 4.5: Left: The di-electron invariant mass distribution from DLS [1] for $p+p$ collision at a beam energy of 1.04 GeV in comparison to model calculations [20]. Right: Invariant mass distribution of measured e^+e^- pairs. Black circles: HADES data for $p+p$ at 1.25 GeV, open red circles: DLS data for $p+p$ at 1.27 GeV, blue triangles: DLS data for $p+p$ at 1.04 GeV.

data as well. These restricted HADES data can then be directly compared to the published $d\sigma/dM$ distributions from DLS [132]) assuming HADES pair acceptance at high M_{ee} and high p_t is 30%. The result is given in Fig. 4.5 (right panel). Within statistical and systematical errors, the HADES and the DLS data are in good agreement.

This results is not surprising since agreement between DLS and HADES was already demonstrated before for $C+C$ collisions at 1 GeV/u. However, surprising is that the model calculations so far were not able to satisfactorily describe the DLS data for elementary reactions as well as for heavy-ion collisions. It will be interesting to compare the calculations with the new data, which has in particular a good coverage in the π_0 Dalitz region, and see whether HADES provides a solution to this "theory puzzle" (see section 4.5).

4.4 $p + p$ and $n + p$ data in transport model calculations

Obviously, it is not a trivial task to interpret the di-electron data at SIS/Bevalac energies. The difficulties come from the non-equilibrium nature of all reactions. Transport models have to incorporate all the various sources that contribute to the experimental spectra. In order to compare our results to theoretical descriptions, di-electrons obtained by the HSD¹ and the IQMD [82] transport models were filtered with the HADES acceptance and normalized to the respective π^0 multiplicity. Figure 4.6 shows examples of the inclusive di-electron invariant mass distribution obtained in $p+p$ collisions at a beam energy of $E_{kin} = 1.25$ GeV together with transport model calculations. The data are compared with the HSD transport calculations performed by Bratkovskaya *et al.* [98] (see Fig. 4.6, left panel) and results of IQMD transport calculations performed by Aichelin *et al.* [133] (see Fig. 4.6, right panel). At low masses a prominent $\pi^0 \rightarrow e^+e^-\gamma$ peak dominates the spectra. In the intermediate-mass region Dalitz decays of $\Delta \rightarrow Ne^+e^-$ and NN bremsstrahlung are the major sources. The HSD model reproduce the $p+p$ experimental data in the whole mass range quite well. The IQMD model can reproduce

¹HSD version from October 2007 including NN bremsstrahlung á-la Kaptari *et al.* is used here

the shape of the $p+p$ mass spectra, however, has a problem with the overall normalization on the a 40% level in the whole mass range. It is also seen that the relative contributions of individual components like from Δ Dalitz decay and NN bremsstrahlung are very different in these models. The situation becomes more difficult for the $n+p$ data. Figure 4.7 shows examples of inclusive di-electron invariant mass distributions obtained in $n+p$ collisions at a beam energy $E_{kin} = 1.25$ GeV together with the transport model calculations introduced above. The effect of the neutron momentum distribution in the deuteron is included in the HSD and IQMD calculations for $d+p$ reactions without selection of the $n+p$ channel. One should point out that the experimental spectator proton mechanism is not fully implemented in these calculations. Nevertheless, this first comparison shows that both models fail in reproducing the $n+p$ data in the mass region above the π^0 Dalitz decay range. Again, the contribution of individual sources

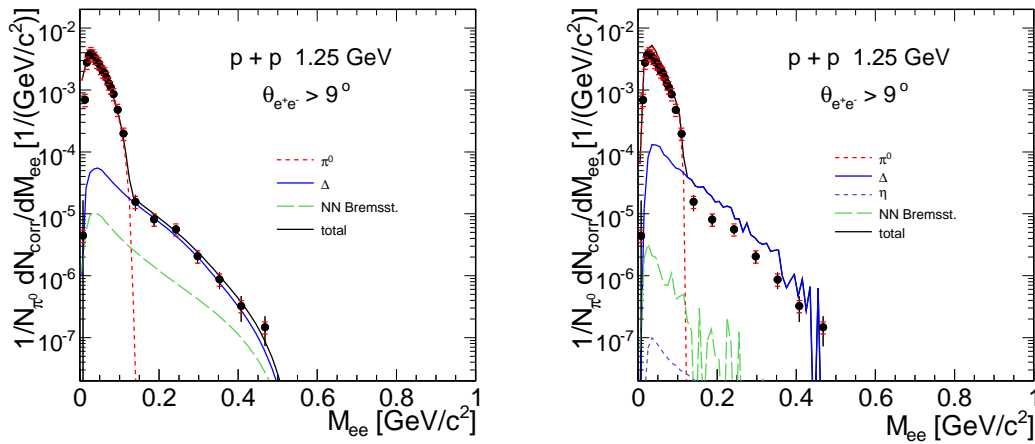


Figure 4.6: Invariant mass distribution of e^+e^- pairs measured in $p+p$ interactions at a beam energy of 1.25 GeV compared with HSD (left panel) and IQMD (right panel) transport model calculations. Dashed-dotted line: π^0 Dalitz, red solid line: Δ^+ Dalitz, green dashed line: NN bremsstrahlung, black solid line: total cocktail.

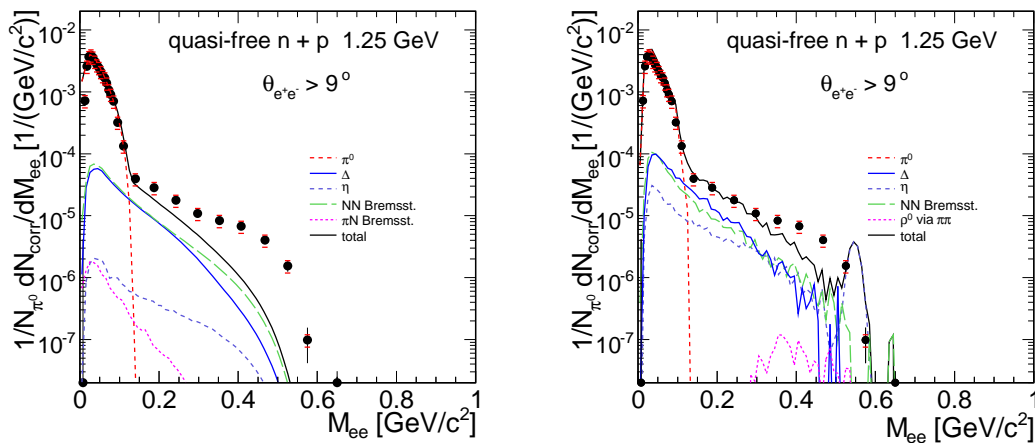


Figure 4.7: Invariant mass distribution of e^+e^- pairs measured in $d+p$ interactions at a beam energy of 1.25 GeV/u compared with HSD (left panel) and IQMD (right panel) transport model calculations. Dashed-dotted line: π^0 Dalitz, red solid line: $\Delta^{+,0}$ Dalitz, green dashed line: NN bremsstrahlung, blue dashed line: η . Dashed magenta line: HSD - πN bremsstrahlung, IQMD - ρ meson production via $\pi\pi$ annihilation. Black solid line: total cocktail.

differs by factors between the models. The high data quality clearly shows beyond errors that something is still missing in the transport calculations. A possible answer will be given in section 4.6.2.

4.5 $p+p$ and $n+p$ data in Pluto

Simulations are an integral part of the experimental program associated with scattering experiments and particle accelerators. The Pluto package [126] is a generic event generator which has numerous elementary production mechanisms and hadronic as well as (semi-)leptonic decay built in. Moreover, it allows also to simulate heavy-ion induced reactions by using a fireball model (thermalized source) and tabulated production cross sections. The development of PLUTO was mainly motivated by the physics program of the HADES experiment and should serve to provide reference spectra based on experimental information to the largest extent possible. Recent developments of the Pluto event generator were triggered by ongoing discussions about the role of the virtual nucleon-nucleon bremsstrahlung ($NN \rightarrow \gamma^* NN$) in di-electron production in heavy-ion and elementary collisions at kinetic beam energies of 1 – 2 GeV/u Ref. [134]. Particular attention was paid to the mass-dependent branching ratio of the Δ resonance. It is very essential to properly model the yield and the spectral slope of the dileptons emerging from Δ Dalitz decay. Here is a short summary of what has been used to generate the di-electron cocktail in Pluto.

π^0 **MESON**: The yield of the π^0 Dalitz decay is taken from the experimentally known cross sections of the π^0 [25] (see also section 3.6.1) and the $\pi^0 \rightarrow \gamma^* \gamma \rightarrow e^+ e^- \gamma$ branching ratio is taken to be (BR= 1.2%) [45].

$\Delta(1232)$ **RESONANCE**: Following the usual Ansatz discussed in Ref. [24], a relativistic form of the Breit-Wigner distribution has been used. For the Dalitz decay $\Delta \rightarrow N \gamma^* \rightarrow N e^+ e^-$, the mass-dependence of the width is calculated from the matrix element extracted from Ref. [135]. The decay rate is taken from Krivoruchenko *et al.* [93]. The electromagnetic form factor is exchangeable for each decay (Dipole fit, VMD²) mode individually. The dipole fit description follows the approach from Ref. [93]. As expected from the decay $\Delta \rightarrow N \gamma$, the magnetic transition plays the dominant role. Therefore we use the magnetic transition form factor $G_M = 3$, and electric and Coulomb transition form factors $G_E = G_C = 0$. The branching ratio at the pole mass of the Δ of BR($\Delta \rightarrow N e^+ e^-$) is calculated and it found to be 4.19×10^{-5} . This branching ratio is consistent with the photon decay times the electromagnetic coupling constant α (which would result in BR = 4.01×10^{-5}) for the conversion of the virtual photon into a electron pair. In the Dalitz decays of nucleon resonances, the VMD model is usually applied for the description of the resonance transition form factors. The two-component Iachello [136, 137] VMD Δ form factor has been implemented in Pluto. The Δ decays proceed exclusively through the ρ -meson. Differences between the dipole fit and the VMD approach are expected to become visible in the higher mass region, i.e. for ($M_{ee} > 0.3$ GeV/ c^2).

SUB-THRESHOLD η PRODUCTION: Here, the neutron momentum distribution in the deuteron is taken into account for the $d+p$ reaction. The first measurement of the cross section of the quasi-free $pn \rightarrow pn\eta$ reactions has been carried out at the CELSIUS storage ring using a deuterium internal cluster jet target [28]. Figure 4.8 shows the extracted energy dependence of the quasi-free $pn \rightarrow pn\eta$ cross sections, together with data on other η production channels,

²Vector Meson Dominance

both free and quasi-free, as a function of the center-of-mass energy. A parametrization of these measurements is implemented in Pluto.

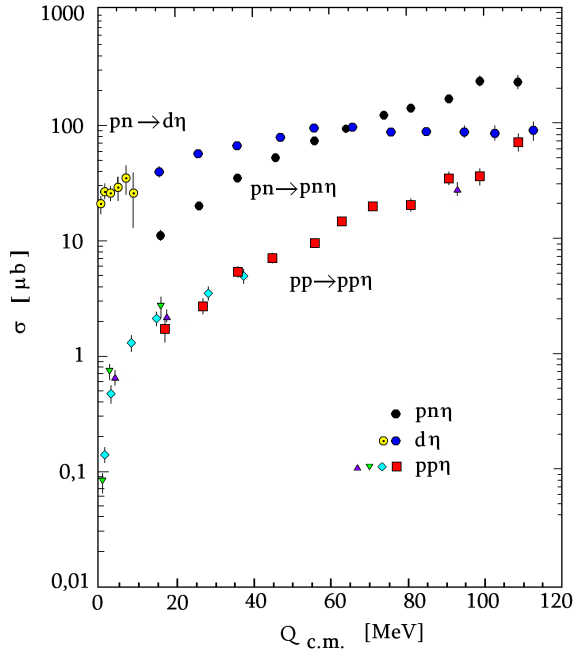


Figure 4.8: Total cross sections for the quasi-free $pn \rightarrow pn\eta$ reaction together with other free and quasi-free $p+N$ reactions as a function of the center-of-mass energy. The errors shown are statistical only. Black circles: $pn \rightarrow pn\eta$ channel Ref. [28], yellow and blue circles: $pn \rightarrow d\eta$ channel Refs. [29, 30], violet triangle, inverse green triangle, blue square and red square: $pp \rightarrow pp\eta$ channel Ref. [31, 32, 33, 29].

NN BREMSSTRAHLUNG: Since numerical values for the OBE³ calculations from Kaptari *et al.* are not available but only published spectra, the calculated cross sections were digitized for different energies and a parametrization of all channels, i.e. elastic, inelastic and coherent production, were implemented in Pluto. These calculations include a prediction for the HADES $n+p$ and $p+p$ measurements. Figure 4.9 shows the comparison of the results from the parametrization as implemented in Pluto with the original calculations from Ref. [34]. Solid lines represent the total cross section including all interferences. One can see that the two calculations agree perfectly. The same is true for quasi-free $n+p$ reactions.

FINAL STATE INTERACTIONS (FSI): When discussing near-threshold vector meson production in NN reactions final state interactions (FSI) between nucleons play an important role for the total cross section and for the population of the phase space. With increasing di-electron mass, the kinematical range of excitation energy shrinks so that FSI effects are expected to increase. The effect of the FSI is already included in all cases where the total cross section is taken from measured data. The FSI in the OBE framework is based on the inverse Jost function formalism Ref. [138], which provides a good description of NN interaction and phase shifts at low relative momenta and has also been introduced in Pluto.

Now the results of the Pluto model are filtered with the HADES acceptance and directly compared to the measured data. Figure 4.10 shows a comparison of the di-electron cocktail generated with Pluto with measured $p+p$ and $n+p$ data. The $p+p$ data can be described by the incoherent sum of the π^0 , Δ á-la Krivoruchenko (dipole fit) and NN bremsstrahlung á-la Kaptari. In comparison to the HSD less Δ , more NN bremsstrahlung have been observed, although the same cross sections are used. On the other hand, the di-electron cocktail composed from the π^0 and Δ Dalitz decays, when the Δ electromagnetic transition form factor is calculated using the VMD, also good description for $p+p$ data (see Fig. 4.12, left panel). If one would add to this cocktail the NN bremsstrahlung contribution, it will overestimate the

³One Boson Exchange model

data. The η contribution becomes important for the di-electron production in $n+p$ reactions. However, adding only the η component to the di-electron cocktail is not enough to describe the experimental data. In comparison to the HSD we have less Δ , the same amount of NN bremsstrahlung, and more η -meson. Recently, the HSD transport model has also included η production cross sections from [29], and now contribution of the η component is consistent to one used in our Pluto cocktail. The $n+p$ data clearly exhibit further additional sources. Before we discuss them, let us clarify the situation with the other components, i.e. Δ Dalitz decay and NN bremsstrahlung.

As the NN bremsstrahlung process as included in the new OBE calculations from Kaptari *et al.* [34] is widely discussed in context with the interpretation of the $C+C$ data, we have a closer look on the comparison of these calculations to the HADES data for $p+p$ and $n+p$ in-

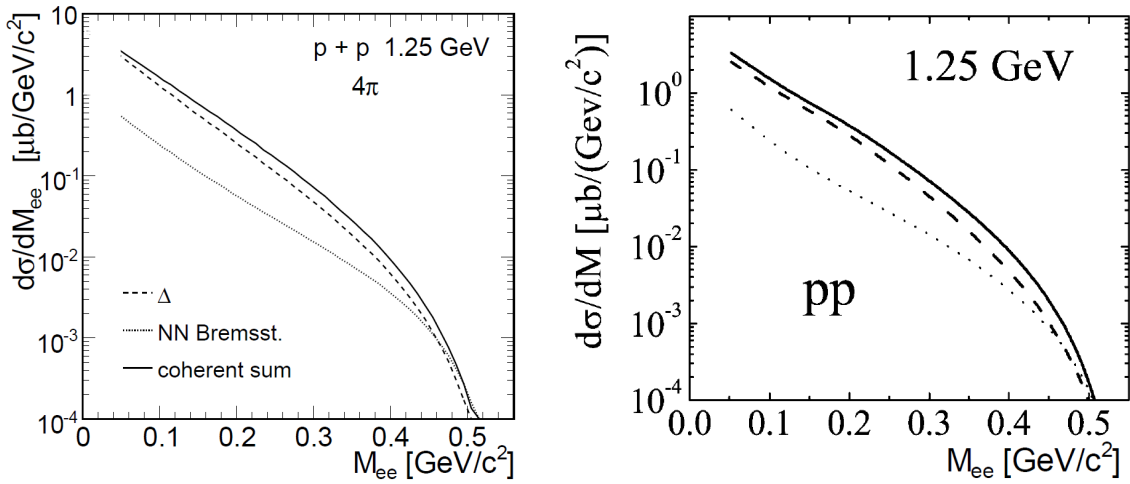


Figure 4.9: Invariant mass distribution of e^+e^- pairs in proton-proton collisions: the dashed (dotted) curves depict the contribution of diagrams with bremsstrahlung from $\gamma\Delta N$ (γNN) vertices. The solid lines are the results of calculations of the total cross section as coherent sum of nucleon and Δ contributions. Left: Pluto parametrization, right: picture from Ref. [34].

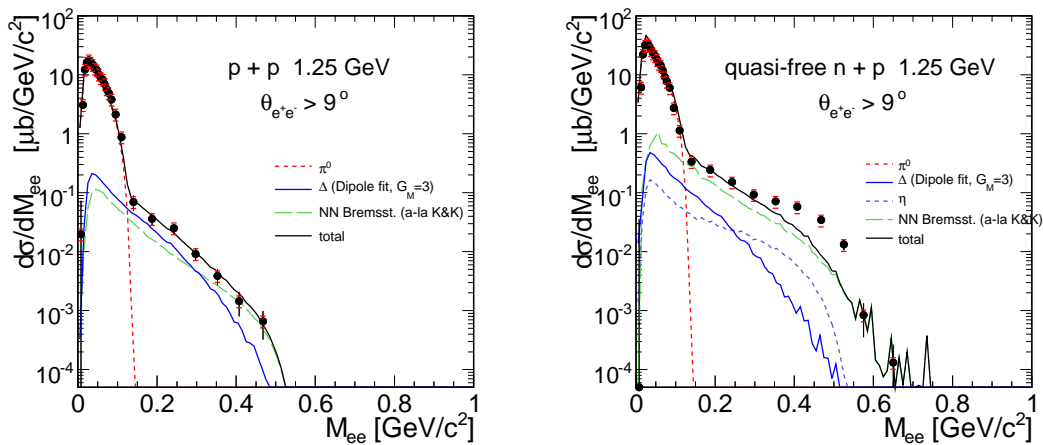


Figure 4.10: Invariant e^+e^- mass distribution measured in $p+p$ (left panel) and $n+p$ (right panel) interactions at a beam energy of 1.25 GeV/u. Blue dashed-dotted line: π^0 Dalitz decay, red solid line: Δ Dalitz decay (dipole fit, $G_M = 3$), green dashed line: NN bremsstrahlung component á-la Kaptari *et al.*, blue dashed line: η -meson, black solid line: total incoherent cocktail.

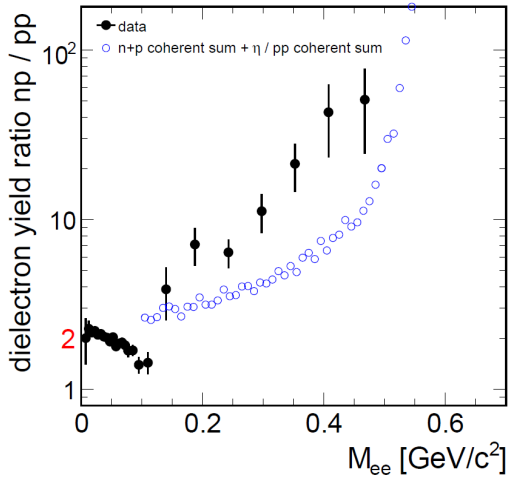


Figure 4.11: The di-electron yield ratio as a function of invariant mass measured in $n+p$ and $p+p$ interactions at 1.25 GeV/u kinetic beam energy with the prediction for HADES. Black solid circle: data, blue open circles: $(\sigma^{np} + \sigma^\eta)/\sigma^{pp}$ from Kaptari *et al.* [34].

teractions. Thus, we compare the above discussed results of the OBE model from Kaptari *et al.* with the HADES data. The well known η contribution ($pn \rightarrow pn\eta$ and $pn \rightarrow d\eta$) was added to the coherent sum from these OBE calculations. Figure 4.11 shows a comparison of the di-electron yield ratio as a function of invariant mass measured in $n+p$ and $p+p$ interactions at 1.25 GeV/u kinetic beam energy with the prediction for HADES. Only statistical uncertainties are included in the error bars in this figure. The general trend of the mass dependence of the $\sigma^{n+p}/\sigma^{p+p}$ ratio is reproduced by this theory, however the yield in the high-mass region is too low and in the π^0 region the di-electron yield is unfortunately not calculated.

As ratio plots can hide important information it is better to look at the individual spectra itself. In Fig. 4.12 the $p+p$ (left panel) and $n+p$ (right panel) data are compared to the coherent sum of all contributing terms (NN bremsstrahlung, Δ) in the OBE framework. One can clearly see that the theoretical curve does not describe the data, for $p+p$, already the Δ contribution of Kaptari *et al.* partially lies above the data. The Δ resonance contribution from Kaptari *et al.* is also compared to the one used in Pluto (Krivoruchenko *et al.* [93]). A factor of 2 – 4 difference

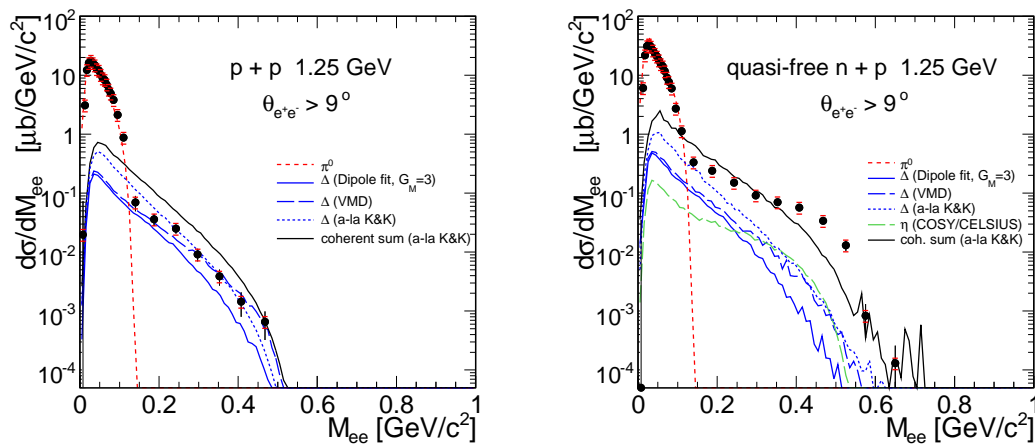


Figure 4.12: Invariant mass distribution of e^+e^- pairs measured in $p+p$ (left panel) and $n+p$ (right panel) interactions at a beam energy of 1.25 GeV/u. Blue dotted-dashed line: π^0 Dalitz, black solid line: coherent sum (NN bremsstrahlung, Δ) from Kaptari *et al.*, blue dashed line: Δ from Kaptari *et al.*, blue solid line: Δ from Krivoruchenko *et al.* (Dipole fit), blue (dotted) dashed line demonstrates the effect of including the Δ form factor from the VMD model.

is observed here. Also a factor of 2 – 4 was observed by Bratkovskaya *et al.* for the difference in the NN bremsstrahlung contribution from Kaptari *et al.* to the one previously used in HSD. For the new HSD calculations, the NN bremsstrahlung from Kaptari *et al.* is included in the transport model by simply scaling the NN bremsstrahlung amplitude by a factor of 4. We have seen, however, that in HSD the NN bremsstrahlung cross section is scaled only for $n+p$ reactions, not for $p+p$.

Our data for the invariant-mass spectrum in the reaction $np \rightarrow npe^+e^-$, extracted from the tagged subreaction in $dp \rightarrow p_{sp}npe^+e^-$, point to a shoulder at intermediate values of the di-electron invariant mass. Such a structure is hardly described within the hitherto calculations. As it has been shown, understanding the elementary channels remains challenging.

4.6 Possible avenues for understanding the experimental dilepton spectra from $p+p$ to $^{12}\text{C}+^{12}\text{C}$ collisions

*I am enough of an artist
to draw freely upon my imagination.
Imagination is more important than knowledge.
Knowledge is limited.
Imagination encircles the world.
(Albert Einstein)*

4.6.1 Experimental ansatz for understanding the di-electron production in NN interactions

The increase in the $\sigma^{n+p}/\sigma^{p+p}$ ratio (see Fig. 4.11) as a function of increasing mass can be partially attributed to the fact that the largest possible pair mass is higher for the $n+p$ system than for the $p+p$ system due to the additional neutron momentum distribution in the deuteron. Therefore, there has to be an enhancement in the $\sigma^{n+p}/\sigma^{p+p}$ ratio in the kinematical limit of $p+p$ reactions. It has been shown (see Fig. 4.10) that part of the enhanced di-electron yield measured in $n+p$ reactions can be explained by the η Dalitz decay contribution. The cross section for η production in the $n+p$ system is almost an order of magnitude higher than in the $p+p$ system near the η threshold. Figure 4.13 (left panel) demonstrates the difference between the di-electron yield measured in $n+p$ and $p+p$ interactions at 1.25 GeV/u. The spectra of $n+p$ and $p+p$ are subtracted from each other, in addition the η contribution was subtracted from the $n+p$ data using the CELCIUS measurement. As the spectra were normalized to N_{π^0} the factor 2 difference in the π^0 yield is naturally taken into account, and the drop of the di-electron yield to zero at the masses below 0.15 GeV/c² is just because of the π^0 subtraction. Our next step is model dependent. We subtract the contribution of NN bremsstrahlung from Kaptari *et al.* for both systems, $p+p$ and $n+p$ separately. These NN bremsstrahlung contributions were shown as they give the highest yield of all models discussed so far. Figure 4.13 (right panel) shows the result of this subtraction. We attribute the remaining excess to another mechanism, i.e. the Dalitz decay of higher-lying baryonic resonances as will be discussed in following. The numer-

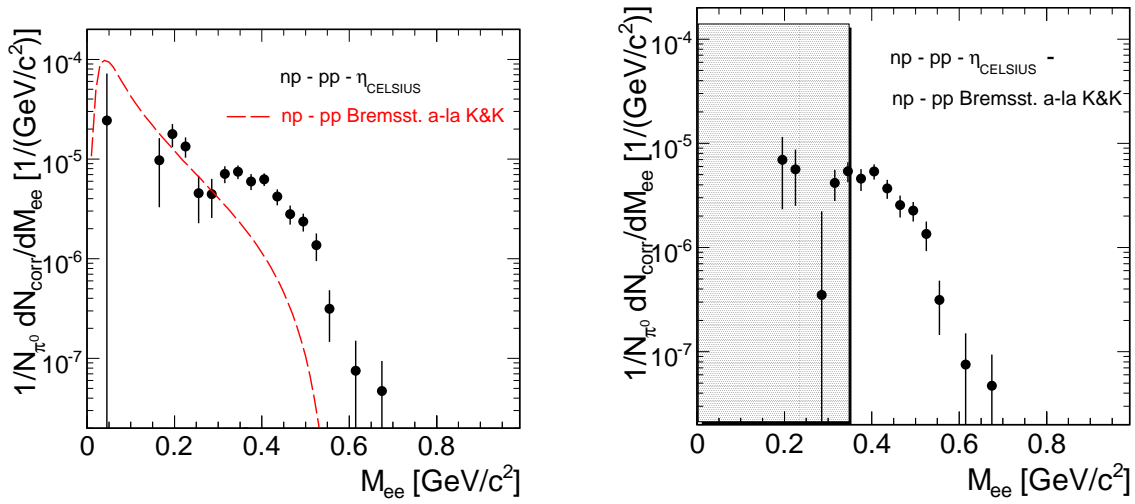


Figure 4.13: Left: Difference of the di-electron yield measured in $n+p$ and $p+p$ interactions at 1.25 GeV after subtraction of the η contribution from the $n+p$ data. Black circles: data, red dashed line: NN bremsstrahlung á-la Kaptari *et al.* Right: after subtraction of the NN bremsstrahlung contribution separately from each system, $p+p$ and $n+p$. The grey box shows the region where the $\Delta(1232)$ is still contributing to the di-electron spectrum.

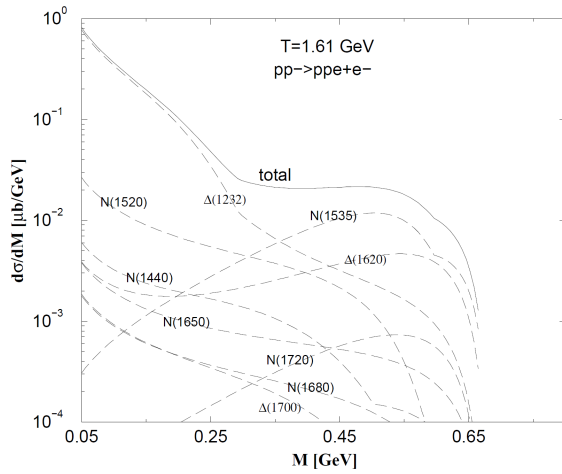


Figure 4.14: The dilepton production cross section $pp \rightarrow e^+e^-pp$ through the nucleon resonances Δ , N^* , and Δ^* at a kinetic beam energy of $E_{kin} = 1.61$ GeV [35].

ical results [35] demonstrate that besides the $\Delta(1232)$ resonance, the $N^*(1535)$, $N^*(1520)$ and $\Delta(1620)$ can have considerable contributions to the dilepton production. Figure 4.14 shows the resonance contributions for a proton kinetic energy of $E_{kin} = 1.61$ GeV. At moderate invariant masses $M_{ee} < 0.35$ GeV/ c^2 of the dilepton pair, the resonance contributions are dominated by the $\Delta(1232)$. At larger masses $M_{ee} > 0.35$ GeV/ c^2 , contributions from the heavier resonances become dominant. Our kinetic beam energy is only 1.25 GeV, therefore their contribution should be less in (there is not enough energy available), however, in $d+p$ collisions due to the contribution from the neutron momentum distribution in the deuteron it is possible to excite higher-lying baryonic resonances. It was conjectured that higher-lying baryonic resonances can contribute to the mass region below the vector meson (ρ , ω) pole mass due to off-shell propagation of intermediate vector mesons[5]. And it looks like that our $n+p$ data follow just this scenario.

4.6.2 Experimental ansatz for understanding the di-electron production in AA interactions

In view of this strong isospin dependence the questions arises, whether the $C+C$ data can be explained by a superposition of individual NN collisions. A similar comparison has been performed earlier by the DLS collaboration [139]. They compared 1 GeV $p+p$ and $p+d$ data with $C+C$ data at 1 GeV/u. The $C+C$ spectra had been normalized to the $p+d$ data to facilitate the comparison of their shape, which turned out to be very similar. The goal here is to use the normalization to the produced neutral pions and check in the π^0 Dalitz region if this assumption is justified. HADES measured $C+C$ interactions at 1 GeV/u and $p+p$ and $n+p$ reactions at 1.25 GeV. However, before the comparison of the di-electrons from heavy-ion collisions with di-electrons from elementary reactions can be performed, we first have to discuss possible systematic uncertainties due to the slight difference in beam energy used for the two studies. At low masses ($M_{ee} < 0.15 \text{ GeV}/c^2$) the π^0 Dalitz decay peak dominates the spectra. Each di-electron spectrum is normalized to the corresponding number of π^0 , thus taking into the account the difference in pion production. Following the assumption of dominant pion production via Δ resonance, the effect of the energy difference on Δ production naturally cancels with the normalization to the corresponding number of π^0 . This is, however, not any longer true for the η production, as the η production proceeds close to the threshold and consequently differs between 1 GeV/u and 1.25 GeV/u. However, the η production in $C+C$ at 1 GeV/u beam energy is just about the same as for $n+p$ interactions at 1.25 GeV/u because seemingly differences in the Fermi momenta for the two reactions compensates the higher beam energy and the isospin dependencies (see Fig. 4.15). It should be noted, that both cross sections are experimentally known.

$^{12}C+^{12}C$ collisions are proceeding through a substantial number of $p+p$, $n+p$, $p+n$ and $n+n$ interactions. For $C+C$ at a kinetic beam energy of 1 GeV/u the analysis of charged pions by HADES [129] can be used to extract the mean neutral pion multiplicity per participant nucleon. As $C+C$ is an isospin symmetric system all pions should be produced with the same yield, thus we get $\langle N_{\pi^0} \rangle / \langle A_{\text{part}} \rangle |_{CC} = 0.061 \pm 0.007$ with $\langle A_{\text{part}} \rangle |_{CC} = 6$. The obtained pion multiplicity per participant nucleon agrees well with previous measurements of charged and neutral pions [17]. For NN collisions at a kinetic beam energy of 1.25 GeV/u we can calculate

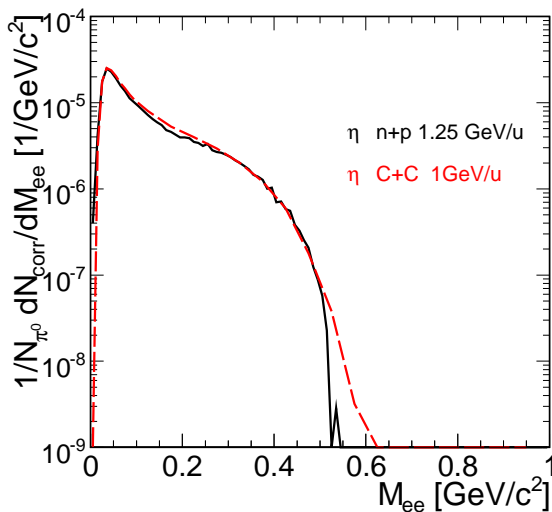


Figure 4.15: Comparison of the η production in $C+C$ collisions at 1 GeV/u and in $n+p$ collisions at 1.25 GeV/u. Dashed red line: the η multiplicity is taken from the TAPS measurement in the two-gamma decay channel Refs.[36, 37]. Black line: the η production in $n+p$ interactions measured by CELSIUS collaboration Refs. [28]. No extra scaling than the one to the π^0 production is done.

the multiplicity per participant nucleon using the following relation:

$$N^{pp} = \frac{\langle N_{\pi^0}^{pp} \rangle}{\langle A_{\text{part}} \rangle} = \frac{\sigma_{\pi^0}^{pp} / \sigma_{\text{reaction}}^{pp}}{\langle A_{\text{part}} \rangle} = 0.048, \quad (4.1)$$

where $\sigma_{\pi^0}^{pp} = 4.45$ mb is the π^0 cross section (see section 3.6.1), $\sigma_{\text{reaction}} = 45.7$ mb is the total reaction cross section for $p+p$ interactions [23], and $\langle A_{\text{part}} \rangle$ is 2. For $n+p$ collisions we get:

$$N^{np} = \frac{\langle N_{\pi^0}^{np} \rangle}{\langle A_{\text{part}} \rangle} = \frac{\sigma_{\pi^0}^{np} / \sigma_{\text{reaction}}^{np}}{\langle A_{\text{part}} \rangle} = 0.10, \quad (4.2)$$

where $\sigma_{\pi^0}^{np} = 8.56$ mb (see section 3.6.1), and $\sigma_{\text{reaction}}^{np} = 41.9$ mb [23].

For simplicity, in the following we assume that $p+p$ and $n+n$ collisions are equally likely: $P^{pp} = P^{nn}$ and $\sigma_{\pi^0}^{pp} = \sigma_{\pi^0}^{nn}$. The probability for a $p+p$ reaction is:

$$P^{pp} = \frac{\sigma_{pp}}{\sigma_{pp} + \sigma_{np}} = \frac{45.7}{(45.7 + 41.9)} = 0.52. \quad (4.3)$$

The probability for a $n+p$ reaction is equivalently:

$$P^{np} = \frac{\sigma_{np}}{\sigma_{pp} + \sigma_{np}} = \frac{41.9}{(45.7 + 41.9)} = 0.48. \quad (4.4)$$

We construct an extrapolated π^0 yield for $C+C$ from $p+p$ and $n+p$ as:

$$\frac{\langle N_{\pi^0} \rangle}{\langle A_{\text{part}} \rangle} \Big|_{CC \text{ extrap.}} = P^{pp} \cdot N^{pp} + P^{np} \cdot N^{np}, \quad (4.5)$$

where P^{pp} and P^{np} is estimated with Eqs. 4.3 and 4.4, N^{pp} and N^{np} is calculated with Eqs. 4.1 and 4.2. Putting everything together, the estimated pion multiplicity per participant nucleon for $C+C$ data based on $p+p$ and $n+p$ reactions amounts to:

$$\frac{\langle N_{\pi^0} \rangle}{\langle A_{\text{part}} \rangle} \Big|_{CC \text{ extrap.}} = 0.073 \pm 0.015. \quad (4.6)$$

The error is dominated by uncertainties in the pion cross section. Comparing this extrapolated number with the measurement in $C+C$ we recognize that the yield is higher by 16%. However, the energy dependence of the π^0 yield is not yet included here: at a kinetic beam energy of 1.25 GeV/u the pion multiplicity is higher by about 20% compared to 1 GeV/u [4]. Scaling the $C+C$ result to 1.25 GeV would yield:

$$\frac{\langle N_{\pi^0} \rangle}{\langle A_{\text{part}} \rangle} \Big|_{CC@1.25 \text{ GeV/u}} = 0.0732 \pm 0.007, \quad (4.7)$$

which is in perfect agreement with our $p+p$ and $n+p$ extrapolated value. Now one can try to compose the full di-electron spectra in $C+C$ collisions from a superposition of $p+p$ and $n+p$ data assuming the following relation:

$$\frac{1}{N_{\pi^0}} \frac{dN}{dM_{ee}} \Big|_{CC} = \frac{1}{4} \cdot (2 \cdot P^{pp} \cdot \frac{1}{N_{\pi^0}} \frac{dN}{dM_{ee}} \Big|_{pp} + 2 \cdot P^{np} \cdot \frac{1}{N_{\pi^0}} \frac{dN}{dM_{ee}} \Big|_{np}), \quad (4.8)$$

and since the difference in the probability of the $p+p$ and the $n+p$ reaction is only 2%, we thus deduce:

$$\frac{1}{N_{\pi^0}} \frac{dN}{dM_{ee}} \Big|_{CC} = \frac{1}{2} \cdot \left(\frac{1}{N_{\pi^0}} \frac{dN}{dM_{ee}} \Big|_{pp} + \frac{1}{N_{\pi^0}} \frac{dN}{dM_{ee}} \Big|_{np} \right). \quad (4.9)$$

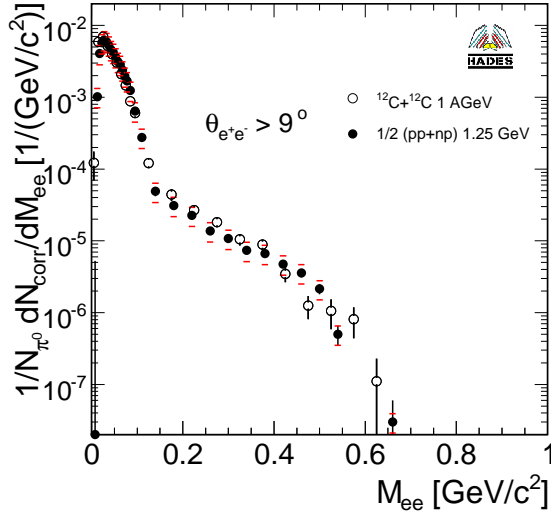


Figure 4.16: HADES invariant mass spectra for $1/2 \cdot (M_{ee}^{pp} + M_{ee}^{np})$ at 1.25 GeV/u and $C+C$ at 1 GeV/u systems. Open black circle: $C+C$ system, close black circle: $1/2 \cdot (M_{ee}^{pp} + M_{ee}^{np})$ experimental cocktail.

Fig. 8.2 shows the $C+C$ data compared to the experimental cocktail made of $p+p$ and $n+p$ data based on the Eq. 6.1. From the results one can see, that the di-electron production in $C+C$ collisions at SIS energies can indeed be explained by a superposition of elementary $p+p$ and $n+p$ collisions. Once the bombarding energy per nucleon in heavy-ion collisions becomes comparable to the nucleon rest mass, nuclear matter initially under normal conditions in the target and projectile nuclei undergoes a gradual transition into resonance matter. This state of matter we are probing with HADES. Due to strong phase space limitations at these energies, a sound theoretical description of electron pair production requires here a proper treatment of off-shell propagation of resonances and vector mesons. The "DLS puzzle" has been solved for heavy-ion collisions experimentally Ref.[3]. The theoretical interpretation of the elementary collisions are not yet fully consistent.

Chapter 5

Di-electron measurements with the CBM detector system at FAIR

*The best way to predict the future is to invent it.
(Alan Kay)*

The HADES experiment exploits the possibilities of di-electron measurements in heavy-ion collisions up to $2 \text{ GeV}/u$. With the upcoming new FAIR, a new possibility to systematically study the microscopic properties of dense baryonic matter up to beam energies of $35 \text{ GeV}/u$ will open. Measurements will be possible in an energy range, which was not used for such studies before and a full excitation function for electron pair production up to the lowest SPS energies will be reached. The HADES spectrometer will run at energies of $8 \text{ GeV}/u$ and with medium heavy nuclei (Ni). For the higher beam energies and heavier nuclei (Au), measurements will be conducted with the new Compressed Baryonic Matter (CBM) detector. The future international FAIR in Darmstadt aims for a multifaceted forefront science program by providing beams of stable and unstable nuclei as well as antiprotons in a wide range of intensities, energies and with optimum beam quality [140]. A sketch of FAIR together with the existing GSI facilities is presented in Fig. 5.1. It consists of a configuration of interlinked machines for accelerating and storing of high-quality particle beams. The core of the facility will be two large synchrotrons with rigidities of 100 Tm and 300 Tm (SIS100 and SIS300). UNILAC and SIS18 will pre-accelerate the ions before they are injected into SIS100. The goal of SIS100 is to generate intense pulses of ions for producing secondary beams of rare nuclei, and proton beams for producing antiprotons. Accelerated heavy ions stripped off their electrons are fed into SIS300 and will be used by experiments using slow extraction and maximum energy. Coupled to the SIS100/300 rings is a complex system of further rings into which the beams are sent, and then de-accelerated, stored and refined for specific experiments.

Up to five research programs can be carried out at the same time. The FAIR research program comprises: (1) the CBM detector to study high-energy nucleus-nucleus collisions; (2) the PANDA detector for hadron physics experiments using cooled high-energy antiproton beams; (3) the NUSTAR detectors used for experiments on the structure of unstable nuclei and on nuclear astrophysics; (4) experimental setups for Plasma Physics (PP) and (5) Atomic Physics (AP).

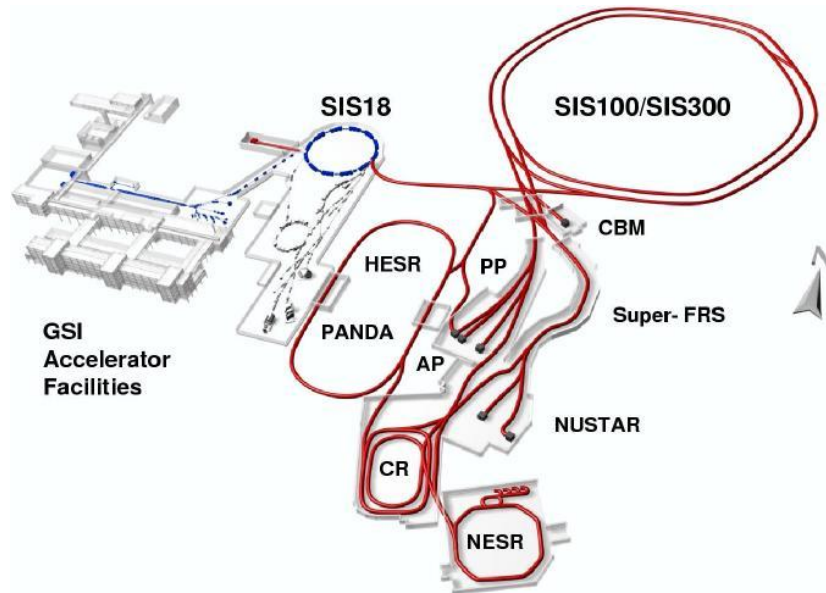


Figure 5.1: Layout of the FAIR accelerator complex.

The CBM experiment is considered as one of the core projects of the future accelerator facility FAIR. The CBM experiment will make use of proton beams with energies of 10 – 89 GeV, and of nuclear beams with energies of 10 – 44 GeV/u. An upgraded HADES detector will explore the lower energies between 2 and 10 GeV/u.

5.1 The CBM research program

The CBM research program is focused on the study of the equation-of-state of dense baryonic matter, the search for the phase boundary between hadronic and partonic matter (including the QCD critical endpoint), the search for modifications of hadron properties in the dense baryonic medium, and for the onset of chiral symmetry restoration. The experimental program of CBM comprises the measurements of open and hidden charm, low-mass vector mesons decaying into dilepton pairs, strange and multi-strange hadrons, collective flow of hadrons and event-by-event fluctuations.

*THAT IS THE QUESTION
Co-existence
or no existence.
(Hamlet Anno Domini)*

Phase transitions occur above a critical energy density and can only be observed if the matter extends over a certain volume. Therefore, a key feature of the CBM experimental program is a systematic and comprehensive measurement of excitation functions and system size dependencies of all observables. Particular emphasis will be put on rare diagnostic probes which are not accessible by other experiments in this energy range.

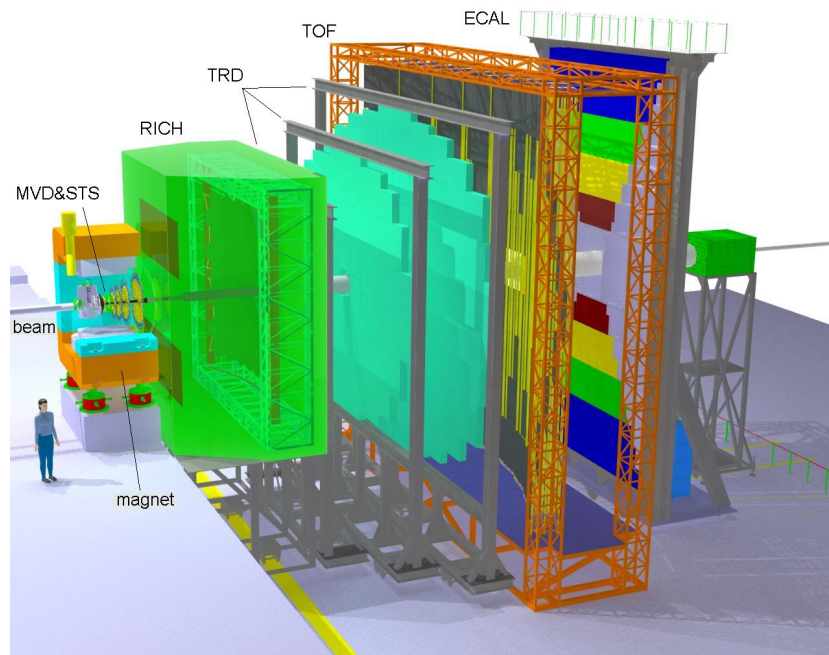


Figure 5.2: Layout of the CBM experiment with detectors for electron identification [38].

5.2 The CBM detector

The CBM experiment is being designed to measure hadronic, leptonic and photonic observables. The technical challenge of the CBM experiment is to identify both, hadrons and leptons, and to detect rare probes out of the reaction zone formed in central heavy-ion collisions. The experiment has to provide high-resolution secondary vertex determination and a high speed trigger and data acquisition system. In this work I will focus on the layout of the CBM experiment of the year 2007/2008. Many design studies exploring the capabilities of the proposed detector setup with respect to the observables are in progress and thus the layout is still subject of change.

The current layout of the CBM experimental setup is sketched in Fig. 5.2. The core of the experiment will be a silicon tracking and vertex detection system installed in a large acceptance dipole magnet. The STS¹ consists of low-mass silicon micro-strip detectors and may be complemented by one or two hybrid-pixel detector layers. In addition an ultra thin and highly-granulated MVD² is placed at 10 cm behind the target in order to measure the displaced decay vertices of charmed mesons. The STS is followed by the RICH³ and the TRD⁴ for electron identification and the TOF⁵ wall for hadron identification. The setup will be completed by the ECAL⁶ for the measurement of direct photons and neutral mesons decaying into photons in selected regions of phase space, and by the PSD⁷ needed for the determination of the collision centrality and the orientation of the reaction plane. As an alternative approach to

¹Silicon Tracking System

²Micro-Vertex pixel Detector

³Ring Imaging Cherenkov detector

⁴Transition Radiation detector

⁵Time-of-Flight

⁶Electromagnetic Calorimeter

⁷Projectile Spectator Detector

the di-electron measurement the MuCH⁸ for the identification of muons with momenta above $1.5 \text{ GeV}/c$ is foreseen. The hadron absorbers would be removed in order to identify hadrons using the TOF wall.

The experimental strategy how to assess best the low-mass vector mesons by means of their electromagnetic decay is under careful investigation. The strong benefit of a di-electron measurements is that electron pairs do not impose phase space limitations accessing the very low mass region of the pair mass spectrum. A measurement of virtual photons through muon pairs restrict the invariant mass spectrum to the region above the 2-muon threshold of $210 \text{ MeV}/c^2$. An advantage of a muon pair measurement is the absence of the strong physical background sources like the π^0 Dalitz decay in the electron channel. However, in both cases purity and efficiency of the lepton identification has to be studied carefully in simulations as they have a large impact on the physics performance. In parallel detector R&D has to prove that measurements can be done with the necessary performance. Currently, simulations for di-electron and di-muon pairs show a similar performance despite their completely different background sources. As CBM will be the only experiment studying dileptons in this energy range in the future, a complementary measurements of both channels would be an independent crosscheck and thus a very valuable add-on in the systematic investigation of any achieved results.

5.2.1 The Silicon Tracking System (MVD and STS)

The experimental concept of CBM is to track charged particles directly behind the target with a compact detector system. MVD and STS are the central components of the CBM experiment and have the following tasks:

⁸Muon Chamber/absorber system

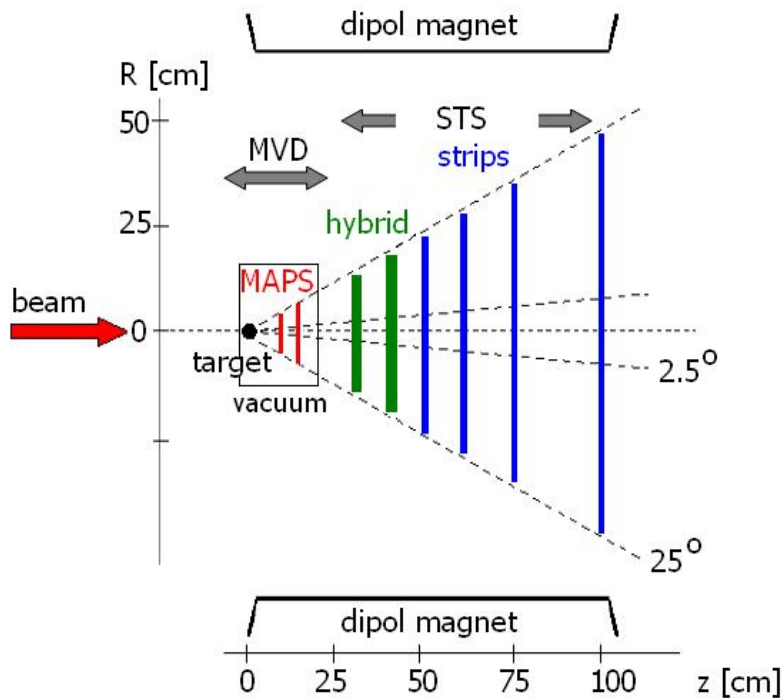


Figure 5.3: Schematic cross section of the Silicon Tracking and Vertex Detection System. The dashed lines indicate the maximum and minimum angular coverage of the STS.

- momentum measurement for charged tracks with $\Delta p/p = 1\%$ ($0.5 < p/(\text{GeV}/c) < 12$),
- vertex determination with a resolution of better than $50 \mu\text{m}$,
- efficient recognition of electron pairs from π^0 decays (Dalitz, $\gamma\gamma$).

A particular aspect of the system is to achieve high track reconstruction efficiency in a high track density environment also for short tracks, i.e. such tracks only passing part of the tracking system. It is therefore essential to get redundant information from the detector system. The reconstruction of track pairs originating from secondary vertices, in particular γ conversions in the detector material, will be essential to reduce the combinatorial background in the electron pair spectrum. The system requirements include a very low material budget, radiation tolerant sensors with high spatial resolution, and a fast readout.

The main tracker

The actual concept of the detection system is shown in Fig. 5.3. In its current version the STS consists of up to 6 tracking stations of silicon pixel and strip detectors. They are located between 30 and 100 cm downstream of the target in the 1 m long gap of a superconducting dipole magnet with 1 Tm bending power, covering laboratory polar angles from 2.5° to 25° . Two hybrid pixel detectors (LHC-type [141]) may be arranged at 30 and 40 cm downstream of the target providing unambiguous space points of the particle trajectories. The sensors are sufficiently radiation hard, however, their material budget is about $800 \mu\text{m}$ and even larger if cooling is taken into account. The bulk area (1.5 m^2) of the tracking stations will be covered with silicon strip detectors. Ongoing design studies concentrate on open questions such as whether an excellent tracking performance can be achieved by using only silicon strip detectors? If not, pixel detectors are considered for the innermost region of the stations around the beam pipe where the track densities are highest.

The Micro-Vertex Detector

The MVD in general has two high-resolution silicon pixel detectors located 10 and 20 cm downstream of the target. A drawing from first design studies of the MVD detector is shown

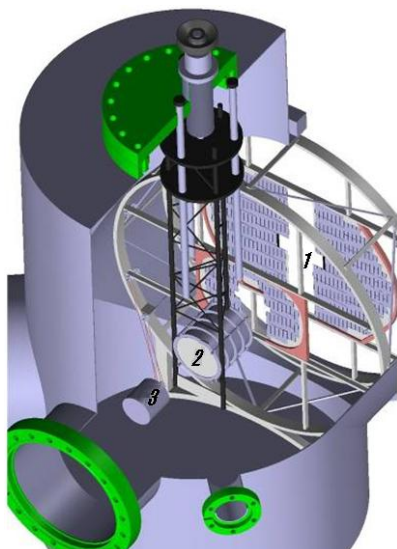


Figure 5.4: First design studies of the MVD detector. 1: MAPS stations can be moved to allow beam tuning, 2: target holder, 3: engine to move detector stations.

in Fig. 5.4. The MVD will be installed for dedicated measurements of open charm where the secondary vertex has to be determined with high resolution, and for electron measurements where close pairs have to be rejected in order to reduce the combinatorial background (see section 6.5.1).

These tasks require detectors with excellent position resolution and a very low material budget in order to reduce multiple scattering. These requirements are met by Monolithic Active Pixel Sensors (MAPS). The pixel size will be between $25 \times 25 \mu\text{m}^2$ and $40 \times 40 \mu\text{m}^2$. For the latter size a position resolution of $\sigma = 3 \mu\text{m}$ can be achieved. The MAPS detector R&D is focused on the improvement of the radiation tolerance and the readout speed. The goal is to develop detectors which survive a radiation dose of 10^{13} neq which corresponds to 10^{12} minimum bias $^{197}\text{Au}+^{197}\text{Au}$ collisions at $25 \text{ GeV}/u$ beam energy. The MVD detector will only be included in the set-up when needed because it will restrict maximum interaction rates due to its limited readout speed to approximately 100 kHz.

5.2.2 Superconducting dipole magnet

The dipole magnet serves for bending of the charged particle trajectories. A gap of larger than 1 m is required to provide sufficient space for the STS. A possible realization of the magnet concept is shown in Fig. 5.5. The magnetic field is calculated using the TOSCA [142] code and has been implemented in the GEANT [143] simulation code. A bending power of about 1 Tm has to be provided by the magnet in order to achieve a momentum resolution of about 1%. However, this relatively high magnetic field decreases the efficiency towards low momentum particles. In particular, this effect reduces the probability to reconstruct Dalitz decay of π^0 mesons which results in an increase of the combinatorial background for low-mass vector mesons. A solution to this problem will be discussed in chapter 6.1.3.

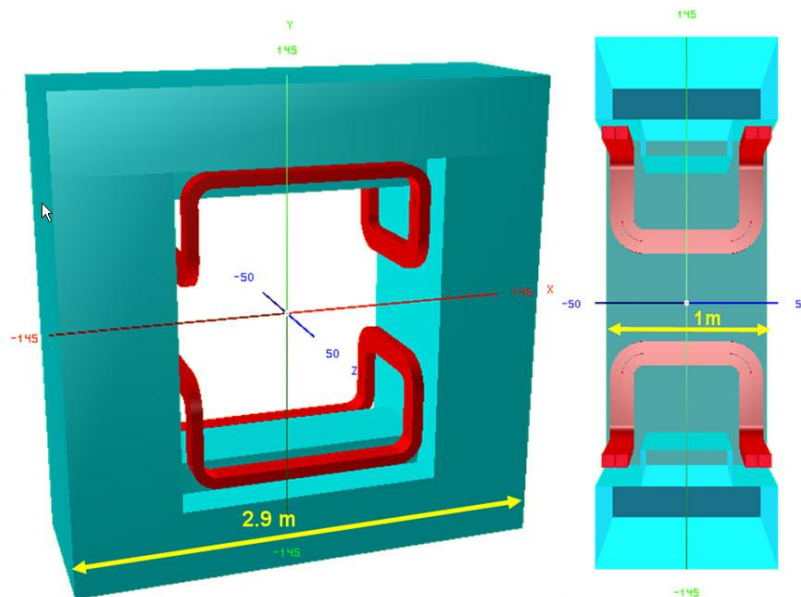


Figure 5.5: Possible realization of the superconducting dipole magnet [38].

5.2.3 Ring Imaging Cherenkov detector

The RICH detector will be positioned between the silicon tracking station and the first transition radiation detector. In order to minimize external pair conversion and multiple scattering, low material budget along the particle trajectories is an issue. The RICH detector will be placed about 1.5 m downstream the target and consists of a ~ 3 m long gas radiator, two arrays of spherical hexagonal mirrors, two photodetector planes and corresponding support structure. The layout of the RICH detector is shown in Fig. 5.6. The basic concept of a RICH detector is the following: if a charged particle with a velocity $v > c/n$ traverses a radiator medium (with refractive index n of the medium) Cherenkov light is emitted with an angle $\cos\theta_c = 1/(\beta \cdot n)$ along the particle trajectory. The Cherenkov photons are focused by a spherical mirror onto a UV-sensitive detector, creating a ring-like image.

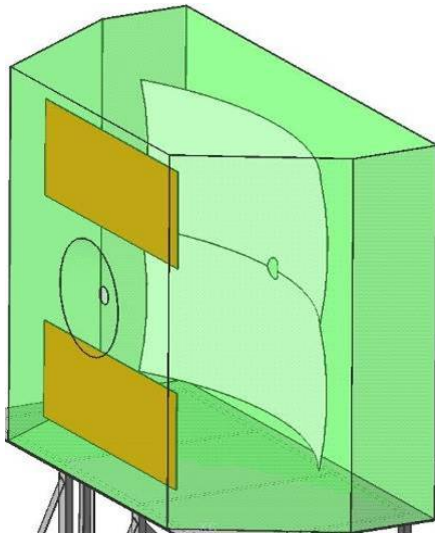


Figure 5.6: RICH detector as implemented into the CBM simulation framework. Light green: gas vessel made of aluminum walls filled with the Cherenkov radiator gas. Two rectangular sectors of the spherical mirrors are positioned in the downstream part of the gas vessel. The photodetector consists of two rectangular planes positioned inside the gas vessel on its upstream wall [39].

The RICH detector is designed to provide identification of electrons and suppression of pions in the momentum range of electrons from low-mass vector meson decays, i.e. from lowest momenta up to 10 – 12 GeV/c. These requirements define possible gaseous radiators for the RICH detector. Assuming that we will be able to separate pions from electrons up to 90% of the maximum Cherenkov opening angle θ_c . The resulting momentum range for π identification is illustrated in Fig. 5.7 in dependence on the Lorentz factor $\gamma_{th} = 1/\sqrt{1 - 1/n^2}$. A radiator with $\gamma_{th} > 38$ would be ideal, because then the Cherenkov angle of pions is less than 90% of θ_c for all momenta smaller than 12 GeV/c. Possible radiator gases under investigation are N_2 ($\gamma_{th} = 41$) and CO_2 ($\gamma_{th} = 33$).

The most important consideration concerning the mirror material will come from global tracking simulations: STS and TRD tracks have to be connected with high precision which limits length and material budget of the RICH detector. The maximum length will reflect in the radius of curvature as no intermediate reflecting mirrors are foreseen. The mirror gives the largest contribution to the material budget of the RICH, the maximum allowable radiation length will determine whether glass mirrors can be used or a lightweight material such as carbon. Currently, two arrays of spherical hexagonal glass mirrors with radius of curvature of $R = 450$ cm and a thickness of 4 – 6 mm are foreseen. The coating should provide highest reflection for the full range of photons not absorbed in the gas and detected by the photodetector, i.e. down to about $\lambda_{min} = 160 - 180$ nm (where λ_{min} is lower wavelength limit). This requirement can be met by a mirror substrate of very low surface roughness with a MgF_2 protected aluminum coating.

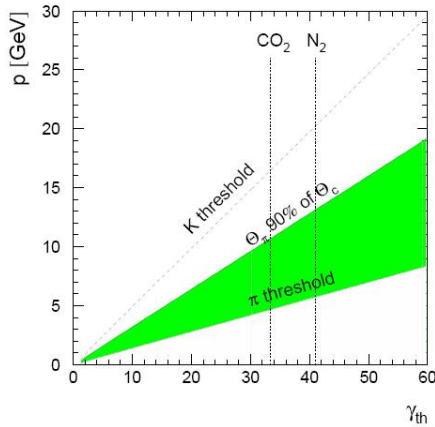


Figure 5.7: Momentum threshold for Cherenkov light production for pions and kaons in dependence on γ_{th} . Also shown is the momentum at which the opening angle of pions corresponds to 90% of the opening angle of electrons. The green/grey band thus indicates the approximate region of pion identification in dependence on γ_{th} [39].

The Cherenkov light emitted from charged particles is focused on two focal planes, positioned downstream of the magnet at $R/2 = 225$ cm distance to the mirrors. Currently two photodetector planes are planned to consist of Hamamatsu multi-anode photo multipliers. The photodetectors are shielded by the dipole magnet yoke to reduce the background from particles crossing the photodetector plane. No additional window between the radiator and the photodetector is foreseen. The main requirements for the photodetector are high granularity, high geometrical efficiency and high detection efficiency of photons in a wavelength range down to $\sim 160 - 180$ nm. The current overall material budget of the RICH detector is about 3% of X_0 .

5.2.4 Transition Radiation detector

Three Transition Radiation Detector stations have to provide sufficient identification capability for high energy electrons and positrons ($\gamma > 2000$) which are mainly used to reconstruct J/Ψ mesons and additional pion suppressions for momenta large than 1.5 GeV/c. The TRD detectors would then also serve as tracking detectors bridging the gap between the STS and the TOF wall. The required pion suppression is a factor larger than 100 and the required position resolution is of the order of $200 - 300$ μm . Transition radiation is produced by relativistic charged particles crossing the interface of two media of different dielectric constants. The total energy loss of a charged particle during the transition depends on its Lorentz factor $\gamma = E/mc^2$.

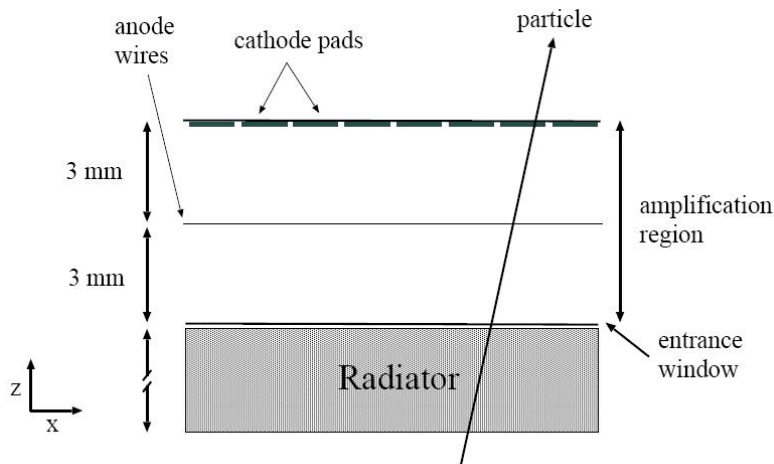


Figure 5.8: Layout of the MWPC prototypes built at GSI and in Bucharest

The intensity of the emitted radiation is roughly proportional to the particle's energy E . The characteristics of this electromagnetic radiation makes it suitable for particle identification, particularly of electrons with momenta larger than $1.5 \text{ GeV}/c$. The transition radiation photons produced by electrons have wavelengths in the X-ray range, with energies typically in the range from 5 to 15 keV. However, the number of produced photons per interface crossing is very small: for particles with $\gamma = 2000$, about 0.8 X-ray photons are transmitted. Usually several layers of alternating materials or composites are used to collect enough transition radiation photons for an adequate measurement. On the other hand the total thickness of the detector in terms of radiation length has to be kept as small as possible to minimise multiple scattering and conversions. The gas mixture of the readout detectors is based on Xe in order to maximize the absorption of transition radiation produced by the radiator. In CBM three TRD stations each consisting of 4 detector layers are foreseen. Every second TR layer is rotated by 90° . The detector stations are located at 5 m, 7.25 m and 9.5 m downstream the target, the total active detector area amounts to about 600 m^2 . Depending on the polar angle cell sizes of length $1 - 10 \text{ cm}^2$ are foreseen such that the occupancy always stays below 5%. The overall material budget X/X_0 amounts to approximately $\leq 15 - 20\%$. The inner part of the TRD has to work at rates up to 100 kHz/cm^2 and to stand high doses (charged particles) up to 16 krad/year [144]. Prototype gas detectors based on multi-wire proportional chambers with pad readout have been built and tested with particle rates of up to 100 kHz/cm^2 without deterioration of the performance [145].

5.2.5 The timing Resistive Plate Chambers (RPC)

An array of Resistive Plate Chambers will be used for hadron identification via TOF measurements. The TOF wall is located 10 m downstream of the target and covers an active area of about 160 m^2 . The required time resolution is on the order of 80 ps. For 10 MHz minimum bias $Au+Au$ collisions the innermost part of the detector has to work at rates up to 20 kHz. The development of timing RPCs is focused on high rate capability, low resistivity material, long term stability and the realization of large arrays with overall excellent timing performance. At

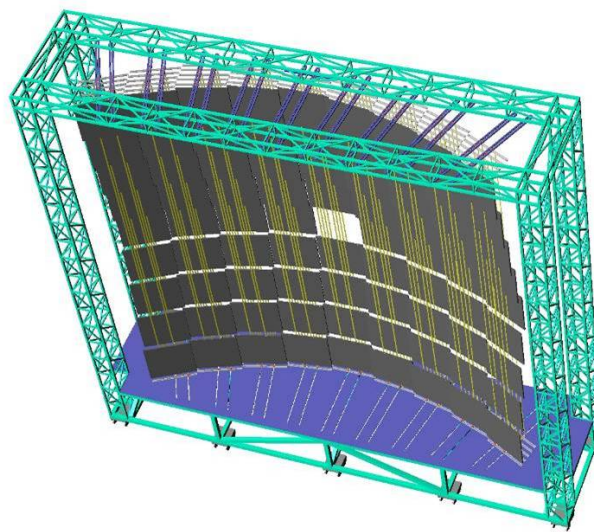


Figure 5.9: TOF wall as implemented into the CBM simulation framework. Rear view of the TOF wall, divided into 9 towers [38].

large polar angles the detector occupancy is 10 times lower than in the innermost part. A natural choice for the readout of the outer part could be a strip layout which has been successfully tested by HADES in 2007 [107], [108]. With this prototype a time resolution below 80 ps was obtained with rates up to 1 kHz/cm².

Based on the experience gained during the HADES upgrade, the geometry and response of the TOF detector has been included in the CBM simulation framework. A first approach to the final mechanical structure has been accomplished, where a distribution of the wall in towers is currently foreseen (see Fig. 5.9).

5.2.6 The Electromagnetic Calorimeter

A "shashlik" type calorimeter as installed in the HERA-B, PHENIX and LHCb experiments will be used to measure direct photons and neutral mesons decaying into photons. The ECAL will be composed of modules which consist of about 150 layers of lead and scintillator material, with cell sizes of 3×3 cm², 6×6 cm², and 12×12 cm². The "shashlik" modules can be arranged either as a wall or in a tower geometry with variable distance from the target. The phase space to be covered is still an issue in ongoing simulation studies.

5.2.7 The Projectile Spectator detector

The centrality of the collision and orientation of the reaction plane are fundamental parameters in the study of heavy-ion reactions to be measured by the PSD. A very precise characterization of the event class is of crucial importance for the analysis of event-by-event observables. A good resolution of the event plane is mandatory for flow measurements and correlation studies. The detector is designed to measure the number of non-interacting nucleons from a projectile nucleus in nucleus-nucleus collisions. The PSD is a fully compensating modular lead-scintillator calorimeter which provides a very good and uniform energy resolution. A prototype detector has been successfully tested in the NA61 experiment at CERN [146].

5.2.8 The Data Acquisition and online event selection (DAQ)

All detector systems of the CBM experiment have to be designed such that they can stand the extreme conditions posed by heavy-ion reactions at 35 GeV/u beam energy at interaction rates up to 10 MHz, which corresponds to roughly 10^{10} tracks per second in the CBM acceptance. The key requirement driving the trigger and DAQ architecture of the CBM experiment is the efficient detection of rare probes like open charm, J/Ψ mesons, or low-mass dimuon pairs in the high-multiplicity environment of a heavy-ion collision.

Assuming an archiving rate of 1 GByte/s and an event volume of about 40 kByte for minimum bias $^{197}\text{Au}+^{197}\text{Au}$ collisions, an event rate of 25 kHz can be accepted by the data acquisition system. Therefore, measurements with event rates of 10 MHz require (online) event selection algorithms which reject the background events containing no signal by a factor of 400 or more. For open charm production the trigger will be based on an online search for secondary vertices which requires high speed tracking and event reconstruction in the STS and MVD. For low-mass electron pairs no online selection is possible due to the large number of rings per event in the RICH caused by the material budget in front of the detector.

Chapter 6

Data analysis



If trying to find something is like looking for a needle in a haystack...

Vectors mesons detected in their dileptonic decay channel are expected to be unique probes of the conditions in the evolving fireball. The decay dileptons of ρ , ω , ϕ and J/ψ will leave the collision zone without interactions thus carrying undistorted information on the vector meson properties in the hot and dense matter. All vector mesons in the dileptonic decay channel are rare probes, either because the branching ratio is on the order of $10^{-4} - 10^{-5}$ only (low-mass vector mesons) or because their multiplicity is so small (charmonium). The experimental challenge is to suppress the large physical background on the one hand and to provide a clean identification of electrons on the other hand.

This chapter will now focus on the optimization of the CBM experimental layout and simulation studies exploring the capabilities of the proposed detector setup with respect to e^+e^- pair reconstruction. The performed simulations can be separated in the following way:

- generic simulations - throughout this study, we assume perfect track reconstruction and particle identification thus studying the ideal performance of the detector;
- realistic simulations - realistic detector response, track reconstruction and electron identification are taken into account as far as possible according to our current knowledge.

6.1 Input to the simulations

6.1.1 Event generator

The simulations were performed for central ($b = 0$ fm) $^{197}\text{Au}+^{197}\text{Au}$ collisions at a beam energy of $25\text{ GeV}/u$. The final state phase space distributions of hadrons were generated using the relativistic transport code UrQMD. The phase space distributions of electrons and positrons from purely leptonic and semi-leptonic (i.e. Dalitz) decays of light vector mesons (ρ^0 , ω , ϕ) were obtained using the Pluto event generator. To enhance the statistics for these rare decays one decay of a vector meson was embedded into each UrQMD event. In the analysis, contributions from these enhanced sources were normalized according to their mean multiplicities as predicted by the HSD model and the branching ratios. The mean multiplicities, decay channels and branching ratios of background and signal lepton sources are presented in Table 6.1. An additional background will come from π^\pm misidentified as electrons. In central $\text{Au}+\text{Au}$ collisions at $25\text{ GeV}/u$ beam energy about $500\pi^\pm$ are produced per event. On average, there is one leptonic decay of light vector mesons (excluding η Dalitz) in 400 central $\text{Au}+\text{Au}$ collisions at $25\text{ GeV}/u$ beam energy. In Fig. 6.1 the cocktail of electron pair sources integrated over the full phase space is shown for central $\text{Au}+\text{Au}$ collisions at $25\text{ GeV}/u$ as it was used as input to the simulation.

An important effect that has to be taken into account for realistic simulations of hadronic interactions is the deviation of resonance shapes from fixed-width Breit-Wigner distributions, which is typically modeled as a mass-dependence in the resonance width. This is particularly

Particle	N/event	Decay channel	Branching Ratio
π^0	365	$e^+e^-\gamma$	1.198×10^{-2}
η	36	$e^+e^-\gamma$	5.0×10^{-3}
ω	38	$e^+e^-\pi^0$ e^+e^-	5.9×10^{-4} 7.07×10^{-5}
ρ^0	23	e^+e^-	4.44×10^{-5}
ϕ	1.28	e^+e^-	3.09×10^{-4}

Table 6.1: Mean meson multiplicities, their dominant leptonic decay channels and branching ratios for central $\text{Au}+\text{Au}$ collisions at $25\text{ GeV}/u$ beam energy

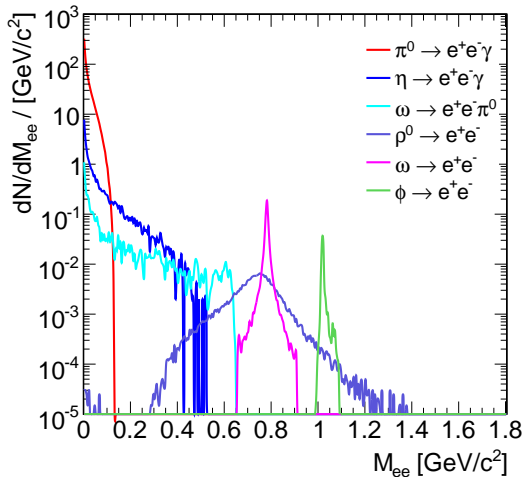


Figure 6.1: Invariant mass distribution for central $\text{Au}+\text{Au}$ collisions at $25\text{ GeV}/u$ (full phase space). Description: from left to right. Red: π^0 Dalitz decay; dark blue: η Dalitz decay; blue: ω Dalitz decay; green: ρ^0 , magenta: ω , violet: ϕ direct dilepton decay.

important for resonances with large widths, such as the ρ meson. The ρ meson mass distribution is generated by including a Breit-Wigner shape around the pole mass, thermal phase space factors, and a factor $1/M^3$ to account for vector meson dominance in the decay into e^+e^- . In addition, the ansatz followed here is that the ρ is governed by the 2-pion phase space in order to be comparable to transport code calculations [147]. However, this cut-off behavior at $2 \cdot M_\pi$ is still under discussion. All particles were finally propagated through the detector system with the simulation framework CbmRoot [148] using the GEANT3 package. Fig. 6.2 shows the transverse momentum versus rapidity distribution of accepted electron pairs from π^0 (main background source) and ρ^0 meson decay, i.e. for $\pi^0 \rightarrow \gamma e^+e^-$ and $\rho^0 \rightarrow e^+e^-$. Please note that the majority of pairs from pion decay appears at low or moderate transverse momentum.

The proposed CBM detector setup is different from previous di-electron experiments as e.g. CERES or HADES. In those experiments electron identification is performed in front of the magnetic field and main material budget due to tracking detectors. The CBM setup is in this respect vice versa: there will be no detector system which can provide particle identification in front of the magnetic field. That means that all close pairs (pairs with small opening angle, $\theta < 2^\circ$) are "opened" by the magnetic field before the electron identification is performed. Therefore we expect difficulties to fully reconstruct close pairs and maybe an increase of the combinatorial background due to partially reconstructed γ conversion pairs. Hence, the rejection strategy has to rely to a large extent on the track topology of pairs in the silicon tracking stations.

It is the main purpose of my work to study the respective performance of the proposed CBM detector setup for low-mass vector meson measurements with di-electrons. Due to the reason indicated above, special focus is set on the tracking performance of MVD and STS tracking systems in the given geometry and to indicate directions for possible modifications of the spectrometer design in order to improve it further.

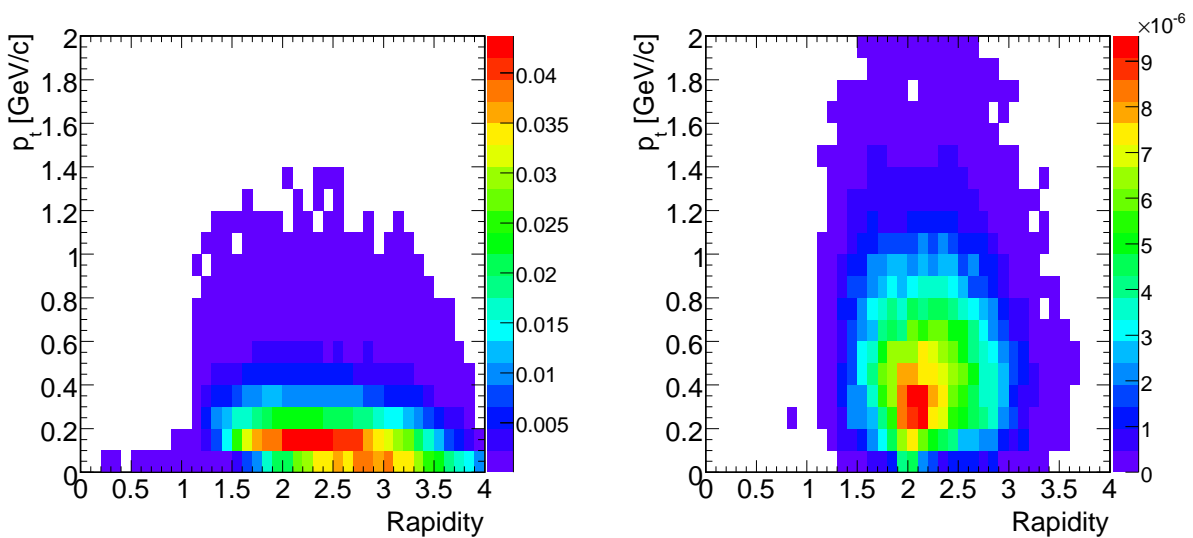


Figure 6.2: Transverse momentum versus rapidity distribution. Left: for π^0 Dalitz decay, right: for ρ^0 meson.

6.1.2 Characteristics of the background

The dominant background sources are random combinations of electrons and positrons from π^0 Dalitz decay and γ conversion. In a central $^{197}\text{Au}+^{197}\text{Au}$ collision at 25 GeV/u beam energy about 360 π^0 mesons are produced, which immediately decay into $e^+e^-\gamma$ ($\Gamma/\Gamma_{tot} = 0.012$) and to 2γ ($\Gamma/\Gamma_{tot} = 0.988$). A characteristic feature of conversion and Dalitz decays is the moderate decay momentum of the electron pair. This generally leads to small opening angles as shown in Fig. 6.3 (left panel) and comparatively small laboratory momenta (see Fig. 6.3, right panel).

Consequently, in many cases one low-momentum partner traverses only one or up to three STS stations and can hence not be reconstructed as it is shown in Fig. 6.4. The tracking algorithm requires four consecutive hits assigned to an individual track. Therefore the tracks were categorized in the following way, numbers given in brackets are the corresponding number of e^+/e^- per event:

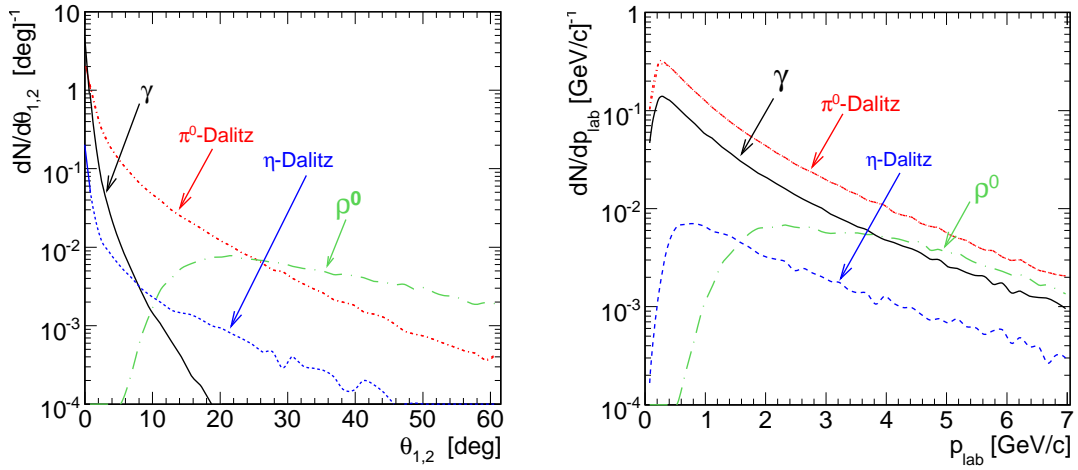


Figure 6.3: Left: Opening angle distribution for central $Au+Au$ collisions at 25 GeV/u (full phase space). Right: Momentum distribution of di-electron sources (central $Au+Au$ collisions at 25 GeV/u, full phase space).

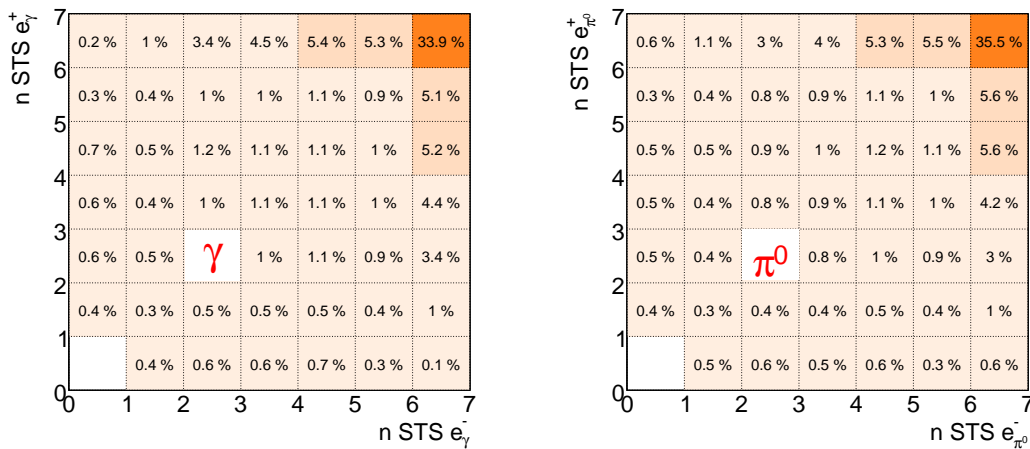


Figure 6.4: Number of STS stations traversed by e^+ vs. e^- from γ conversion (left panel) and π^0 Dalitz decay (right panel).

- Track Fragment (to be referred as TF): not reconstructed track (only single hits left in MVD):
 $[N_{\text{TrackFragment}}^{\pi^0} = 0.27, N_{\text{TrackFragment}}^{\gamma} = 0.13]$;
- Track Segment (to be referred as TS): reconstructed track (momentum and charge information):
 $[N_{\text{TrackSegment}}^{\pi^0} = 0.33, N_{\text{TrackSegment}}^{\gamma} = 0.15]$;
- Global Track (to be referred as GT): track identified as electrons: $[N_{\text{acc}}^{\pi^0} = 1.08, N_{\text{acc}}^{\gamma} = 0.49]$.

On the Track Segment level all charged particles (≈ 700 in the geometrical acceptance) are included in the analysis (see section 6.5.1). Despite their particular decay pattern, a large number of electron pairs from γ conversion are fully tracked (see Fig. 6.4). Such pairs are quite unique in as much as they combine to very small invariant masses, so they are best removed by an invariant mass cut before the other background rejection methods are applied to the electron and positron tracks (will be discussed in section 6.5.1).

6.1.3 Modifications of the detector set-up

Substantial reconstruction capability for low-momentum tracks is essential for identifying electron pairs from γ conversion and Dalitz decay of π^0 , as the topology of these processes has a relevant fraction where tracks with moderate laboratory momentum are accompanied by very soft tracks which are rapidly bend out of the acceptance of the tracking station (see Fig. 6.5). An important requirement for efficient background rejection is to enable an opening angle measurement even for pairs where one of the tracks is not reconstructed. The excellent two hit resolution in the MAPS detector ($< 100 \mu\text{m}$) gives then a chance to reject close pairs by measuring a distance between closest hits (for details see section 6.5.2). In order to use this feature one has to work out a realistic concept how to suppress the magnetic field between the target and the first MVD station. One possible solution how to increase the acceptance for low momentum particles (Track Segments) is to reduce the magnetic field to 70% of its nominal value. This of course will affect the momentum resolution of the tracks (see section 6.2). The final detector configuration will result from a trade of background rejection capability against invariant mass resolution. To further improve the acceptance of the Track Segments, the size of the tracking stations 1 to 6 (MVD 1, 2, STS 1 – 4) were increased based on the following generic simulations. All hits detected in the first MVD station were extrapolated to the z position of the second MVD station ($z = 20 \text{ cm}$), from the second MVD to the z position of the first station of the main tracker ($z = 30 \text{ cm}$) etc. In Fig. 6.6 hit distributions in the plane of x versus y for e^+ and e^- from γ conversion and π^0 Dalitz decay extrapolated from the second MVD to the position of the first STS are shown. Based on this generic simulation, the size of the MVD and STS stations were increased by a factor 1.5 in the bending direction of the magnetic field. By now this modified setup has become the standard for the CBM setup.

The occupancy of the extended detector areas is small. Thus high detector granularity is not an issue here. These extended detector areas can be covered by long strips adding less than 10% new channels to the STS setup. Another possibility would be an installation of additional silicon detectors left and right of each station. The increase of the STS stations is needed to increase the acceptance of the Track Segments. As the increased detector acceptance is needed in the STS only for an increased reconstruction probability of low momentum tracks, the size of the other detectors as RICH, TRD and TOF are not affected.

It is important to understand how many additional tracks will be reconstructed by this change. For this purpose realistic simulations including track reconstruction have been used.

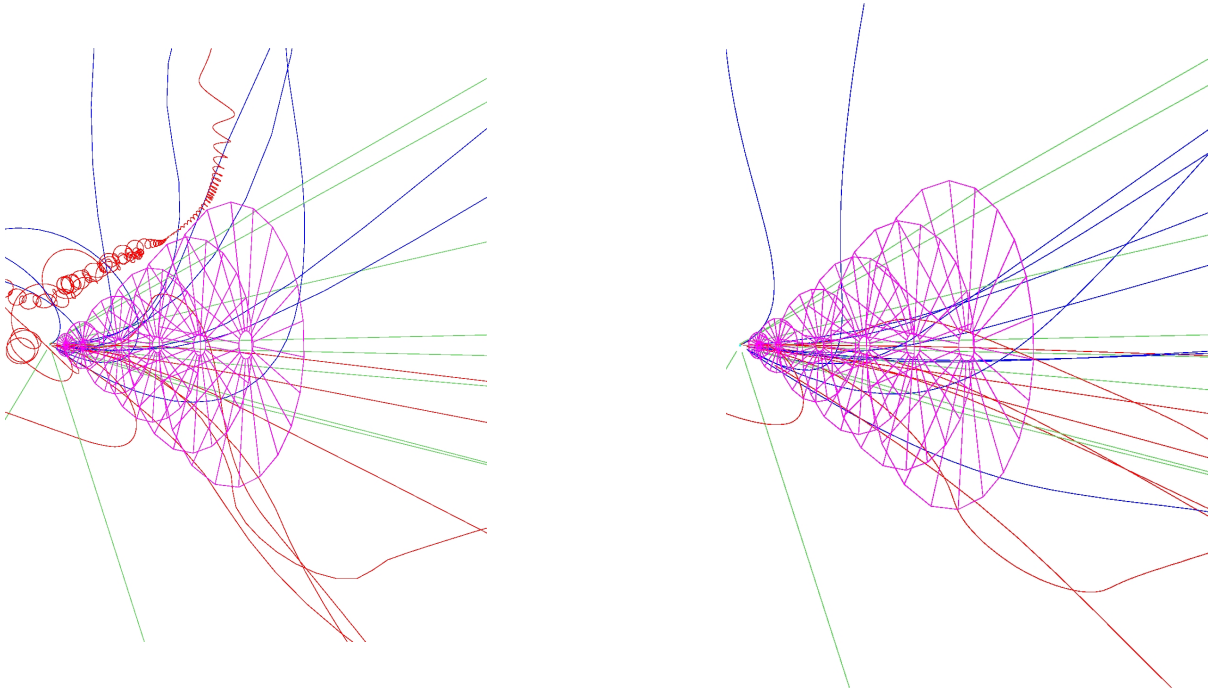


Figure 6.5: Trajectories of γ (green), e^+ (magenta), e^- (blue) from π^0 Dalitz decay. Left: $B_{max} = 1.1$ T, right: $B_{max} = 0.7$ T.

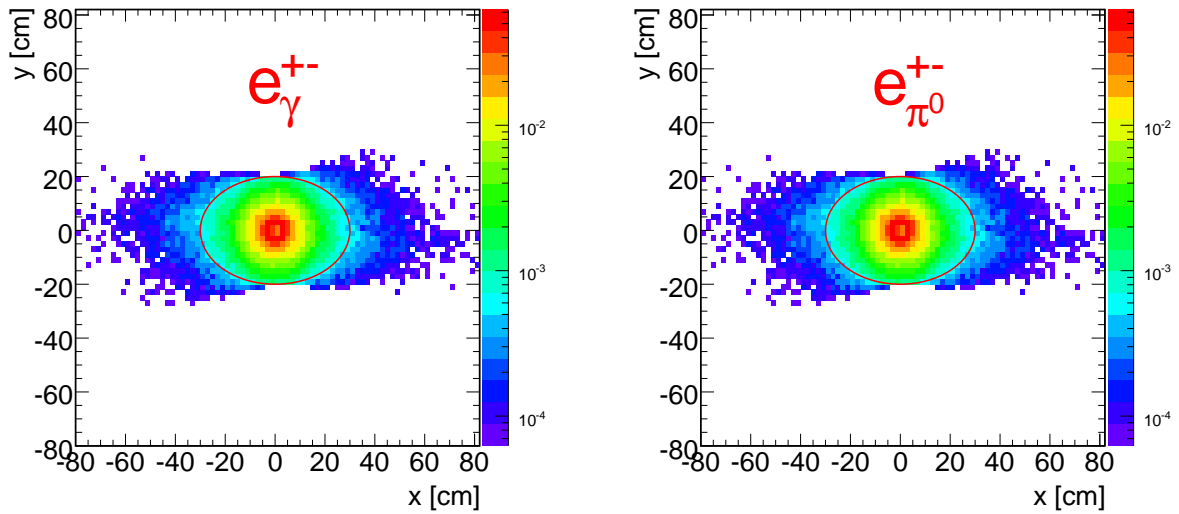


Figure 6.6: Distribution of x versus y hit positions for e^+ and e^- from γ conversion (left panel) and π^0 Dalitz decay (right panel) extrapolated from $z = 20$ cm to $z = 30$ cm.

Two cases were considered: the first contained the standard geometry of the STS, the second contained the enlarged STS stations, while for both the magnetic field value was reduced to 70% of its nominal value. The number of reconstructed primary tracks with momenta below 500 MeV/c was compared: 42 tracks per event have been reconstructed by using the standard STS geometry and scaled field and 53 tracks using the enlarged geometry. For comparison: 34 tracks with momenta below 500 MeV/c can be reconstructed using the standard STS geometry and full field. This increase of reconstructed tracks using the enlarged STS stations corresponds to an improvement of 26% in the reconstruction capability of low momentum tracks.

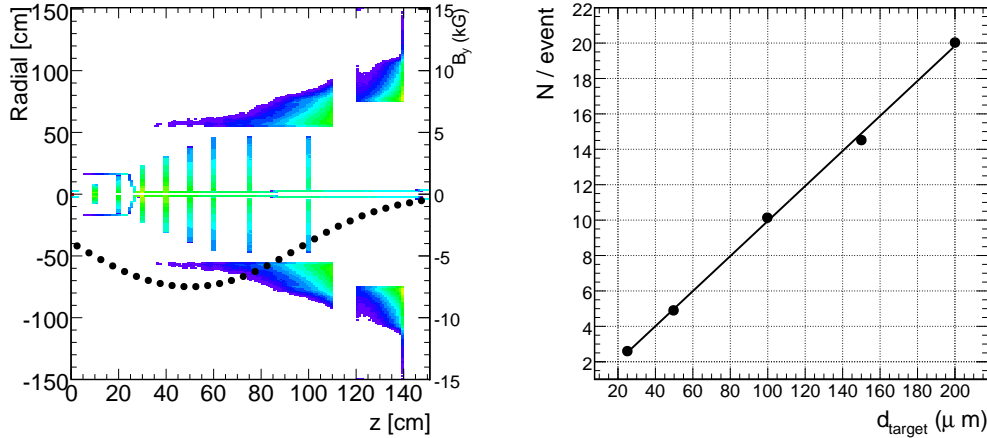


Figure 6.7: Left: Radial vs. longitudinal distribution of emission sites for positrons created through γ conversion. Contributions come from the target, the tracking stations, the beam pipe and the magnet yoke. The y component of the magnetic field is also shown (black circles). Right: Number of γ /event from conversion in the target material as a function of the target thickness.

As one can see from Fig. 6.7 (left panel), most of the photons from π^0 decay are converted outside the acceptance of the tracking stations, however a substantial background still arises from conversion in the target (see Fig. 6.7 (left panel), red spot at $R = 0$ cm, $z = 0$ cm). In order to minimize the number of e^\pm from γ conversion in the target, a single $25 \mu\text{m}$ thick (0.1% nuclear interaction length) gold target was used in the simulation. For example, with a $25 \mu\text{m}$ thick Au target, $365\pi^0$ produced in central $Au+Au$ collisions at $25 \text{ GeV}/u$ beam energy lead to about $7e^\pm$ pairs from the target (see Fig. 6.7, right panel); 4 from π^0 Dalitz decay, and 3 from γ conversion in the target. Note that the number of e^\pm from the π^0 Dalitz decay does not depend of the target thickness while the number of e^\pm from γ conversion of course does. This background source remains unchanged. A 1% nuclear interaction gold target could result in the conversion of about 25γ 's. When running CBM the usage of a segmented target could be discussed.

6.2 Event reconstruction

The CbmRoot simulation framework [148] allows full event reconstruction and particle identification. Simulated events are reconstructed using different track and ring reconstruction routines. For particle identification RICH, TRD and TOF information is combined for each track. Realistic detector response is taken into account as far as possible. Detector resolution and granularity are still implemented in a generic way not yet taking into account the detailed structures, detector response and the supporting material:

- **STS:** The current design of the double-sided micro-strip sensors foresees a stereo angle of $7 - 15^\circ$, a strip pitch of $50 - 60 \mu\text{m}$, a strip length between 20 and 60 mm, and a thickness of $200 - 300 \mu\text{m}$ of silicon. The total material budget including support structures and cables may amount to about $400 - 800 \mu\text{m}$ silicon equivalent, but is not homogeneously distributed. So far, the material of the stations has been implemented in the CBM

simulation and analysis framework as slices of silicon with a thickness equivalent to the total average material expected for a realistic detector. In the current simulation 2 MAPS detectors with the thickness of $200\ \mu\text{m}$, 2 Hybrid Pixel Detectors with $700\ \mu\text{m}$ thickness and 4 Strip detectors with $400\ \mu\text{m}$ thickness each are used. This results in a total thickness of $3.4\ \text{mm}$ silicon equivalent. During the hit digitization, a specific detector structure was projected onto the volumes.

- **RICH:** Values for photon absorption in the radiator gas, the reflectivity of the mirror and the quantum efficiency of the photodetector have been taken from existing experiments, literature, and Hamamatsu specifications. The detector granularity is taken from the H8500 MAPMT design, extra space for support frames is left.
- **TRD:** One layer of the TRD consists of a radiator, composed of polypropylene foils with air gaps, and a readout chamber filled with a Xe/CO₂ (85%/15%) mixture. A mylar foil of $25\ \mu\text{m}$ thickness acts as detector gas barrier. The simulated TR-radiation is tuned to measured data. No specific detector granularity is used but hits are smeared with a Gaussian assuming $200\ \mu\text{m}$ resolution in x and $300\ \mu\text{m}$ in y .
- **TOF:** The RPC of the TOF consists of Al-Gas-Glass-Gas-Al material layers with corresponding widths of $0.2 - 0.12 - 0.54 - 0.12 - 0.2\ \text{cm}$. The design and material budget were assumed similar to those of the ALICE-TOF detector [149]. The time resolution of $80\ \text{ps}$ was used in the simulation.

As it has been discussed in section 6.1.3 for the di-electron measurement special running conditions will be used. A single $25\ \mu\text{m}$ gold target is foreseen. The magnetic field is lowered to 70% of its nominal value and the size of the STS stations 1 to 6 is increased in order to increase the acceptance for low-momentum particles necessary for efficient rejection of di-electrons coming from γ conversion and Dalitz decay of π^0 .

6.3 Track reconstruction

A typical central $Au+Au$ collision in the CBM experiment will produce up to 700 tracks in the MVD station. The large track density together with the presence of a non-homogeneous magnetic field makes the reconstruction of events complicated. A cellular automaton method [150] is used to reconstruct tracks in the tracking system. This method creates short track segments (tracklets) in neighboring detector planes and links them into tracks. First, using all groups of neighboring chambers the algorithm generates a set of tracklets. A set of cuts, which reflect the geometrical acceptance of the detector system (e.g. forward tracks with minimum 4 consecutive hits), is applied to select tracklets corresponding to tracks with enough hits to be reconstructed. A reconstructed track is assigned to a generated particle, if at least 70% of its hits have been caused by this particle [151]. Track and vertex fitting have been done with a Kalman filter-based procedure [152, 153]. The Kalman filter-based algorithm reconstructs the primary vertex with an accuracy of $4\ \mu\text{m}$ for the longitudinal and better than $1\ \mu\text{m}$ for the transversal component of the primary vertex position.

The efficiency of the track reconstruction for particles detected in at least four stations is presented in Fig. 6.8, left panel. Tracks of high momentum particles are reconstructed very well with efficiencies of 99%. Considerable effort went into the problem of tracking in the STS for low momentum tracks because a large fraction of soft tracks suffers significantly from multiple

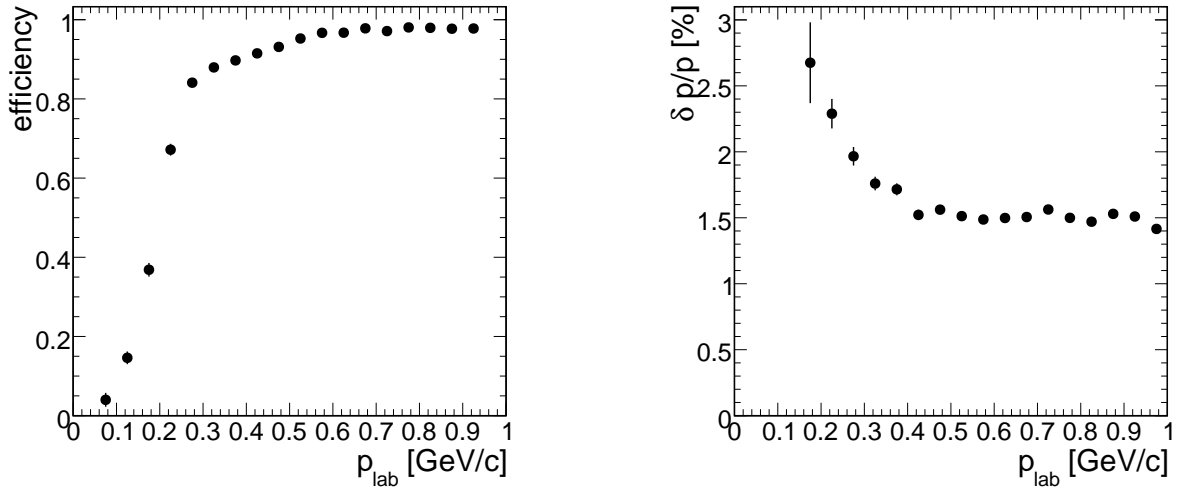


Figure 6.8: Track reconstruction efficiency ($p < 1$ GeV/c) for tracks coming from the target region (left panel); momentum resolution in the STS (right panel).

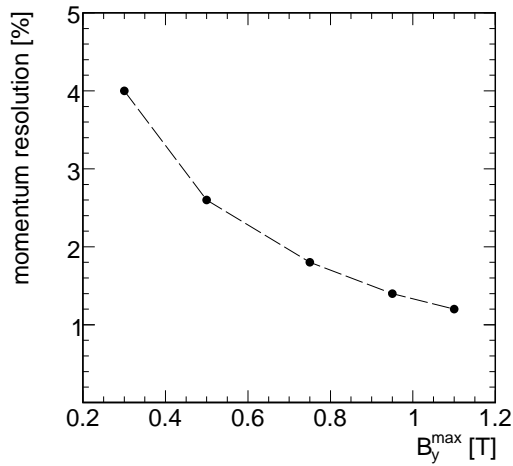


Figure 6.9: The momentum resolution integrated for a $p < 1$ GeV/c as a function of the maximum y component of the magnetic field value (B_y).

scattering in the detector material. This finally lead to a lower reconstruction efficiency of 89.5% integrated over momenta below 1 GeV/c. The reduction of the magnetic field to 70% of its nominal value results in a momentum resolution well below 2% (see Fig. 6.8, right panel) for $p > 300$ MeV/c. Further reduction of the magnetic field will reduce the momentum resolution more strongly, e.g. at $B_y^{\text{max}} = 0.3$ T the momentum resolution would increase up to 4% (see Fig. 6.9).

6.4 Electron identification

An important requirement for efficient background rejection is high efficiency and high purity of the identified electrons. The electron identification includes the full CBM detector setup, ring recognition and ring-track matching algorithms. The particle identification with the RICH detector is performed by a measurement of the Cherenkov angle/ring radius and the momentum of the particle determined in the STS. The RICH part of the particle identification requires the following steps:

- ring finding;
- ring center and ring radius determination;
- matching of rings with tracks.

A Hough Transform is used for ring reconstruction providing $\sim 90\%$ efficiency (see Fig. 6.14, magenta line). All reconstructed tracks are reflected at the mirror in order to give the center of a Cherenkov ring. A rather large material budget is located in front of the RICH detector, therefore most rings stem from secondary electrons produced upstream. Electron tracks coming from γ conversion in the STS material or in the magnet yoke very often are not reconstructed by the tracking system.

Due to the high track density another hadron track from the primary vertex (mostly pions) extrapolated to the photodetector could be matched to the ring. Each ring is matched to a track based on combining ring-track pairs with the smallest distance between the ring center and the track extrapolation. The large number of reconstructed primary tracks and the high ring densities lead to a certain probability of accidental ring-track mismatches. The distance between the track extrapolation and the ring center as a function of the reconstructed momentum is shown in Fig. 6.10. For comparison, the distance between track extrapolation and ring center as a function of momentum for truly matched electrons is shown in the right panel of Fig. 6.10. A

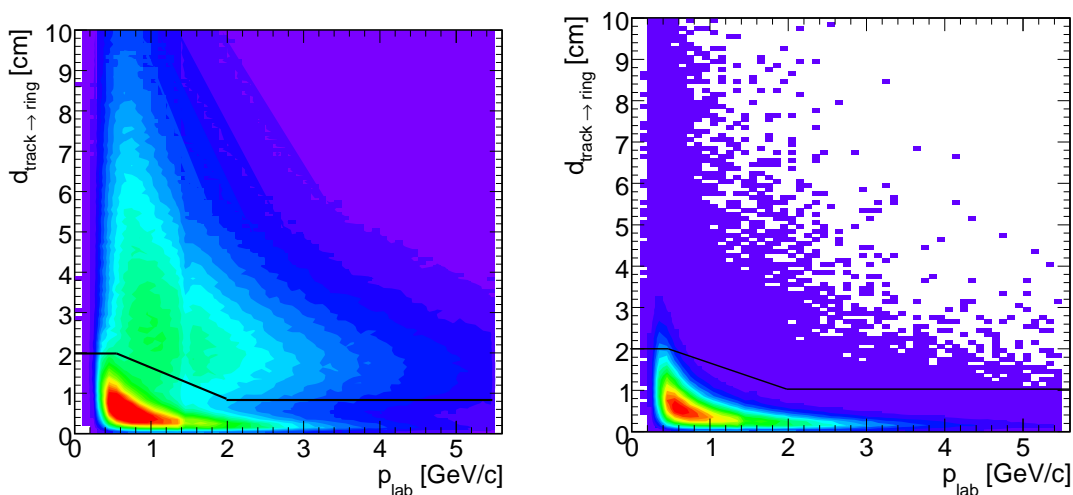


Figure 6.10: Distance between track extrapolation and ring center as a function of reconstructed momentum. Left: all matches, right: truly identified electrons. The black line indicates the cut region.

momentum dependent cut is applied to reject mismatches. A cut at 2 cm for momenta below 0.5 GeV/c and 1 cm for momenta above 2 GeV/c rejects $\leq 2\%$ truly identified electrons but most of the mismatches.

Another background source are fake rings. In particular in the inner region of the photodetector ring densities are very high leading to the creation of fake rings from random combinations of close hits. As the fake rings differ from true ones, e.g. by the hit distribution along the ring, trained artificial neural networks were used in order to suppress fake rings. The following ring parameters were found to be essential for a successful rejection of fake rings: the number of hits in a narrow corridor around the ring, the hit distribution along the ring, the number of hits on the ring, the distance between closest track projection and ring center, and the radial position of the ring on the photodetector plane. The trained neural network gives continuous output values between -1 and 1 , -1 resembles wrong, $+1$ good electron rings. A cut value of -0.5 was selected (see Fig. 6.11, left panel), rejecting 1% of true electron rings. After the ring quality and ring-track matching quality cuts, electrons are chosen by a $\pm 3\sigma$ cut around the mean electron radius (see Fig. 6.11, right panel) [154].

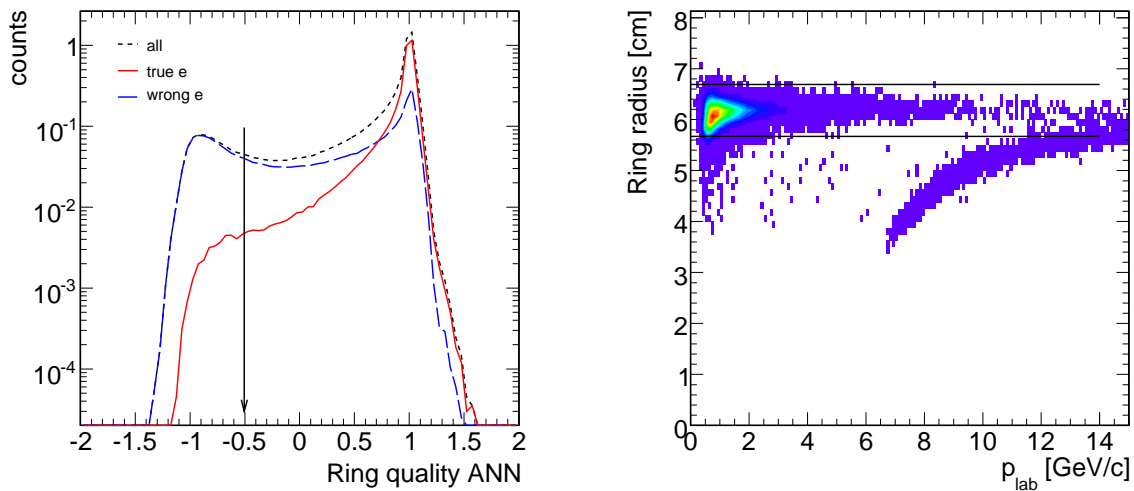


Figure 6.11: Rich ring quality selection with artificial neural network, -1 = wrong electrons, $+1$ = true electrons (left panel). Radius versus momentum for reconstructed rings (right panel).

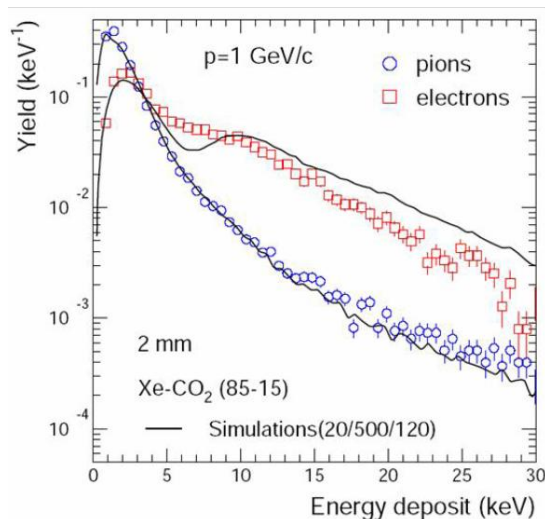


Figure 6.12: Energy loss of pions and electrons at 1.5 GeV/c momentum measured for a single TRD layer.

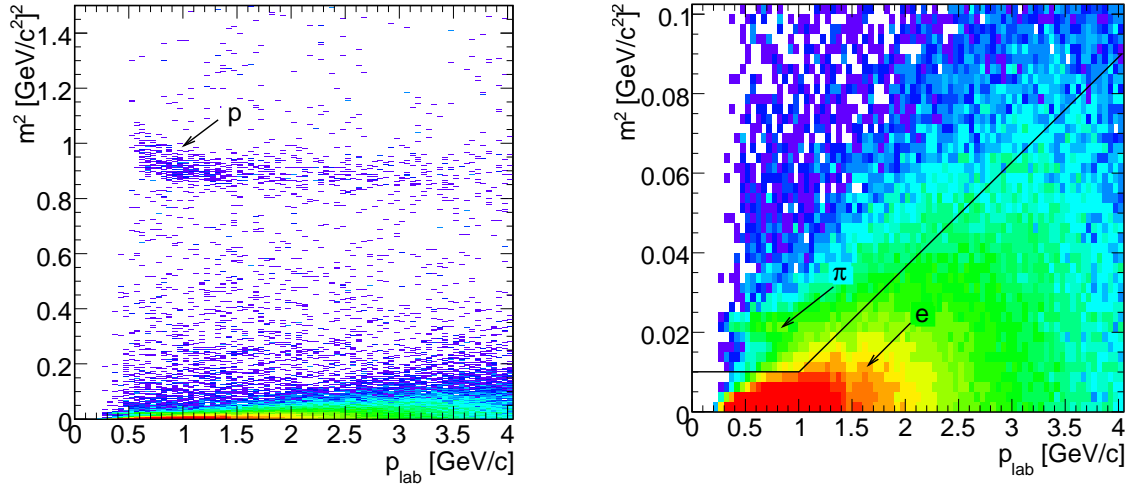


Figure 6.13: Left: Squared mass versus momentum measured in the TOF wall after electron identification in RICH. Right: a zoom into the electron and pion region is shown. The black line indicates the cut region.

The resulting misidentification of electrons is due to ring-track mismatches typically of rings from secondary electrons with hadron tracks from the primary vertex. These misidentified electrons can be further suppressed by using information from the TRD and TOF detectors. Tracks reconstructed in the STS and identified as electrons in the RICH are prolonged through the TRD stations and matched to hits in the TOF detector. The contribution of misidentified pions can be suppressed to below 10^{-4} including a statistical analysis of the energy loss spectra in the 12 TRD layers (see Fig. 6.12). The combined electron identification efficiency is reduced by 10% for $p > 2 \text{ GeV}/c$. Mismatches of proton tracks to electron rings can be fully eliminated using TOF information see Fig. 6.13, left panel. In addition, pions with momenta below $1 \text{ GeV}/c$ can be further suppressed (see Fig. 6.13, right panel). The squared mass of charged particles m^2 is calculated from the length traversed by the particle and the measured time of flight. A momentum dependent squared mass cut was applied to the tracks being reconstructed and identified as electrons in the RICH and TRD detectors.

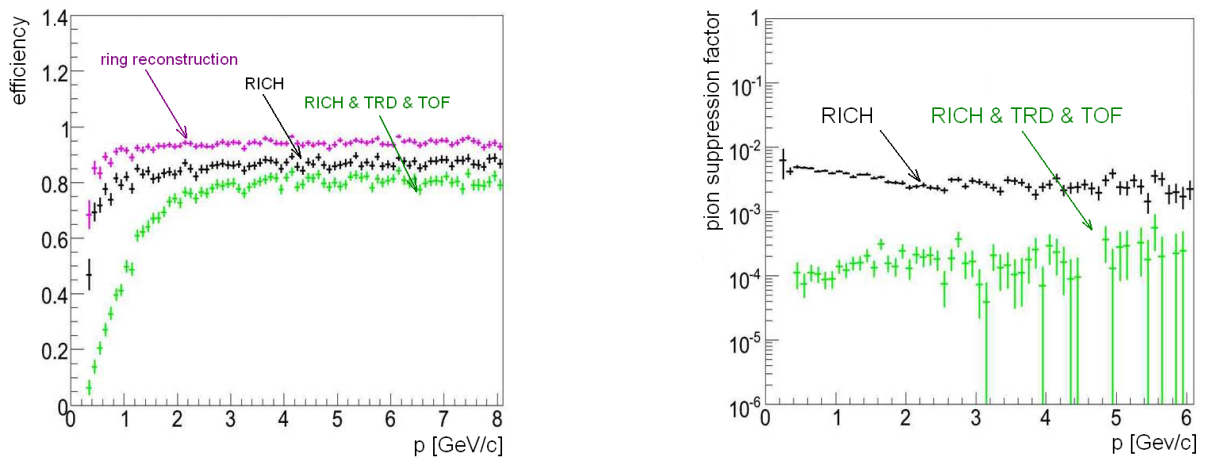


Figure 6.14: Left: Electron identification efficiency: magenta line - ring reconstruction efficiency. Right: Pion suppression factor. Black line: identification efficiency and pion suppression using RICH information only, green line: combination of RICH, TRD and TOF.

After the combined electron identification, each of the identified tracks is associated to its Monte Carlo information for studying the quality assessment of the electron identification. Important quantities are:

$$\text{Efficiency} = \frac{\text{truly identified electrons}}{\text{electrons in RICH acceptance}},$$

and

$$\text{Pion suppression} = \frac{\text{pions identified as electrons}}{\text{pions in RICH acceptance}}.$$

The electron identification efficiency as a function of track momentum is shown in Fig. 6.14 (left panel). After the full identification procedure, close to 80% of electron efficiency is achieved for $p > 2 \text{ GeV}/c$. The drop in efficiency towards low momentum, e.g. for $p < 1 \text{ GeV}/c$ the electron reconstruction efficiency is 40% only, results from tracking, ring finding efficiencies, and TRD and TOF acceptance losses compared to the RICH detector. The pion suppression using only RICH information is about 500. A suppression factor of 10^{-4} (see Fig. 6.14) with an electron efficiency of $\sim 50\%$ for $p < 2 \text{ GeV}/c$ and 80% for $p > 2 \text{ GeV}/c$ is achieved when including a momentum dependent squared mass cut from TOF information and a cut on the statistical analysis of the energy loss spectra in the 12 TRD layers.

6.5 Background rejection strategy

Losing one glove is certainly painful, but nothing compared to the pain, of losing one, throwing away the other, and finding the first one again.

(Piet Hein - Grooks)

The main task of the analysis is to recognize and reject as many of the partially reconstructed leptons from γ conversion and π^0 Dalitz decays as possible (Track Fragments, Track Segments see section 6.1.2). Fig. 6.15 shows the combinatorial background topology. In case the Track Fragment can not be found or the Track Segment can not be reconstructed by the track reconstruction procedure, Global Tracks (tracks identified as electrons) from two different processes will contribute to the e^+ and e^- sample. It is very difficult to reject such tracks, since their properties are too similar to the signature of signal tracks.

The strategy of background rejection comprises three steps. The first step is to identify and reject true pairs originating from γ conversion, the second step is to remove single tracks where the true partner was not fully reconstructed, the third step is to assign pairs with a characteristic pattern to π^0 Dalitz pairs which then are filled to the histograms but not used for combinatorics any more. A transverse momentum cut on single tracks might be used. The cuts to be described in the following sections are not optimized in a strict sense, i.e. by maximizing the significance in the final invariant mass spectrum. Instead, reasonable cut values are chosen by comparing the signal to the main background source. The cut values can be changed depending on the physics interest.

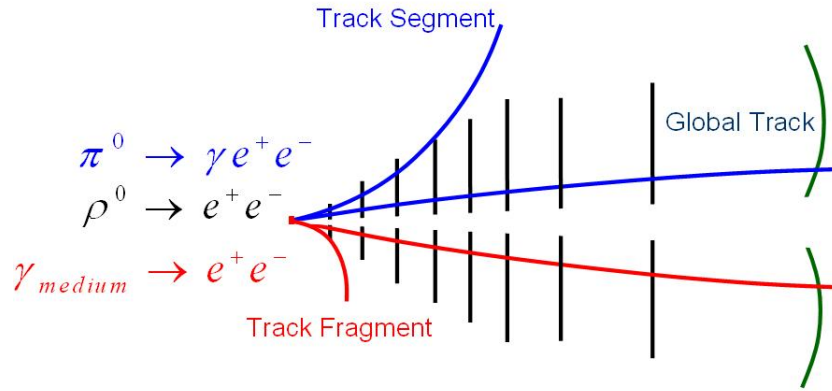


Figure 6.15: Topology of the combinatorial background. Blue: tracks from π^0 Dalitz decay, red: tracks from γ conversion. Schematic view of the MVD and STS (black line), and the RICH detector (green line).

6.5.1 Conversion pair cut

From the right panel in Fig. 6.4 it can be seen that 30% of the electron pairs originating from conversion in the target are fully reconstructed. Conversion pairs have very small invariant masses and are thus essentially located below $25 \text{ MeV}/c^2$ (see Fig. 6.16, left panel). In this analysis, we assume that all reconstructed pairs which have an invariant mass smaller than $25 \text{ GeV}/c^2$ stem from γ conversion. Tracks forming such pairs are fully removed from the sample in this first step. By the γ cut combinatorial background can be suppressed by 20%, γ conversion pairs by more than 3 orders of magnitude.

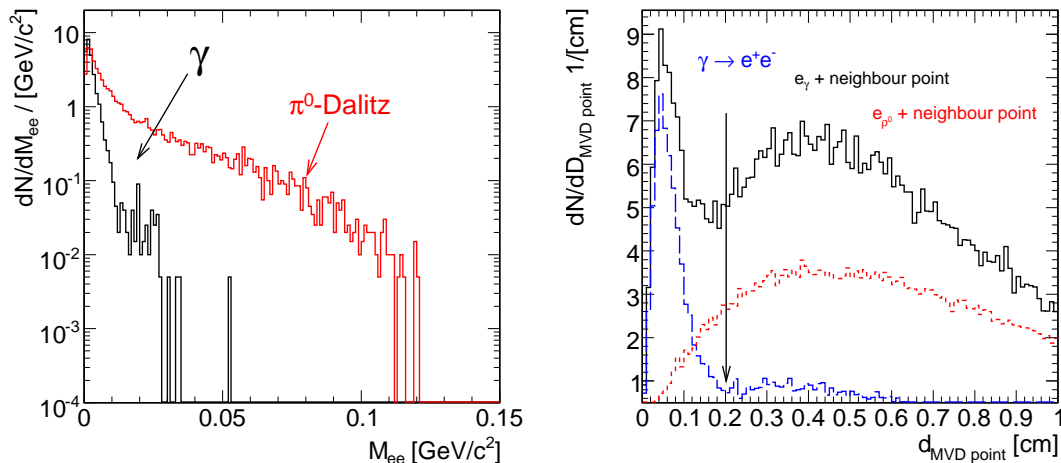


Figure 6.16: Left: Invariant mass spectra of reconstructed e^+e^- from π^0 Dalitz (red) and γ (black). Right: Distance to the nearest neighbor hit in the 1st MVD station. The magnetic field is even reduced to 30% of its nominal value. Black: $e_\gamma +$ closest MVD hit; blue: true γ conversion; red: $e_{\rho^0} +$ closest MVD hit, scaled by factor 200. The figure shows the distribution after the previous (γ) cut. The black line indicates the chosen cut value.

6.5.2 Single track cuts

Hit topology cut

An important characteristic for conversion pairs is the small opening angle. Since the integrated magnetic field between target and the first MVD station is small, the distance between the partners remains small up to the first 10 cm. If one track of a pair was not even reconstructed as a Track Segment but only left a hit in the first MVD, this feature can be used. To reject the remaining track of such a pair we inspect the vicinity of the Full Track in the first MVD station.

Fig. 6.16 (right panel) shows the distance between the intersection point of an electron track in the first MVD station to its nearest neighbor hit. For this study the magnetic field was reduced to 30% of its nominal value. The distance between e^+ and e^- coming from γ conversions is shown in blue and peaks at small distances (d_{MVD}). Random combinations (combinations between e^\pm from γ conversion or e^\pm from ρ^0 decay with a MVD hit from any Track Fragment) appear at larger distances ($d_{\text{MVD}} = 400 \mu\text{m}$). The distance between electrons from ρ meson decay is about $400 \mu\text{m}$ due to the large opening angle (opening angle for the ρ decay is about 30°). Contributions of γ conversion can be strongly suppressed by removing all pairs with d_{MVD} smaller than $200 \mu\text{m}$. This first analysis, however, was based on generic simulations without realistic detector response. No track reconstruction was performed and ideal electron identification was assumed.

As discussed in section 6.1.3, the magnetic field can be decreased to 70% only in order to keep the momentum resolution below 2% (see Fig. 6.9). Still, the acceptance for low momentum particles is increased compared to the full field. With a decrease to 70%, the clear signature of Fig. 6.16 (right panel) is washed out as e^+/e^- from γ conversion are already too far apart after 10 cm. Additional momentum information from the reconstructed track can be used. Fig. 6.17 shows the distance between the intersection point of an electron track in the first MVD station to its nearest neighbor hit (which was not assigned to any track) as a function of momentum of the fully identified electron track for different sources of lepton tracks. Since no particle ID nor even a charge can be assigned to this next neighbor hit all charged particles can

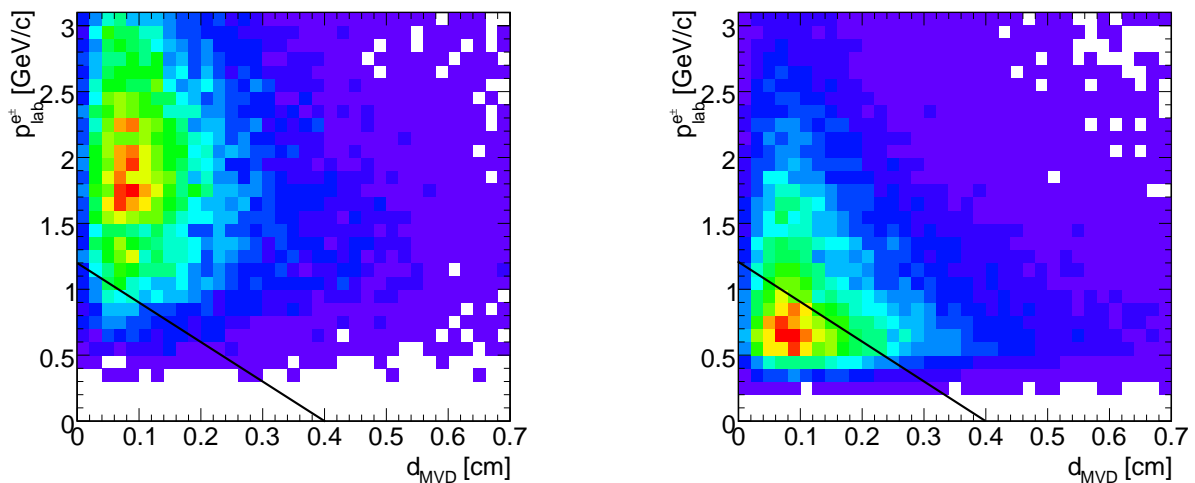


Figure 6.17: Distance to nearest neighbor hit in the 1st MVD station versus momentum of the fully identified e^\pm from ρ^0 (left panel) and from γ (right panel). Black line indicates the cut region.

potentially appear as fake partners. Hence, in particular in the region of highest track density, a cut on d_{MVD} alone can substantially remove signal tracks. Tracks will be removed if d_{MVD} is below 0.4 cm and the momentum of the fully identified electron is below 1.2 GeV/c. An optimization of this cut will further reject background coming from γ conversion. By the d_{MVD} cut combinatorial background can be suppressed by 25%.

One strategy under discussion is to suppress the magnetic field only in the region between target and first MVD station. The excellent two hit resolution in the MAPS detector ($< 100 \mu\text{m}$) gives then a chance to reject close pairs. This analysis, however, has to be studied in more detail based on realistic simulations. A realistic concept how to suppress the magnetic field between the target and first MVD has to be worked out. The rejection power of conversion pairs could potentially be improved by using energy loss information in the first MVD. However, particle identification in a thin silicon layer turns to be very challenging [155].

Track topology cut

As can be seen from Fig. 6.17 still a large fraction of conversion tracks survive the cut described before. In the next step we try to identify true partners of background tracks which survive the previous cut (hit topology cut) in the class of Track Segments. On the Track Segment level information about particle momentum and charge is available, but there is still no information on particle identification. We use information about the opening angle between an identified electron track to its closest neighbor Track Segment ($\theta_{e^\pm, \text{rec}}$) and the product of the e^\pm momentum and the Track Segment momentum ($\sqrt{p_{e^\pm} \cdot p_{\text{rec}}}$). Fig. 6.18 shows the correlation between $\theta_{e^\pm, \text{rec}}$ and $\sqrt{p_{e^\pm} \cdot p_{\text{rec}}}$ for different sources of identified electron tracks.

A wedge cut as indicated in Fig. 6.18 is used to reject background. The ratio (number of combinations in the cut region/total number of combinations) was calculated for different combinations (signal electron track ($e_{\rho^0}^\pm$) + closest neighbor, background track ($e_{\pi^0}^\pm$ or e_γ^\pm) + closest neighbor). An optimum value was reached for $\theta_{e^\pm, \text{rec}}$ below 2° and $\sqrt{p_{e^\pm} \cdot p_{\text{rec}}}$ below

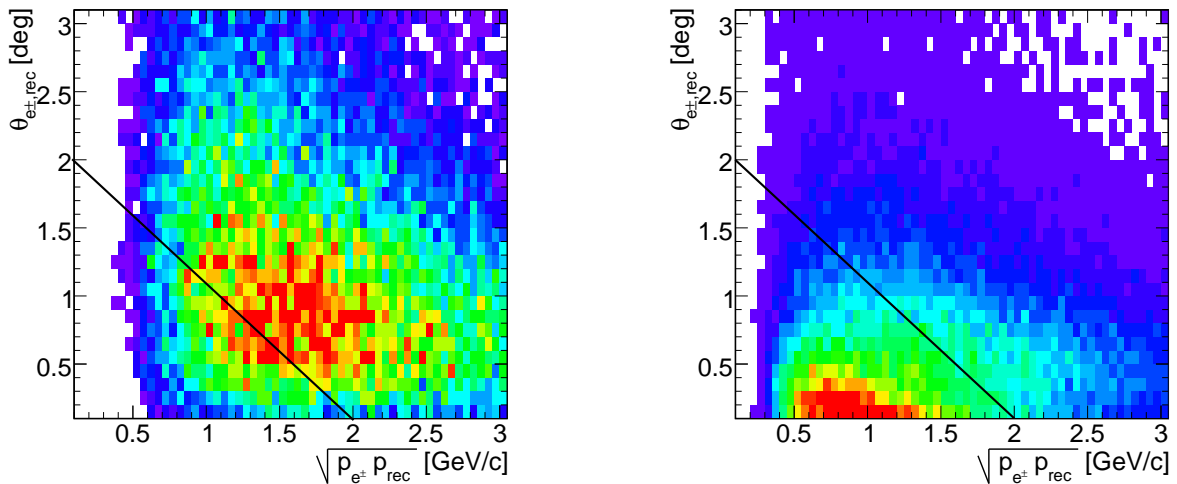


Figure 6.18: Correlation between $\theta_{e^\pm, \text{rec}}$ vs. $\sqrt{p_{e^\pm} \cdot p_{\text{rec}}}$. The distribution is separately shown for cases where the Full Track stems from ρ^0 (left panel) and photon conversion (right panel), respectively. The figure shows the distribution after the previous cuts. Tracks belonging to a pair inside the triangle are rejected.

$2 \text{ GeV}/c$. If the properties of any pair lie below a combination of these cut values, the identified electron track is rejected. This cut remove successfully a large fraction of identified electrons from π^0 Dalitz decay and also γ conversion, i.e. 80% of those background tracks. Just 10% of the total combinatorial background survive after this cut, but 50% of the ρ meson and 80% of ω and ϕ .

Transverse momentum of identified leptons

Finally we exploit the transverse momentum of fully reconstructed tracks. Again, due to the small decay momentum and the strong exponential fall-off of the pion center-of-mass momentum the lepton tracks from the background sources are predominantly at low p_t . As it has been discussed in section 1.1.3 (see Fig. 1.4) the ρ -meson spectral function shows that in the region of small p_t medium effects might enhance the strength of ρ -meson like states. A comparatively high transverse momentum cut-off will exclude a substantial part of the phase space where the modification of the ρ meson spectral function is expected to be most prominent. Fig. 6.19 (left panel) shows the transverse momentum distributions of fully reconstructed tracks. By removing tracks with $p_t \leq 0.2 \text{ MeV}/c$ one significantly lowers the combinatorial background (only 3 – 10% of the background still contribute into the pair sample) but at the expense of rejecting also an interesting region of the phase space. Such a cut also removes a further large fraction of contributions to the signal invariant mass spectrum originating from Dalitz-decay sources, i.e. π^0 ($\varepsilon = 2\%$), η ($\varepsilon = 5\%$), ω ($\varepsilon = 7\%$). The transverse momentum cut thus has to be applied with care (see section 7.2).

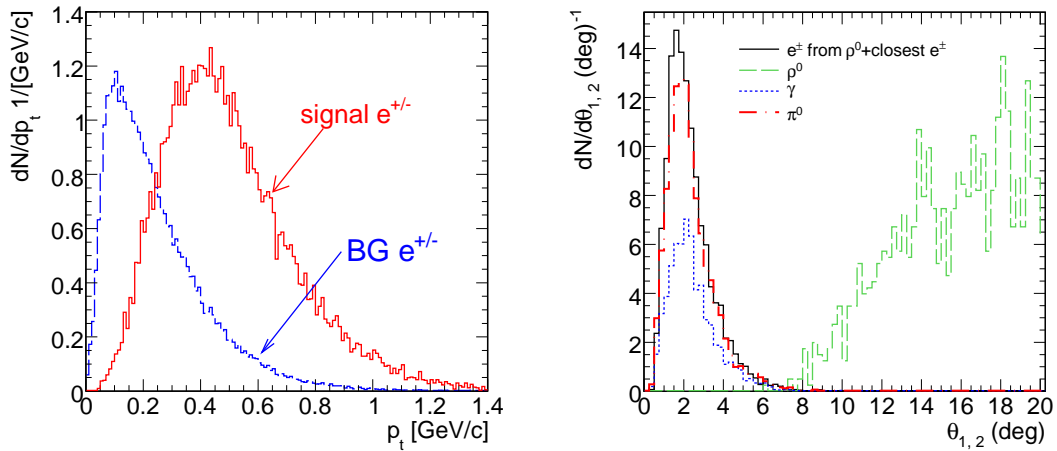


Figure 6.19: Left: Transverse momentum distribution. Red: leptons from background sources, blue: leptons from signal (enhanced by factor of 1000). The cut value is $0.2 \text{ GeV}/c$. The figure shows the distributions after all previous cuts. Right: Opening angle distribution for electron pairs from π^0 Dalitz decay (red), γ conversion (green), η Dalitz decay (blue) and ρ^0 decay (magenta). The figure shows the distribution after all previous cuts.

6.5.3 Pair cuts

Opening angle cut

The main interest of low-mass pair spectroscopy is to reconstruct ρ^0 , ω and ϕ mesons. In case these vector mesons decay exclusively into a pair of electrons, the rest mass of the meson is fully transformed into decay momentum. Hence these pairs will generally appear with a considerable opening angle (see Fig. 6.3, left panel). In contrast, pairs from γ conversion and also from Dalitz decays of light mesons feature small opening angles. Fig. 6.19 (right panel) shows the opening angle distributions for a number of different sources. Note the strong rise towards small opening angles for all but the exclusive vector meson decays. In the analysis electron-positron pairs with an opening angle of $\theta_{1,2} \leq 2^\circ$ are removed. The efficiency of the opening angle cut is very small. This cut mainly removes contribution from π^0 Dalitz decay (1%) and rejects very little of the combinatorial background (below 1%).

π^0 Dalitz decay reconstruction

Finally, pairs with an invariant mass below $0.2 \text{ GeV}/c^2$ are assumed to stem from π^0 Dalitz decays. The respective invariant mass is filled to the histogram but the corresponding tracks are not further used to form other pairs.

All cuts established for background rejection are summarized in Table 6.2 in the order they are applied.

Cut type	Cut name	Cut value
pair cut	small invariant mass cut (γ conversion cut)	$0.025 \text{ GeV}/c^2$
single track cut	d_{MVD} vs. p_{e^\pm} (hit topology cut)	0.4 cm and $1.2 \text{ GeV}/c$
single track cut	$\theta_{e^\pm, \text{rec}}$ vs. $\sqrt{p_{e^\pm} \cdot p_{\text{rec}}}$ (track topology cut)	2° and $2 \text{ GeV}/c$
single track cut	cut on p_t of identified leptons (p_t cut)	$0.2 \text{ GeV}/c$
pair cut	opening angle cut	2°
pair cut	π^0 Dalitz decay reconstruction	$0.2 \text{ GeV}/c^2$

Table 6.2: Cuts established for background rejection and their optimized cut values.

Chapter 7

Results

7.1 Mass spectra

The invariant mass spectrum of electron pairs including full event reconstruction and electron identification after applying background rejection cuts is shown in Fig. 7.1 (right panel). For comparison, the respective contribution before background rejection is shown in the left panel Fig. 7.1. The cut efficiency is shown in Fig. 7.2 separately for each analysis step and for three different invariant mass regions:

- $0 < M_{ee}/(\text{GeV}/c^2) < 0.2$ - region dominated by π^0 Dalitz;
- $0.2 < M_{ee}/(\text{GeV}/c^2) < 0.6$ - region in which an enhancement of dileptons is expected due to medium contributions ("enhancement region");
- $0.6 < M_{ee}/(\text{GeV}/c^2) < 0.9$ - ω, ϕ region.

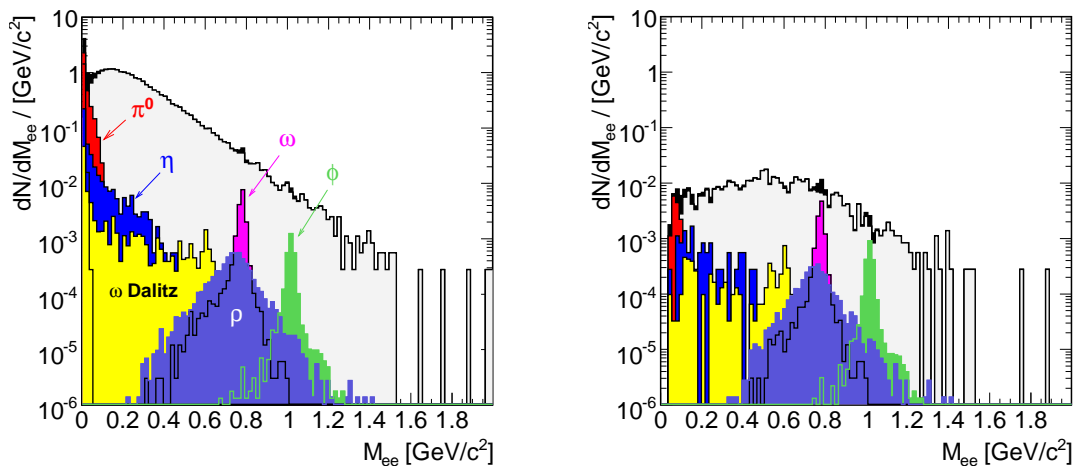


Figure 7.1: Invariant mass spectra before (left panel) and after (right panel) all cuts. The simulation was performed for $2 \cdot 10^5$ central $Au+Au$ collisions at $25 \text{ GeV}/u$. From left to right the different contributions are shown: red: π^0 Dalitz, dark green: γ , dark blue: η Dalitz, blue: ω Dalitz, magenta: ω , green: ρ^0 , violet: ϕ , black fill: all e^+e^- pairs, grey fill: combinatorial background.

It is defined as the ratio of background (or signal) contribution after the rejection cut to background (or signal) contribution before any cut has been applied. As signal all correlated pairs originating from one source (π^0 , η , ω Dalitz decay, ρ , ω , ϕ direct decay) are counted. The combinatorial background is generated by random combinations between e^+ and e^- from different dilepton sources as well as misidentified tracks. 100% of the signal or background efficiency corresponds to the number of identified pairs. For clarity, the cut efficiency for each signal source (correlated e^+e^- pairs) is shown in Fig. 7.3.

The most effective cuts to reduce background in the enhancement region (i.e. $0.2 < M_{ee}/(\text{GeV}/c^2) < 0.6$) are the Track Topology cuts (d_{MVD} and $\theta_{e^\pm, \text{rec}}$ vs. $\sqrt{p_{e^\pm} \cdot p_{\text{rec}}}$ discussed in section 6.5.2) and the cut on the single track transverse momentum (p_t). It should be noted however, that these cuts at the same time remove a substantial part of the π^0 , η , ω Dalitz contributions (see Fig. 7.3). The final decision on whether to apply the p_t cut or not will also be driven by the final physics focus on the pair spectrum. In contrast, the opening angle cut does not effect the background contribution in the enhancement region although more than 60% of the remaining Dalitz pairs are removed.

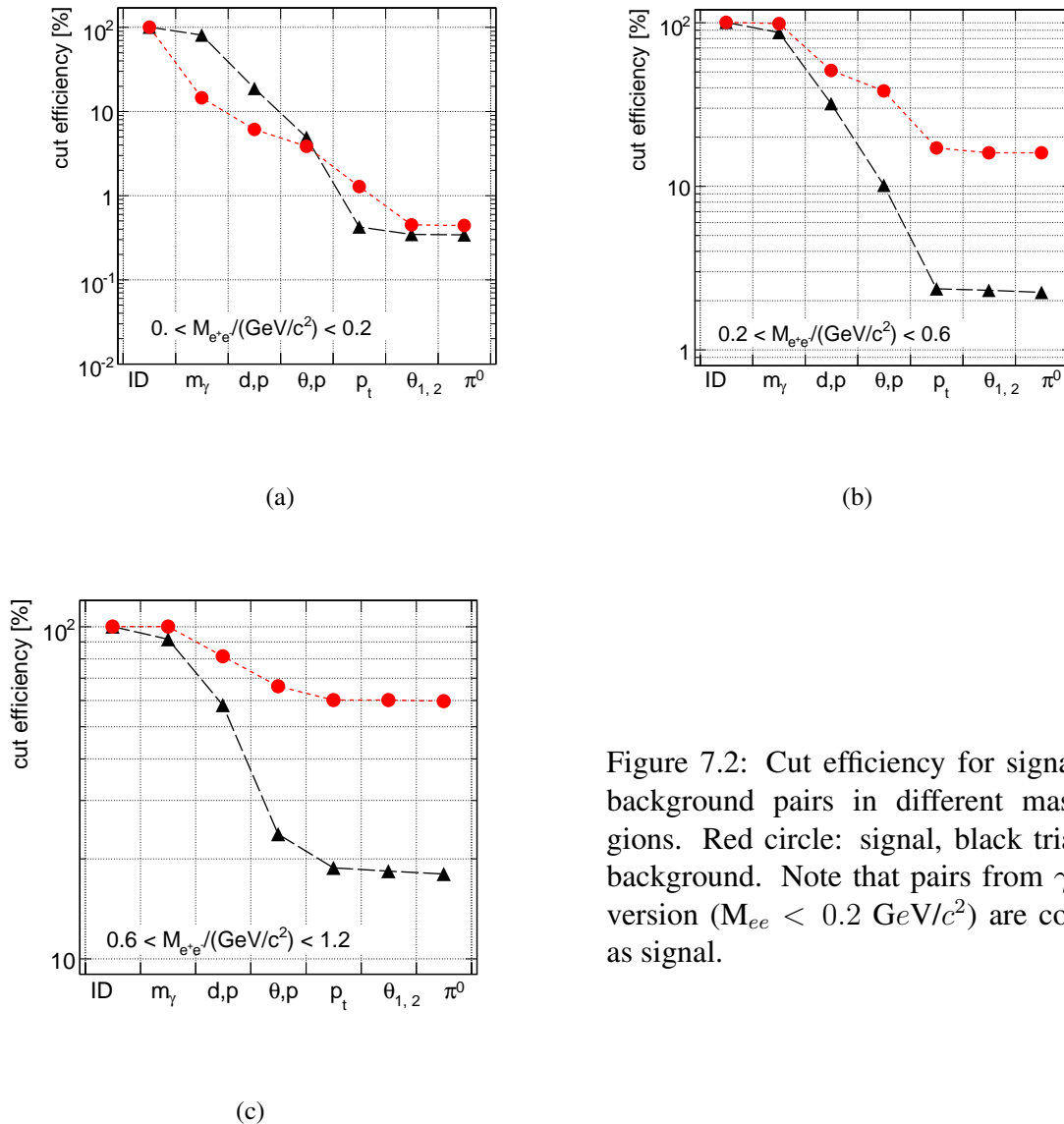


Figure 7.2: Cut efficiency for signal and background pairs in different mass regions. Red circle: signal, black triangle: background. Note that pairs from γ conversion ($M_{ee} < 0.2 \text{ GeV}/c^2$) are counted as signal.

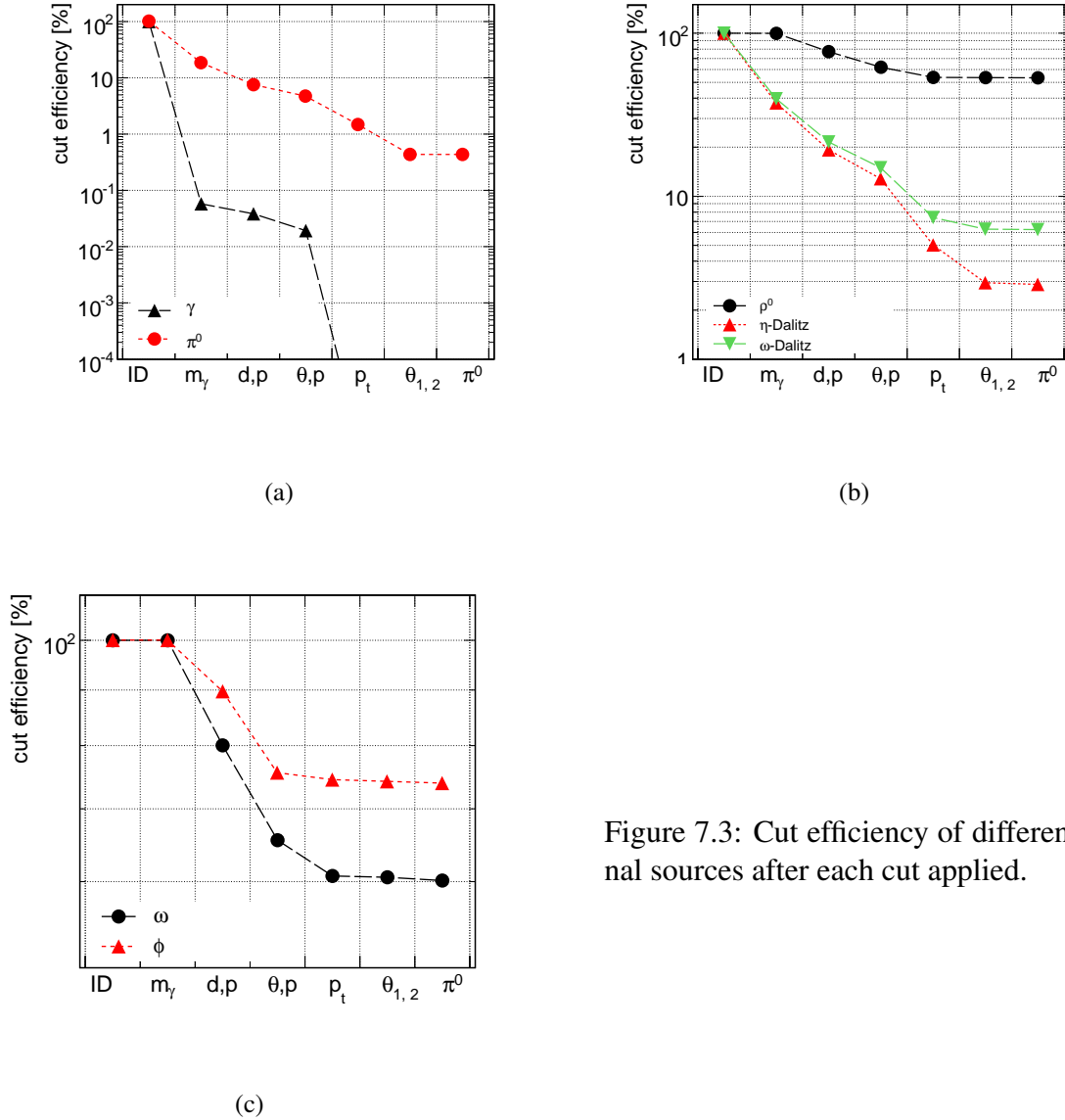


Figure 7.3: Cut efficiency of different signal sources after each cut applied.

The systematic behaviour of the Signal-to-Background (S/B) ratio is shown in Fig. 7.4. In the vector meson mass region, the S/B ratio steadily increases with each cut applied. At this level of background rejection, the maximum of the ω peak is just touching the combinatorial background. Indeed, the ω and ϕ signal are visible above the combinatorial background. The S/B ratio in a $\pm 2\sigma_m$ range around the ω pole mass is 0.4 at a total signal efficiency of 6.7%. For the invariant mass region above $200 \text{ MeV}/c^2$ an integrated S/B ratio of 1/16 is obtained.

The same analysis strategy was applied for electron pair reconstruction in central $Au+Au$ collisions at 15 and 35 GeV/u beam energy. The invariant mass spectra of electron pairs including full event reconstruction and electron identification before (left panel) and after (right panel) applying background rejection cuts is shown in Fig. 7.5 and Fig. 7.6. The event statistics ($6.5 \cdot 10^4$) is more than a factor 2 smaller compared to the central $Au+Au$ collisions at 25 GeV/u . The S/B ratio for the three beam energies is depicted in Fig. 7.4 (right panel). Particle multiplicities at lower energies decrease as shown in Table 7.1. This of course reduces the signal and combinatorial background at the same time. However, the signal decreases linearly while the background goes down quadratically. Therefore the S/B ratio is typically higher at lower

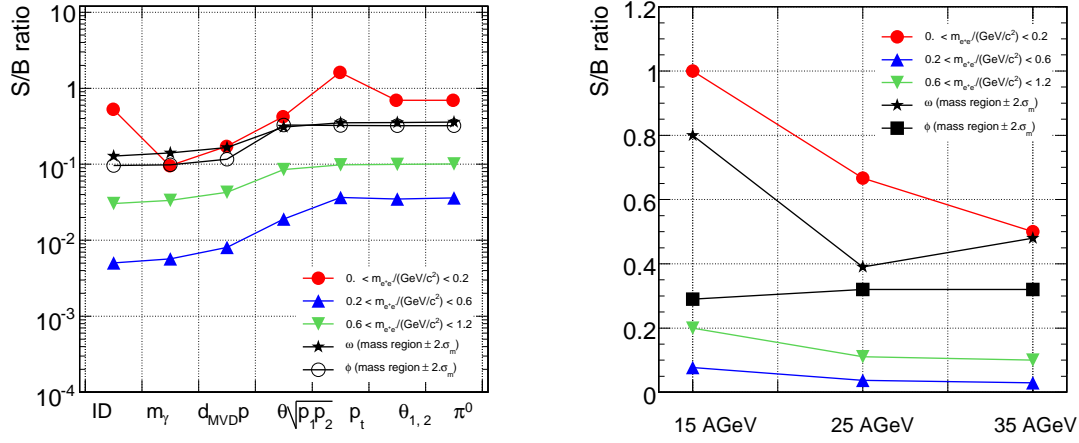


Figure 7.4: Left: Signal-to-background ratio as a function of cut type. Right: Signal-to-background ratio for central $Au+Au$ collisions at different beam energies after all cuts have been applied.

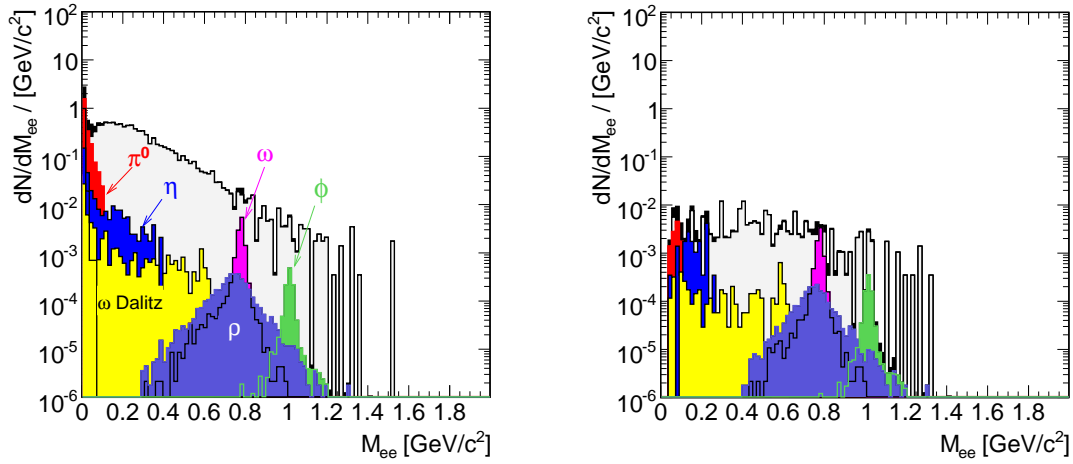


Figure 7.5: Invariant mass spectra before (left panel) and after (right panel) all cuts for $6.5 \cdot 10^4$ central $Au+Au$ collisions at $15 \text{ GeV}/u$. From left to right the different contributions are shown: red: π^0 Dalitz, dark green: γ , dark blue: η Dalitz, blue: ω Dalitz, magenta: ω , green: ρ^0 , violet: ϕ , black fill: all e^+e^- pairs, grey fill: combinatorial background.

energies. The larger increase from 15 to 25 GeV/u beam energy compared to the one from 25 to 35 GeV/u is due to the fact that the pion multiplicity increases by 27% in the first and only by 13% in the second step.

As shown in Fig. 7.7 (left panel), the combinatorial background after background rejection cuts is dominated by the physical background, mostly by e^+e^- from Dalitz decay of π^0 (see Fig. 7.7, right panel). The reconstructed neutral pions, however, predominantly appear at higher p_t very similar to signal p_t . This leads to a difficulties in the further suppression of the combinatorial background. The background from misidentified particles and fake rings is of an approximately same size, even somewhat smaller compared to the background from the physical source.

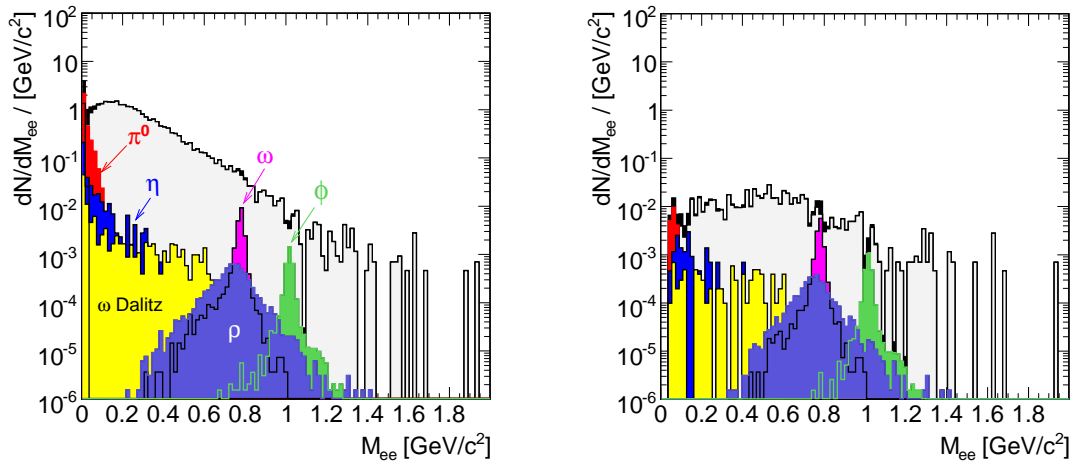


Figure 7.6: Invariant mass spectra before (left panel) and after (right panel) all cuts for $6.5 \cdot 10^4$ central $Au+Au$ collisions at $35 \text{ GeV}/u$. From left to right the different contributions are shown: red: π^0 Dalitz, dark green: γ , dark blue: η Dalitz, blue: ω Dalitz, magenta: ω , green: ρ^0 , violet: ϕ , black fill: all e^+e^- pairs, grey fill: combinatorial background.

particle	15 GeV/u	25 GeV/u	35 GeV/u
π^0	264	365	382
π^+	261	332	386
π^-	293	386	423
η	23	36	40
ω	27	38	46
ρ^0	15	23	26
ϕ	0.5	1.28	1.5

Table 7.1: Mean pion and vector meson multiplicities from UrQMD for central $Au+Au$ collisions at 15, 25 and 35 GeV/u beam energy.

7.2 The phase space coverage

Fig. 7.8 shows the transverse momentum versus rapidity distribution of detected electron pairs from ρ^0 meson decays. Note that neither the detector geometrical acceptance nor the analysis procedure does introduce phase space limitations (good coverage of the midrapidity region) for the reconstruction of vector mesons. The reconstructed electron pairs from π^0 Dalitz decay predominantly appear at higher p_t .

However, a wide phase space coverage in the transverse momentum-rapidity plane is not the only distribution that has to be carefully controlled. It is expected that electromagnetic radiation from the dense phase of the collision appears at low transverse momentum: pion-pion fusion which is being the dominant process for populating ρ -like states in a hot pion gas will favor ρ mesons located at low invariant mass and low transverse momentum. The acceptance of signal pairs in the p_t -mass plane from the NA60 and CERES dilepton experiments is shown in Fig. 7.9. Both experiments have difficulties to access low pair p_t and low masses at the same time. The NA60 experiment measures low-mass vector mesons via their electromagnetic decay to muons using the muon absorber technique. This technique works perfectly well for high momentum muons, the major difficulty for NA60 lies in the identification of low-momentum

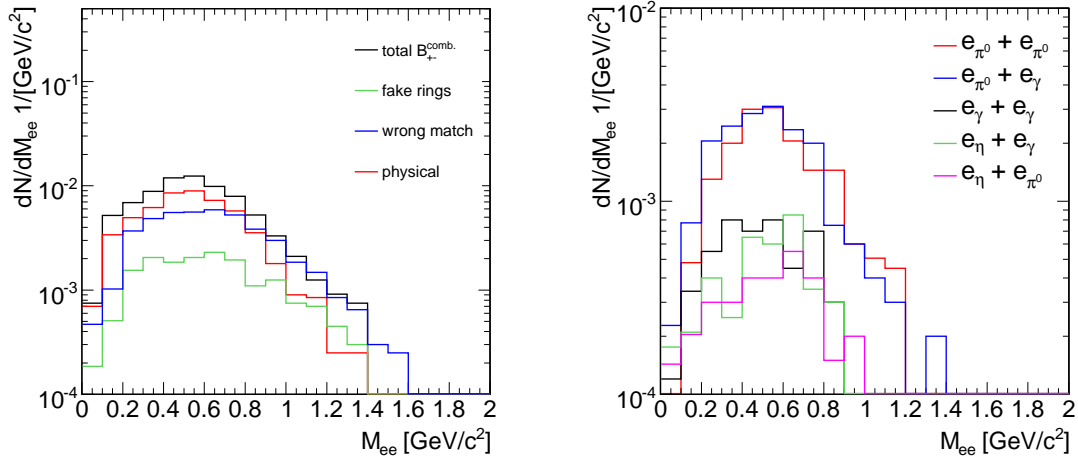


Figure 7.7: Left: Combinatorial background cocktail. Right: Detail composition of the combinatorial background contributing to the physical sources. All identification and background rejection cuts are applied.

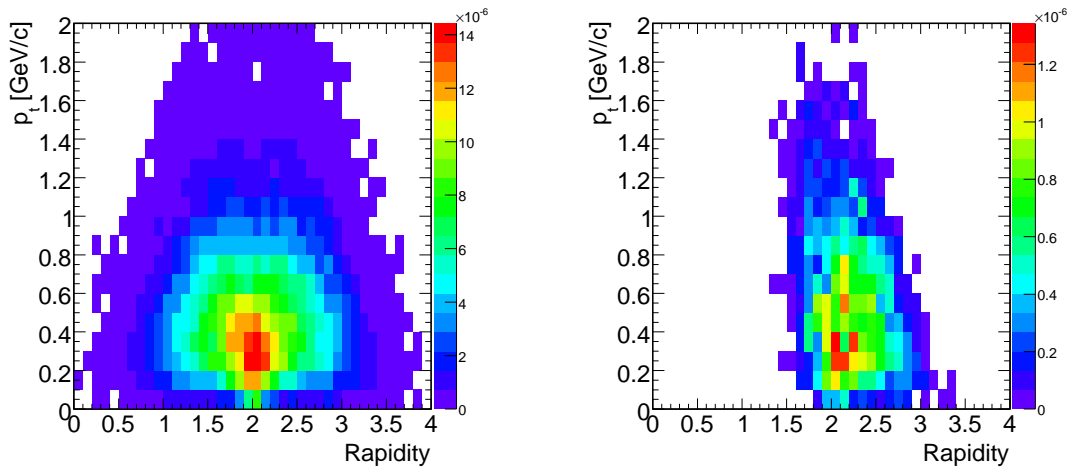


Figure 7.8: Transverse momentum versus rapidity distribution for ρ^0 in the full phase space (left panel) and after all cuts (right panel) for 2×10^5 central $Au+Au$ collisions at 25 GeV/u. Midrapidity for 25 GeV/u beam energy is equal 2.

muons. The acceptance of low transverse momentum muons ($p_t < 200$ MeV/c) drops by almost 2 orders of magnitude if compared to muons with large transverse momentum ($p_t > 500$ MeV/c) [156] (see Fig. 7.12, upper right panel). A measurement of dilepton pairs with muons is naturally restricted to the invariant mass region above the 2-muon threshold of 2 times 210 MeV/c². The CERES experiment, on the other hand, has to apply a transverse momentum cut of 0.2 GeV/c on single electron tracks in order to suppress a huge combinatorial background from Dalitz decays of neutral pions (see Fig. 7.12, upper left panel).

Special care should thus be taken by the CBM experiment to cover this range experimentally. In Fig. 7.10 (left panel), the transverse momentum versus invariant mass distribution for correlated pairs after all background rejection cuts including a transverse momentum cut of 0.2 GeV/c is presented. Indeed, the region at very low pair p_t and low mass has no coverage. The question arises whether this is just due to the transverse momentum cut or due to a restriction in the geometrical acceptance of CBM? In Fig. 7.10 (right panel), the p_t -mass distribution

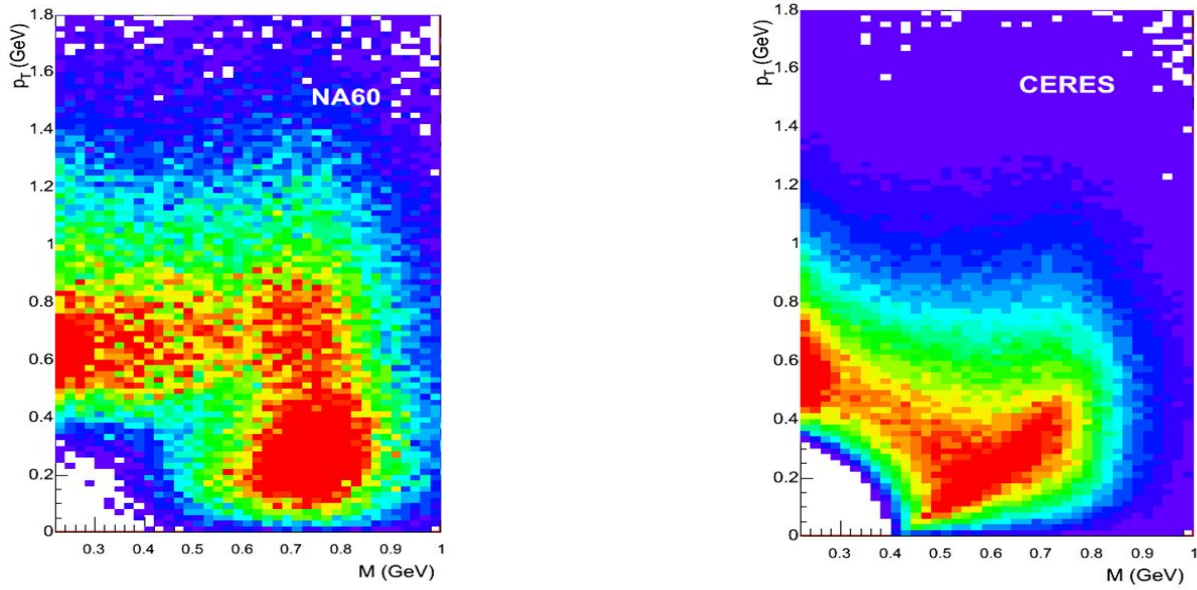


Figure 7.9: Transverse momentum versus invariant mass distribution of the identified dilepton pairs obtained from experimental data of the NA60 dimuon experiment (left panel) and the di-electron CERES experiment (right panel). Note that the mass axis is zero suppressed. Compilation by S. Damjanovic (NA60 collaboration).

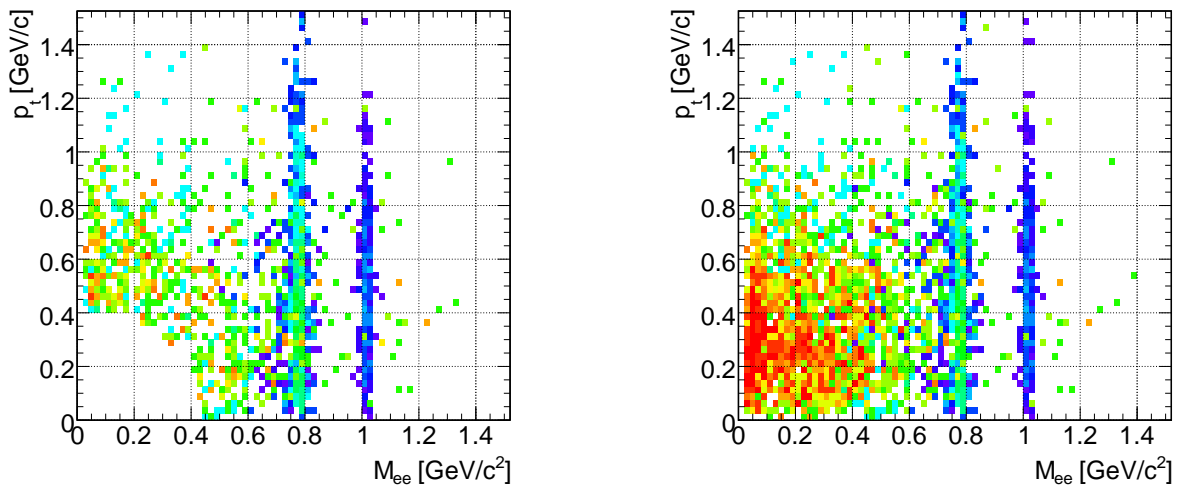


Figure 7.10: Distribution of accepted signal e^+e^- pairs in the transverse momentum and invariant mass plane after all cuts. Left: including p_t cut of 0.2 GeV/c, right: excluding any p_t cut. The data shown correspond to $2 \cdot 10^5$ simulated central Au+Au collisions at 25 GeV/u.

excluding any transverse momentum cut is presented. The acceptance is extended up to very low transverse momenta and very low masses. This shows that the CBM geometrical acceptance allows to access the lowest invariant masses in a wide range of transverse momentum. Fig. 7.12 shows the signal pair detection probability for CERES, NA60 experimental data and for CBM simulated data. For CBM simulated data a rather flat pair detection for all pair p_t is observed (note, no single electron p_t cut is applied).

However, "there's no such thing as a free lunch" (H. Wallace, 1943). Of course, if removing the transverse momentum cut, the S/B ratio in particular in the enhancement region drops. In

Fig. 7.11 the resulting e^+e^- invariant-mass distribution without transverse momentum cut is shown. The ω signal is still visible on top of the combinatorial background, the S/B ratio in the ω mass region is also unchanged, however, in the region where an enhanced di-electron yield is expected, i.e. from 0.2 to 0.6 GeV/c^2 the S/B ratio drops from 1/27 to 1/50. Numerical values of the S/B ratio and the signal efficiency with and without the transverse momentum cut are summarized in Table 7.2.

Mass range	S/B, $p_t > 0.2 \text{ GeV}/c$	ε [%], $p_t > 0.2 \text{ GeV}/c$	S/B, all p_t	ε [%], all p_t
$M_{ee} / (\text{GeV}/c^2) < 0.2$	0.68	0.008	0.41	0.07
$0.2 < M_{ee} / (\text{GeV}/c^2) < 0.6$	0.04	1	0.02	2.4
$0.6 < M_{ee} / (\text{GeV}/c^2) < 1.2$	0.1	6.3	0.08	7.1
ρ	-	4.7	-	5.5
ω	0.4	6.7	0.31	7.3
ϕ	0.32	9.4	0.32	9.7

Table 7.2: Signal-to-Background ratio and signal efficiency for central $Au+Au$ collisions at 25 GeV/u with and without single electron p_t cut.

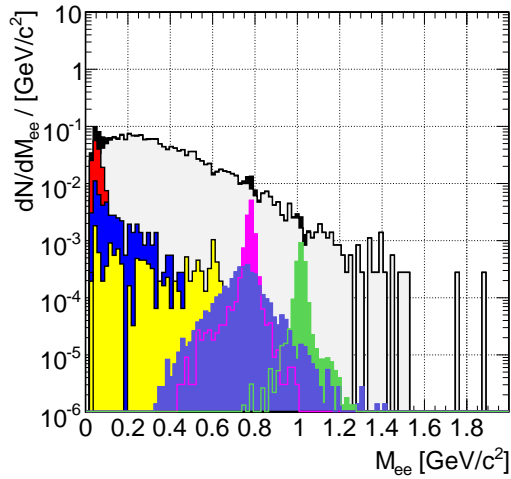


Figure 7.11: Invariant mass distribution after all cuts excluding any p_t cut. The data shown correspond to $2 \cdot 10^5$ simulated central $Au+Au$ collisions at 25 GeV/u .

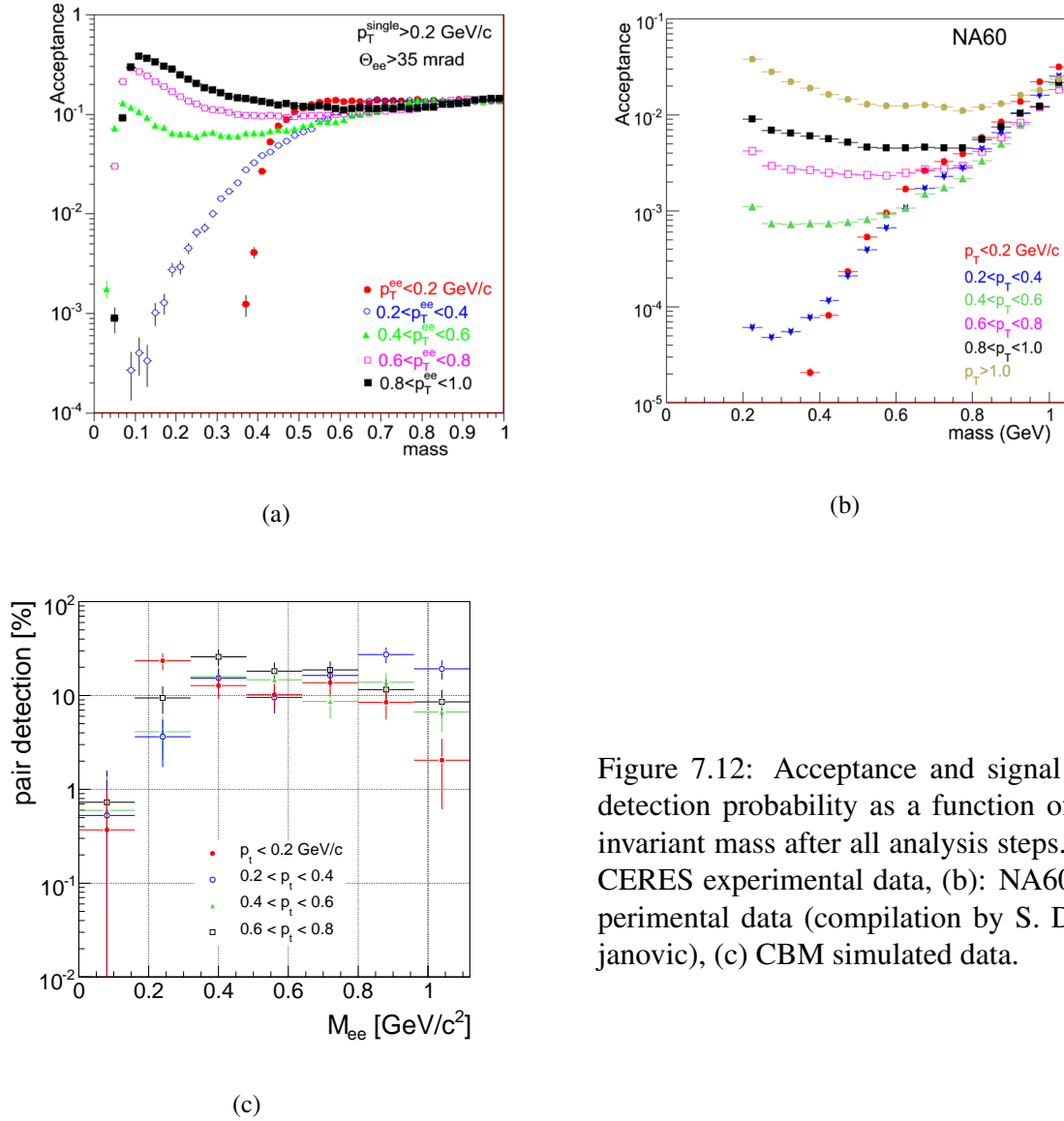


Figure 7.12: Acceptance and signal pair detection probability as a function of the invariant mass after all analysis steps. (a): CERES experimental data, (b): NA60 experimental data (compilation by S. Damjanovic), (c) CBM simulated data.

7.3 Comparison of the expected performance to existing dilepton experiments

A strong excess of dilepton pairs over the yield expected from neutral meson decays was observed by hitherto existing high energy heavy-ion dilepton experiments (HELIOS/CERES, NA60, PHENIX). Experimentally, it took a long time to master the challenges of very rare signals and enormous combinatorial background.

Clear signs of an excess of dileptons above the known decay sources at SPS energies were obtained by the CERES collaboration [40]. For proton induced interactions ($p+Be$ and $p+Au$), the low-mass vector meson spectra can be satisfactorily explained by electron pairs from hadron decays within the systematic errors. In the $S+Au$ system, however, an enhancement over the hadronic contribution by a factor of 0.5 ± 0.7 (stat) ± 2.0 (syst) in the invariant mass range $0.2 < M_{ee} / (\text{GeV}/c^2) < 1.5$ is observed. The experimental result from CERES for $S+Au$ in the low-mass region is shown in Fig. 7.13 (left panel). This experimental finding attracted a lot of attention from the theory side. Relying on ρ meson production without in-medium effects the

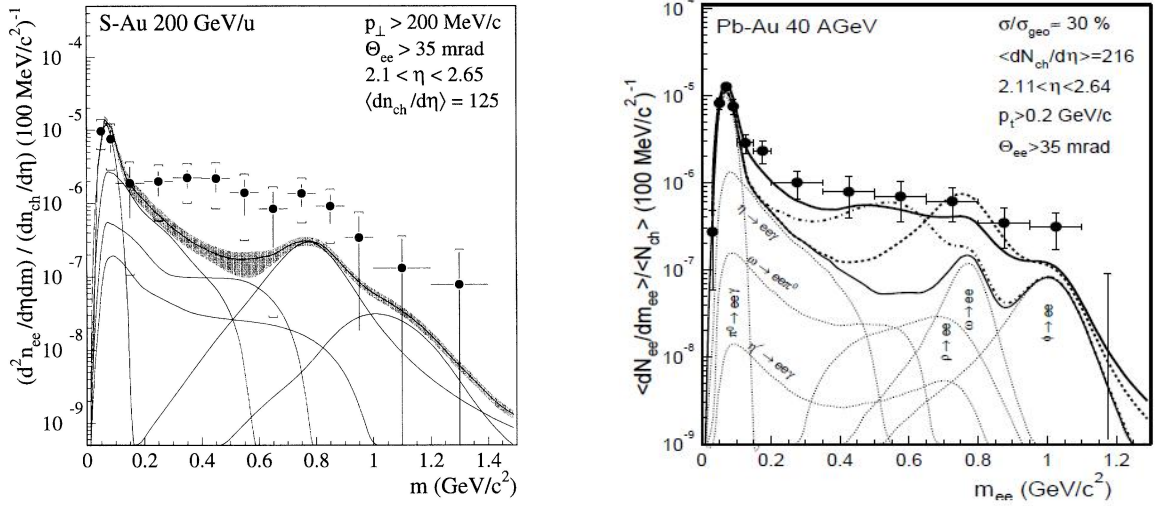


Figure 7.13: Left: Inclusive e^+e^- spectra in $S+Au$ collisions at 200 GeV/u beam energy showing the data (full circles) and various contributions from known hadron decays only; the shaded region indicates the systematic error on the summed contributions [40]. Right: Inclusive e^+e^- mass spectrum in $Pb+Au$ collisions at 40 GeV/u beam energy, compared to the hadron decay cocktail with (lower lines) and without medium modifications (upper lines) [41].

bulk of the excess below the pole mass of the ρ could not be described. Only switching-on in-medium effects, e.g. mass shifts or broadening lead to a satisfactory description. Unfortunately the data do not allow to discriminate between the two scenarios.

The next step taken by CERES was a measurement of low-mass electron pairs in $^{108}\text{Pb}+^{197}\text{Au}$ collisions at 158 GeV/u beam energy and a selection of the 35% most central events [42]. The

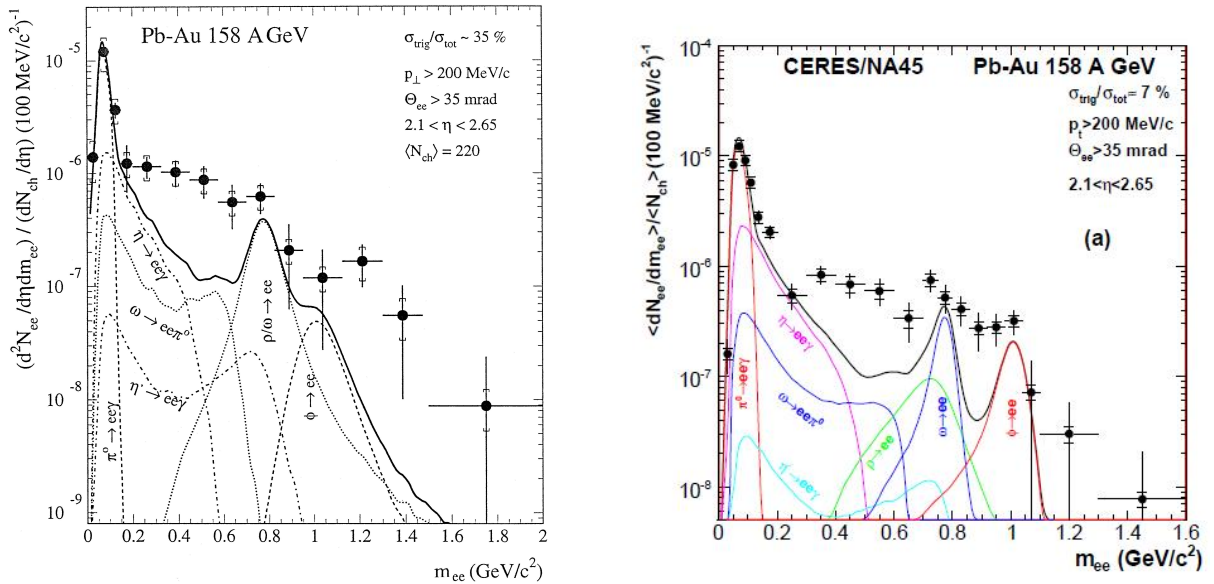


Figure 7.14: Left: Inclusive e^+e^- mass spectrum from CERES in $Pb+Au$ collisions at 158 GeV/u beam energy normalized to the observed charged-particle density. Statistical errors are shown as bars, the systematic errors are given independently as brackets. The full line represents the e^+e^- yield from hadron decays scaled from p-induced collisions. The contributions of individual decay channels are also shown [42]. Right: same distribution after the CERES upgrade [6].

observed pair yield integrated over the range of invariant masses $0.2 < M_{ee}/(\text{GeV}/c^2) < 2.0$ is enhanced by a factor of 2.31 ± 0.4 (stat.) ± 0.9 (syst.). In 2000 the experimental setup of CERES was upgraded by a downstream radial drift TPC¹ which is operated inside an inhomogeneous magnetic field. Employing tracking information from the TPC, the mass resolution of the spectrometer was improved to $\Delta m/m = 3.8\%$ in the region of the ϕ meson mass. The e^+e^- pair production in central $Pb+Au$ collisions at the same beam energy was remeasured and reported in Ref. [6]. The presented result is based on an analysis of 25 million $Pb+Au$ events and a centrality selection of $\sigma/\sigma_{geo} = 7\%$. The observed enhancement in the mass region from 0.2 to 1 GeV/c^2 with respect to the "hadronic cocktail" is a factor 2.45 ± 0.21 (stat.) ± 0.35 (syst.) ± 0.58 (decays). Experimental results from CERES for $Pb+Au$ collisions in the low-mass region are shown in Fig. 7.14.

In Ref. [41] the CERES collaboration reports on measurements of low-mass electron-positron pairs in $^{108}Pb+^{197}Au$ collisions at a beam energy of 40 GeV/u . The observed pair yield integrated over the range of invariant masses $0.2 < M_{ee}/(\text{GeV}/c^2) < 1$ is enhanced over the expectation from neutral meson decays by a factor of 5.9 ± 1.5 (stat.) ± 1.2 (syst.) ± 1.8 (decays), somewhat larger than previously observed at the higher energy of 158 GeV/u (see Fig. 7.13, right panel). A big step forward in technology, leading to completely new standards of the data quality in the dilepton field, has recently been achieved by the NA60 experiment at the CERN SPS. NA60, a third-generation experiment was built to study low-mass vector mesons via their electromagnetic decay to muon pairs in 158 GeV/u $^{115}In+^{115}In$ collisions [7]. Fig. 7.15 (left panel) shows the centrality-integrated net dimuon mass spectrum

¹Time Projection Chamber

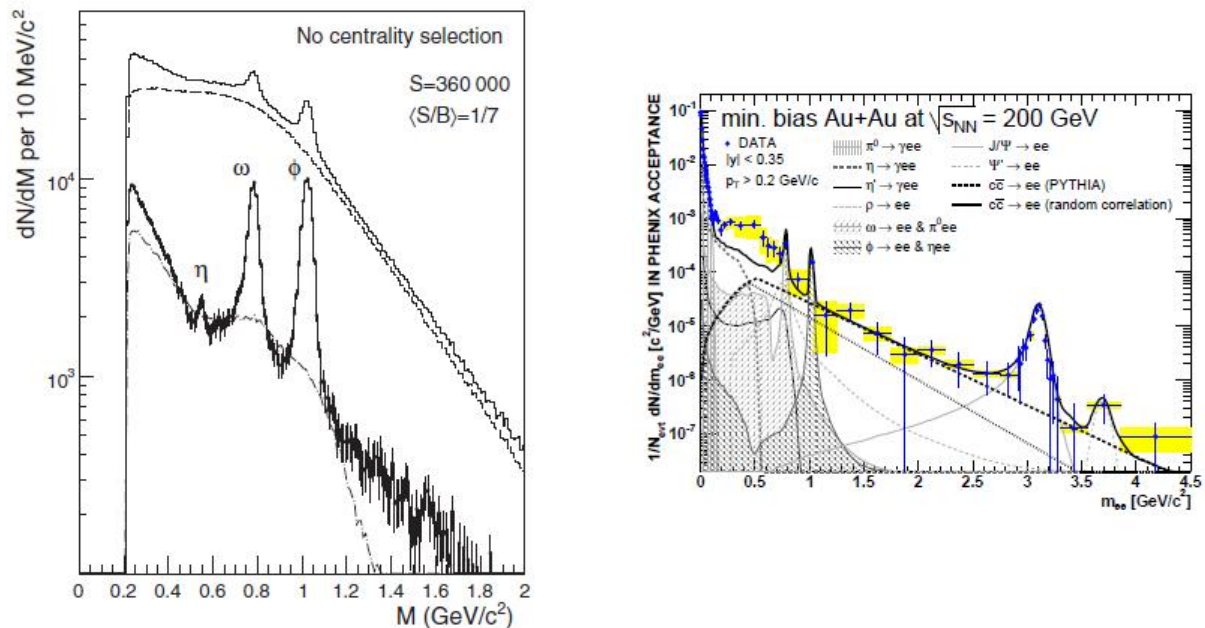


Figure 7.15: Left: Mass spectra of the opposite-sign dimuons (upper histogram), combinatorial background (dashed line), signal fake matches (dashed-dotted line), and resulting signal (histogram with error bars) from the NA60 collaboration for minimum bias $In+In$ collisions at 158 GeV/u beam energy [7]. Right: Invariant e^+e^- pair yield compared to the yield from expected hadronic decays from the PHENIX collaboration in minimum bias $Au+Au$ collisions at $\sqrt{s_{NN}} = 200$ GeV . Statistical (bars) and systematic (grey boxes) uncertainties are shown separately; the mass range covered by each data point is given by the horizontal bars [43].

for $In+In$ collisions at 158 GeV/u beam energy. A significant excess of pairs is observed above the yield expected from neutral meson decays. The subsequent analysis is done in four classes of collision centrality defined through the charged-particle multiplicity density: peripheral ($4 < N_{ch} < 30$), semiperipheral ($30 < N_{ch} < 110$), semicentral ($110 < N_{ch} < 170$), and central ($170 < N_{ch} < 240$). The S/B ratios for an invariant mass range from 0.2 to 1.2 GeV/c² associated with the individual centrality classes are 2, 1/3, 1/8, and 1/11, respectively [156]. The PHENIX experiment extends the dilepton measurements into a new energy regime by exploring $^{197}Au+^{197}Au$ collisions at a center of mass energy of $\sqrt{s_{NN}} = 200$ GeV [43]. In minimum bias $Au+Au$ collisions the di-electron yield in the mass range between 150 and 750 MeV/c² is enhanced by a factor of 3.4 ± 0.2 (stat.) ± 1.3 (syst.) ± 0.7 (model) compared to the expectation from a model of hadron decays that well reproduces the mass spectrum in $p+p$ collisions (see Fig. 7.15, right panel). The PHENIX experiment has to deal with an enormous combinatorial background. Different techniques are applied in order to understand and control systematic errors. Adding the statistical error and the uncertainty due to the event rejection in quadrature PHENIX claims an accuracy of 0.25% on the normalization, which is according to the PHENIX collaboration assumed to be a conservative estimate and is taken as an upper limit for the systematic uncertainty. All achieved experimental results are summarized in Table 7.3.

Experiment	System	$\sqrt{s_{NN}}$	$\frac{dN_{ch}}{d\eta}$	Enhancement	S/B
CERES	$Pb+Au$	8.86	216	5.9	1/6
CERES ($\sigma/\sigma_{tot} = 28\%$)	$Pb+Au$	17.3	245	2.31	1/13
CERES ($\sigma/\sigma_{tot} = 7\%$)	$Pb+Au$	17.3	350	2.45	1/21
NA60 (central)	$In+In$	17.3	193	3	1/11
NA60 (semi-central)	$In+In$	17.3	133	2	1/8
NA60 (semi-peripheral)	$In+In$	17.3	63	2	1/3
NA60 (peripheral)	$In+In$	17.3	17	1.5	2
CERES	$S+Au$	19.5	125	5	1/4.3
PHENIX ($\sigma/\sigma_{tot} = 10\%$)	$Au+Au$	200	650	3.4	1/500
CBM (b=0) (free cocktail)	$Au+Au$	5.6	250	to be measured	1/9
CBM (b=0) (free cocktail)	$Au+Au$	7.1	300	to be measured	1/16
CBM (b=0) (free cocktail)	$Au+Au$	8.3	350	to be measured	1/18

Table 7.3: Overview of existing dilepton experiments. S/B ratios for integrating invariant masses larger than 0.2 GeV/c². For CBM S/B ratios can of course only be given without any medium contribution, i.e. "free hadronic cocktail" only.

From a parametrization of the published enhancement factors as function of center of mass energy (see Fig. 7.16, left panel), we might expect an enhancement factor not smaller than 6 in central $Au+Au$ collisions at 25 GeV/u. Fig. 7.16 (right panel) shows the experimental hadron yields at midrapidity produced in central nucleus-nucleus collisions as a function of center of mass energy [44]. A clear correlation between the S/B ratio (see Table 7.3) and $dN_{ch}/d\eta$ can be seen. Interestingly, all experiments so far seem to follow this dependence (see Fig. 8.3), although the sources of the combinatorial background are very different. The $dN_{ch}/d\eta$ for CBM was estimated based on Fig. 7.16 (right panel). Thus for central $Au+Au$ collisions at 15 GeV/u beam energy we expect 250 charged particles per rapidity unit at midrapidity, 300 for $Au+Au$ collisions at 25 GeV/u beam energy and 350 for $Au+Au$ collisions at 35 GeV/u beam energy. For CBM, we therefore deduce a S/B ratio of $6 \times 1/9$ for central $Au+Au$ collisions at 15 GeV/u, $6 \times 1/16$ for central $Au+Au$ collisions at 25 GeV/u and $6 \times 1/18$ for central $Au+Au$ collisions at 35 GeV/u ($M_{inv} > 0.2$ GeV/c²). As Fig. 8.3 demonstrates, this performance is well

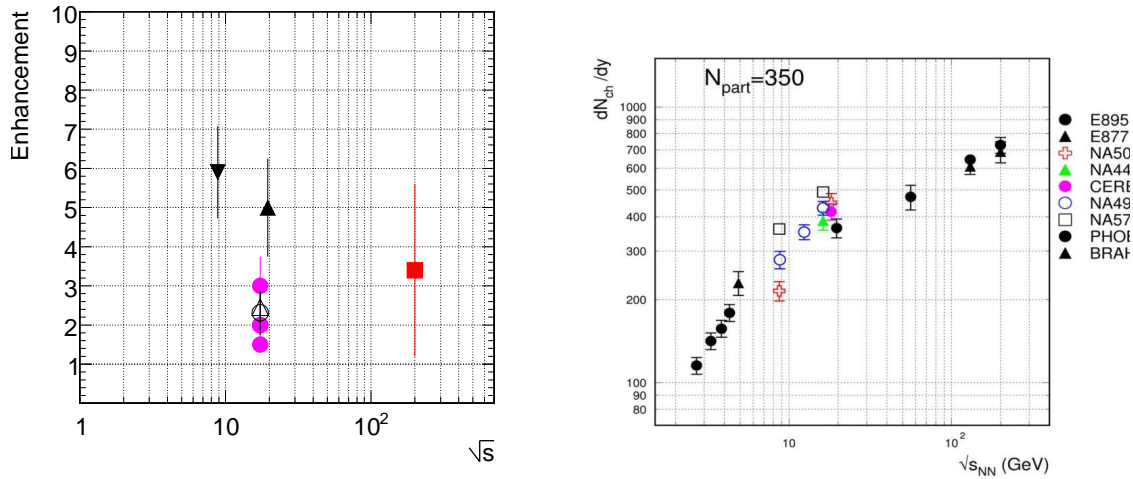


Figure 7.16: Left: Enhancement factors observed by different experiments as a function of the center of mass energy. Circles: NA60 data ($In+In$) for four centrality bins; inverse filled triangle: CERES data ($Pb+Au$ at 40 GeV/u); open circle: CERES data ($Pb+Au$ at 158 GeV/u, 28% most central collisions); open triangle: CERES data ($Pb+Au$ at 158 GeV/u, 7% most central collisions); filled triangle: ($S+Au$ at 200 GeV/u, no centrality selection); square: PHENIX data. Right: The energy dependence of experimental hadron yields at midrapidity produced in central nucleus-nucleus collisions [44].

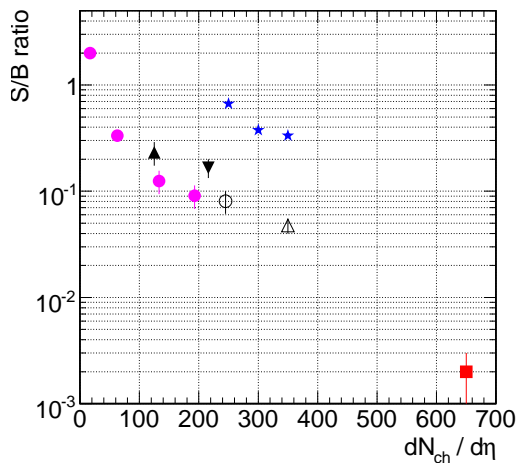


Figure 7.17: Integrated S/B ratios for M_{inv} larger than $0.2 \text{ GeV}/c^2$ measured by existing dilepton experiments as a function of the number of charged particles at midrapidity in one rapidity unit. Circles: NA60 data for four centrality bins; triangles, open circle: CERES data, square: PHENIX data, star: CBM assuming an enhancement factor of 6.

competitive with previous experiments measuring dileptons in heavy-ion collisions at similar charged track densities.

Besides a good S/B ratio large statistics are very important. Indeed, the high accumulated statistics is part of the big success of the NA60 experiment. In Table 7.4, yields for 10 weeks of CBM running are calculated based on the assumption that the data recording rate will be 1 GByte/s and the size of one event is on the average approximately 40 kByte for minimum bias $Au+Au$ collisions. Without online event selection by high-level triggers this rate corresponds to a reaction rate of 25 kHz for minimum bias $Au+Au$ collisions at FAIR energies. With a 0.1% interaction target beam intensities of $2.5 \cdot 10^7$ ions/s are required which is well below the maximum beam intensity of 10^9 ions/s planned for FAIR. The thin target therefore places no

limitation for the low-mass vector meson studies. No online event selection besides probably a centrality trigger for selected runs is foreseen for the investigation of low-mass electron pairs. The statistics of the simulated data presented so far (10^5 events) is equivalent to only ~ 10 s beam on target. Large statistic allowing for systematic studies of dilepton production in CBM should therefore be available.

Particle	N	BR	ε [%]	R/s [MHz]	Y/s	$Y/10 w$
ρ	4.6	$4.4 \cdot 10^{-5}$	4.7	0.025	0.21	$1.3 \cdot 10^6$
ω	7.6	$7.1 \cdot 10^{-5}$	6.7	0.025	1	$6 \cdot 10^6$
ϕ	0.256	$3.1 \cdot 10^{-4}$	9.4	0.025	0.17	$1 \cdot 10^6$

Table 7.4: Estimated particle yields for minimum bias $Au+Au$ collisions at 25 GeV/u based on HSD calculations. N = multiplicity in minimum bias collisions (= 1/5 of central collisions), BR = branching ratio, ε = efficiency ($p_t > 0.2$ GeV/c), R/s = reaction rate, Y/s = particle yield per second, and $Y/10 w$ = particle yield per 10 weeks [46].

In this chapter we have shown with simulations including realistic detector descriptions to our current knowledge that CBM will well be able to measure low mass electron pairs in central $Au+Au$ collisions from 15 – 35 GeV/u beam energy. The expected performance, in terms of S/B ratio is well comparable to existing dilepton experiments. A strong benefit of the CBM will be that due to a large availability of beam time and high reaction rates large statistics will be collected. This will allow for a multi-differential and systematic analysis of interesting observables.

Chapter 8

Summary and Outlook

In this thesis the measurements of inclusive di-electron production in $p+p$ and $n+p$ interactions at $E_{kin} = 1.25 \text{ GeV}/u$ were presented. We observe a large enhancement in the di-electron production in $n+p$ relative to $p+p$ reactions in the mass region above the Dalitz decay of the π^0 meson. There is also a strong difference between the shape of the $n+p$ and $p+p$ mass spectra. The $p+p$ mass spectrum is much steeper than the one for $n+p$ collisions. A strong bremsstrahlung contribution in $n+p$ interactions has been predicted within the framework of a covariant OBE model [34]. One of the the questions addressed by this model is how the resonance contributions have to be treated along with the bremsstrahlung in coherent calculations. We investigate the contribution of NN bremsstrahlung by a comparison of di-electron yields in $p+p$ and $n+p$ reactions. Its detailed dependence on pair mass was explored by the di-electron yield ratio $(\frac{dN}{dM_{ee}})^{np} / (\frac{dN}{dM_{ee}})^{pp}$.

Comparing the $p+p$ data to the Pluto cocktail one clearly see that the $p+p$ invariant mass spectrum can be nicely described by the sum of the π^0 Dalitz and Δ Dalitz decays when the Δ electromagnetic transition form factor is calculated using the VMD model. The incoherent sum of the π^0 , Δ (Dipole fit), and NN bremsstrahlung from [34] provides also good description of the $p+p$ data. The η contribution becomes important for the di-electron cocktail of $n+p$ data. The di-electron spectra measured in $n+p$ interactions exhibit further additional sources, i.e. higher-lying baryonic resonances which are not included in our simple Pluto cocktail. Comparing our results to HSD and IQMD transport model calculations one observes a rather good agreement in the whole mass range. However, contributions of individual components like from Δ Dalitz decay and NN bremsstrahlung are very different in these models. Both models fail to reproduce the $n+p$ data in the mass region above π^0 Dalitz. The high data quality clearly shows beyond errors that something is still missing in the transport calculations.

The HSD transport model uses a parametrization of bremsstrahlung motivated by recent OBE calculations from Kaptari *et al.*, which is found to be larger by a factor of 2 – 4 compared to earlier results. To clarify this, we compared the $p+p$ data with the coherent sum of the Δ and NN bremsstrahlung terms of this model. The measured di-electron yield is overestimated by this model by a factor of 2 – 4. Already the Δ contribution from this OBE model is found to be a factor of ~ 2 higher than the Δ contribution as given in the Refs. [35, 92, 20]. The same difference has been observed for $n+p$ data.

Results on di-electron production in elementary collisions provide an important baseline for any measurement of the di-electron production in heavy-ion collisions. Our new data offer the possibility to compare the experimental cocktail based on $p+p$ and $n+p$ data to $^{12}\text{C}+^{12}\text{C}$ data. This can shed light on the origin of the excess observed in heavy-ion collisions at SIS energies.

The di-electron production in $C+C$ collisions at SIS energies can indeed be explained by a superposition of elementary $p+p$ and $n+p$ collisions. Once the bombarding energy per nucleon in heavy-ion collisions becomes comparable to the nucleon rest mass, nuclear matter initially under normal conditions in the target and projectile nuclei undergoes a gradual transition into resonance matter. From the measured meson multiplicities in central $C+C$ collisions at kinetic beam energies below $2 \text{ GeV}/u$ it can be concluded that in this energy regime 20 – 30% of all nucleons are excited to resonance states. Therefore, the dominant medium radiation should be driven by nucleons and baryonic resonances in the system. A sound theoretical description of electron pair production requires here a proper treatment of off-shell propagation of resonances and vector mesons. The "DLS puzzle" has been solved for heavy-ion collisions experimentally Ref.[3]. The theoretical interpretation of the elementary collisions are not yet fully consistent.

As part of this thesis a feasibility study of di-electron measurements in the future CBM experiment at FAIR has been presented. The analysis strategy for the reconstruction of low-mass vector mesons with the proposed CBM detector setup has been discussed. We have presented results for low-mass electron pair reconstruction in central $^{197}\text{Au}+^{197}\text{Au}$ collisions at 15, 25 and 35 GeV/u beam energy. With a first detector concept and realistic simulations a good performance of low-mass vector meson measurements was demonstrated. Results from feasibility studies were compared to data from existing dilepton experiments [6, 7, 91]. From a parametrisation of the published enhancement factors as function of \sqrt{s} and $dN_{ch}/d\eta$, we expect this factor not to be smaller than 6 in central $\text{Au}+\text{Au}$ collisions at 25 GeV/u beam energy. For CBM, we thus deduce a S/B ratio of $6 \times 1/16$ for $M_{inv} > 0.2 \text{ GeV}/c^2$. We demonstrate that the achieved performance is well competitive with previous experiments measuring dileptons in heavy-ion collisions at similar charged track densities.

There are currently many regions of the nuclear matter phase diagram which are explored by experiments measuring dilepton production in heavy-ion collisions, most notable HADES, CERES, NA60, and PHENIX. The CBM measurements will contribute to this list in future and in particular extend the dilepton measurement to the region of highest net baryon densities as they can be achieved in heavy-ion collisions from 15 – 35 GeV/u beam energy. Finally, the combination of all results will allow to conclude about the possible restoration of chiral symmetry in hot and dense nuclear matter and its relation to the QGP phase transition.

Zusammenfassung

In dieser Arbeit wurde die Produktion von Elektronenpaare in $p+p$ und $d+p$ Reaktionen bei einer Strahlenergie von $E_{kin} = 1.25 \text{ GeV}/u$ untersucht. Die Messungen wurden mit dem HADES-Spektrometer an der GSI durchgeführt. Teil der Arbeit waren auch eine Machbarkeitsstudie zur Elektronenpaar-Spektroskopie mit dem zukünftigen CBM-Experiment. Eine Analysestrategie für die Rekonstruktion von Vektormesonen niedriger Massen wurde entwickelt und kritisch diskutiert.

1. Einführung

Die Eigenschaften von Hadronen in dichter baryonischer Materie stellen ein wichtiges Gebiet experimenteller und theoretischer Hadronenphysik dar. Insbesondere erwartet man aus dem Studium möglicher Modifikationen ihrer Eigenschaften im Medium Hinweise auf eine (teilweise) Wiederherstellung der spontan gebrochenen chiralen Symmetrie bei hohen Temperaturen und Baryondichten. Im Experiment sind Modifikationen von Hadronen schwierig zu beobachten, da die in Schwerionenkollisionen erzeugte Materie nur für etwa $(10 - 12) \text{ fm}/c$ existiert. Eine der besten Möglichkeiten die Eigenschaften derartiger heißer und dichter Materie zu untersuchen, bieten Zerfälle von kurzlebigen Vektormesonen (ρ , ω und ϕ) in Leptonenpaare, da ihre Lebensdauer ähnlich der des erzeugten Feuerballs ist. Weiterhin koppeln diese Mesonen direkt an den elektromagnetischen Strom. Der gemessene Viererimpuls eines Leptonenpaares beinhaltet die entsprechenden Informationen über das Mutterteilchen. Da die Leptonenpaare den Feuerball nahezu ohne Wechselwirkung verlassen, tragen sie diese Informationen darüber hinaus ungestört in den Detektor und werden so zu einer wichtigen Observable um nach Änderungen der Eigenschaften von Hadronen im Medium zu suchen. Verschiedene Experimente haben bereits die Herausforderung angenommen und die Verteilung der invariante Masse (M_{l+l-} , $l = e, \mu$), des Transversalimpulses p_t und der Rapidität y der emittierten Paare zu rekonstruieren. Dabei ist die invariante Masse des Leptonenpaares äquivalent zur invarianten Masse des zerfallenden Teilchens und kann nach

$$M_{l+l-} \cdot c^2 = \sqrt{(E_{l+} + E_{l-})^2 - (\vec{p}_{l+} \cdot c + \vec{p}_{l-} \cdot c)^2}$$

berechnet werden.

Um die invariante Masse zu rekonstruieren, müssen im Experiment die Leptonenpaare mit hoher Effizienz, guter Impulsauflösung und sauberer Teilchenidentifizierung gemessen werden. Die größte Herausforderung bei der Messung von Vektormesonen niedriger Masse über ihren Zerfall in ein Elektronenpaar liegt in der Unterdrückung des physikalischen Untergrundes durch Elektronenpaare von π^0 Dalitz-Zerfällen und γ -Konversionen, insbesondere der hierdurch verstärkt auftretenden kombinatorischen Paare. Für eine gute Unterdrückung des Untergrundes braucht man weiterhin einen sehr sauber identifizierten Satz von Elektronenkandidaten.

2. Datenanalyse in HADES

HADES ist ein Detektorsystem, das speziell für die Messung von Elektronenpaare ausgelegt wurde. HADES deckt ein breites Physikprogramm ab, welches die Untersuchung der Elektronenpaar-Emission in Schwerionenkollisionen sowie die Elektronenpaar-Produktion in elementaren Reaktionen beinhaltet, wie auch andere Experimente, die die elektromagnetische Struktur der Hadronen untersuchen sollen. Vier Ebenen von Driftkammern dienen der Rekonstruktion der Teilchenspuren und ihres Impulses. Dabei befinden sich zwei der Kammern vor, die anderen beiden Kammern hinter einem Magnetfeld mit einem maximalen Fluss von 0.7 Tesla. Elektronen und Positronen werden im RICH und den TOF/TOFino Detektoren identifiziert, die letzteren werden in der Vorwärtshemisphäre durch einen elektromagnetischen Pre-Shower Detektor zur weiteren Unterdrückung von schnellen Hadronen ergänzt. Die identifizierten Elektronen und Positronen werden dann zu Paare kombiniert, indem alle möglichen Kombinationen pro Ereignis berechnet werden. Viele dieser Paare tragen allerdings nur zum kombinatorischen Untergrund bei, der durch Analysebedingungen unterdrückt werden muss. Um nun die absolute Multiplizität der produzierten Elektronenpaare zu berechnen, muss auf Effizienzverluste aufgrund der Untergrundunterdrückung sowie der Elektronenidentifizierung korrigiert werden. Auch mögliche Nachweisbeschränkungen aufgrund des verwendeten Triggers müssen korrigiert werden. Die korrigierten Paarspektren aus den elementaren $p+p$ und (aus $d+p$ extrahierten) $n+p$ -Reaktionen werden anschließend noch auf die Anzahl der elastisch gestreuten Protonen normiert. Diese Ereignisse wurden ebenfalls mit dem HADES-Detektor vermessen. Die geometrische Akzeptanzverluste werden nicht korrigiert da hierzu Annahmen zur Phasenraumverteilung gemacht werden müssten. Um die experimentellen Daten mit theoretischen Rechnungen zu vergleichen wurde vielmehr ein Akzeptanzfilter entwickelt. Die hier diskutierte Akzeptanz bezieht sich dabei auf die Wahrscheinlichkeit, dass ein am Vertex emittiertes Teilchen die aktiven Bereiche des Detektors durchfliegt und somit nachgewiesen wird. Die Akzeptanz beinhaltet damit die impulsabhängige Ablenkung im Magnetfeld. Nicht berücksichtigt sind in diesem Filter das Detektoransprechverhalten und Rekonstruktionseffizienzen, da diese in den Daten bereits vor dem Vergleich mit der Theorie korrigiert wurden.

3. Ergebnisse

In Abbildung 8.1 sind die spektralen Verteilungen der rekonstruierten invarianten Massen der Elektronenpaare aus $p+p$ und $n+p$ -Reaktionen dargestellt. Die Spektren sind je auf die Anzahl elastischer Wechselwirkungen normiert. Man beobachtet in den Elektronenpaar-Spektren aus $n+p$ -Reaktionen im Vergleich zu $p+p$ -Reaktionen einen großen Überschuss an produzierten Paare im Bereich oberhalb der Beiträge aus π^0 Dalitz-Zerfällen. Weiterhin ist die Form der Massenspektren sehr unterschiedlich, das $p+p$ -Spektrum ist deutlich steiler als das $n+p$ -Spektrum. Die Daten wurden mit einem Pluto-Cocktail, Rechnungen im Rahmen des OBE Modells und Ergebnissen der Transportmodelle HSD und IQMD verglichen. Mit einem Pluto-Cocktail aus Beiträgen von π^0 und Δ Dalitz-Zerfällen, wobei der elektromagnetische Formfaktor für die Δ -Resonanz im Rahmen des VMD Modells berechnet wird, erhält man eine sehr gute Beschreibung des Elektronenpaar-Spektrums aus $p+p$ -Reaktionen. Für das Massenspektrum aus $n+p$ -Reaktionen ist zusätzlich der Beitrag von η -Mesonen zu berücksichtigen.

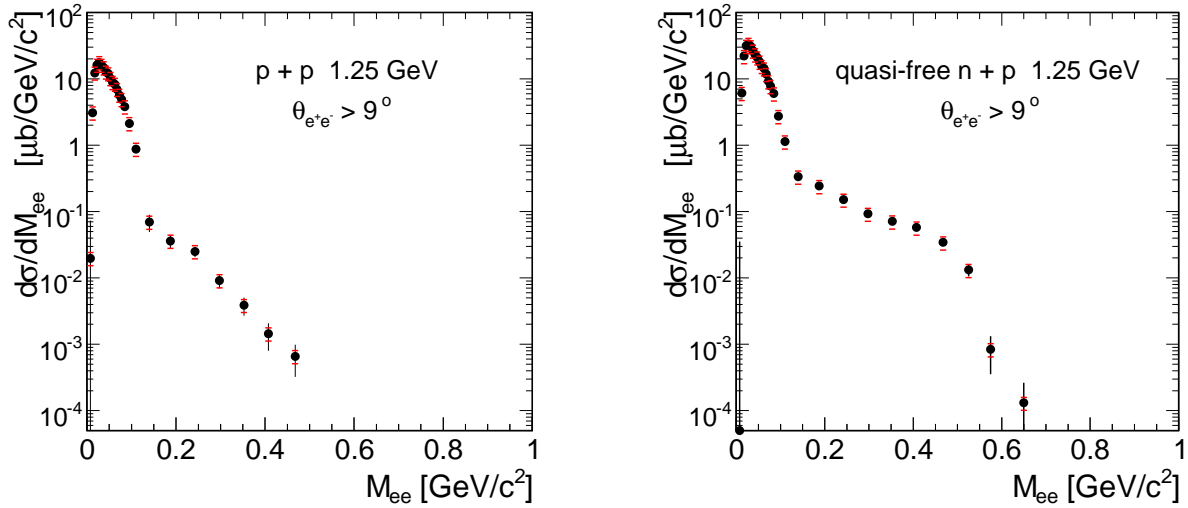


Figure 8.1: Invariante Massenverteilung von e^+e^- Paare in $p+p$ (links) und $n+p$ (rechts) Reaktionen bei einer Strahlenergie von 1.25 GeV/u. Statistische Fehler sind als vertikale Striche, systematische Fehler mit horizontalen Balken dargestellt.

Zur vollständigen Beschreibung des Elektronenpaar-Spektrums aus $n+p$ -Reaktionen sind allerdings noch weitere Quellen nötig. In dieser Arbeit wird die Hypothese aufgestellt, dass die Berücksichtigung von Beiträgen aus höher liegenden baryonischen Resonanzen eine bessere Beschreibung erlauben würde. Diese Begründung findet Unterstützung in der später diskutierten sehr guten Übereinstimmung der Elektronenpaar-Spektren aus $^{12}C+^{12}C$ -Kollisionen mit einer Darstellung in der die Beiträge aus $p+p$ und $n+p$ mit gleichem Gewicht überlagert sind und ebenfalls auf die Anzahl der neutralen Pionen normiert wurde.

Weiterhin wurden die Ergebnisse mit Transportrechnungen der HSD und IQMD Modelle verglichen. Beide Modelle reproduzieren die $p+p$ Daten im gesamten Massenbereich recht gut. Allerdings sind die Beiträge einzelner Komponenten (Δ Dalitz-Zerfall, NN -Bremsstrahlung) sehr unterschiedlich sodass sich kein konsistentes Bild ergibt. Beide Modelle können die gemessenen $n+p$ Daten nicht im Massenbereich oberhalb der π^0 Dalitz-Zerfälle beschreiben. In $n+p$ -Reaktionen ist im Rahmen von Rechnungen innerhalb des OBE Modells ein großer Beitrag durch Bremsstrahlungsprozesse vorausgesagt worden. Der NN -Bremsstrahlungsbeitrag kann experimentell durch einen Vergleich der $p+p$ und $n+p$ Ergebnisse abgeschätzt werden. Dazu wurde das Verhältnis $(\frac{dN}{dM_{ee}})^{np}/(\frac{dN}{dM_{ee}})^{pp}$ berechnet und diskutiert. Im HSD Modell wird eine Parametrisierung der Bremsstrahlung genutzt, die von diesen neueren OBE Rechnungen von Kaptari *et al.* [34] motiviert ist. Dieser Beitrag ist allerdings um einen Faktor 2 – 4 höher im Vergleich zu früheren Rechnungen. Um die Gültigkeit dieses Ansatzes zu untersuchen, wurden die $p+p$ und $n+p$ Daten mit der kohärenten Summe aus Δ -Produktion und NN -Bremsstrahlung der OBE Rechnung verglichen. Die gemessene Paarausbeute in $p+p$ wird mit diesem Ansatz um gerade den genannten Faktor 2 – 4 überschätzt. Allein der Beitrag der Δ -Resonanz der OBE Rechnung ist um einen Faktor 2 – 4 höher als die Δ Beiträge in Refs. [35, 92, 20]. Dieselbe Diskrepanz beobachtet man in den $n+p$ Daten. Eine einfache Skalierung der NN -Bremsstrahlungsbeiträge in HSD erscheint daher fraglich. Da allerdings die Autoren von HSD durch genau diese Skalierung das "DLS Puzzle" als gelöst betrachten, d.h. die Paarproduktion in $C+C$ -Kollisionen sehr gut beschreiben, ist diese Aussage neu zu untersuchen. Da die HADES $p+p$ und $n+p$ Daten nicht korrekt beschrieben werden treten Zweifel auf ob nicht die gute Übereinstimmung zwischen dem HSD Modell und den $C+C$

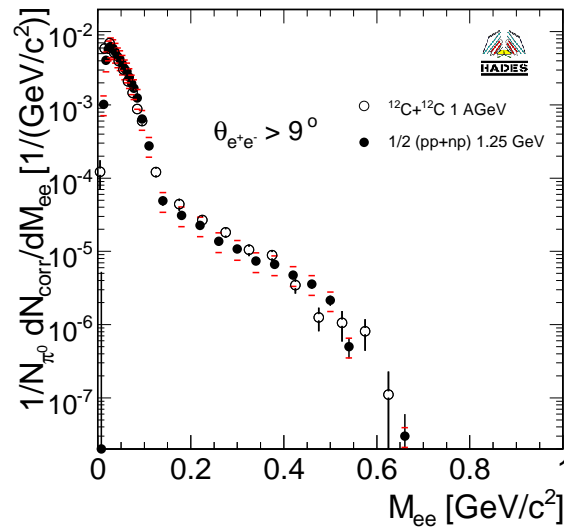


Figure 8.2: Invariante Massenverteilung von e^+e^- Paare in $C+C$ -Kollisionen bei einer Strahlenergie von $1 \text{ GeV}/u$ (offene Kreise) sowie der kombinierten Daten aus $p+p$ und $n+p$ -Kollisionen als $1/2 \cdot (M_{ee}^{pp} + M_{ee}^{np})$ bei $1.25 \text{ GeV}/u$ (schwarze Kreise). Die Spektren sind je auf die Anzahl der π^0 normiert.

Daten nur in der Summe des Cocktails gelingt aber nicht durch die richtige Beschreibung der Cocktail-komponenten. Die Ergebnisse zur Elektronenpaar-Produktion in elementaren Reaktionen bieten eine wichtige Grundlage für das Verständnis der Paarproduktion in Schwerionenstößen. Die Daten dieser Arbeit erlauben es, einen experimentell basierten Cocktail aus $p+p$ und $n+p$ Daten mit den Ergebnissen in $C+C$ zu vergleichen. Dieser Vergleich kann Licht auf den Ursprung des beobachteten Überschusses von Elektronenpaare aus $C+C$ -Kollisionen im Vergleich zu vorhandenen Modellen in Schwerionenkollisionen an SIS Energien werfen. Insbesondere kann die Rolle von NN -Bremsstrahlungsprozessen untersucht werden. In Bild 8.2 werden die $C+C$ Daten mit einem experimentellen Cocktail verglichen, der aus den $p+p$ und $n+p$ Resultaten wie folgt berechnet wurde: $M_{ee}^{CC} = 1/2 \cdot (M_{ee}^{pp} + M_{ee}^{np})$. Ganz natürlich können so die Ergebnisse in $C+C$ als Überlagerung von elementaren $p+p$ und $n+p$ Stößen erklärt werden. Die gemessenen Multiplizitäten von Mesonen in zentralen $C+C$ -Reaktionen bei Strahlenergien von $1 \text{ GeV}/u$ zeigen, dass in diesem Energiebereich (20–30)% aller Nukleonen zu Resonanzen angeregt werden. Das bei $1 \text{ GeV}/u$ erzeugte Medium in $C+C$ -Kollisionen ist somit wohl auch durch baryonische Resonanzen und ihre Dalitz-Zerfälle dominiert. Diese Beobachtung stützt die aufgestellte Hypothese, dass der Di-Elektronen Beitrag von Zerfällen von Baryonen höherer Massen in den Modellen nicht genügend berücksichtigt ist. Wegen der starken Einschränkungen des zur Verfügung stehenden Phasenraumes erfordert eine sorgfältige theoretische Beschreibung der Elektronenpaar-Produktion bei diesen Energien allerdings eine saubere Behandlung der Propagationen von Resonanzen und Vektormesonen abseits der Massenschale. Weiterhin muss die Rolle der Kopplung von baryonischen Resonanzen und Vektormesonen, insbesondere dem ρ , quantitativ verstanden werden.

4. Elektronenpaar-Spektroskopie in CBM

Eine Variation von experimentellen Bedingungen wie der Kollisionsenergie oder der Zentralität hat eine Untersuchung der angeregten Kernmaterie bei verschiedenen Temperaturen und Baryonendichten zum Ziel. In hochenergetischen Schwerionenkollisionen wurden in den letzten Jahren Dileptonenspektren am SPS ($\sqrt{s} \sim (10 - 20) \text{ GeV}/u$) und RHIC ($\sqrt{s} = 200 \text{ GeV}/u$) gemessen. Neue experimentelle Ergebnisse der CERES und NA60 Kollaborationen am SPS und der PHENIX-Kollaboration am RHIC zeigen einen deutlichen Überschuss von Leptonenpaare über den Erwartungen im Massenbereich von $(0.3 - 0.7) \text{ GeV}/c^2$. Alle Experimente deuten darauf hin, dass Baryonen einen starken Einfluss auf diesen Überschuss haben, allerdings existieren keine Daten in dem Bereich sehr starker Kompression von Kernmaterie und höchster Netto-Baryonendichte, der mit Schwerionenkollisionen von $(8 - 45) \text{ GeV}/u$ Strahlenergie erreichbar ist. Das geplante CBM-Experiment bei FAIR wird ein speziell ausgelegtes Experiment zur Messung von Schwerionenkollisionen sein, mit dem das QCD Phasendiagramm bei moderaten Temperaturen aber hohen Netto-Baryonendichten untersucht werden soll. Im Energiebereich von CBM wird Kernmaterie auf das bis zu 10 fache normaler Kernmateriedichte komprimiert werden, wobei Energiedichten von einigen GeV/fm^3 erreicht werden. Die experimentelle Herausforderung von CBM ist, sowohl Hadronen als auch Leptonen zu identifizieren und seltene Proben zu messen, die in der Wechselwirkungszone in zentralen Schwerionenstößen erzeugt werden. Die Leptonenpaarspektroskopie ist eine der zentralen Kernpunkte im CBM-Experiment. Es ist daher wichtig, in Simulationen zu zeigen, dass mit dem vorgesehenen experimentellen Aufbau Leptonenpaare mit genügender Präzision gemessen werden können.

In dieser Arbeit wurden detaillierte Simulationen zur Messung von Elektronenpaare für zentrale ($b = 0$) $^{197}\text{Au}+^{197}\text{Au}$ -Kollisionen bei einer Strahlenergie von $15 \text{ GeV}/u$, $25 \text{ GeV}/u$ und $35 \text{ GeV}/u$ durchgeführt. In der Analyse werden zunächst die Spuren im Silizium Tracking System rekonstruiert. Für die Elektronen-Identifizierung wird der ganze CBM-Detektor verwendet. Nach eine Qualitätsselektion von RICH Ringen und Ring-Spur Verknüpfungen werden Elektronen im RICH durch einen $\pm 3\sigma$ Schnitt um den mittleren Radius für Elektronen ausgewählt. Eine Pionen Unterdrückung in der Elektronenidentifizierung von 10^4 kann erreicht werden, wenn weiterhin der Energieverlust der Spuren in den 12 TRD Stationen sowie die Flugzeitmessung im TOF Detektor berücksichtigt werden.

Dominierende Untergrundquellen, die durch geeignete Spurselection unterdrückt werden sollen, sind zufällige Kombinationen von Elektronen und Positronen aus π^0 Dalitz-Zerfällen und γ -Konversionen. In zentralen $\text{Au}+\text{Au}$ -Kollisionen werden etwa 360 π^0 -Mesonen produziert, die sofort in $e^+e^-\gamma$ ($\Gamma/\Gamma_{tot} = 0.012$) und 2γ ($\Gamma/\Gamma_{tot} = 0.988$) zerfallen. Eine charakteristische Eigenschaft von Konversionselektronen oder Elektronen aus Dalitz-Zerfällen ist der moderate Zerfallsimpuls des Elektronenpaares. Das führt im Allgemeinen zu kleinen Öffnungswinkeln und kleinen Laborimpulsen. Das CBM-Detektorkonzept unterscheidet sich von bisherigen Elektronenpaar-Experimenten wie CERES oder HADES dahingehend, dass die Elektronenidentifizierung nicht vor dem Magnetfeld und den Tracking Detektoren stattfindet sondern anschliessend. Daher werden die Paare mit kleinem Öffnungswinkel ($\theta < 2^\circ$) vom Magnetfeld geöffnet bevor sie evtl. als Elektronen identifiziert werden können. Man würde daher Probleme erwarten, solche Paare zu identifizieren und für die weitere Analyse zu verwerfen, so dass der Untergrund wegen dieser partiell rekonstruierten Elektronenpaare signifikant ansteigen könnte. Eine sorgfältige Untersuchung dieser neuen experimentellen Umgebung ist

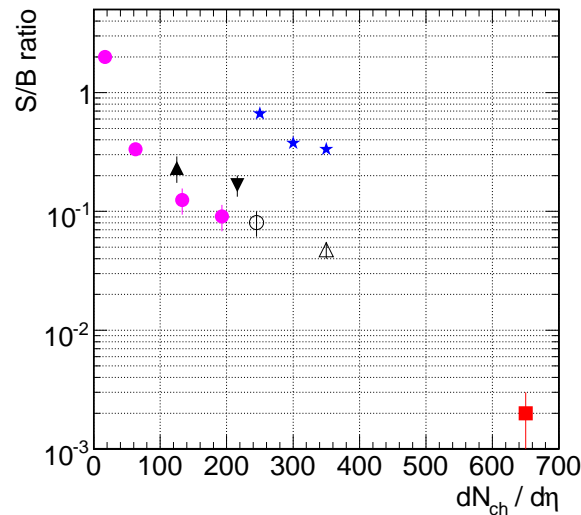


Figure 8.3: Signal-zu-Untergrund Verhältnis in Leptonenpaare Massenspektren für $M_{inv} > 0.2 \text{ GeV}/c^2$, gemessen von Experimenten an SPS (CERES (Dreiecke und offene Kreise), NA60 (Kreise)) und RHIC (PHENIX (Quadrat)), in Abhängigkeit von der Anzahl der geladenen Teilchen bei mittlerer Rapidität. Im Vergleich dazu (Sterne) sind nach den jetzigen Simulationen erwartete S/B Verhältnisse für CBM eingezeichnet unter Annahme eines Leptonenpaar-Überschusses um einen Faktor 6 für $M_{inv} > 0.2 \text{ GeV}/c^2$.

daher nötig. Die in dieser Arbeit entwickelte Strategie zur Reduzierung des Untergrundes basiert zu einem großen Teil auf der Topologie der im Silizium Tracking System rekonstruierten Spuren und Spurenpaare. Dafür werden im wesentlichen drei Schritte durchgeführt: Zunächst werden Paare identifiziert und verworfen, die aus γ -Konversionen stammen. Danach werden einzelne Spuren verworfen, für die der Partner nicht vollständig rekonstruiert werden konnte aber einzelne Hits oder Spurfragmente im Detektor hinterlassen hat. Im dritten Schritt werden Paare mit einer typischen π^0 -Dalitz Signatur zwar in die Massenspektren gefüllt aber nicht weiter in der Kombinatorik verwendet. Spuren mit kleinen Transversalimpulsen können zusätzlich verworfen werden. Die verwendeten Selektionskriterien wurden nicht im strengen Sinne optimiert, z.B. durch eine Analyse der maximalen Signifikanz im endgültigen invarianten Massenspektrum. Stattdessen wurden sinnvolle Werte anhand der Vergleiche von Signal und Untergrundbeiträgen gewählt. Um möglichst viele der partiell rekonstruierten Elektronenpaare zu messen und damit den Untergrund zu unterdrücken wurden Veränderungen am ursprünglichen Detektorkonzept vorgeschlagen.

Mit diesem Detektorkonzept für CBM wurden möglichst realistische Simulationen durchgeführt und es konnte demonstriert werden, dass mit dem vorgeschlagenen Detektoraufbau Vektormesonen niedriger Massen präzise vermessen werden können. Die in Simulationen erzielten Signal-zu-Untergrund Verhältnisse wurden mit Messungen von existierenden Experimenten [6, 7, 91] verglichen, dafür muss allerdings der hier nicht simulierte aber in Experimenten gemessene Leptonenpaare Überschuss berücksichtigt werden. Parametrisiert man die gemessenen Faktoren des Leptonenpaare Überschusses über die Erwartungen in Abhängigkeit von \sqrt{s} und $dN_{ch}/d\eta$, so sollte dieser Faktor für zentrale $Au+Au$ -Kollisionen bei $25 \text{ GeV}/u$ Strahlenergie nicht kleiner als 6 sein. Daher würde man für CBM ein Signal-zu-Untergrund Verhältnis von $6 \times 1/16$ für $M_{inv} > 0.2 \text{ GeV}/c^2$ erwarten. Wie in Bild 8.3 zu sehen ist, wäre eine solche Messung sehr gut vergleichbar mit bisher durchgeführten Untersuchungen bei ähnlichen Multipliz-

itäten. Ein großer Vorteil von CBM gegenüber CERES als einzigem bisherigen Elektronenpaar-Experiment in diesem Energiebereich ist die hohe erwartete Statistik an gemessenen Ereignissen sowie eine gute Massenauflösung. Systematische Studien der Elektronenpaar-Produktion bei höchsten Baryondichten sind damit durchführbar.

Zur Zeit werden viele Regionen des QCD Phasendiagramms von Experimenten untersucht, die Leptonenpaar-Spektren vermessen. CBM wird in Zukunft im Bereich höchster Netto-Baryondichten beitragen. Eine Kombination all dieser Ergebnisse sollte es letztlich ermöglichen, die Frage nach der Wiederherstellung der spontan gebrochenen Chiralen Symmetrie in heißer und dichter Kernmaterie sowie die Beziehung zum QGP Phasenübergang zu verstehen.

Appendix A

The Clebsh-Gordan coefficients

$\Delta(1232)$ is an isospin 3/2 state which is decaying into N (isospin 1/2) and π (isospin 1) via the strong interaction while conserving the isospin (see Table A.1).

The relative weights of the final $N\pi$ states are given by the Clebsh-Gordan coefficients which can be found in [45]. In case of, e.g. the Δ^+ decay the corresponding wave function reads [157]:

$$|\xi(\frac{1}{2}, \frac{1}{2})\rangle = \sqrt{\frac{2}{3}}|\phi_1(\frac{1}{2}, -\frac{1}{2})\rangle|\phi_2(1, 1)\rangle - \sqrt{\frac{1}{3}}|\phi_1(\frac{1}{2}, \frac{1}{2})\rangle|\phi_2(1, 0)\rangle. \quad (\text{A.1})$$

Resulting branching ratios for the various $N\pi$ channels are summarized in Table A.2.

Δ^+	$\longrightarrow p\pi^0$	Δ^0	$\longrightarrow n\pi^0$
1/2	1/2 0	-1/2	-1/2 0
	$\longrightarrow n\pi^+$		$\longrightarrow p\pi^-$
1/2	-1/2 1	-1/2	1/2 -1
Δ^{++}	$\longrightarrow p\pi^+$	Δ^-	$\longrightarrow n\pi^-$
3/2	1/2 1	-3/2	-1/2 -1

Table A.1: Decay channels with isospin-3 components of $\Delta(1232)$.

Δ^+	$\longrightarrow p\pi^0$	$\longrightarrow n\pi^+$
	2/3	1/3
Δ^0	$\longrightarrow n\pi^0$	$\longrightarrow p\pi^+$
	2/3	1/3

Table A.2: Branching ratios for $\Delta^+(1232)$ and $\Delta^0(1232)$.

Bibliography

- [1] R.J. Porter *et al.* (DLS Collaboration), "Di-electron cross section measurements in nucleus-nucleus reactions at 1 AGeV", Phys. Rev. Lett. **79** (1997) 1229.
- [2] G. Roche *et al.* (DLS Collaboration), "First observation of di-electron production in proton-nucleus collisions below 10 GeV", Phys. Rev. Lett. **61** (1988) 1069.
- [3] G. Agakichiev *et al.* (HADES Collaboration), "Study of di-electron production in $^{12}\text{C}+^{12}\text{C}$ collisions at 1 AGeV", Phys. Lett. **B 663** (2008) 43 [arXiv:0711.4281 [nucl-exp]].
- [4] G. Agakichiev *et al.* (HADES Collaboration), "Di-electron production in $^{12}\text{C}+^{12}\text{C}$ collisions at 2 AGeV with HADES". Phys. Rev. Lett. **98** (2007) 052302 [arXiv:0608031 [nucl-ex]].
- [5] C. Fuchs, K. Shekhter, "Dilepton production in heavy-ion collisions at intermediate energies", Phys. Rev. **C 68** (2003) 014904 [arXiv:nucl-th/0305015].
- [6] D. Adamova *et al.* (CERES Collaboration), "Modification of the ρ meson detected by low-mass electron-positron pairs in central $Pb+Au$ collisions at 158 AGeV", Phys. Lett. **B 666** (2006) 425 [arXiv:nucl-ex/0611022].
- [7] R. Arnaldi *et al.* (NA60 Collaboration), "First measurement of the ρ spectral function in high-energy nuclear collisions", Phys. Rev. Lett. **96** (2006) 162302 [arXiv:nucl-ex/0605007].
- [8] K. Redlich, P. Braun-Munzinger and J. Stachel, "Particle production in heavy-ion collisions", (2003) [arXiv:nucl-th/0304013].
- [9] J. Cleymans and K. Redlich, "Chemical and thermal freeze-out parameters from 1 AGeV to 200 AGeV", Phys. Rev. **C 60** (1999) 054908 [arXiv:nucl-th/9903063].
- [10] B.J. Schäfer and J. Wambach private communication (2007).
- [11] M. Post and U. Mosel, "Vector mesons and baryon resonances in nuclear matter", Nucl. Phys. **A 699** (2002) 169 [arXiv:nucl-th/0108017].
- [12] R. Rapp and J. Wambach, "Low mass dileptons at the CERN SPS: evidence for chiral restoration?", Eur. Phys. J. **A 6** (1999) 415 [arXiv:hep-ph/9907502].
- [13] A. Drees (private communication of A. Drees with R. Rapp and J. Wambach) [arXiv:hep-ph/9909229].

- [14] S. Damjanovic *et al.* (NA60 Collaboration), "Thermal dileptons at SPS energies", *J. Phys. G* **35** (2008) 104036 [arXiv:nucl-ex/0805.4153].
- [15] R. Rapp and J. Wambach, "Chiral symmetry restoration and dileptons in relativistic heavy-ion collisions", *Adv. Nucl. Phys.* **25** (2000) [arXiv:hep-ph/9909229].
- [16] G.E. Brown and M. Rho, "Scaling effective Lagrangians in a dense medium", *Phys. Rev. Lett.* **66** (1991) 2720.
- [17] R. Averbeck *et al.* (TAPS Collaboration), "Production of π^0 and η mesons in carbon-induced relativistic heavy-ion collisions", *Z. Phys. A* **359** (1997) 65.
- [18] S.D. Gupta J. Zhang and C. Gale, "Momentum-dependent nuclear mean fields and collective flow in heavy-ion collisions", *Phys. Rev. C* **50** (1994) 1617 [arXiv:nucl-th/9405006].
- [19] W. Wilson *et al.*, "Inclusive di-electron cross sections in $p+p$ and $p+d$ interactions at beam energies from 1.04 GeV to 4.88 GeV", *Phys. Rev. C* **57** (1998) 1865 [arXiv:nucl-ex/9708002].
- [20] R. Shyam and U. Mosel, "Dilepton production in nucleon-nucleon collisions revisited", *Phys. Rev. C* **79** (2009) 035203 [arXiv:0811.0739 [hep-ph]].
- [21] V. Pechenov and G. Agakichiev, *Particle and Nuclei (Letters 2)* (2000) 1001.
- [22] A. Rustamov, "Exclusive η meson reconstruction in proton-proton collisions at 2.2 GeV with HADES spectrometer and high resolution tracking", Phd thesis, Technische Universität Darmstadt, Germany (2006).
- [23] Baldini *et al.*, "Landolt-Bornstein vol. 12", Springer (1987) Berlin.
- [24] S. Teis *et al.*, "Pion production in heavy-ion collisions at SIS energies", *Z. Phys. A* **356** (1997) 421.
- [25] J. Bystricky *et al.*, "Energy dependence of nucleon-nucleon inelastic total cross section", *J. Physique* **48** (1987) 1901.
- [26] J. Bystricky and F. Lehard, "Nucleon-nucleon scattering data", *Physics Data (N11 – 1 (1978), N11 – 2 (1981))*.
- [27] F. Shimizu *et al.*, "Measurement of the pp cross sections in the momentum range 0.9 – 2.0 GeV/c", *Nucl. Phys. A* **386** (1982) 571.
- [28] H. Calén *et al.*, "Measurement of the quasifree $p + n \rightarrow p + n + \eta$ reaction near threshold", *Phys. Rev. C* **58** (1998) 2667.
- [29] H. Calén *et al.*, "Measurement of the quasifree $p + n \rightarrow d + \eta$ reaction near threshold", *Phys. Rev. Lett.* **79** (1997) 2642.
- [30] H. Calén *et al.*, "Threshold structure of the quasifree $p + n \rightarrow d + \eta$ reaction", *Phys. Rev. Lett.* **80** (1998) 2069.
- [31] A.M. Bergdolt *et al.*, "Total cross section of the $p + p \rightarrow p + p + \eta$ reaction near threshold", *Phys. Rev. D* **48** (1993) 2969.

- [32] E. Chiavassa *et al.*, "Measurement of the $p + p \rightarrow p + p + \eta$ total cross section between 1.265 GeV and 1.5 GeV", Phys. Lett. **B 322** (1994) 270.
- [33] H. Calén *et al.*, "The $p + p \rightarrow p + p + \eta$ reaction near the kinematical threshold", Rhys. Lett. **B 366** (1996) 39.
- [34] B. Kämpfer and L.P. Kaptari, "Di-electron bremsstrahlung in intermediate-energy pn and Dp collisions", Nucl. Phys. **A 764** (2006) 338.
- [35] M. Krivoruchenko *et al.*, "Dilepton production in proton proton collisions at Bevalac energies", J. Phys. **G 29** (2003) 603 [arXiv:nucl-th/0010056].
- [36] R. Holzmann *et al.*, "Contribution of π^0 and η Dalitz decays to the dilepton invariant-mass spectrum in 1 AGeV heavy-ion collisions", Phys. Rev. **C 56** (1997) 2920.
- [37] R. Averbek *et al.*, "Production of π^0 and η mesons in carbon-induced relativistic heavy-ion collisions", Z. Phys. **A 359** (1997) 65.
- [38] CBM experiment, Progress Report (2007) <http://www.gsi.de/documents/DOC-2008-May-3-1.pdf>.
- [39] CBM experiment, Technical Status Report (2005) <http://www.gsi.de/onTEAM/dokumente/public/DOC-2005-Feb-447.html>.
- [40] G. Agakishiev *et al.* (CERES Collaboration), "Enhanced production of low mass electron pairs in 200 GeV/u S+Au collisions at the CERN SPS", Phys. Rev. Lett. **75** (1995) 1272.
- [41] D. Adamova *et al.* (CERES Collaboration), "Enhanced production of low-mass electron-positron pairs in 40 AGeV Pb+Au collisions at the CERN SPS", Phys. Rev. Lett. **91** (2003) 042301 [arXiv:nucl-ex/0209024].
- [42] G. Agakishiev *et al.* (CERES Collaboration), "Low-mass e^+e^- pair production in 158 AGeV Pb+Au collisions at the CERN SPS, its dependence on multiplicity and transverse momentum", Phys. Lett. **B 422** (1998) 405 [arXiv:nucl-ex/9712008].
- [43] A. Toia *et al.* (PHENIX Collaboration), "Measurements of dilepton continuum at the PHENIX experiment at RHIC", PoS CPOD07 (2007) 037 [arXiv:0711.2118 [nucl-ex]].
- [44] P. Braun-Munzinger, A. Andronic and J. Stachel, "Hadron production in central nucleus-nucleus collisions at chemical freeze-out", Nucl. Phys. **A 772** (2006) 167 [arXiv:nucl-th/0511071].
- [45] W-M Yao *et al.*, "Nuclear and particle physics", J. Phys. **G 33** (2006) 299.
- [46] CBM experiment, "Lecture Notes in Physics", Springer (2008) in preparation.
- [47] Z. Fodor and S.D. Katz, "Critical point of QCD at finite T and μ , lattice results for physical quark masses", JHEP **0404** (2004) 050 [arXiv:hep-lat/0402006].
- [48] F. Karsch *et al.*, "Where is the chiral critical point in 3-flavor QCD?", Nucl. Phys. Proc. Suppl. **129** (2003) 614 [arXiv:hep-lat/0309116].

- [49] A. Schmitt, K. Rajagopal (For a review with references to original literature see M.G. Alford and T. Schafer), "Color superconductivity in dense quark matter", *Rev. Mod. Phys.* **80** (2008) 1455 [arXiv:0709.4635 [hep-ph]].
- [50] Larry McLerran, "Quarkyonic Matter and the phase diagram of QCD", (2008) [arXiv:0808.1057v1 [hep-ph]].
- [51] L. McLerran and R.D. Pisarski, "Phases of dense quarks at large N_c ", *Nucl. Phys. A* **796** (2007) 83 [arXiv:0706.2191 [hep-ph]].
- [52] L. McLerran, Ch. Sasaki and K. Redlich, "Quarkyonic matter and chiral symmetry breaking", (2008) [arXiv:0812.3585v1 [hep-ph]].
- [53] Relativistic Heavy Ion Collider at BNL <http://www.bnl.gov/rhic/>.
- [54] Large Hadron Collider at CERN <http://lh.web.cern.ch/lhc/>.
- [55] C. Blume *et al.*, "Review of results from the NA49 collaboration", *J. Phys. G* **31** (2005) 685 [arXiv:nucl-ex/0411039].
- [56] M. Gázquez and M.I. Gorenstein, *Acta Phys. Pol.* **B 30** (1999) 2707.
- [57] K. Rajagopal, M. Stephanov and E. Shuryak, "Signatures of the tricritical point in QCD", *Phys. Rev. Lett.* **81** (1998) 4816 [arXiv:hep-ph/9806219].
- [58] K. Rajagopal, M. Stephanov and E. Shuryak, "Event-by-event fluctuations in heavy-ion collisions and the QCD critical point", *Phys. Rev. D* **60** (1999) 114028 [arXiv:hep-ph/9903292].
- [59] C. Alt *et al.* (NA49 Collaboration), "Centrality and system size dependence of multiplicity fluctuations in nuclear collisions at 158 AGeV", *Phys. Rev. C* **75** (2007) 064904 [arXiv:nucl-ex/0612010].
- [60] Y. Nambu, "Dynamical symmetries and fundamental fields", *Proceedings of the Second Coral Gables Conference on Symmetry Principles at High Energy* (1965).
- [61] M. Gell-Mann and Y. Neeman, "The Eightfold way: a review with a collection of reprints", W.A. Benjamin QCD161:G4, (1964).
- [62] T. Hatsuda and S.H. Lee, "QCD sum rules for vector meson in the nuclear medium", *Phys. Rev. C* **46** (1992) 34.
- [63] S. Leupold and U. Mosel, "On QCD sum rules for vector mesons in nuclear medium", *Phys. Rev. C* **58** (1998) 2939 [arXiv:nucl-th/9805024].
- [64] J.J. Sakurai, "Theory of strong interactions", *Annals Phys.* **11** (1960) 1.
- [65] F.V. Murphy and D.E. Yount, "Photons as hadrons".
- [66] M. Harada and K. Yamawaki, "Wilsonian matching of effective field theory with underlying QCD", *Phys. Rev. D* **64** (2001) 014023 [arXiv:hep-ph/0009163].
- [67] L.M. Barkov *et al.*, "Electromagnetic pion form factor in the timelike region", *Nucl. Phys. B* **256** (1985) 365.

- [68] G.E. Brown and M. Rho, "Chiral restoration in hot and/or dense matter", Phys. Rept. **269** (1995) 333 [arXiv:hep-ph/9504250].
- [69] B.L. Friman, M. Herrmann and W. Norenberg, "Properties of rho mesons in nuclear matter", Nucl. Phys. A **560** (1993) 411.
- [70] G. Chanfray and P. Schuck, "The Rho meson in dense matter and its influence on dilepton production rates", Nucl. Phys. A **555** (1993) 329.
- [71] S. Leupold *et al.*, "The spectral function of the ρ meson in nuclear matter", Nucl. Phys. A **632** (1998) 109 [arXiv:nucl-th/9708004].
- [72] G. Chanfray, R. Rapp and J. Wambach, "Medium modifications of the rho meson at CERN SPS energies", Phys. Rev. Lett. **76** (1996) 368 [arXiv:hep-ph/9508353].
- [73] E. Oset, D. Cabrera and M.J. Vicente Vacas, "Chiral approach to the rho meson in nuclear matter", Nucl. Phys. A **705** (2002) 90 [arXiv:nucl-th/0011037].
- [74] R. Rapp and C. Gale, "Rho properties in a hot gas: dynamics of meson resonances", Phys. Rev. C **60** (1999) 024903 [arXiv:hep-ph/9902268].
- [75] G.F. Bertsch and S. Das Gupta, "A guide to microscopic models for intermediate-energy heavy-ion collisions", Phys. Rep. **160** (1988) 189.
- [76] C.M. Ko and Q. Li, "Relativistic Vlasov-Uehling-Uhlenbeck model for heavy-ion collisions", Phys. Rev. C **37** (1988) 2270.
- [77] W. Ehehalt and W. Cassing, "Relativistic transport approach for nucleus nucleus collisions from SIS to SPS energies", Nucl. Phys. A **602** (1996) 449.
- [78] J. Aichelin *et al.*, Phys. Rep. **202** (1991) 233.
- [79] H. Stöcker, H. Sorge and W. Greiner, Annals Phys. **192** (1989) 266.
- [80] S.A. Bass *et al.*, "Microscopic models for ultrarelativistic heavy-ion collisions", Prog. Part. Nucl. Phys. **41** (1998) 255 [arXiv:nucl-th/9803035].
- [81] The Giessen Boltzmann-Uehling-Uhlenbeck project <http://gibuu.physik.uni-giessen.de/GiBUU>.
- [82] C. Hartnack *et al.*, Eur. Phys. J. A **1** (1998) 151 [arXiv:nucl-th/9811015].
- [83] E. Santini *et al.*, "Dilepton production in heavy-ion collisions with in-medium spectral functions of vector mesons", (2008) [arXiv:0811.2065 [nucl-th]].
- [84] G.D. Westfall *et al.*, "Nuclear fireball model for proton inclusive spectra from relativistic heavy-ion collisions", Phys. Rev. Lett. **37** (1976) 1202.
- [85] J. Stachel, "Tests of thermalization in relativistic nucleus-nucleus collisions", Nucl. Phys. A **610** (1996) 509.
- [86] T. Renk and J. Ruppert, "From $In+In$ to $Pb+Pb$ collisions: Lessons from high-precision dilepton measurements", (2006) [arXiv:hep-ph/0603110].

- [87] S.D. Drell and T.-M. Yan, "Massive lepton-pair production in hadron-hadron collisions at high energies", *Phys. Rev. Lett.* **25** (1970) 316.
- [88] M. Sekimoto *et al.*, "Spectrometer for measurements of ϕ mesons in nuclear matter produced through 12 GeV $p+A$ reactions", *Nucl. Instrum. Meth. A* **516** (2004) 390.
- [89] M.H. Wood *et al.*, "Light vector mesons in the nuclear medium". *Phys. Rev. C* **78** (2008) 015201 [arXiv:0803.0492 [nucl-ex]].
- [90] H. van Hees and R. Rapp, "Dilepton radiation at the CERN Super Proton Synchrotron", *Nucl. Phys. A* **806** (2008) 339 [arXiv:0711.3444 [hep-ph]].
- [91] A. Toia *et al.* (PHENIX Collaboration), " e^+e^- pairs: A Clock and a thermometer of heavy-ion collisions", *J. Phys. G* **35** (2008) 104037 [arXiv:0805.0153 [nucl-ex]].
- [92] R. Shyam and U. Mosel, "Role of baryonic resonances in the dilepton emission in nucleon-nucleon collisions", *Phys. Rev. C* **67** (2003) 065202 [arXiv:hep-ph/0303035].
- [93] M.I. Krivoruchenko *et al.*, "Comment on delta radiative and Dalitz decays", *Phys. Rev. D* **65** (2002) 017502 [arXiv:nucl-th/0104045].
- [94] C. Gale and J. Kapusta, "Dilepton radiation from high temperature nuclear matter", *Phys. Rev. C* **35** (1987) 2107.
- [95] H.Z. Huang *et al.*, "Di-electron yields in $p+d$ and $p+p$ collisions at 4.9 GeV", *Phys. Lett. B* **297** (1992) 233.
- [96] W.K. Wilson *et al.*, "Di-electron measurements in $p+p$ and $p+d$ interactions from $E_{beam} = 1$ GeV to 4.9 GeV", *Phys. Lett. B* **316** (1993) 245.
- [97] W. Cassing, U. Mosel, M. Schafer and T.S. Biro, " e^+e^- production in proton neutron collisions", *Phys. Lett. B* **221** (1989) 1.
- [98] E.L. Bratkovskaya and W. Cassing, "Dilepton production and off-shell transport dynamics at SIS energies", *Nucl. Phys. A* **807** (2008) 214 [arXiv:0712.0635 [nucl-th]].
- [99] R. Gernhäuser, "Ein ringabbildener Cherenkovdetektor zur Untersuchung schwerer Projectilefragmente", Phd thesis, Technische Universität München, Germany (1998).
- [100] L. Fabbietti, "Study of the e^+e^- pair acceptance in the dilepton spectrometer HADES", Phd thesis, Technische Universität München, Germany (2003).
- [101] T. Bretz, "Magnetfeldeigenschaften des Spektrometers HADES", Master thesis, Technische Universität München, Germany (1999).
- [102] M. Sánchez García, "Momentum reconstruction and pion production analysis in the HADES spectrometer at GSI", Phd thesis, Universidade de Santiago De Compostela, Spain (2003).
- [103] C. Müntz *et al.* (HADES Collaboration), "The HADES tracking system", *Nucl. Instrum. Meth. A* **535** (2004) 242.
- [104] C. Garabatos *et al.* (HADES Collaboration), "Optimisation of low-mass drift chambers for HADES", *Nucl. Instrum. Meth. A* **412** (1998) 38.

- [105] H. Bokemeyer *et al.* (HADES Collaboration), "Development of low-mass drift chambers for the HADES spectrometer", Nucl. Instrum. Meth. A **477** (2002) 397.
- [106] C. Agodi *et al.* (HADES Collaboration), "The HADES time-of-flight wall", Nucl. Instrum. Meth. A **492** (2002) 14.
- [107] D. Belver *et al.*, "The HADES RPC inner TOF Wall", (2008).
- [108] A. Blanko *et al.*, "In-beam measurements of the HADES-TOF RPC wall", (2008).
- [109] I. Fröhlich, "A general purpose trigger and readout board for HADES and FAIR-Experiments", IEEE Trans.Nucl.Sci.**55** (2008) 59.
- [110] K. Lapidus, "Analysis of di-electron production in $d+p$ interactions at 1.25 GeV/u with HADES", Phd thesis (in preparation), Institut of Nuclear Research, Russian Academy of Science, Moskow, Russia.
- [111] HYDRA - HADES analysis package <http://www-hades.gsi.de/>.
- [112] ROOT - An object oriented data analysis framework <http://root.cern.ch/>.
- [113] ORACLE Database <http://www.oracle.com/>.
- [114] J. Bielčik, "Dilepton spectroscopy with HADES", Phd thesis, Technische Universität Darmstadt, Germany (2004).
- [115] A. Toia, "Performance of the HADES spectrometer for dilepton identification in the reaction $C+C$ at 1 – 2 AGeV", Phd thesis, Justus-Liebig-Universität Giessen, Germany (2004).
- [116] M. Sudol, "Measurement of low-mass e^+e^- pair production in 2 AGeV $C+C$ collisions with HADES", Phd thesis, Johann Wolfgang Universität Frankfurt am Main, Germany (2007).
- [117] Y. C. Pachmayer, "Dielektronenproduktion in $^{12}C+^{12}C$ Kollisionen bei 1 GeV/u pro nukleon", Phd thesis, Johann Wolfgang Universität, Frankfurt am Main, Germany (2008).
- [118] Status of Runge Kutta tracking in HYDRA (2006) <http://hades-wiki.gsi.de/pub/SimAna/RungeKuttaTrackingStatus/>.
- [119] P.V.C. Hough, "Methods and means for recognition complex patterns", U.S.Patent **3(069654)** (1962) 32.
- [120] S. Spataro, "Characterization of the HADES spectrometer in $p+p$ collisions at 2.2 GeV: elastic scattering and exclusive η reconstruction", Phd thesis, Università degli Studi di Catania, Italy (2002).
- [121] S. Eidelman *et al.*, Phys. Lett. **B 592** (2004).
- [122] J. Otwinowski, "Pomiar widm par e^+e^- wyprodukowanych w zderzeniach $^{12}C+^{12}C$ przy energii $E_{kin} \leq 2.0$ AGeV przy uzyciu spektrometra HADES", Phd thesis, Jagiellonian University, Krakow, Poland (2003).

- [123] J. Pietraszko, "System pozycyjnie czułych komor drutowych do identyfikacji elektronów i pozytronów w spektrometrze HADES", Phd thesis, IF Uniwersytet Jagielloński, Krakow, Poland (2001).
- [124] M. Gázdzicki and M.I. Gorenstein, "Background subtraction from the dilepton spectra in nuclear collisions", (2000) [arXiv:hep-ph/0003319].
- [125] Augustin-Louis Cauchy, "Cours d'analyse de l'École Royale Polytechnique, premier partie, Analyse algébrique", Editrice Clueb Bologna, Paris (1821).
- [126] I. Fröhlich *et al.*, "Pluto: A Monte Carlo simulation tool for hadronic physics", PoS ACAT2007 (2007) 076 [arXiv:0708.2382 [nucl-ex]].
- [127] Pluto: A Monte Carlo simulation tool for hadronic physics <http://www-hades.gsi.de/>.
- [128] HADES internal report, "M3 trigger efficiency" (2007) <http://hades-wiki.gsi.de/pub/SimAna/>.
- [129] G. Agakichiev *et al.* (HADES Collaboration), "Measurement of charged pions in $^{12}\text{C}+^{12}\text{C}$ collisions at 1 AGeV and 2 AGeV with HADES", (2009) [arXiv:0902.4377 [nucl-ex]].
- [130] D. Albers *et al.* (EDDA Collaboration), "Proton-proton elastic scattering excitation functions at intermediate energies", Phys. Rev. Lett. **78** (1997) 1652.
- [131] A. Yegneswaran *et al.*, "The Dilepton spectrometer", Nucl. Instrum. Meth. **A 290** (1990) 61.
- [132] W.K. Wilson *et al.*, "Inclusive di-electron cross sections in $p+p$ and $p+d$ interactions at beam energies from 1.04 GeV to 4.88 GeV", Phys. Rev. **C 57** (1998) 1865 [arXiv:nucl-ex/9708002].
- [133] J. Aichelin private communication (2008).
- [134] I. Fröhlich *et al.*, "The Pluto event generator: status and recent developments", to be published (2008).
- [135] L.G. Landsberg, "Electromagnetic decays of light mesons", Phys. Rep. **128** (1985) 301.
- [136] Q. Wan and F. Iachello, "A unified description of baryon electromagnetic form factors", Int. J. Mod. Phys. **A 20** (2005) 1846.
- [137] Q. Wan, Phd thesis (2007).
- [138] A. Sibirtsev and W. Cassing, "Final state interactions in near threshold meson production from $p+p$ collisions", (1999) [arXiv:nucl-th/9904046].
- [139] W.K. Wilson. Acta Phys. Pol. **B 29** (1998) 3291.
- [140] FAIR Baseline Technical Report (2006) <http://www.gsi.de/fair/reports/btr.html>.
- [141] N. Wermes, "Pixel detectors for particle and imaging applications", Nucl. Instrum. Meth. **A 512** (2003) 277 [arXiv:hep-ex/0209014].
- [142] TOSCA, Vector Fields <http://www.vectorfields.com/content/view/27/50/>.

- [143] GEANT: Detector description and simulation tool <http://consult.cern.ch/writeup/geant/>.
- [144] A. Andronic *et al.* (CBM collaboration), "The TRD of the CBM experiment", Nucl. Instrum. Meth. **A 563** (2006) 349.
- [145] M. Petris *et al.*, "High counting rate transition radiation detector", Nucl. Instrum. Meth. **A 581** (2007) 406.
- [146] A. Laszlo *et al.*, "NA61/Shine at the CERN SPS", PoS CPOD07 (2007) 054 [arXiv:0709.1867 [nucl-ex]].
- [147] S. Vogel, D. Schumacher and M. Bleicher, "Theoretical analysis of dilepton spectra in heavy-ion collisions at GSI-FAIR energies", Acta Phys. Hung. **A 27** (2006) 451 [arXiv:nucl-th/0608041].
- [148] CbmRoot simulation framework <http://cbmroot.gsi.de/>.
- [149] R. Arnaldi *et al.*, "A new approach to linear filtering and prediction problems", Nucl. Instrum. Meth. **A 451** (2000) 462.
- [150] I. Kisel, I. Abt, D. Emeliyanov and S. Masciocchi, "CATS: A cellular automaton for tracking in silicon for the HERA-B vertex detector", Nucl. Instrum. Meth. **A 489** (2002) 389.
- [151] I. Kisel *et al.* (CBM Collaboration), "Event reconstruction in the CBM experiment", Nucl. Instrum. Meth. **A 566** (2006) 85.
- [152] R.E. Kalman, "A new approach to linear filtering and prediction problems", Transaction of the ASME, Journal of Basic Engineering 82 (1960) 35.
- [153] R. Frühwirth *et al.*, "Data Analysis Techniques for High-Energy Physics", Cambridge University Press; 2 edition (2001).
- [154] Ring recognition in the CBM RICH detector, CBM-RICH-note-2008-001 <http://www.gsi.de/documents/DOC-2008-Jan-29-1.pdf>.
- [155] M. Deveaux, "Development of fast and radiation hard Monolithic Active Pixel Sensor (MAPS) optimized for open charm meson detection with the CBM - vertex detector", Phd thesis, Johann Wolfgang Goethe Universität, Frankfurt am Main, Germany (2007).
- [156] S. Damjanovic *et al.* (NA60 Collaboration), "NA60 results on the ρ^0 spectral function in $In+In$ collisions", Nucl. Phys. **A 783** (2007) 327 [arXiv:nucl-ex/0701033]
- [157] D. Perkins, "Introduction to high energy physics", Addison-Wesley Publishing Company (1987).

Acknowledgements

I would like to gratefully acknowledge my advisor, Prof. Dr. Joachim Stroth for his support, scientific advice and insightful discussions and suggestions. His critique and guidance has added substantial value to my research. I am also extremely grateful to the Prof. Dr. Peter Senger for giving me an exciting job. Thanks to both of you for given me the freedom to pursue various projects without objection.

I will forever be thankful to Dr. Claudia Höhne. In her I found another strong supporter of my work.

It has been a wonderful experience to work within the CBM and HADES collaborations. However it is difficult to recall every person that has assisted, contributed or more importantly encouraged me to pursue these studies. I thank all my CBM and HADES collaborators for being excellent teachers, always available for scientific discussions. I hope that being sometimes in a hurry or stressed did not prevent me for expressing my thanks to you at the appropriate moment during the last four years. I hope we can continue our cooperation in the coming years.

No matter what I don't have. No matter what I don't get. I have a gift that is no cost to anyone who enters my heart. Thank you, my family, for encouraging me so much in life and helped me become the person I am today. I am proud that I belong to you and that you belong to me; I love you all more than I have words to express. Thank you, for your special charm.

Lebenslauf

Tetyana Galatyuk

Geburtsdatum: 10. September 1981
Geburtsort: Kuznetsovsk, Ukraine

1988 – 1998 Besuch der allgemeinbildenden Schule N4
in Kuznetsovsk, Ukraine.

1998 – 2003 graduiert an der Kiev National Taras Shevchenko Universität,
Fachbereich Physik, Spezialfach Kernphysik und
Elementarteilchen Physik:

Juni 2002 bestandene Staatsprüfung in Allgemeine Physik,
Verteidigung der Bachelorarbeit bei Dr. I. Kadenko.
Thema der Bachelorarbeit "Development of the
cross section libraries for the thermal reactor type
using WIMS-D/5B code."

Juni 2003 bestandene Staatsprüfung in Kernphysik und
Elementarteilchen Physik, Verteidigung der Masterarbeit
"Modeling of the transient for VVER-440 (Rivne NPP)
reactor type using RELAP-5/3D code" bei Dr. I. Kadenko.

2003 – 2004 angestellt am Rivne Kernkraftwerk,
in der Abteilung für Nuklearsicherheit.

seit October 2005 Mitarbeiter an der Gesellschaft für
Schwerionenforschung, Darmstadt, Deutschland.
Doktorand am Institut für Kernphysik der
Goethe–Universität Frankfurt am Main
bei Prof. Dr. Joachim Stroth.

